

**NUMERICAL MODELING OF ROCK CUTTING AND ITS ASSOCIATED
FRAGMENTATION PROCESS USING THE FINITE ELEMENT METHOD**

by

María Carolina Jaime

B.S. in Civil Engineering, Universidad de Los Andes, 2002

M.S. in Civil Engineering, Universidad de Los Andes, 2003

Submitted to the Graduate Faculty of
the Swanson School of Engineering in partial fulfillment
of the requirements for the degree of
Doctor of Philosophy

University of Pittsburgh

2011

UNIVERSITY OF PITTSBURGH
SWANSON SCHOOL OF ENGINEERING

This dissertation was presented

by

María Carolina Jaime

It was defended on

November 22nd, 2011

and approved by

Isaac K. Gamwo, Ph.D., Researcher
National Energy Technology Laboratory, U.S. Department of Energy

Anthony Iannacchione, Ph.D., Associate Professor,
Department of Civil and Environmental Engineering

Albert To, Ph.D., Assistant Professor,
Department of Mechanical Engineering and Materials Science

Julie M. Vandenbossche, Ph.D., Assistant Professor,
Department of Civil and Environmental Engineering

Dissertation Director: Jeen-Shang Lin, Sc.D., Associate Professor,
Department of Civil and Environmental Engineering

Copyright © by María Carolina Jaime
2011

NUMERICAL MODELING OF ROCK CUTTING AND ITS ASSOCIATED FRAGMENTATION PROCESS USING THE FINITE ELEMENT METHOD

María Carolina Jaime, PhD

University of Pittsburgh, 2011

As the need for reaching fuel reserves at greater depths increases, over the past 30 years scientists have been exploring and developing the technology required to efficiently drill rock at highly pressured environments; yet, there are still gaps in the understanding of the physical phenomena involved. One of the basic problems has to do with the cutter-to-rock interaction during the cutting process.

This study employs the Finite Element Method (FEM) to investigate the mechanics of rock cutting because of its flexibility in handling material heterogeneity, nonlinearity and boundary conditions. Using the FEM to model fracturing of a brittle material like rock –and consequently treating its discontinuous chips– is a challenging undertaking that requires the tackling of a sequence of complex problems: As the cutter advances and touches the rock material, a contact problem first arises. This is followed by nonlinear deformation and the determination as to when and whether the rock would fail. Subsequently, the question of how to initiate the fragmentation process has to be resolved if the rock fails. The cycle repeats starting with a new contact problem after new surfaces are generated due to fracture.

At present, few researchers have focused on crack initiation and subsequent crack propagation, but even fewer have accounted for actual chip formation, and none has considered the dynamic interaction amongst chips, newly formed surfaces, and the cutter. One important goal of this study is to advance the modeling such that it is possible to follow the cutter in a complete cutting process in a credible manner.

A framework of three-dimensional FEM modeling was developed so that the fragmentation process observed in laboratory rock scratching tests could be properly simulated. A thorough calibration of the rock material model was carried out, together with extensive

sensitivity analyses of contact models, damage based failure and its associated fracture modeling using the commercial software LS-DYNA.

This study was able to obtain ductile failure mode for shallow cuts, and brittle failure for deep cuts as observed in the laboratory, all without *a priori* setting on the failure modes. Also, cutting force magnitudes and tendencies obtained from the study correlated well with published results of the physical experiments. Moreover, in a limited scope, this study also investigated the effects of applying external hydrostatic pressure on rock cutting. Preliminary numerical results indicate a good comparison with few published data. Lastly, theoretical models for obtaining cutting forces were assessed, providing a better understanding of their limitations and usability.

TABLE OF CONTENTS

PREFACE.....	XX
1.0 INTRODUCTION	1
1.1 BACKGROUND	1
1.2 MOTIVATION	2
1.3 PROBLEM STATEMENT	4
1.4 STATE OF THE ART IN ROCK CUTTING MODELING	5
1.4.1 The Use of the Finite Element Method	5
1.4.1.1 The Explicit FEM	6
1.4.1.2 The Finite Element Approximation	7
1.4.1.3 Central Difference Scheme for Explicit Time Integration.....	9
1.4.2 Previous Research on Rock Cutting Modeling	10
1.4.2.1 Some Numerical Approaches Used	10
1.4.2.2 Numerical Contributions Through the Use of FEM	14
1.5 RESEARCH OBJECTIVES AND SCOPE	18
1.5.1 Main Objective.....	18
1.5.2 Specific Objectives.....	18
2.0 EXPERIMENTAL BENCHMARK.....	20
2.1 LABORATORY SCRATCHING TESTS	20
2.1.1 Mechanics of the Scratching Tests.....	23
2.1.1.1 Deep Cut Experiments	23
2.1.1.2 Shallow Cut Experiments	24
2.1.2 Force Signals from Scratching Tests.....	25
2.2 LABORATORY CHARACTERIZATION FOR PARAMETER CALIBRATION...	26

2.2.1	Experimental Isotropic Compression.....	26
2.2.2	Experimental Triaxial Compression	27
2.2.3	Experimental Triaxial Extension	29
2.2.4	Experimental Failure Envelopes	30
2.3	GENETIC ALGORITHM FOR CURVE-FITTING OPTIMIZATION.....	30
3.0	ROCK BEHAVIOR THROUGH CONSTITUTIVE MODELS	32
3.1	MODELING ROCK WITH CONCRETE CONSTITUTIVE LAWS	32
3.1.1	Definition of the Failure Criterion	33
3.1.2	Stress State before Failure.....	34
3.2	ROCK MATERIAL MODELS IN LS-DYNA.....	35
3.2.1	Mat_105 – Damage 2 Model.....	37
3.2.1.1	Mat_105 Input Calibration.....	39
3.2.2	Mat_111 – Johnson Holmquist Concrete Model	40
3.2.2.1	Damage Accumulation in Mat_111	40
3.2.2.2	Pressure-Volume Relationship in Mat_111	41
3.2.2.3	Mat_111 Input Calibration.....	42
3.2.3	Mat_72R3 – Concrete Damage Rel. 3 Model.....	44
3.2.3.1	Mat_72R3 Input Calibration	45
3.2.3.2	Compressive Meridians in Mat_72R3	46
3.2.3.3	Calculation of Current Deviatoric Stress in Mat_72R3	49
3.2.3.4	Tensile Meridians in Mat_72R3	50
3.2.3.5	Damage Accumulation in Mat_72R3	52
3.2.3.6	Pressure-Volume Relationship in Mat_72R3	53
3.2.4	Mat_159 – Continuous Surface Cap Model.....	55
3.2.4.1	Mat_159 Input Calibration.....	56
3.2.4.2	Plasticity Surface in Mat_159.....	57
3.2.4.3	Cap Hardening in Mat_159.....	61
3.2.4.4	Shear Hardening Surface in Mat_159.....	65
3.2.4.5	Damage Accumulation in Mat_159	66
3.2.4.6	Regulating Mesh Size Sensitivity in Mat_159.....	68

3.2.4.7	Visco-plastic Rate Effects in Mat_159	70
4.0	SINGLE ELEMENT TESTS FOR MATERIAL MODEL VALIDATION	72
4.1	TEST SETUP	72
4.2	VALIDATION OF MAT_105	73
4.3	VALIDATION OF MAT_111	75
4.3.1	Triaxial Stress-Strain Response in Mat_111	75
4.3.2	Strength at Failure in Mat_111	78
4.4	VALIDATION OF MAT_72R3	79
4.4.1	Triaxial Stress-Strain Response in Mat_72R3	80
4.4.2	Strength at Failure in Mat_72R3	83
4.5	VALIDATION OF MAT_159	84
4.5.1	Triaxial Stress-Strain Response in Mat_159	84
4.5.2	Strength at Failure in Mat_159	87
4.6	COMPARISON OF TEST RESULTS: LABORATORY VS. SIMULATION	90
4.6.1	Isotropic Compression	90
4.6.2	Triaxial Compression	91
4.6.3	Triaxial Extension	92
4.6.4	Failure Envelope	93
5.0	CALIBRATION OF THE ROCK CUTTING MODEL.....	94
5.1	THE ROCK DOMAIN	94
5.1.1	Mesh Sensitivity	94
5.1.2	Rock Specimen Geometry	95
5.1.3	Boundary Conditions	96
5.2	CONTACT FORMULATION	98
5.2.1	Cutter-Rock Contact	98
5.2.1.1	Constraint Contact Formulation	99
5.2.1.2	Rigid Wall Contact Simplification	102
5.2.2	Rock-Rock Contact	103
5.2.2.1	Penalty Contact Formulation	103

5.2.2.2	Contact Stiffness Calculation.....	104
5.2.2.3	Calibration of Penalty Contact Parameters.....	105
5.3	CRACK INITIATION AND FRAGMENT FORMATION.....	106
5.3.1	Element Erosion.....	107
5.3.1.1	Treatment of the Mass of Eroded Elements.....	107
5.3.2	Sensitivity Analysis of “Added” Erosion Criteria.....	108
5.3.3	Sensitivity Analysis of Erosion Criteria in Mat_159.....	111
5.4	ANALYSIS OF FORCES FROM SIMULATIONS.....	118
5.4.1	Force Signal Filtering and Calibration.....	118
5.4.1.1	Butterworth Filter on Simulation Force Signal.....	119
5.4.1.2	Force Signal Calibration: Experiment vs. Simulation.....	119
5.4.2	Factors Affecting Resulting Cutting Forces and Chip Formation.....	122
5.4.2.1	System Damping.....	124
5.4.2.2	Cutting Velocity.....	132
5.4.2.3	Damage Recovery.....	138
6.0	NUMERICAL SIMULATION OF CUTTING ON ROCK SLABS.....	144
6.1	MODEL GEOMETRY.....	144
6.1.1	Rock Specimen Geometry.....	144
6.1.2	Cutter Geometry.....	146
6.2	SIMULATION OUTPUT.....	147
6.2.1	Deep Cut Simulation Output.....	147
6.2.2	Shallow Cut Simulation Output.....	151
6.2.3	The Effect of Cutting Depth on the Force.....	155
6.3	EROSION ANALYSIS FOR SLAB CUT SIMULATIONS.....	158
6.4	SPECIFIC ENERGY IN ROCK CUTTING.....	163
6.4.1	Background on Specific Energy.....	163
6.4.2	Specific Energy for Slab Cutting Simulations.....	163
7.0	NUMERICAL SIMULATION OF GROOVE CUTTING IN ROCK.....	165
7.1	MODEL GEOMETRY.....	165

7.1.1	Rock Specimen Geometry.....	165
7.1.2	Cutter Geometry.....	168
7.2	GROOVE CUT SIMULATION OUTPUT	168
7.2.1	Stresses Caused by Different Groove Size	168
7.2.2	The Effect of Groove Size on the Horizontal Cutting Force	170
7.3	EROSION ANALYSIS FOR GROOVE CUT SIMULATIONS	173
7.4	SPECIFIC ENERGY IN GROOVE CUTTING.....	182
7.5	EDGE EFFECT IN GROOVE CUTTING	185
8.0	GROOVE CUTTING IN ROCK UNDER PRESSURE	189
8.1	EXPERIMENTAL BENCHMARK OF GROOVE CUTTING UNDER PRESSURE	
	190	
8.1.1	Experiment Setup.....	190
8.1.2	Experimental Results	191
8.2	NUMERICAL SIMULATION OF PRESSURED GROOVE CUTTING IN ROCK	192
8.2.1	Model Geometry	193
8.2.1.1	Rock Specimen Geometry	193
8.2.1.2	Cutter Geometry.....	194
8.2.2	Application of Hydrostatic Pressure	195
8.2.2.1	Important considerations to define LOAD_DENSITY_DEPTH	196
8.2.2.2	Additional Recommendations.....	199
8.2.3	Pressured Groove Cut Simulation Output.....	200
8.3	EROSION AND SPECIFIC ENERGY FOR PRESSURED GROOVE CUT	
	SIMULATIONS.....	202
9.0	VALIDATING THE F.E. MODELS THROUGH THEORETICAL SOLUTIONS .	207
9.1	MERCHANT MODEL (1944)	208
9.1.1	Inclination of the Cutting Force	210
9.2	EVANS MODEL (1961)	211
9.2.1	Horizontal Slab-Cut Forces Based on Evans Model.....	213
9.3	NISHIMATSU MODEL (1972)	214

9.3.1	Horizontal Slab-Cut Forces Based on Nishimatsu Model	217
9.4	DETOURNAY & ATKINSON MODEL (2000)	218
9.4.1	Horizontal Slab-Cut Forces Based on Detournay and Atkinson Model	219
9.5	NUMERICAL VS. EXPERIMENTAL VS. ANALYTICAL SOLUTIONS	220
10.0	CONCLUDING REMARKS	225
10.1	SUMMARY AND CONCLUSIONS	225
10.1.1	Rock Behavior through a Sound Constitutive Model	225
10.1.2	Configuring LS-DYNA's Capabilities to Simulate Rock Cutting	226
10.1.3	Simulating Scratch Tests on a Rock Slab (Two-dimensional Cutting)	227
10.1.4	Simulating Scratch Tests with a Groove (Three-dimensional Cutting)	228
10.1.5	On the Computation of a True Specific Energy	228
10.1.6	The Effect of the Groove Edges on the Cutting Force	229
10.1.7	Groove Cutting Under Hydrostatic Pressure	230
10.1.8	Comparing the Results with Analytical Solutions	230
10.2	RECOMMENDATIONS FOR FUTURE WORK	231
BIBLIOGRAPHY		233

LIST OF TABLES

Table 1-1: Previous research in rock cutting modeling	11
Table 2-1: Mechanical properties of Vosges Sandstone.....	23
Table 3-1: Concrete and rock material models in LS-DYNA	36
Table 3-2: “Damage 2” material attributes in LS-DYNA	37
Table 3-3: Input Parameters for MAT_105	39
Table 3-4: Input Parameters for MAT_111	44
Table 3-5: Input Parameters for MAT_72R3.....	46
Table 3-6: Stress factor vs. Accumulated effective plastic strain.....	50
Table 3-7: Strain rate enhancement function.....	51
Table 3-8: Equation of state (EOS_TABULATED_COMPACTON) for MAT_72R3	54
Table 3-9: Input Parameters for MAT_159 (First trial).....	56
Table 5-1: Nodal degrees of freedom in FE models.....	97
Table 5-2: Calibrated input parameters for Penalty Contact	106
Table 5-3: Erosion criteria available in LS-DYNA	108
Table 5-4: Erosion criteria analyzed.....	109
Table 5-5: Characteristics of the force time history in the lab experiments and simulations.....	118
Table 5-6: Combinatory of critical input parameters for sensitivity analysis.....	124
Table 5-7: Final sensitivity analysis: Resultant cutting forces	128
Table 6-1: Simulated cutting sequence on Vosges Sandstone at a depth of 3.6 mm (damage contours).....	148

Table 6-2: Horizontal force signals at different cutting depths for slab cut simulations	156
Table 6-3: Output parameters for slab cut simulations in the ductile regime	164
Table 7-1: Dimensional information of the groove cut rock models.....	167
Table 7-2: Effective Stress (contours) when cutter displacement is 8.6 mm in all groove cutting cases	169
Table 7-3: Horizontal force signals at different cutting depths and widths for groove cut simulations	171
Table 7-4: Coefficient determination for F_{mean} expression as a function of groove size.....	173
Table 7-5: Output parameters for groove cut simulations in the ductile regime	183
Table 8-1: Calculated values of $D_{surface}$ corresponding to each modeled pressure.....	199
Table 9-1: Inclination of the total cutting force measured in the laboratory	211
Table 9-2: Horizontal force as a function of cutting depth according to Evans Model.....	214
Table 9-3: Horizontal force as a function of cutting depth according to Nishimatsu Model	217
Table 9-4: Adjusted horizontal force as a function of cutting depth according to Nishimatsu Model	217
Table 9-5: Horizontal force as a function of cutting depth according to Detournay and Atkinson Model	220
Table 9-6: Average horizontal cutting force from numerical, experimental, and analytical solutions	221

LIST OF FIGURES

Figure 1-1: PDC cutter (left), drill bit (right) (Kappele 2009).....	2
Figure 1-2: Oil well drilling scenario. Detail of a PDC bit at bottom hole (NETL 2007).....	2
Figure 1-3: Rock cutting simulation by Jonak (2001)	14
Figure 1-4: Rock cutting simulated with RFPA2D (Kou et al. 1999)	15
Figure 1-5: Cutting simulation on Catoosa Shale at 1.905 mm (0.075 in) of depth (Sunal 2009)	16
Figure 1-6: Apparent crack formation and chip formation (Tulu 2009).....	17
Figure 2-1: Rock Strength Device (FPMS 2007)	21
Figure 2-2: Forces acting on a sharp cutter.....	21
Figure 2-3: Scratch test on sandstone slab at shallow depth (Degrain et al. 2009)	22
Figure 2-4: Brittle failure on Berea Sandstone while cutting at 4 mm of depth.....	24
Figure 2-5: Ductile failure on Berea Sandstone while cutting at 0.3 mm of depth	25
Figure 2-6: Horizontal force during test at 3.6 mm depth of cut (Richard 1999).....	25
Figure 2-7: Horizontal force during test at 0.3 mm depth of cut (Richard 1999).....	26
Figure 2-8: Experimental isotropic compression of Vosges sandstone (Bésuelle et al. 2000).....	27
Figure 2-9: Experimental triaxial compression of Vosges sandstone (Bésuelle et al. 2000)	28
Figure 2-10: Experimental triaxial extension of Vosges sandstone (Bésuelle et al. 2000)	29
Figure 2-11: Experimental strength at failure of Vosges sandstone (Bésuelle et al. 2000).....	30
Figure 3-1: Schematic failure surface of concrete in 3D stress space (Chen 2007)	33
Figure 3-2: Deviatoric cross-section of the failure surface.....	34
Figure 3-3: Maximum compressive failure envelope fitting by Mat_111	43

Figure 3-4: Failure surfaces (a) and concrete constitutive behavior (b) in Mat_72R3 model	45
Figure 3-5: Maximum failure surface fitting by Mat_72R3	47
Figure 3-6: Residual surface fitting by Mat_72R3	48
Figure 3-7: Initial yield surface fitting by Mat_72R3.....	49
Figure 3-8: Equation of state for MAT_72R3	54
Figure 3-9: General shape of the yield surface in Mat_159 model (Murray 2007b).....	55
Figure 3-10: Compressive shear surface fitting by Mat_159.....	58
Figure 3-11: Tensile shear surface fitting by Mat_159.....	59
Figure 3-12: Torsion shear surface fitting by Mat_159	60
Figure 3-13: Cap curvature model (Fossum and Brannon 2004)	62
Figure 3-14: Example of parameter determination on isotropic compression curve (Murray 2007b).....	63
Figure 3-15: Isotropic compression curve fitting by Mat_159	65
Figure 4-1: Nodal degrees of freedom in one-element tests	73
Figure 4-2: Simulated triaxial compression with Mat_105 under different confinement	74
Figure 4-3: Simulated triaxial compression with Mat_111 under different confinement	76
Figure 4-4: Simulated triaxial extension with Mat_111 under different confinement	77
Figure 4-5: Simulated strength at failure with Mat_111.....	79
Figure 4-6: Simulated triaxial compression with Mat_72R3 under different confinement.....	81
Figure 4-7: Simulated triaxial extension with Mat_72R3 under different confinement.....	82
Figure 4-8: Simulated strength at failure with Mat_72R3	83
Figure 4-9: Simulated triaxial compression with Mat_159 under different confinement	85
Figure 4-10: Simulated triaxial extension with Mat_159 under different confinement	86
Figure 4-11: Example plots of the failure surfaces of LS-DYNA Model 159 in the meridian plane	87
Figure 4-12: Failure envelope in triaxial compression	88

Figure 4-13: Failure envelope in triaxial extension	88
Figure 4-14: Simulated strength at failure with Mat_159.....	89
Figure 4-15: Pressure vs. Volume strain - Comparison between experimental and simulated results	90
Figure 4-16: TXC Effective stress (MPa) vs. axial strain - Comparison of experimental and simulated results.....	91
Figure 4-17: TXC Volume strain vs. axial strain - Comparison of experimental and simulated results	91
Figure 4-18: TXE Effective stress (MPa) vs. axial strain - Comparison of experimental and simulated results.....	92
Figure 4-19: TXE Volume strain vs. axial strain - Comparison of experimental and simulated results	92
Figure 4-20: Effective stress (MPa) vs. Pressure (MPa) - Comparison of experimental and simulated results.....	93
Figure 5-1: Different element types evaluated in rock cutting	95
Figure 5-2: Rigid-wall-prism and its node-checking box	99
Figure 5-3: Penetration removal process (Bala 2006)	104
Figure 5-4: Erosion criteria sensitivity analysis on Mat_72R3 – Color fringe of Equivalent stress	110
Figure 5-5: Erosion criterion in Mat_159, ERODE = 1.00 – Color fringe of <i>Damage</i> value	113
Figure 5-6: Erosion criterion in Mat_159, ERODE = 1.05 – Color fringe of <i>Damage</i> value	114
Figure 5-7: Erosion criterion in Mat_159, ERODE = 1.10 – Color fringe of <i>Damage</i> value	115
Figure 5-8: Eroded volume fraction from rock piece during cutting simulation in Mat_159	116
Figure 5-9: Horizontal force during erosion criteria assessment in Mat_159	117
Figure 5-10: Validation of force signals from 0.3-mm shallow-cut	120
Figure 5-11: Validation of force signals from 3.6-mm shallow-cut	120
Figure 5-12: Validation of force magnitude from 0.3-mm shallow-cut	121
Figure 5-13: Validation of force magnitude from 3.6-mm deep-cut	122

Figure 5-14: Effect of damping coefficients applied to a 1-degree-of-freedom oscillator (Hallquist 2006).....	126
Figure 5-15: Effect of damping coefficients on simulated horizontal cutting forces	129
Figure 5-16: Damping sensitivity in deep-cut simulation: Force signals	130
Figure 5-17: Damping sensitivity in deep-cut simulation: Chip formation.....	131
Figure 5-18: Effect of cutting velocity on horizontal cutting forces from deep-cut simulation. .	133
Figure 5-19: Cutting velocity and RECOV sensitivity in deep-cut simulation: Force signals...	134
Figure 5-20: Cutting velocity and RECOV sensitivity in deep-cut simulation: Chip formation	135
Figure 5-21: Effect of cutting velocity on horizontal cutting forces from shallow-cut simulation	136
Figure 5-22: Cutting velocity sensitivity in shallow-cut simulations	137
Figure 5-23: Modulus degradation with strength -example for concrete under cyclic loading (Murray 2007a)	139
Figure 5-24: Preliminary simulation of 3.6-mm deep rock cut with RECOV = 0.....	140
Figure 5-25: Preliminary simulation of 3.6-mm deep rock cut with RECOV = 0.5.....	140
Figure 5-26: Preliminary simulation of 3.6-mm deep rock cut with RECOV = 1.....	141
Figure 5-27: Preliminary simulation of 3.6-mm deep rock cut with RECOV = 10.....	141
Figure 5-28: Preliminary simulation of 3.6-mm deep rock cut with RECOV = 10.5.....	142
Figure 5-29: Preliminary simulation of 3.6-mm deep rock cut with RECOV = 11.....	142
Figure 6-1: Rock model geometry for slab cuts.....	145
Figure 6-2: Cutter geometry for slab cuts	146
Figure 6-3: Horizontal force during simulation of Vosges Sandstone cutting (3.6-mm deep)...	147
Figure 6-4: Cutting sequence on Berea Sandstone at 4-mm deep. LEFT: Simulation, RIGHT: Laboratory	152
Figure 6-5: Horizontal force during simulation of Vosges Sandstone cutting (0.3-mm deep)...	153
Figure 6-6: Simulated cutting sequence on Vosges Sandstone at a depth of 0.3 mm	153

Figure 6-7: Cutting sequence on Berea Sandstone at 0.3-mm deep. LEFT: Simulation, RIGHT: Laboratory	154
Figure 6-8: Slab horizontal cutting force as a function of depth. Laboratory vs. Simulation **	155
Figure 6-9: The effect of cutting depth on the slab-cut simulation forces.....	157
Figure 6-10: Visualization of eroded elements in slab-cut simulations.....	159
Figure 6-11: Eroded volume fraction during each slab-cut simulation	160
Figure 6-12: Measurement of crushed material for slab cut simulations.....	161
Figure 7-1: Rock model geometry for groove cuts.....	166
Figure 7-2: Groove cutting force as a function of depth. (a) Simulation vs. (b) Laboratory.....	172
Figure 7-3: Visualization of deleted elements in groove-cut simulations: $w = 2.56$ mm, $d =$ variable (half model shown).....	174
Figure 7-4: Visualization of deleted elements in groove-cut simulations: $w = 5$ mm, $d =$ variable (half model shown).....	175
Figure 7-5: Visualization of deleted elements in groove-cut simulations: $w = 10$ mm, $d =$ variable (half model shown).....	176
Figure 7-6: Visualization of deleted elements in groove-cut simulations: $w = 15$ mm, $d =$ variable (half model shown).....	177
Figure 7-7: Measurement of crushed material with respect to nominal depth in groove cut simulations	179
Figure 7-8: Measurement of crushed material with respect to nominal width in groove cut simulations	180
Figure 7-9: Measurement of crushed material with respect to nominal area in groove cut simulations	181
Figure 7-10: Specific energy as a function of w/d ratio: Simulation vs. Lab	184
Figure 7-11: Specific energy as a function of w/d ratio in FE simulations.....	186
Figure 7-12: Variation of normalized forces in slab and groove cutting as a function of depth	187
Figure 7-13: Groove cutting sketch	188
Figure 8-1: Cutting tool for confined experiments of rock cutting (Kaitkay and Lei 2005)	190

Figure 8-2: Experimental cutting forces at a 34.4-MPa confinement pressure (Kaitkay and Lei 2005).....	191
Figure 8-3: Experimental average force as a function of hydrostatic pressure (Kaitkay and Lei 2005).....	192
Figure 8-4: Rock model geometry for groove cutting under pressure.....	193
Figure 8-5: Cutter geometry for groove cutting under pressure	194
Figure 8-6: Interpretation of hydrostatic pressure for definition of LOAD_DENSITY_DEPTH	197
Figure 8-7: Density vs. depth curve for use in LOAD_DENSITY_DEPTH definition	198
Figure 8-8: Simulation results during rock cutting under different hydrostatic pressures	201
Figure 8-9: Eroded internal energy during groove cut simulations under pressure.....	203
Figure 8-10: Eroded volume fraction during groove cut simulations under pressure	203
Figure 8-11: Visualization of eroded elements in groove cut simulations under pressure	204
Figure 8-12: Horizontal force and specific energy in groove cut simulations under pressure ...	205
Figure 8-13: Cutting force vs. confining pressure for Carthage Limestone (Garcia-Garavito 1998)	206
Figure 8-14: Cutting force variation with respect to the borehole pressure for Mancos Shale (Prakash 1982).....	206
Figure 9-1: Chip formation diagram according to Merchant (1944)	208
Figure 9-2: Schematic of rock cutting according to Evans (1961)	212
Figure 9-3: Orthogonal rock-cutting forces and stresses according to Nishimatsu (1972)	215
Figure 9-4: Rock-cutting problem definition according to Detournay and Atkinson (2000).....	218
Figure 9-5: Mean horizontal forces: numerical vs. experimental vs. analytical solutions	222
Figure 9-6: Mean peak horizontal forces: numerical vs. experimental vs. analytical solutions.	223

PREFACE

From both my parents I received the best preparation for the life I now lead. My father was the first achiever I knew; there is nothing I can say that fully acknowledges the hand he had in what was to become my character, and indeed my desire for accomplishment. Along with him, my mother and her unconditional sacrifices for the loved ones, have greatly contributed to the culmination of this important stage in my life. *Infinitas gracias por todo, mamita.*

From the University of Pittsburgh, I wish to offer profound thanks to my advisor, Dr. Jeen-Shang Lin, for having given me the opportunity to work on stimulating investigations at needed times, for guiding and supporting me, for teaching me what is relevant within the research arena, and more importantly, for his patience and his rightful leniency throughout my doctoral studies. I also want to thank my advisory committee members for taking the time to review my work and for providing me with valuable technical observations. Moreover, their moral support and wise advice are much appreciated. To Jessica Benner and Jorge Mendoza, thanks for being the well-rounded colleagues and friends who offered me the right boost, the right chat, the right coffee, the right hug, and the right company when mostly needed.

Mr. Suri Bala, of Livermore Software Technology Corporation, provided immeasurable assistance on the working of the FEM program LS-DYNA; his contributions are sincerely appreciated. On the other hand, the financial support of the National Energy Technology Laboratory through research in drilling under extreme conditions by means of RDS contract DE-AC26-04NT41817 and RES contract DE-FE0004000 is also acknowledged.

I could not have made it through the last few months of writing without my supportive posse at Consol Energy Inc. Special thanks must go to my “new” mentor Greg Hasenfus and to Dave Draskovich, for their constant backing and their belief in me.

The greatest proportion of my gratitude, however, goes to my son, Jacobo, and my spouse, Luis Carlos, who bore with me during these long, laborious years of graduate school. Their permanent love, encouragement and patience are the motives to reach this goal.

To the lovely force that drives my live, my son Jacobo

1.0 INTRODUCTION

1.1 BACKGROUND

While domestic oil reserves remain plentiful at present, this supply is increasingly concentrated in geologically challenging and operationally complex settings such as deep formations, deep-water offshore, and lower permeability formations. Drilling a well into a reservoir is an expensive and time-consuming operation. From an economic perspective, the drilling rate of penetration (ROP) is the single most important factor in determining the cost of drilling a well (Schlumberger Data and Consulting Services 2005). Low ROP, e.g. 0.914 to 1.524 m/hr (3 to 5 ft/hr) is mainly a result of the elevated compressive strength of the highly overburdened formations encountered at greater depths. The extreme environment found at bottom-hole could reach pressures up to 206.8 MPa (30,000 psi) and temperatures up to 250 °C (481 °F).

At first, the tricone bits with hardened inserts used for drilling hard formations at shallower depths were applied as wells went deeper. However, at larger depths it is complicated to identify when the tricone bit's bearings have failed, which can occur more frequently when larger weight is applied to the bit in a deep well. This can lead to repeated failures, lost cones, higher costs, and lower overall ROP.

A solution to the drawback of using tricone bits under extreme conditions was the introduction of fixed cutter bits with Polycrystalline Diamond Compact (PDC) cutters. The PDC cutting surface has synthetic polycrystalline diamonds bonded to a tungsten-carbide stud or blade (see Figure 1-1). This type of bit holds the record for single-run footage in a well, i.e. 6,700 meters (22,000 feet), and it typically drills several times faster than tricone bits, particularly in softer formations (NETL 2010). Each PDC cutter placed on the bit removes a given amount of rock depending on bit design, operating conditions, and bit motion.

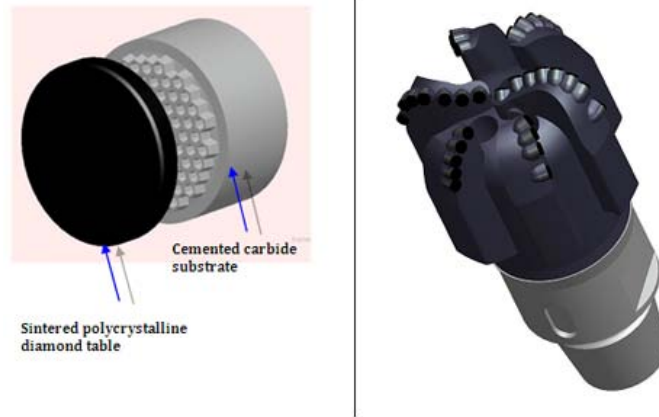


Figure 1-1: PDC cutter (left), drill bit (right) (Kappele 2009)

1.2 MOTIVATION

It is crucial to understand and be able to predict the dynamics at the cutter-to-rock interface in the bottom of a well because the optimum performance of a PDC bit is based on the force developed from the interaction between rock and cutters (see Figure 1-2). This force magnitude depends upon the volume of rock removed by each cutter, the rock strength, and the cutter geometry, among others.

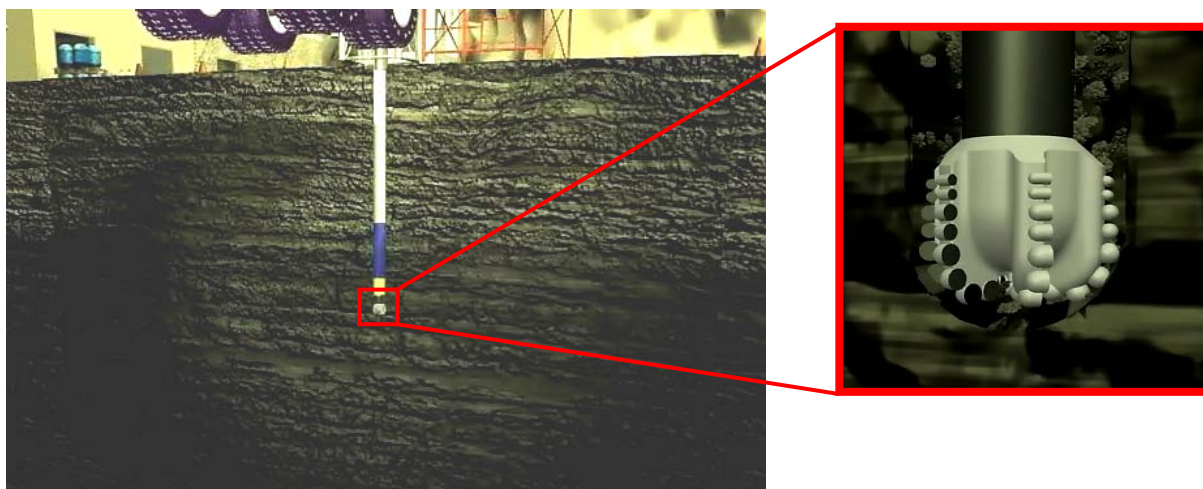


Figure 1-2: Oil well drilling scenario. Detail of a PDC bit at bottom hole (NETL 2007)

During the past 30 years, scientists have been exploring and developing the technology required to efficiently drill rock at high-pressure conditions; nevertheless, there is still a gap in understanding all the physical phenomena that take place during the cutting process.

Failure, fracture, or fragmentation of rock by mechanical tools has been extensively investigated by analytical, experimental, and numerical methods. Generally, experimental and numerical studies are performed with the aim of validating what the analytical theories propose. Physical tests on rocks in a controlled environment are rather direct and the results are easily accepted. However, due to random factors, especially the intrinsic heterogeneity in natural materials, quite a number of tests are necessary in order to rule out the influence of such random factors. This makes the cost rather high and yields rather limited results. In addition, one can only acquire knowledge of the final stage with ordinary measuring equipment and experimental methods, and obtain very little understanding of the breakage process (Kou et al. 2004). On the other hand, numerical modeling often yields reliable results for a given set of conditions, and sometimes offers useful visualization of breakage processes, although it constantly includes some important simplifications. Therefore, an ideal approach is to combine numerical modeling with physical tests.

The numerical methods most widely used for analysis of the rock fracture process are the finite difference method (FDM), the finite element method (FEM), the boundary element method (BEM) and the discrete element method (DEM). Due to its flexibility in handling material heterogeneity, nonlinearity and boundary conditions, the FEM is perhaps the most widely applied numerical method in engineering today with many well developed and verified commercial codes with large capacities in terms of computing power, material complexity and user friendliness.

The purpose of this research work lies on the difficulty of reproducing quantitatively and realistically the fragmentation process documented in rock cutting experiments, by modeling the problem through FEM. Once the simulations yield consistent results based on proper validation of fracture modes and cutting forces, as well as validation of the stress-strain behavior of rock in different standard stress states, it is then possible to implement the proposed methodology into modeling rock drilling in high-pressure environments.

1.3 PROBLEM STATEMENT

The idea of using FEM to model fracturing of a solid material and consequently treat discontinuous elements or groups of elements (chips) has been a challenge to rock cutting scientists and, in general, to researchers attempting to model the interaction between a penetrator (cutter) and a solid, breakable target (rock). The challenge appears as a sequence of complex problems due to the highly nonlinear nature of the process and the material involved. As the penetrator advances and touches the target material, a contact problem first arises. The contact problem is followed by nonlinear deformation and the difficulty of determining when and whether or not the material fails. Subsequently, the question of how to initiate the fragmentation process after the material fails has to be resolved. This cycle repeats starting with a new contact problem after new surfaces are generated due to fracture.

Furthermore, when simulating problems involving impact and fracturing there is a consensus in the research community that, although powerful in tracking element properties and in incorporating complex material models, the typical pure Lagrangian mesh-based technique of the FEM presents limitations such as:

- Inability to use a simple but realistic crack propagation formulation;
- Numerical instabilities caused by local mesh distortions due to highly concentrated loads, especially in dynamic large deformation analysis; and,
- High computational costs and loss of accuracy when implementing adaptivity or remeshing procedures to reduce mesh entangling.

The aforementioned problems may well be the reason why the literature search did not find prior FEM work modeling the complete dynamic process of rock cutting. A limited amount of research has focused on crack initiation and subsequent crack propagation (see Section 1.4.2); however, it does not account for actual chip formation or for the dynamic interaction amongst chips, newly formed surfaces, and the cutter. This is precisely what the proposed study is intended to do.

1.4 STATE OF THE ART IN ROCK CUTTING MODELING

As mentioned in Section 1.2, the most frequently used numerical methods for modeling the rock-tool interaction problem are the finite difference method (FDM), the finite element method (FEM), the boundary element method (BEM) and the discrete element method (DEM).

This investigation is part a larger research effort –funded by the U.S. Department of Energy– that is aimed at establishing a numerical framework that is capable of modeling the process of a drill cutter advancing into HPHT rock and its associated rock fragmentation. To this end, this DOE-supported project was set out to use a continuum approach, i.e. FEM, and a discrete approach, i.e. DEM.

1.4.1 The Use of the Finite Element Method

In looking for the best continuum method to employ, the FEM is found to be the most reliable for simulating the rock cutting process. The FEM has been the most popular numerical method in engineering sciences, including rock mechanics and rock engineering (Jing 2003). Its popularity is largely owed to the flexibility in treating material heterogeneity, nonlinear deformability (mainly plasticity), complex boundary conditions, and dynamic problems, in conjunction with reasonable efficiency in dealing with complex constitutive models and even fracturing.

The interest of this investigation is to discretize the continuum domain of the rock in such a way that it can mimic a particle assembly, which should be able to fracture when subjected to a failure stress state. In this order of ideas, the BEM does not serve the purpose because its discretization scheme is limited to the boundaries of the domain. In addition, the BEM is not capable of treating inhomogeneous, nonlinear problems (Gaul 2004).

As far as the FDM is concerned, it has a certain level of rivalry with the FEM. In the FDM, every derivative in the set of governing equations is replaced directly by an algebraic expression written in terms of the field variables (e.g., stress or displacement) at discrete points in space (Itasca 2001). Without iterative solutions of the global matrix of the system of equations as in the FEM, the FDM has an advantage in simulating complex constitutive material behavior, such as plasticity and damage. However, explicit representation of fractures is not easy in the FDM because it requires continuity of the functions between the neighboring nodes. Therefore, the

FDM uses the smeared crack approach (Fang and Harrison 2002) or nulled elements (Tulu et al. 2008) to catch material failure or damage propagation of the elements without specifically creating fracture surfaces in the model. This fact makes the FDM not suitable for simulating the fragmentation process in rock cutting.

Taking advantage of LS-DYNA's excellent functionalities and high performance, this well-known commercial software has been selected to serve the purpose of this research work. LS-DYNA is a program that analyzes large deformation behavior of structures by using a time-stamp history in explicit form, and has advantages in fields such as crash/shock analysis, falling shock analysis, plastic forming analysis, and penetration/crack/fracture analysis. In those fields, LS-DYNA is a highly reliable program with several proven introduction in industries like the automotive, the metal forming and the defense.

1.4.1.1 The Explicit FEM

The explicit FEM was originally developed to solve problems in wave propagation and impact engineering, but it is currently used for many other applications such as sheet metal forming, underwater simulations, failure analysis, glass forming, metal cutting, pavement design, and earthquake engineering, among others. The implicit FEM becomes expensive when thousands of timesteps must be taken to solve a dynamic problem because of the cost of inverting stiffness matrices to solve the large sets of nonlinear equations, especially for models with thousands of degrees of freedom or when nonlinearities are present. In an explicit FEM, the solution can be achieved without forming a global stiffness matrix. The solution is obtained on an element-by-element basis and therefore a global stiffness matrix does not have to be formed. As a result, the explicit approach can treat large three-dimensional models (thousands of degrees of freedom) with comparatively modest computer storage requirements. Other advantages include easy implementation and accurate treatment of general nonlinearities. However, the explicit method is conditionally stable and therefore small timesteps must be used. For stable computations, the time step is selected by the computer code such that (for undamped problems):

$$\Delta t \leq \frac{l}{c_w} \tag{1-1}$$

where l is related to the smallest element size and c_w is its fastest wave speed (speed at which stress waves travel in the element). The physical interpretation of this condition for linear displacement elements is that Δt must be small enough so that information does not propagate across more than one element in a timestep, therefore this could result in excessive simulation times as the level of discretization increases.

1.4.1.2 The Finite Element Approximation

Three steps are required to complete a FEM analysis: 1) domain discretization, 2) local approximation, and 3) assemblage and solution of the global matrix equation. The domain discretization involves dividing the deformable body occupying a spatial domain V into a finite number of internal contiguous elements of regular shapes defined by a fixed number of nodes, N_{nod} . In the case of linear elasticity, the domain V can be described by the following equations:

$$\varepsilon_{ij} = \frac{1}{2} \left(\frac{\partial u_i}{\partial x_j} + \frac{\partial u_j}{\partial x_i} \right) \quad . . . \text{strain-displacement (kinematic) eqs.} \quad (1-2)$$

$$\sigma_{ij} = D_{ijkl}^e \varepsilon_{kl} \quad . . . \text{stress-strain (constitutive) equations} \quad (1-3)$$

$$\frac{\partial \sigma_{ij}}{\partial x_j} + \bar{b}_i = 0 \quad . . . \text{equilibrium (static) equations} \quad (1-4)$$

In the above, u_i is the displacement vector, ε_{ij} is the column matrix of strain components, σ_{ij} is the column matrix of stress components, \bar{b}_i is the vector of body forces, and D_{ijkl}^e is the elastic material stiffness matrix.

In the standard displacement version of the FEM, the displacement components are approximated as linear combinations of suitably chosen interpolation –or *shape*– functions $N_I(\mathbf{x})$, where $I = 1, 2, \dots, N_{nod}$, and \mathbf{x} is the vector of Cartesian components x_1, x_2 , and x_3 . A typical property of the FE shape functions is that each of them is associated with one of N_{nod} nodes of the domain, and the value of the I -th shape function is equal to one at node number I and equal to zero at all other nodes. The displacement approximation is defined as

$$\mathbf{u}_i(\mathbf{x}) = \sum_{l=1}^{N_{nod}} N_l(\mathbf{x}) d_{li} \quad i = 1, 2, 3 \quad (1-5)$$

where d_{li} are unknown displacement parameters. In matrix notation, the approximation in Equation (1-5) is rewritten as

$$\mathbf{u}(\mathbf{x}) = \mathbf{N}(\mathbf{x})\mathbf{d} \quad (1-6)$$

Similarly, the kinematic Equations (1-2) provide an approximation of the strains,

$$\boldsymbol{\varepsilon}(\mathbf{x}) = \boldsymbol{\partial}\mathbf{u}(\mathbf{x}) = \boldsymbol{\partial}\mathbf{N}(\mathbf{x})\mathbf{d} = \mathbf{B}(\mathbf{x})\mathbf{d} \quad (1-7)$$

where $\mathbf{B} = \boldsymbol{\partial}\mathbf{N}$ is the *strain-displacement matrix* –or B-matrix– containing the derivatives of the shape functions with respect to the spatial coordinates.

Substituting the strain approximation (1-7) into the constitutive equations (1-3) we obtain the stress approximation

$$\boldsymbol{\sigma}(\mathbf{x}) = \mathbf{D}_e(\mathbf{x})\boldsymbol{\varepsilon}(\mathbf{x}) = \mathbf{D}_e(\mathbf{x})\mathbf{B}(\mathbf{x})\mathbf{d} \quad (1-8)$$

where the argument \mathbf{x} at \mathbf{D}_e marks explicitly that the elastic properties may be position-dependent.

Although the approximations of displacements, strains and stresses satisfy the kinematic and constitutive equations exactly, the static differential equations of equilibrium (1-4) in general cannot be satisfied exactly at every point of the body, i.e., in a strong sense, because the adopted approximations depend only on a finite number of unknown displacement parameters. Instead of using the static equations directly, they are replaced by the *principle of virtual work*, which leads into the *weak form* of the equilibrium equations. The weak form introduces an arbitrary matrix of virtual displacement parameters, $\delta\mathbf{d}$, in its integral-based equality.

Taking into account that \mathbf{d} and $\delta\mathbf{d}$ are not functions of the spatial coordinates and as such can be taken out of the integrals of the virtual work equations (Jirásek 2007), the weak form of the equilibrium equations can be written as

$$\mathbf{d}^T \mathbf{K}_e^T \delta \mathbf{d} = \mathbf{f}_{ext}^T \delta \mathbf{d} \quad (1-9)$$

where

$$\mathbf{K}_e = \int_V \mathbf{B}^T(\mathbf{x}) \mathbf{D}_e(\mathbf{x}) \mathbf{B}(\mathbf{x}) dV \quad (1-10)$$

is the (global) elastic stiffness matrix and

$$\mathbf{f}_{ext} = \int_V \mathbf{N}^T(\mathbf{x}) \bar{\mathbf{b}} dV \quad (1-11)$$

is the (equivalent) external force vector. Equation (1-9) is satisfied for $\delta \mathbf{d}$ if and only if

$$\mathbf{f}_{ext} = \mathbf{K}_e \mathbf{d} \quad (1-12)$$

These are the discretized equations of equilibrium from which it is possible to compute the unknown displacement parameters \mathbf{d} .

1.4.1.3 Central Difference Scheme for Explicit Time Integration

As stated before, in an explicit FEM, the solution can be achieved without forming a global stiffness matrix. LS-DYNA uses the central-difference method, which is characteristic of explicit methods for direct time integration. In this method, the solution is determined in terms of previous (before current timestep t_n) elastic displacements and time derivatives of these displacements. By using this method, the finite element solution is then obtained using the following equations (with no damping):

$$\dot{\mathbf{u}}_{t_{n+\frac{1}{2}}} = \dot{\mathbf{u}}_{t_{n-\frac{1}{2}}} + \Delta t_n \mathbf{M}^{-1} \left(\mathbf{f}_{ext,t_n} - \int_V \mathbf{B}^T \boldsymbol{\sigma}_{t_n} dV \right) \quad (1-13)$$

$$\mathbf{u}_{t_{n+1}} = \mathbf{u}_{t_n} + \Delta t_{n+\frac{1}{2}} \dot{\mathbf{u}}_{t_{n+\frac{1}{2}}} \quad (1-14)$$

where \mathbf{f}_{ext,t_n} is the vector of applied forces associated with the boundary conditions and body forces at timestep t_n , \mathbf{M} is the mass matrix, and $\int \mathbf{B}^T \boldsymbol{\sigma}_{t_n} dV$ is the internal force vector (Benson 2001).

In each timestep, the velocities and displacements are updated. In general, implicit methods have the form:

$$\mathbf{u}_{t_{n+1}} = f(\dot{\mathbf{u}}_{t_{n+1}}, \ddot{\mathbf{u}}_{t_{n+1}}, \dot{\mathbf{u}}_{t_n}, \dots) \quad (1-15)$$

and therefore the computation of the current nodal displacements requires the knowledge of the time derivatives of $\mathbf{u}_{t_{n+1}}$, which are unknown. Consequently, simultaneous equations need to be solved to compute the current displacements. On the other hand, explicit methods have the form:

$$\mathbf{u}_{t_{n+1}} = f(\mathbf{u}_{t_n}, \dot{\mathbf{u}}_{t_n}, \ddot{\mathbf{u}}_{t_n}, \mathbf{u}_{t_{n-1}}, \dots) \quad (1-16)$$

and therefore the current nodal displacements can be determined in terms of completely historical information consisting of displacements and time derivatives of displacements at previous time steps. If a diagonal mass matrix is used, Equation (1-13) is a system of linear algebraic equations and a solution is obtained without solving simultaneous equations. Once displacements are updated, strains can be computed, which are then used to determine stresses and eventually nodal forces.

1.4.2 Previous Research on Rock Cutting Modeling

1.4.2.1 Some Numerical Approaches Used

Numerous investigators have applied numerical methods to the problem of rock-tool interaction. Table 1-1 summarizes the most relevant examples of numerical studies in rock cutting in the last couple of decades. This table reports the material constitutive models implemented, the type of rock modeled, and the status of the chip formation and fragmentation process.

Table 1-1: Previous research in rock cutting modeling

No.	Numerical Method	Code	Rock constitutive model	Type of rock modeled	Type of crack initiation and fragmentation	Reference
1	FEM (2D)	RFPA	Elastic-brittle model.	Generic. Heterogeneity included throughout elements.	No explicit fracture.	(Tang 1997)
2	FDM (2D)	FLAC	Strain-Softening Mohr-Coulomb Constitutive Model.	Generic, homogeneous	No explicit fracture. Small deformation.	(McKinnon and Garrido 1998)
3	FDM (2D)	FLAC	Elastic perfectly plastic model with a Mohr-Coulomb yield condition and plastic potential.	Generic, homogeneous	No explicit fracture. Small deformation.	(Huang et al. 1998)
4	FEM (2D)	RFPA	Coulomb with tensile cut-off model.	Sandstone. Heterogeneity included throughout elements.	Crack formed by smeared elements. No chip separation.	(Tang et al. 1998)
5	BEM (2D)	In-house code	Maximum tensile strength criterion	Generic, anisotropic, homogeneous	Predefined crack with incremental crack extension with piece-wise linear discretization. No fragmentation.	(Chen et al. 1998)
6	FEM (2D)	RFPA	Mohr-Coulomb model.	Generic. Heterogeneity included throughout elements.	Crack formed by smeared elements. No chip separation.	(Tang et al. 1998)
7	FEM (2D)	ALGOR	Elastic–perfectly plastic model with Drucker–Prager plasticity in tension	Generic, homogeneous	Crack predefined and propagated by remeshing. No chip separation.	(Jonak 2001)
8	FEM (2D)	R-T	Elastic-brittle model.	Generic. Heterogeneity included throughout elements.	Crack formed by smeared elements. No chip separation.	(Liu et al. 2002)
9	FDM (2D)	FLAC	Elasto-plastic Mohr-Coulomb model with stiffness degradation	Generic. Heterogeneity included throughout elements.	Crack formed by smeared elements. No chip separation.	(Fang and Harrison 2002)

Table 1-1 (continued)

No.	Numerical Method	Code	Rock constitutive model	Type of rock modeled	Type of crack initiation and fragmentation	Reference
10	FEM (2D)	LS-DYNA	Elastic plastic damage - Johnson-Holmquist concrete model.	Granite, homogeneous	No explicit fracture. Small deformation.	(Tuomas 2004)
11	DEM	PFC	Parallel bond model	Marble, homogeneous	Crack is formed. Chip is separated.	(Lei et al. 2004)
12	FEM (2D)	R-T	Double elliptic strength criterion with elastic damage.	Granite, marble and sandstone. Heterogeneity included throughout elements.	Crack formed by smeared elements. No chip separation.	(Liu 2004)
13	FEM (2D)	RFPA	Elastic damage	Sandstone. Heterogeneity included throughout elements.	Crack formed by smeared elements. No chip separation.	(Zhu and Tang 2004)
14	DEM with FEM (2D)	In-house code	Elastic plastic with elastic damage (for FEM part)	Sandstone, homogeneous	Crack is formed. Chip is separated. (DEM part)	(Oñate and Rojek 2004)
15	FEM (2D)	In-house code	Quasi-brittle material model	Limestone, homogeneous	Fragmentation has been modeled analytically. There is no evidence of cracks or chip separation.	(Rouabhi et al. 2005)
16	FEM (3D)	LS-DYNA	Elastic plastic model. Erosion of elements upon tensile or shear stress threshold.	Generic, homogeneous	No explicit fragmentation.	(Yu 2005)
17	FDM and DEM (2D)	FLAC and PFC	Mohr-Coulomb plasticity model (for FDM part)	Marble, homogeneous	No explicit fracture. Large deformation.	(Stavropoulou 2006)
18	FDM (2D)	FLAC	Elastic Mohr-Coulomb model	Limestone, homogeneous	No explicit fracture. Small deformation.	(Innaurato et al. 2007)
19	DEM (2D)	In-house code	Elastic perfectly brittle contact model	Sandstone, homogeneous	Crack is formed. Chip is separated.	(Rojek 2007)
20	DEM (2D)	PFC	Linear contact model with contact bonds	Sandstone, homogeneous	Crack is formed. Chip is separated.	(Huang and Detournay 2008)

Table 1-1 (continued)

No.	Numerical Method	Code	Rock constitutive model	Type of rock modeled	Type of crack initiation and fragmentation	Reference
21	FEM (2D)	R-T	Double elliptic strength criterion with elastic damage	Sandstone, marble, granite. Heterogeneity included throughout elements.	Crack formed by smeared elements. No chip separation.	(Liu et al. 2008)
22	FDM (3D)	FLAC	Strain-softening Mohr Coulomb plasticity model	Shale and Sandstone, homogeneous	Elements are "nulled" upon reaching failure. No crack initiated or fragmentation reported.	(Tulu 2009; Tulu et al. 2008)
23	DEM (2D)	PFC	Linear contact model with parallel bonds	Sandstone, heterogeneous	Crack is formed. Chip is separated.	(Block and Jin 2009)
24	DEM (2D)	PFC	Linear contact model with parallel bonds and implementation of particle crushing	Sandstone, heterogeneous	Crack is formed. Chip is separated.	(Mendoza 2010)
25	DEM (3D)	PFC	Linear contact model with parallel and contact bonds	Sandstone, homogeneous	No clear crack formed. Small chips separated, but mostly particles dispersed in space.	(Rojek et al. 2011)
26	DEM (3D)	PFC	Linear contact model with parallel and contact bonds	Sandstone and Limestone, heterogeneous.	No explicit fracture. Particles dispersed in space.	(Su and Akcin 2011)
27	FEM (2D)	RFPFA	Linear elastic damage based on tensile strain or Mohr-Coulomb criteria	Generic. Heterogeneity included throughout elements.	Cracks formed by smeared elements. No chip separation	(Wang et al. 2011)

As can be concluded from the information in Table 1-1, none of the continuum approaches succeeds in modeling explicitly the crack propagation and chip formation and separation seen in rock cutting physical experiments. Currently, the only numerical method presenting such features is the DEM. From the set of DEM simulations found in the literature, (Mendoza 2010) presents the most comprehensive analysis of the dynamic rock-tool interaction.

1.4.2.2 Numerical Contributions Through the Use of FEM

Previous attempts to simulate the rock fragmentation mechanism with the FEM stop when fragments are formed. Some require a prior knowledge of the crack initiation angle to plot a path for element removal or domain remeshing for simulating crack growth (Jonak 2001; Saouma and Kleinosky 1984; Swenson and Ingraffea 1988; Wawrzynek and Ingraffea 1989). Figure 1-3 illustrates the trajectory of the primary crack and distribution of displacements near a cutting wedge with negligible friction simulated by Jonak (2001).

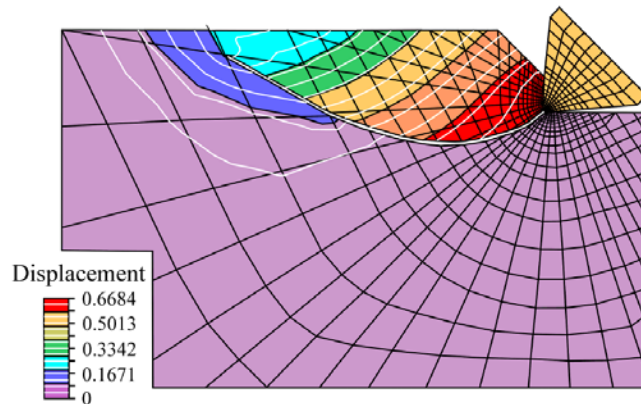


Figure 1-3: Rock cutting simulation by Jonak (2001)

As can be seen in Table 1-1, the great majority of the published two-dimensional studies in FEM belong to the research group at the Division of Mining of the Luleå University of Technology, where the Rock Failure Process Analysis code (RFPA) and the Rock Tool Interaction code (R-T) were developed (Kou et al. 1999; Liu 2004; Liu et al. 2008; Liu et al. 2002; Tang 1997; Wang et al. 2011; Zhu and Tang 2004). The fundamental premise of the RFPA and R-T codes is based on the conceptualization of ‘smeared cracks’ by modifying the material constitutive relations in a particular fashion. By employing this technique, the stress in each element is monitored; when an

element reaches the failure stress or strain threshold, it remains part of the continuum domain but loses its load carrying capacity (stiffness and/or strength) in certain directions. In this way, the cracks are not represented explicitly, but characterized by a change in color for visualization, as shown in Figure 1-4, where the different grey scales represent different values of Young's modulus.

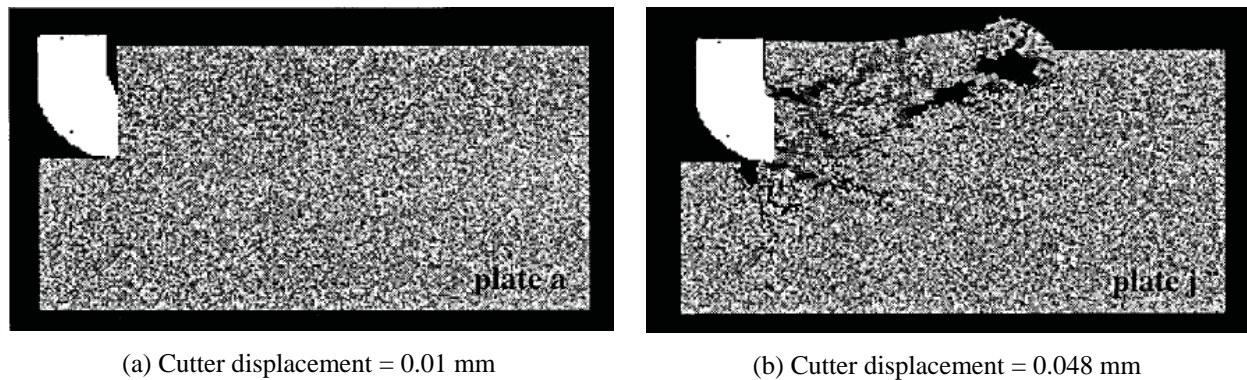


Figure 1-4: Rock cutting simulated with RFPA2D (Kou et al. 1999)

At the time of this literature review preparation, RFPA and R-T were the codes that offered the best results in modeling the fracture mechanics due to rock-tool interaction, as well as the best visualization of cracks. It has been claimed that this approach is capable of giving reasonable estimates of cutter forces and fracture patterns from rock indentation; however, its use is limited in simulating the entire fragmentation process while the cutter continuously moves forward. The program fails to provide real fragment separation as the failed elements still maintain their topological relationship with their neighbors. Additionally, no interfacial relationship for elements around failure zones is incorporated. In conclusion, this technique is not capable of modeling the rock cutting behavior beyond the stages of initial contact followed by crack growth.

Alternatively, only few researchers have implemented the explicit FEM in analyzing the nonlinear transient problem of tool-rock interaction. Tuomas (2004) investigated the effect of the velocity in rock indentation simulations using a complex concrete material model, however, failure of the material is identified by a damage value and actual fracture does not take place. On the other hand, Yu (2005) analyzed the rotation and advance of a continuous miner cutter head

through the use of a dynamic contact model with an *element erosion* algorithm. While this model stayed away from the limitations mentioned in Section 1.3, it did not consider the initiation and growth of cracks in the rock, and neither had it employed a robust constitutive material model that described the nonlinear behavior of rock.

Lastly, in recent published papers and two Master's theses on the simulation of rock and drill cutter behavior, Tulu et al. (2008), Tulu and Heasley (2009), Sunal (2009), and Tulu (2009) –all from West Virginia University– attempt to develop a cutter-rock numerical model used to back analyze laboratory experiments of rock cutting in a HPHT environment, which is the same aim of the investigation in this dissertation. Their approach is based on the use of FLAC3D, which currently presents limitations to address the non-connectivity of failed elements. Their treatment of damaged material is similar to the one that Yu (2005) implements, where elements are "nulled" or erased upon reaching failure, as shown in Figure 1-5.

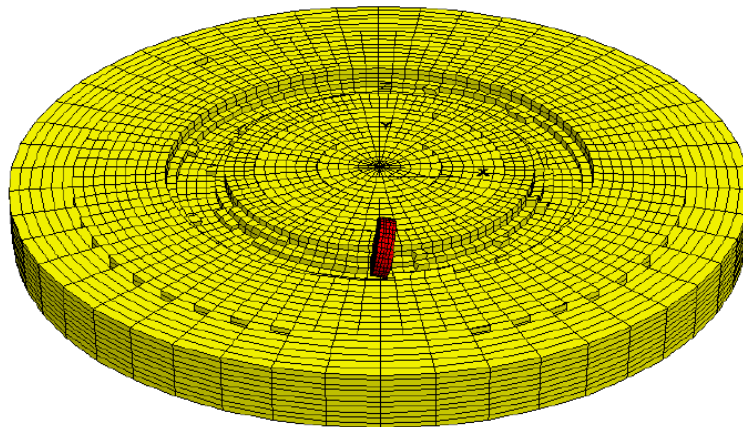


Figure 1-5: Cutting simulation on Catoosa Shale at 1.905 mm (0.075 in) of depth (Sunal 2009)

Although Tulu (2009) claims to have simulated “the propagation of a crack and formation of a chip” with his model, referring to the images in Figure 1-6, the author of the present work considers this fragmentation process unsuccessful. Tulu’s “crack propagation” is simulated by the failure of elements following the Mohr-Coulomb criterion and the removal of elements at a pre-determined percentage of plastic strain, i.e. 30%. On one hand, the user-predefined plastic strain threshold of 30%, for the elements to be nulled from the simulation, appears to be excessive. Accordingly, and along with the inadequate numerical characteristics of the finite

element model and the lack of more robust material constitutive laws, the approach employed by this group of researchers does not seem to reflect the actual natural complex behavior of rock material upon different mechanisms of loading during the cutting process.

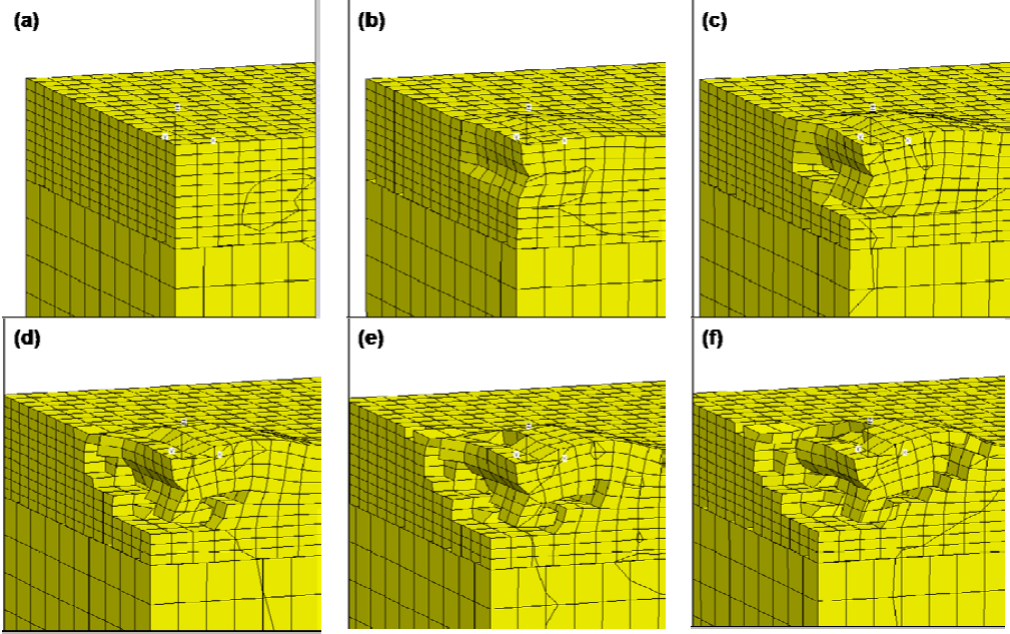


Figure 1-6: Apparent crack formation and chip formation (Tulu 2009)

1.5 RESEARCH OBJECTIVES AND SCOPE

1.5.1 Main Objective

The primary objective of the proposed study is to develop a reliable finite element model that properly simulates the fragmentation process observed in laboratory tests of rock cutting. Both fracture modes and cutting forces from the numerical simulations should correlate with the physical experiments. Subsequently, inclusion of pressure effect to the FEM model would aid in the prediction of the PDC bit performance by building a sound understanding of the rock fracture mode created by a single cutter under HPHT conditions.

1.5.2 Specific Objectives

In order to accomplish the main objective, the following aims have to be fulfilled:

1. To apply an effective and rational contact formulation to treat the contact at the interface between: (a) rock and cutter, (b) cutter and newly formed rock surfaces after fracture, and (c) rock and rock chips.
2. To incorporate a robust constitutive law that is capable of describing the nonlinear elastic-plastic stress-strain response of the rock material under different stress conditions (i.e. compression, tension, and shear). The material model should be well calibrated for it to reproduce the experimental mechanical behavior of the rock as a function of strain rate and pressure.
3. To implement and validate a consistent procedure to initiate cracks as discontinuities that can propagate and eventually connect –forming chips– without knowing a priori the direction and trajectory of the cracks during the rock cutting process. Afterward, the arbitrarily formed chips should act as independent bodies in the finite element domain.

4. To implement the modeling procedure developed herein towards the simulation of a three-dimensional (3D) case of linear scratching tests, where shear on the side walls of a cutting groove is considered.
5. To analyze the effect of cutting depth (d) and cutter width (w) on the specific energy ($\varepsilon = F_x/wd$) of Vosges sandstone. Various depths of cut and cutter widths shall be used in the simulation of 2D and 3D rock cutting tests, and the relationship of specific energy with the ratio w/d would be corroborated with experimental data by Richard (1999).
6. To apply the developed framework to a preliminary FEM model of groove rock cutting under high hydrostatic pressure. The preliminary 3D linear-cutting model is aimed at simulating a laboratory study of the rotational cutting under different pressures, which mimics the drill-bit's single cutter action at great depths in the field.
7. To compare the magnitude of simulated cutting forces with theoretical values obtained from traditional analytical formulae. Validation of numerically obtained forces through analytical forces –calculated based on a single PDC mechanistic performance model– will aid in the authentication of the FEM model developed in this study.

2.0 EXPERIMENTAL BENCHMARK

Beside the analytical theories, a good means to validate the FEM model proposed in this work is to compare the simulated failure mechanisms and cutting forces with data and images from laboratory tests. To this end, the experimental scratching tests on Vosges Sandstone performed by Richard (1999) have been selected as the benchmark for evaluation.

This section also presents the sets of laboratory data to which input parameters of the LS-DYNA material models selected for analysis are fitted and calibrated. A suite of laboratory tests on Vosges sandstone performed by Bésuelle et al. (2000) served as benchmark for the input parameter calibration process, thus their stress-strain response plots are presented in Section 2.2.

Some of the input parameters in the more complex models required the use of advance curve-fitting techniques, for which the *genetic algorithm* from Matlab served the purpose, as explained in Section 2.3.

2.1 LABORATORY SCRATCHING TESTS

Part of the extensive research work by Richard includes two main types of experiments that were run to demonstrate the nature of the cutter's impact on Vosges Sandstone; these are the "shallow cut" and the "deep cut" laboratory tests in the Rock Strength Device (RSD) illustrated in Figure 2-1.

According to Richard, the cutter influence can cause "either ductile and/or brittle failure, with the ductile mode associated with damage of the rock and/or plastic flow, and the brittle mode with the propagation of cracks." Furthermore, he concluded that ductile failure mode took place when the cutting depth is no deeper than 1mm, i.e. shallow cut, whereas a deeper cut would induce brittle failure.

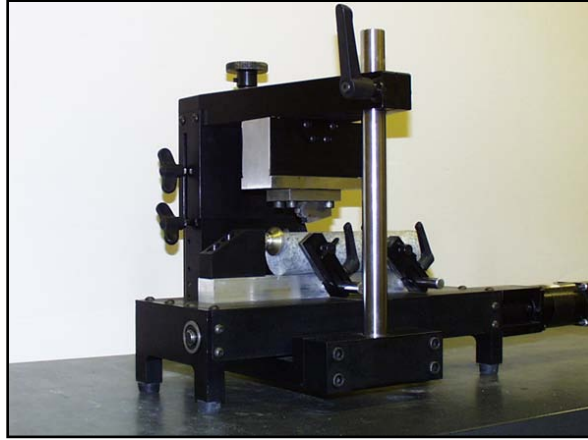


Figure 2-1: Rock Strength Device (FPMS 2007)

In general, the scratching tests are virtually non-destructive, as they involve the removal of rock along the surface of a rock core over a depth, which is typically 1 mm (0.04 in) or less, and over a width of 10 mm (0.4 in). It was developed at the University of Minnesota as an alternative to determine rock properties such as strength in a more economic way than the standard rock mechanical laboratory measurements.

The RSD measures the normal and tangential components of force F^c applied to a cutter (see Figure 2-2) while performing a groove at a constant depth d on the surface of a rock specimen with a sharp tool. The specimen is clamped at the bottom to a static base while a moving frame holding the PDC cutter advances on top of the rock.

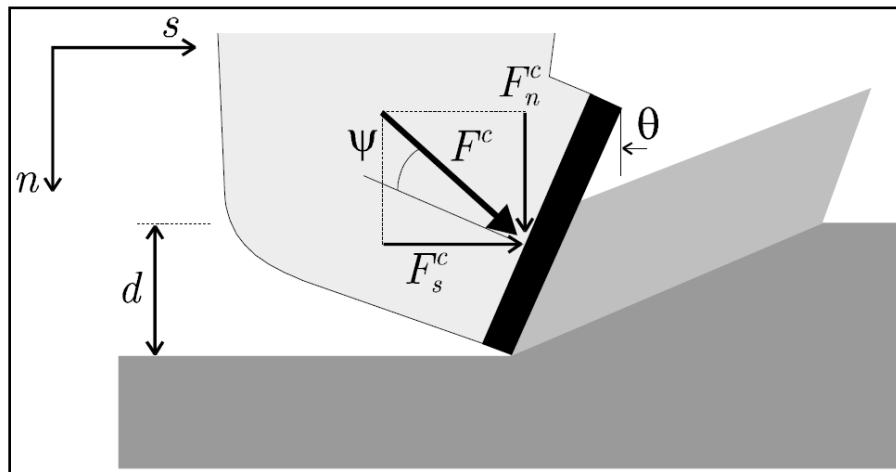


Figure 2-2: Forces acting on a sharp cutter

The test is kinematically controlled, i.e., the relative horizontal velocity v between the cutter and the rock, and the depth of cut d are fixed and remain constant during the test. According to Richard, the cutting process is characterized by the following parameters:

1. the rake angle θ ;
2. the relative velocity v between the cutter and the rock;
3. the depth of cut d ;
4. the cutter geometry description, limited to the width w for the case of rectangular shape cutters; and,
5. the surfaces of contact between the rock and the cutter (the cutting face and its inclination β with respect to the direction of the velocity vector);

The experimental data used in the present study come from tests carried out on slabs of Vosges Sandstone having the same width as the cutter, as shown in Figure 2-3, because the author wanted to remove the possibility of any side effect. The non-constrained dimensions of the rock specimen are 10 mm in thickness, 20 mm in height and between 100 and 200 mm in length. The rock mechanical properties of the studied rock are presented in Table 2-1.

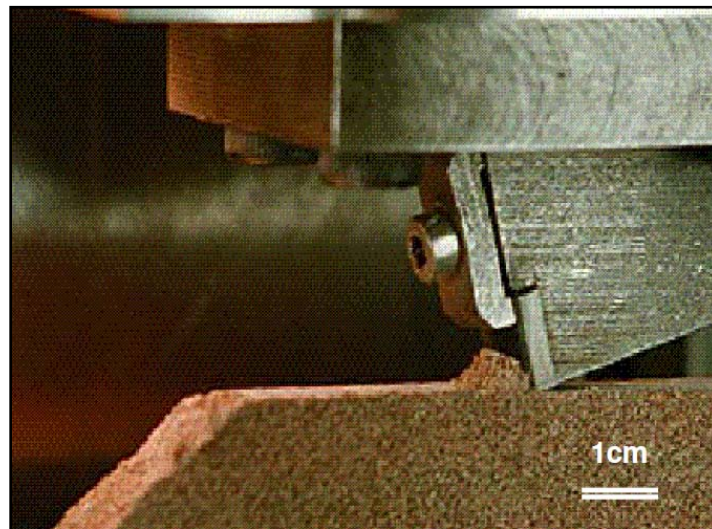


Figure 2-3: Scratch test on sandstone slab at shallow depth (Degrain et al. 2009)

Table 2-1: Mechanical properties of Vosges Sandstone

Mass density	2,000 kg/m ³	(125 lb/ft ³)
Young's modulus	8.25 GPa	(1,196,561 psi)
Poisson's ratio	0.33	
Uniaxial compressive strength	33.1 x10 ⁻³ GPa	(4,801 psi)

2.1.1 Mechanics of the Scratching Tests

A rake angle of 15 degrees is set up constant for all the tests. The following detailed descriptions of the physical phenomena observed during the rock cutting experiments was made by Richard (1999). Deep and shallow cut mechanisms are explained below. Obviously, the frequency and magnitude of these two modes greatly vary with the depth of cut, but they usually coexist at intermediate depths of cut.

2.1.1.1 Deep Cut Experiments

At large depth of cut (typically more than 1 mm for medium strength sandstone), brittle failure occurs, as shown in Figure 2-4. Isolate events can easily be recognized. Macroscopic cracks are initiated from the tool tip and propagated unstably ahead of the cutter. The process is characterized by unstable failure, which is accompanied by significant sounds. The process is cyclic; after a chip is removed, the effective depth of cut is almost zero, and progressively increase until a new chip is formed. The successive increase and abrupt release of stress ahead of the cutter can generate, in the case of very hard rock, vibrations of the entire frame of the testing apparatus.

The crack paths are variable, either going upwards at various inclinations, horizontally ahead of the cutter, or vertically downwards. The first case immediately produces a chip; a horizontal crack creates fragments that could fail under various mechanisms such as buckling, compression, or even deviation of the crack to the surface. Vertical downward cracks lead sometimes to a complete splitting of the specimen. The location of initiation of the crack is not clearly defined. However, some observations tend to show the crack starts slightly above the cutter tip. Rock chips present various shapes and sizes.



Figure 2-4: Brittle failure on Berea Sandstone while cutting at 4 mm of depth

Their size and occurrence frequency increase with depth of cut. In terms of size, they vary from a cluster of a few grains to almost rectangular chips with a height equal to the depth of cut. In brittle material or at very large depth of cut, when cutting in whole cores, the maximum lateral width of the chip can exceed the cutter width. In this case, the failure is really a three-dimensional process. There is, however, no characteristic size of chips at any given depth of cut. Even at large depth of cut, small chips are present.

2.1.1.2 Shallow Cut Experiments

At shallow depth of cut (typically less than 1 mm for a medium strength sandstone), the rock is intensively sheared ahead of the cutter and crushed at the tip. The material is reduced to powder or isolated grains. The cutter contact with the rock does not extend over the full depth of cut, but seems to be limited to a small area at the bottom of the cutting face. The cutting proceeds in a continuous manner, in a sense that no particular event can be isolated while cutting (see Figure 2-5). This cutting mode is mainly characterized by de-cohesion of the constitutive matrix and grains of the rock with grains and powder accumulating progressively in front of the cutter. From this point of view, this cutting mode can be defined as ductile.



Figure 2-5: Ductile failure on Berea Sandstone while cutting at 0.3 mm of depth

2.1.2 Force Signals from Scratching Tests

The difference between the two mechanisms explained above is noticeable in the shape of the force signal. With a homogeneous rock sample (i.e. with no major change of strength along the cutting direction), in this case Vosges Sandstone, the signal in the chipping mode presents a marked saw-tooth pattern (see Figure 2-6), whereas the signal in the ductile mode may be viewed as a white noise (see Figure 2-7). The cutting velocity for the analyzed scratching tests is 4 mm/s, and the forces on the cutter are recorded with a frequency of 100 Hz, resulting in a sampling rate of 25 data/mm.

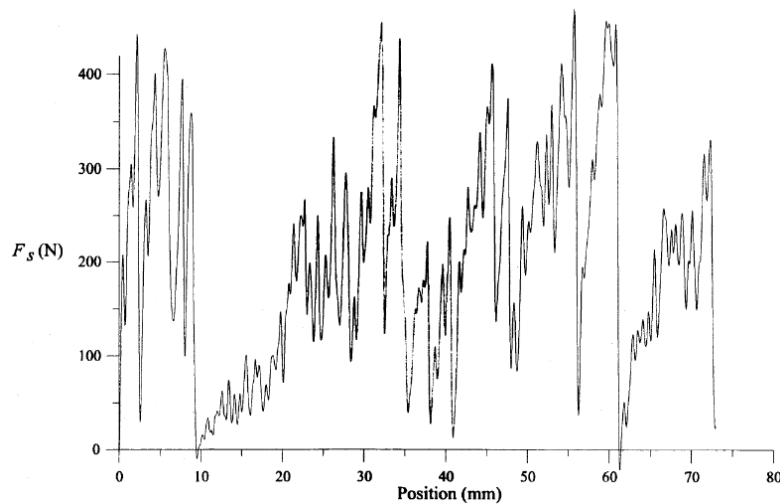


Figure 2-6: Horizontal force during test at 3.6 mm depth of cut (Richard 1999)

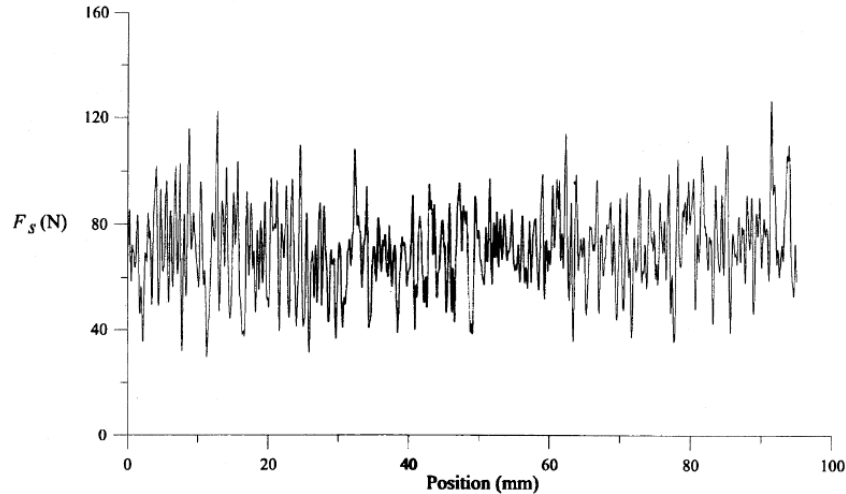


Figure 2-7: Horizontal force during test at 0.3 mm depth of cut (Richard 1999)

The signal representing the brittle cutting mode (chipping) presents more coverage between peaks. In the horizontal direction, we can clearly identify an increase of the force over several millimeters up to a peak, when a crack is initiated. The abrupt drop of the force, after the peak, is associated with unstable propagation of the crack leading ultimately to the formation of a chip.

2.2 LABORATORY CHARACTERIZATION FOR PARAMETER CALIBRATION

The behavior of a Vosges sandstone was studied by Bésuelle et al. (2000). They tested the rock homogeneous behavior with about 60 experiments in isotropic compression, in triaxial compression, and in triaxial extension. A large range of confining pressures, i.e. 0–60 MPa (0–8,702 psi) was investigated, showing a significant evolution of material response.

2.2.1 Experimental Isotropic Compression

Figure 2-8 depicts the experimental curves of the compression test in the mean stress (pressure) versus volumetric strain plane. The origins of the curves of the compression tests are sequentially placed on the curve of the isotropic compression test, after each one's consolidation stage.

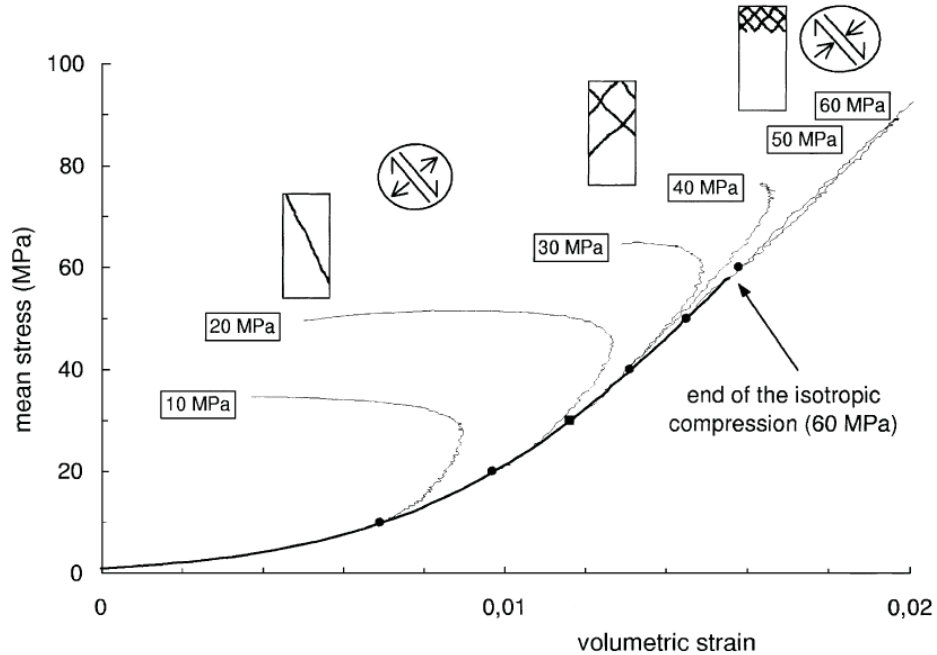
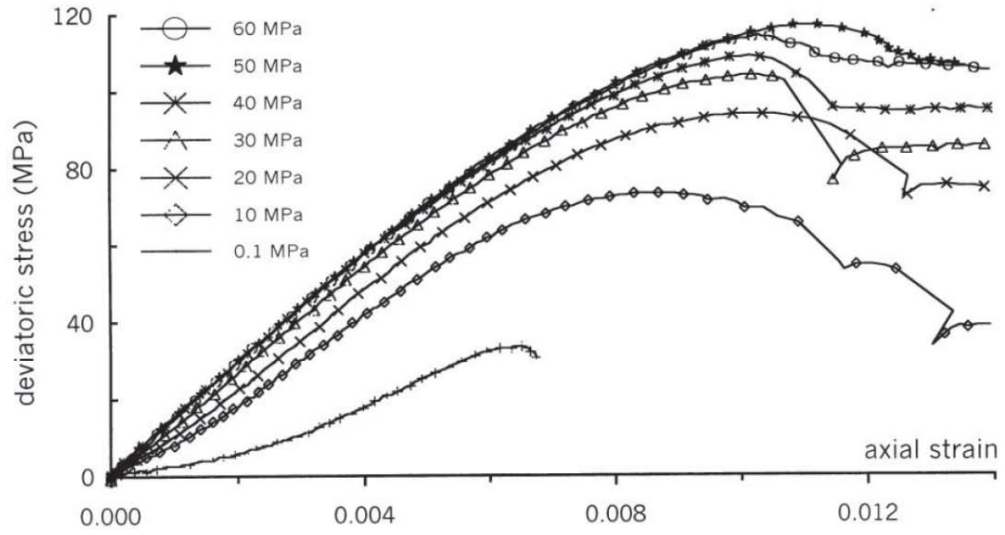


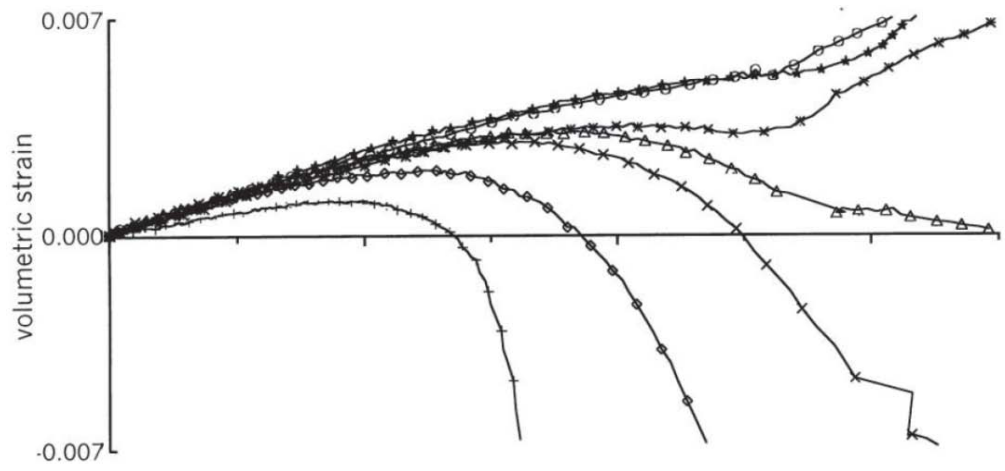
Figure 2-8: Experimental isotropic compression of Vosges sandstone (Bésuelle et al. 2000)

2.2.2 Experimental Triaxial Compression

As shown in Figure 2-9(a), in compression, the loading modulus and the maximum strength increase with confining pressure. However, it seems that after 50 MPa (7,252 psi) of confining pressure, the deviatoric strength reaches a peak, and it is not surpassed by rock compressive strength at greater pressure. As far as volumetric curves are concerned (see Figure 2-9(b)), “an initial contractancy at all confining pressures is observed first. Then, up to the peak stress, depending on the confining pressure, there is either dilatancy –larger at low confining pressure–, or contractancy –small, only at 60 MPa (8,702 psi).” (Bésuelle et al. 2000)



(a) Effective Stress vs. Axial Strain

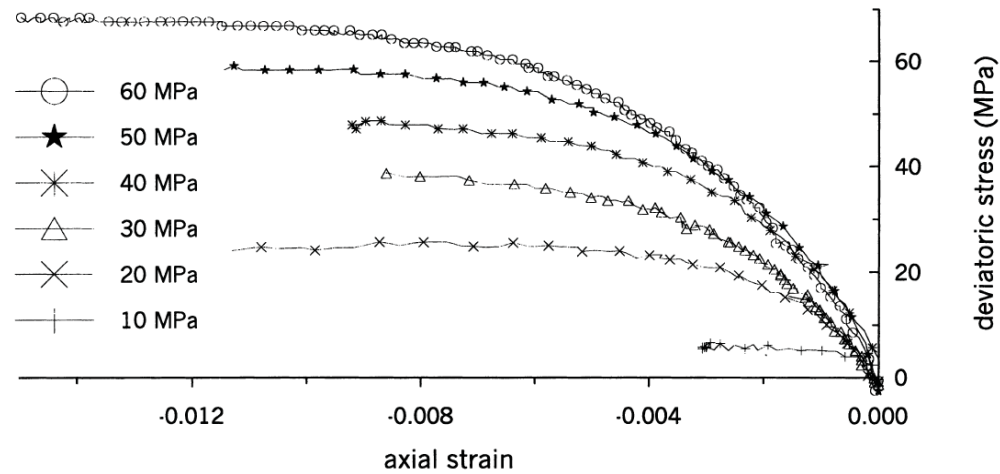


(b) Volumetric Strain vs. Axial Strain

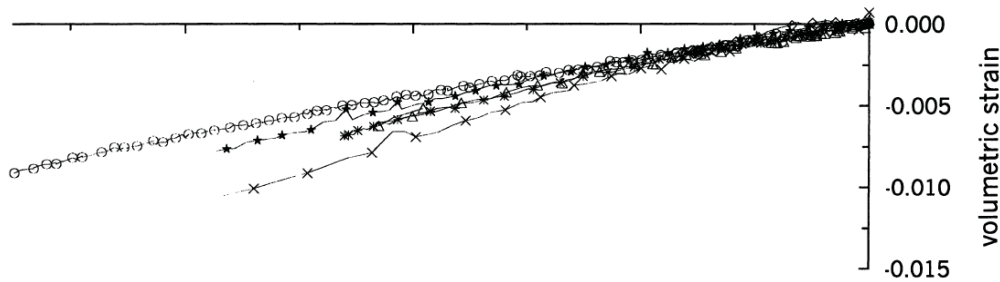
Figure 2-9: Experimental triaxial compression of Vosges sandstone (Bésuelle et al. 2000)

2.2.3 Experimental Triaxial Extension

The behavior of the sandstone in the extension tests is shown in Figure 2-10. The total axial stress at failure for the different confining pressures is almost the same, about 10 MPa (1,450 psi) in traction, which implies a quasi-linear failure curve in the Mohr diagram. However, a test performed at 100 MPa (14,504 psi) confining pressure shows that the curve becomes nonlinear at higher stress, such as for the compression test (Bésuelle et al. 2000). The volumetric dilatancy is quasi-linear with the axial strain, and depends only slightly on the confining pressure.



(a) Effective Stress vs. Axial Strain



(b) Volumetric Strain vs. Axial Strain

Figure 2-10: Experimental triaxial extension of Vosges sandstone (Bésuelle et al. 2000)

2.2.4 Experimental Failure Envelopes

Given the deviatoric stress at failure and its corresponding pressure, the Mohr diagram can be plotted for both compression and extension tests as shown in Figure 2-11.

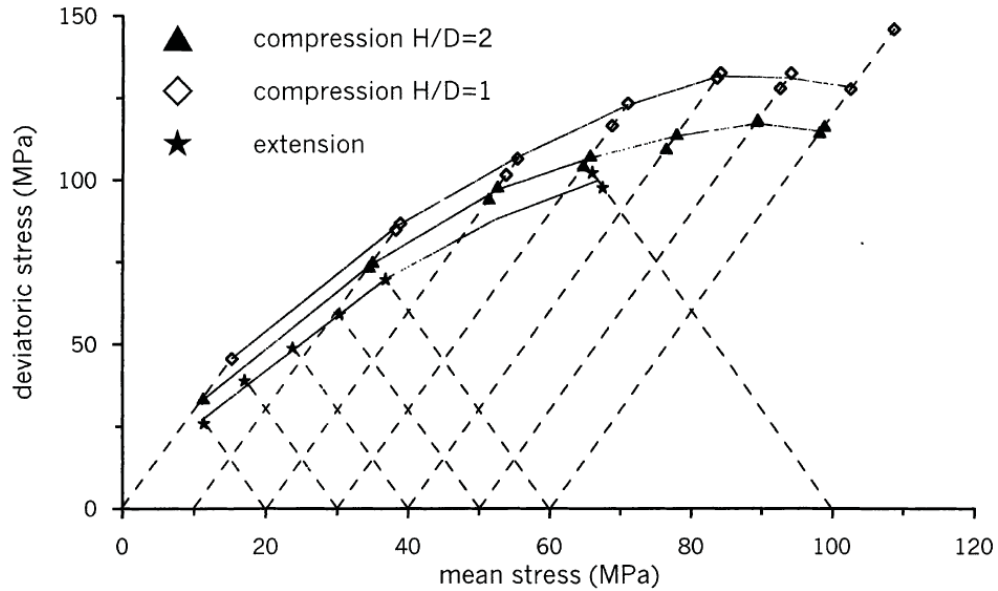


Figure 2-11: Experimental strength at failure of Vosges sandstone (Bésuelle et al. 2000)

2.3 GENETIC ALGORITHM FOR CURVE-FITTING OPTIMIZATION

Complex material models such as Mat_111, Mat_72R3 and Mat_159 consist of nonlinear constitutive relationships (equations). In order to obtain a good fit of these equations to the existing laboratory curves, it is essential to use an advanced technique so the appropriate nonlinear regression is achieved. The *genetic algorithm* method from the Global Optimization Toolbox in Matlab is used for this purpose.

In general, “the genetic algorithm solves optimization problems by mimicking the principles of biological evolution, repeatedly modifying a population of individual points using rules modeled on gene combinations in biological reproduction. Due to its random nature, the genetic algorithm improves your chances of finding a global solution. It enables you to solve unconstrained, bound-constrained, and general optimization problems, and it does not require the functions to be differentiable or continuous.” (The Mathworks 2009)

Herein, the genetic algorithm solver, *ga*, is implemented to minimize an objective function $X = ga(\text{fitnessfcn}, nvars)$, so the result of *ga* is the least squared error. *ga* finds a local unconstrained minimum, x , to the objective function, which accepts the vector X of size 1-by- $nvars$, and returns a scalar evaluated at X . The optimal value of the objective is weakly smaller as $nvars$ are added, by the fact that relatively unconstrained minimization leads to a solution which is weakly smaller than relatively constrained minimization.

3.0 ROCK BEHAVIOR THROUGH CONSTITUTIVE MODELS

One of the biggest challenges associated with modeling the behavior of rock cutting with numerical continuum methods is the difficulty of incorporating a realistic material model that can accurately represent the natural, inhomogeneous characteristics of the physical system.

“It is known that at the initial stage of rock cutting, intense crushing of the rock occurs under the tool and, only then, as cutting progresses, cracks are generated at a certain depth in the rock, leading to the formation of a chip (fragment). The formation of the chip is one of greatest interests, since precisely at this stage the maximum effectiveness of fracturing is achieved.” (Gnuchii et al. 1988)

To predict both the initiation of a fracture (location, size) and further propagation of the crack (growth path), it is necessary to know in detail the stress field, which is highly dependent on the material model performance. This section discusses the material constitutive models evaluated during the course of this work. Ultimately, the selection of one of the material models in LS-DYNA was made, and it is aimed to serve as benchmark for future investigations on rock cutting by means of FEM.

3.1 MODELING ROCK WITH CONCRETE CONSTITUTIVE LAWS

Generally, the behavior of an element in a rock continuum, even in plane stress, cannot be satisfactorily modeled using uniaxial stress-strain characteristics, and the consideration of triaxial stress conditions is desirable for better understanding its behavior. Failure limits in rock can be represented as surfaces in a three-dimensional principal-stress space such as the failure surfaces

for concrete depicted in Figure 3-1, where σ_1 , σ_2 and σ_3 are principal stresses and (in this case) the compressive stresses are negative.

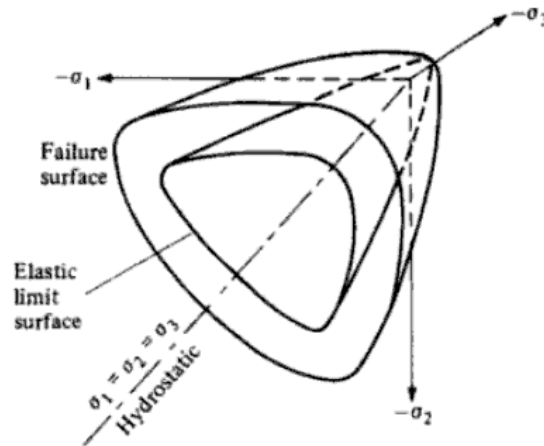


Figure 3-1: Schematic failure surface of concrete in 3D stress space (Chen 2007)

A failure criterion for isotropic materials based upon a state of stress must be an invariant function of the state of stresses, i.e. it must be independent of the choice of the coordinate system by which is defined. Therefore, a failure criterion is usually defined using stress invariants. This is precisely how the different material models assessed in the present work are formulated.

3.1.1 Definition of the Failure Criterion

The general shape of a failure surface in the three-dimensional stress space can best be described by its cross-sectional shapes in the deviatoric plane and its meridians. The cross-sections of the failure surface are the intersection curves between the failure surface and a deviatoric plane, which is perpendicular to the hydrostatic axis. The meridians of the failure surface are the intersection curves between the failure surface and a plane (the meridian plane) containing the hydrostatic axis. Figure 3-2 shows an example of a cross-section of the failure surface.

In this figure, the plane of the paper is the deviatoric plane, and the coordinate axes σ_1 , σ_2 , and σ_3 are projected onto this plane. The two extreme meridian planes (farthest and closest intersections from the hydrostatic axis) are called the compressive meridian and tensile meridian, respectively.

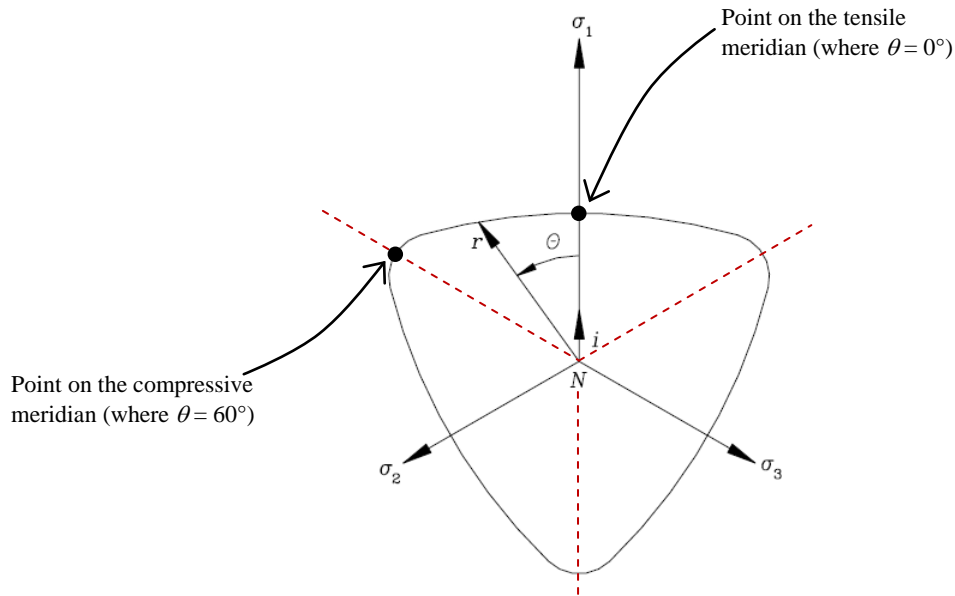


Figure 3-2: Deviatoric cross-section of the failure surface

As shown in Figure 3-2, the cross-section has a triangular shape and it can be defined by a point in the compressive meridian and by a point in the tensile meridian. The path between the compressive and the tensile meridians (distance r as a function of θ) is defined by an elliptical curve developed by Willam and Warnke (1974).

Failure surfaces can be combined with plasticity-based constitutive models for the analysis of three-dimensional concrete or rock. These three-dimensional surfaces are used to construct initial yield surfaces and subsequent loading surfaces, from which the incremental stress-strain relationships of the material can be constructed (Chen 2007). Typically, the strength envelope is defined in the stress space in such way that, once the current state of stress reaches a defined surface, the material fails. However, the particular definitions of the models implemented in this study account for material damage, which takes place after the peak strength is reached. This means that actual failure does not occur immediately upon reaching the failure surface, but it occurs after a damage value exceeds 99%.

3.1.2 Stress State before Failure

The simplest representation of the stress state at a point is obtained by treating the stress state as two components: the hydrostatic part and the deviatoric part. Hydrostatic pressure has a

significant influence on the strain hardening and failure of geomaterials. Under hydrostatic pressure, concrete and rock can be consolidated beyond the limit of elasticity but cannot be crushed to failure; therefore, their compressive failure is governed by the deviatoric components –or shear components– of the stress state.

The yield surface marks the onset of weakening of the material under increasing load. As seen in Figure 3-1, the yield surface has a similar shape to the maximum surface but it is reduced in size. The maximum surface (or failure surface) is fixed in the principal stress space at some distance from the yield surface. During initial loading or reloading, the deviatoric stresses remain elastic until the stress point reaches the initial yield surface. The deviatoric stresses can then increase further until the maximum failure surface is reached. Beyond this stage, the response can be perfectly plastic or soften to a residual surface.

The following sections, 3.2.1 through 3.2.4, contain the description of the constitutive equations that characterize the material models under consideration.

3.2 ROCK MATERIAL MODELS IN LS-DYNA

With the aim of reproducing a realistic behavior of the rock response pre and post-failure during the cutting event, it is critical to implement a complex and rational material model. Fortunately, LS-DYNA contains a comprehensive suite of material models, including specific concretes and geomaterials, from which three were selected and evaluated.

After a detailed survey of the material models available in LS-DYNA, a group of materials, which suitably characterize rock and concrete behavior, was picked. Table 3-1 lists the features present in each of the geomaterials chosen. Each material model in LS-DYNA is represented by a number. If a material model includes any of the following attributes, a “Y” appears in the respective column of Table 3-1.

SRATE- Strain-rate effects

FAIL- Failure criteria

EOS- Equation-of-State for 3D solids and 2D continuum elements

THERM- Thermal effects

ANISO- Anisotropic/orthotropic

DAM- Damage effects

TENS- Tension handled differently than compression in some manner

In addition to the concrete or rock application of these material models, other additional potential applications –in terms of the type of physical behavior– are abbreviated in the table as follows:

CM- Composite

FM- Foam

MT- Metal

Table 3-1: Concrete and rock material models in LS-DYNA

Mat No.	Name	SRATE	FAIL	EOS	THERM	ANISO	DAM	TENS	Implemented also in		Additional potential applications
									ALE	SPH	
16	Pseudo Tensor Geological Model	Y	Y	Y			Y	Y	Y	Y	
25	Inviscid Two Invariant Geologic Cap	Y						Y		Y	
26	Honeycomb	Y	Y			Y		Y			CM, FM
72	Concrete Damage	Y	Y	Y			Y	Y	Y	Y	
78	Soil Concrete		Y				Y	Y	Y		
84	Winfrith Concrete (with rate effects)	Y						Y	Y		FM
96	Brittle Damage	Y	Y			Y	Y	Y	Y		
111	Johnson Holmquist Concrete	Y	Y				Y	Y		Y	
126	Modified Honeycomb	Y	Y			Y	Y	Y			CM, FM
145	Schwer Murray Cap Model	Y	Y				Y	Y		Y	
159	CSCM	Y	Y				Y	Y			
172	Concrete EC2		Y		Y			Y			MT
198	Jointed Rock		Y			Y		Y			

In the beginning of this study, upon inspection of the robustness of each of the materials in Table 3-1, it was determined that Material 72 (MAT_CONCRETE_DAMAGE or MAT_72) was very comprehensive in characterizing the rock behavior in a wide range of stress states. However, little implementation of this material model was found in the literature (see Section 3.2.3), thus some uncertainty arises about its performance as a rock. For this reason, Material 111 (MAT_JOHNSON_HOLMQUIST_CONCRETE or MAT_111) was identified as a potential reliable model, since more studies implementing this model were found (see Section 3.2.2).

In view of the complex nature of Materials 72 and 111, a more straightforward material model was also studied in order to assess the feasibility of some numerical features offered by LS-DYNA. The simple material selected was Material 105 (MAT_DAMAGE_2 or MAT_105)

(see description in Section 3.2.1). Although this material model is not considered among the potential geomaterials listed in Table 3-1, it was implemented in some simulations of rock cutting for comparison purposes. Its numerical attributes are presented in Table 3-2.

Table 3-2: “Damage 2” material attributes in LS-DYNA

Mat No.	Name	SRATE	FAIL	EOS	THERM	ANISO	DAM	TENS	Implemented also in		Potential applications
									ALE	SPH	
105	Damage 2	Y	Y				Y				MT

The above-mentioned material models were subjected to a thorough calibration of their input parameters with the aim of properly simulating the fragmentation evolution observed during the rock cutting experiments. It is important to mention that these models do not contemplate *element erosion* (see Section 5.3.1) implicitly in their formulation, therefore, “addition” of *element erosion* needs to be set up, as provided by LS-DYNA.

Unfortunately, however, it was concluded that the implementation of any of those three material models was limited due to the impossibility to determine a specific erosion criterion (or a combination of criteria) for the deletion of elements. Adequately configured *element erosion* must be able to produce initiation of cracks and eventually would aid in the chipping of rock fragments out of the simulated rock continuum.

There was a need for a rational approach where elements were deleted upon material failure, in par with the constitutive laws of the material model. Ultimately, Material 159 (MAT_CONTINUOUS_SURFACE_CAP_MODEL, or MAT_CSCM or MAT_159) was found to serve this objective (see Section 3.2.4).

3.2.1 Mat_105 – Damage 2 Model

In LS-DYNA, Mat_105 is an elastic isotropic visco-plastic material combined with the Continuum Damage Mechanics (CDM) model proposed by Lemaitre (1984). Although the damage parameter is calculated as a function of pressure (see Equation (3-5)), the effective stress $\bar{\sigma}$ in this model is not pressure dependent. This implies that the application of this material model

is limited and not suitable to simulate geomaterials under pressure (it rather serves to model metal behavior).

The effective stress is identified by:

$$\bar{\sigma} = \frac{\sigma}{1 - D} \quad (3-1)$$

where D is the damage variable. The evolution equation for the damage variable is defined as:

$$\dot{D} = \begin{cases} 0, & r \leq r_D \\ \frac{Y}{S(1 - D)} \dot{r}, & r > r_D \text{ and } \sigma_1 > 0 \end{cases} \quad (3-2)$$

where r is the damage accumulated plastic strain, r_D is the damage threshold (user defined), S is a positive material constant (user defined), Y is the so-called “damage strain-to-energy release rate”, and σ_1 is the maximum principal stress (positive in tension). Variable r can be calculated from:

$$\dot{r} = \dot{\varepsilon}_{eff}^p (1 - D) \quad (3-3)$$

where $\dot{\varepsilon}_{eff}^p$ is the effective plastic strain rate.

On the other hand, the damage strain-to-energy release rate may be calculated by:

$$Y = \frac{\sigma_{eq}^2 R_v}{2E(1 - D)^2} \quad (3-4)$$

where σ_{eq} is the equivalent von-Mises stress, E is the elastic modulus, and the triaxiality variable R_v is defined as a function of the Poisson’s ratio ν and the hydrostatic stress or pressure p :

$$R_v = \frac{2}{3}(1 + \nu) + 3(1 - 2\nu) \left(\frac{p}{\sigma_{eq}} \right)^2 \quad (3-5)$$

It is important to emphasize that in Mat_105 formulation, damage can only develop for tensile stresses, thus $D = 0$ for compressive strains. The principal strain directions are fixed within an integration point as soon as either principal strain exceeds the initial threshold strain in tension.

Mat_105 accounts for strain rate effects using the Cowper and Symonds' model, which scales the yield stress with the factor:

$$\text{strain rate factor} = 1 + \left(\frac{\dot{\epsilon}}{C}\right)^{\frac{1}{P}} \quad (3-6)$$

where C and P are user-defined input parameters, and the strain rate is $\dot{\epsilon} = \sqrt{\dot{\epsilon}_{ij} \dot{\epsilon}_{ij}}$.

3.2.1.1 Mat_105 Input Calibration

As mentioned in Section 3.2, due to the simplicity of Mat_105, this material model was used only to assess the feasibility of some numerical features offered by LS-DYNA. Although it is not considered among the potential geomaterials listed in Table 3-1, it was implemented in some simulations of rock cutting for comparison purposes.

Herein, only parameters that control the elastic-perfectly plastic response of MAT_105 were determined for input, therefore the basic mechanical properties of Vosges Sandstone, as the ones listed in Table 2-1, are used. In addition, damage parameters were calibrated by trial and error such that the performance of the rock cutting simulations appeared reasonable and the mechanisms involved were close to reality. Table 3-3 lists the input parameters used for MAT_105.

Table 3-3: Input Parameters for MAT_105

ρ	$2.0 \times 10^{-6} \text{ kg/mm}^3$	(125 lb/ft ³)
E	5.2 GPa	(754,196 psi)
ν	0.33	
$\sigma_{\text{yield}} = \sigma_c$	$33.1 \times 10^{-3} \text{ GPa}$	(4,801 psi)
r_D	0.003	
S	1.0	
D_C	1.0×10^{-3}	

3.2.2 Mat_111 – Johnson Holmquist Concrete Model

Based on LS-DYNA theory manual (Hallquist 2006), this model can be used for concrete subjected to large strains, high strain rates, and high pressures, and was developed by Holmquist et al. (1993). The equivalent stress is expressed as a function of pressure, strain rate and includes the effect of permanent crushing. The damage value is accumulated as a function of the plastic volumetric strain, equivalent plastic strain, and pressure.

The equivalent stress is defined as:

$$\sigma_{eq} = f_c' \left[A(1 - D) + B \left(\frac{p}{f_c'} \right)^N \right] \left[1 - C \ln \left(\frac{\dot{\epsilon}}{\dot{\epsilon}_0} \right) \right] \quad (3-7)$$

where f_c' is the uniaxial compressive strength, D is the damage parameter, p is pressure, A , B , C and N are user-defined input parameters, and $\dot{\epsilon}_0$ is the reference strain rate, also user defined as an input.

3.2.2.1 Damage Accumulation in Mat_111

The model accumulates damage both from equivalent plastic strain and from plastic volumetric strain and it is expressed as:

$$D = \sum \frac{\Delta \varepsilon_{eq}^p + \Delta \varepsilon_V^p}{D_1 \left(\frac{p}{f_c'} + \frac{T}{f_c'} \right)^{D_2}} \quad (3-8)$$

where T is the maximum tensile hydrostatic pressure, and D_1 and D_2 are material damage constants, all three defined by the user. The denominator of Equation (3-8) represents the plastic strain to fracture under a constant pressure, p . As it is evident from this equation, the concrete material cannot undergo any plastic strain at $p = -T$ and alternatively, the plastic strain to fracture increases as p increases. A third damage constant, EFMIN, should be provided by the user to allow for a finite amount of plastic strain to fracture the material. This is included to suppress fracture from low magnitude tensile waves.

Damage due to plastic volumetric strain is included in Equation (3-8) because concrete will lose cohesive strength during air void collapse. However, under most circumstances, the majority of the damage will occur from equivalent plastic strain.

3.2.2.2 Pressure-Volume Relationship in Mat_111

In a hydrostatic (isotropic) compression plot, the pressure-volume response is separated into three response regions:

1. The first region is linear elastic and occurs at $p \leq P_{crush}$. P_{crush} and ε_V^{crush} (user inputs) are the pressure and volumetric strain respectively, that occur in a uniaxial stress compression test.
2. The second region is referred to as the transition region and occurs at $P_{crush} < p < P_{lock}$. In this region, the air voids are gradually compressed out of the concrete producing plastic volumetric strain. Unloading in this region occurs along a modified path that is interpolated from the adjacent regions.
3. The third region defines the relationship for fully dense material (all air voids removed from the concrete). The air voids are completely removed from the material when the pressure reaches P_{lock} with the corresponding ε_V^{lock} (both user inputs) and the relationship is expressed as:

$$p = K_1 \bar{\varepsilon}_V + K_2 \bar{\varepsilon}_V^2 + K_3 \bar{\varepsilon}_V^3 \quad (3-9)$$

$$\bar{\varepsilon}_V = \frac{\varepsilon_V - \varepsilon_V^{lock}}{1 - \varepsilon_V^{lock}} \quad (3-10)$$

The modified volumetric strain, $\bar{\varepsilon}_V$, is used so that the user-defined constants (K_1 , K_2 , and K_3) are equivalent to those used for material with no voids.

For tensile pressure, $p = K\varepsilon_V$ in the elastic region, $p = K_1\varepsilon_V$ in the fully dense region, and $p = [(1 - F)K + F K_1]\varepsilon_V$ in the transition region. The interpolation factor is:

$$F = (\varepsilon_V^{max} - \varepsilon_V^{crush}) / (\varepsilon_V^{lock} - \varepsilon_V^{crush}) \quad (3-11)$$

where ε_V^{max} is the maximum volumetric strain reached prior to unloading. A similar method is used for compressive unloading except that the higher order terms $K_2 \bar{\varepsilon}_V^{-2}$ and $K_3 \bar{\varepsilon}_V^{-3}$ are included. The tensile pressure is limited to $T(1 - D)$.

3.2.2.3 Mat_111 Input Calibration

The values for some of the input parameters in Mat_111 have been taken from the original formulation reference by Holmquist et al. (1993). These inputs are C , $EFMIN$, D_1 , D_2 , P_{lock} , K_1 , K_2 , and K_3 . The rest of the parameters are calibrated as explained below. Table 3-4 displays the values of all input parameters for Mat_111 as used in this study.

Failure Envelope Parameters

Equation (3-7) provides the relationship between the equivalent (von-Mises) stress and pressure for Mat_111. It also includes the effect of accumulated damage, D , and strain rate, $\dot{\varepsilon}$, on the equivalent stress. When performing the characterization tests explained in Section 2.2, the strain rate during the tests is $\dot{\varepsilon} = 10^{-5} \text{ s}^{-1}$, a quasi-static condition, making the testing strain rate equal to the reference strain rate, $\dot{\varepsilon}_0$; therefore no strain rate effect is experienced. Additionally, during the laboratory tests no damage of the rock is contemplated, thus Equation (3-7) could be used here as:

$$\frac{\sigma_{eff}}{f'_c} = A + B \left(\frac{p}{f'_c} \right)^N \quad (3-12)$$

Using the genetic algorithm, described in Section 2.3, constants A , B , and N are estimated. Figure 3-3 presents the regression that best fits the maximum failure strength envelope.

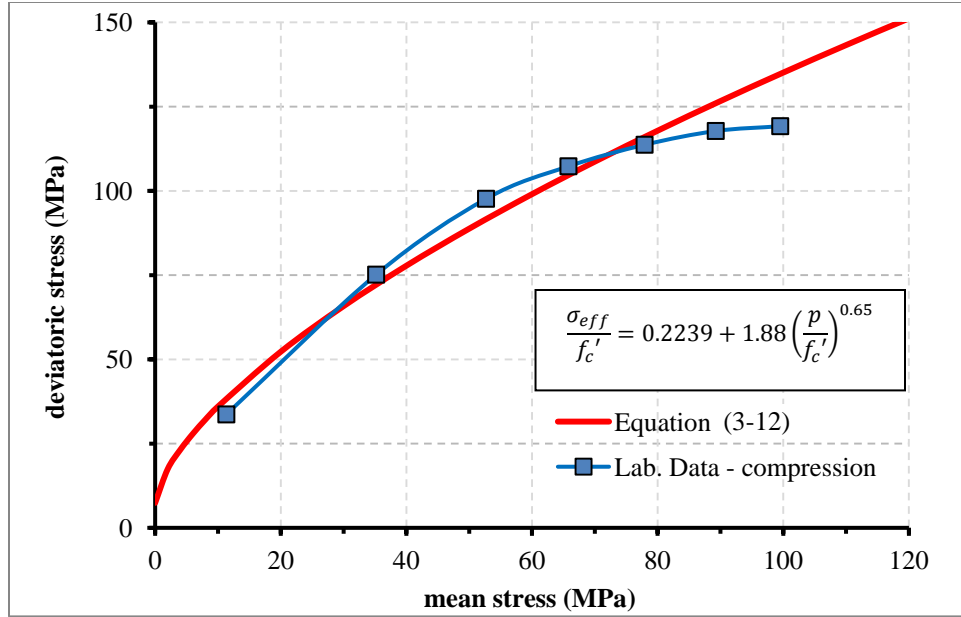


Figure 3-3: Maximum compressive failure envelope fitting by Mat_111

The strength constant σ^*_{max} is estimated by:

$$\sigma^*_{max} = \frac{\sigma_{max}}{f'_c} \approx 4.0 \quad (3-13)$$

Pressure-Volume Relationship Parameters

$$P_{crush} = \frac{f'_c}{3} = 11.03 \text{ MPa (1,600 psi)} \quad (3-14)$$

$$\varepsilon_V^{crush} = \frac{f'_c(1-2\nu)}{E} = 8.882 \times 10^{-4} \quad (3-15)$$

$$\varepsilon_V^{lock} = \left(\frac{\rho_{grain}}{\rho_0}\right) - 1 = 0.325 \quad (3-16)$$

Table 3-4: Input Parameters for MAT_111

ρ_0	2000 kg/m ³ (125 lb/ft ³)	P_{crush}	11.03 MPa (1,600 psi)
G	2,662 GPa (386 x10 ⁶ psi)	ε_V^{crush}	8.882 x10 ⁻⁴
A	0.2239	P_{lock}	800 MPa (116,030 psi)
B	1.88	ε_V^{lock}	0.325
C	0.007	D_1	0.04
N	0.65	D_2	1
f_c'	33.1 MPa (4,801 psi)	K_1	85
f_t	3.1 MPa (450 psi)	K_2	-171
$\dot{\varepsilon}_0$	10 ⁻⁵ s ⁻¹	K_3	208
EFMIN	0.01	FS	0
σ^*_{max}	4	T	4 MPa (580 psi)

3.2.3 Mat_72R3 – Concrete Damage Rel. 3 Model

Mat_72R3, also known as the Karagozian & Case (K&C) model, is an improved and more robust version of Mat_16, Concrete/Geological material model in LS-DYNA. In release III of this concrete model, an automatic input capability was added to generate the input data needed to specify a particular concrete, and the strategy used in fitting the strain softening was modified. Automatic data generation can provide a complete default set of 72 input parameters with knowledge of only the concrete unconfined compressive strength and the system of units (Malvar et al. 1999).

This model is a plasticity-based formulation with three independent failure surfaces, as shown in Figure 3-4, which change shape depending on the level of pressure. The curves above and below the p-axis correspond to compressive and tensile meridians, respectively:

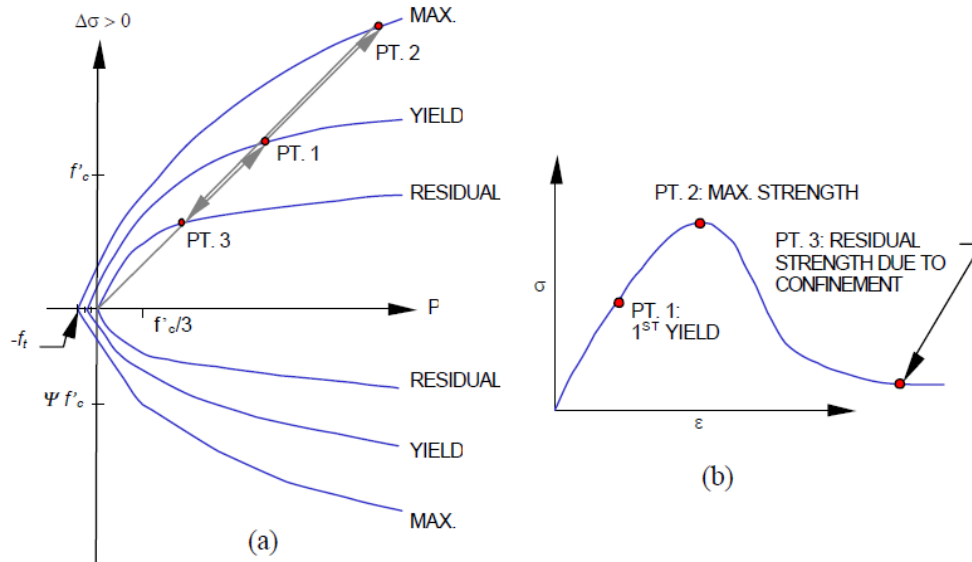


Figure 3-4: Failure surfaces (a) and concrete constitutive behavior (b) in Mat_72R3 model

3.2.3.1 Mat_72R3 Input Calibration

Eight out of twenty-two input parameters in this model were calibrated via the experimental triaxial tests presented in Section 2.2: LABORATORY CHARACTERIZATION FOR PARAMETER CALIBRATION. These parameters are namely the coefficients required for the compressive meridians (see Section 3.2.3.2). Six other input parameters have been generated by the automatic option of MAT_72R3; these are b_1 , b_2 , b_3 (described in Section 3.2.3.5), ω , E_{drop} , and S_λ . Table 3-5 displays the values of all input parameters for Mat_72R3 as used in this study.

In addition to the twenty-two input parameters, Mat 72_R3 requires the input of a tabulated equation of state that relates the volumetric strain of the rock with pressure, therefore the isotropic compression curve of the simulated material perfectly agrees with experimental data. Moreover, a tabulated damage function and a strain-rate effect function have to be defined.

Table 3-5: Input Parameters for MAT_72R3

ρ	$2.0 \times 10^{-6} \text{ kg/mm}^3$ (125 lb/ft ³)	a_0	$6.0 \times 10^{-3} \text{ GPa}$ (870 psi)
ν	0.33	a_1	0.35
f_t	$3.215 \times 10^{-3} \text{ GPa}$ (466 psi)	a_2	4.50 GPa^{-1} ($3.1 \times 10^{-5} \text{ psi}^{-1}$)
b_1	1.60	a_{1f}	0.45
b_2	1.35	a_{2f}	4.50 GPa^{-1} ($3.1 \times 10^{-5} \text{ psi}^{-1}$)
b_3	1.15	a_{0y}	$6.92 \times 10^{-3} \text{ GPa}$ (1,004 psi)
ω	0.5	a_{1y}	0.53
S_λ	100	a_{2y}	12.0 GPa^{-1} ($8.3 \times 10^{-5} \text{ psi}^{-1}$)
N_{out}	4	LOC-WIDTH	1.35 mm (0.05 in)
E_{drop}	1.0	R-SIZE	$39.97 \times 10^{-3} \text{ in / mm}$
N_{points}	13	UCF	$145.0 \times 10^3 \text{ psi / GPa}$

3.2.3.2 Compressive Meridians in Mat_72R3

In the model, the compressive failure surfaces depicted in Figure 3-4 are defined as follows:

$$\Delta\sigma_m = a_0 + \frac{p}{a_1 + a_2 p} \quad (\text{maximum failure surface}) \quad (3-17)$$

$$\Delta\sigma_r = \frac{p}{a_{1f} + a_{2f} p} \quad (\text{residual failure surface}) \quad (3-18)$$

$$\Delta\sigma_y = a_{0y} + \frac{p}{a_{1y} + a_{2y} p} \quad (\text{yield failure surface}) \quad (3-19)$$

where: a_i = input parameters determined from available laboratory data in unconfined compression tests and triaxial compression tests at a range of confining pressures;

$p = (\sigma_1 + \sigma_2 + \sigma_3)/3$ = Pressure (positive in compression);

$\sigma_1, \sigma_2, \sigma_3$ = Principal stresses (positive in compression);

$\Delta\sigma = \sqrt{3J_2}$ = Failure surface for the deviatoric stress (von-Mises stress);

$J_2 = (S_1^2 + S_2^2 + S_3^2)/3$ = Second invariant of the deviatoric stress tensor; and,

S_1, S_2, S_3 = Principal deviatoric stresses.

Maximum Failure Surface

Using the genetic algorithm, constants a_0 , a_1 , and a_2 in Equation (3-17) are estimated from the laboratory triaxial tests in compression. Figure 3-5 presents the regression that best fits the maximum failure strength envelope.

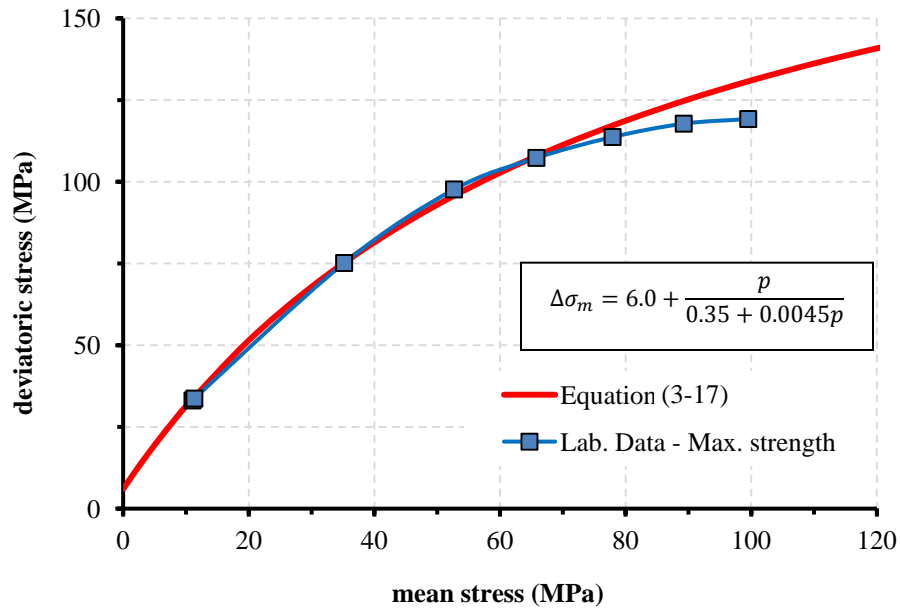


Figure 3-5: Maximum failure surface fitting by Mat_72R3

Residual Failure Surface

The values of experimental residual strength as a function of pressure are taken from Figure 2-9: Experimental triaxial compression of Vosges sandstone (Bésuelle et al. 2000). Similar to the maximum failure surface, the genetic algorithm is used to find constants a_{1f} , and a_{2f} in Equation (3-18). Figure 3-6 presents the regression that best fits the residual strength envelope.

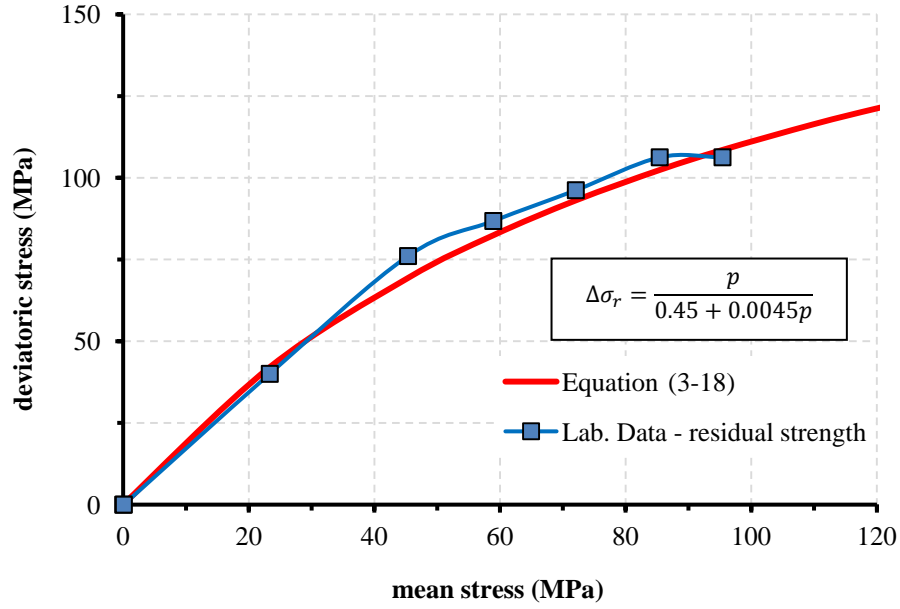


Figure 3-6: Residual surface fitting by Mat_72R3

Initial Yield Surface

Malvar et al. (1997) suggest that this surface is approximately the locus of points at $\Delta\sigma = 0.45 \Delta\sigma_m$ on triaxial compression paths. For a point $(p, \Delta\sigma_m)$ on the maximum failure surface, the corresponding point $(p', \Delta\sigma_y)$ on the yield surface is:

$$\Delta\sigma_y = 0.45 \Delta\sigma_m \quad \text{and} \quad p' = p - \frac{0.55}{3} \Delta\sigma_m \quad (3-20)$$

From the latter equation, p can be rewritten as a function of p' , while the former equation gives $\Delta\sigma_y$ as a function of p :

$$\Delta\sigma_y = 0.45 \left(a_0 + \frac{p}{a_1 + a_2 p} \right) \quad (3-21)$$

Eventually, $\Delta\sigma_y$ can be computed as a function of p' , a_0 , a_1 , and a_2 . This computed curve is then used to obtain a regression that fits the following equation:

$$\Delta\sigma_y = a_{0y} + \frac{p'}{a_{1y} + a_{2y} p'} \quad (3-22)$$

Again, the genetic algorithm is used to find constants a_{0y} , a_{1y} , and a_{2y} in Equation (5-8). Figure 3-7 presents the regression that best fits the initial yield strength envelope.

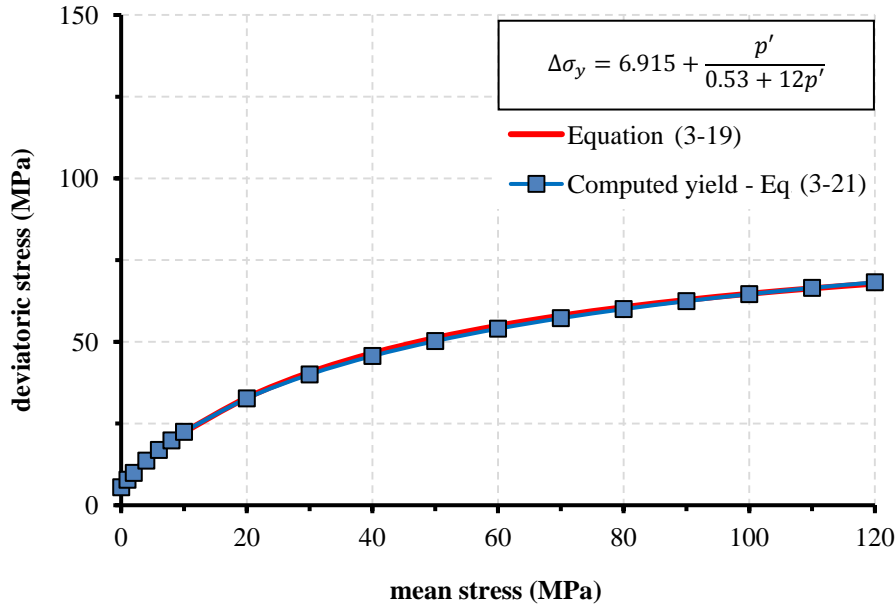


Figure 3-7: Initial yield surface fitting by Mat_72R3

3.2.3.3 Calculation of Current Deviatoric Stress in Mat_72R3

After reaching the initial yield surface but before reaching the maximum failure surface, the current surface is obtained as a linear interpolation between the two:

$$\Delta\sigma = \eta(\Delta\sigma_m - \Delta\sigma_y) + \Delta\sigma_y \quad (3-23)$$

where η varies from 0 to 1 depending on an accumulated effective plastic strain parameter λ . The function $\eta(\lambda)$ has to be entered by the user as a series of (λ, η) pairs in the input file. The value η is intended to begin from zero at $\lambda = 0$, increase to 1 at some value $\lambda = \lambda_m$, and then decrease to zero at some larger value of λ , representing softening. Since λ is a non-decreasing function of time, this would permit $\Delta\sigma$ to sequentially take on the values $\Delta\sigma_y$, $\Delta\sigma_m$, and $\Delta\sigma_r$. Therefore, the function $\eta(\lambda)$ is a parameter that indicates the relative location of the current surface. After

reaching the maximum surface, the current failure surface is similarly interpolated between the maximum and the residual:

$$\Delta\sigma = \eta(\Delta\sigma_m - \Delta\sigma_r) + \Delta\sigma_r \quad (3-24)$$

As a result, the concrete stress-strain behavior will be as the one depicted in Figure 3-4: Failure surfaces (a) and concrete constitutive behavior (b) in Mat_72R3 model.

As mentioned above, the stress factor, η , as a function of the damage parameter –or accumulated effective plastic strain parameter, λ – is a user input for MAT_72R3. Table 3-6 displays input data regarding this damage function, which has been taken from the automatic initialization of MAT_72R3.

Table 3-6: Stress factor vs. Accumulated effective plastic strain

Accumulated effective plastic strain parameter, λ	Stress Factor, η
0	0
8.01E-06	0.85
2.40E-05	0.97
4.00E-05	0.99
5.60E-05	1
7.20E-05	0.99
8.80E-05	0.97
3.20E-04	0.5
5.20E-04	0.1
5.70E-04	0
1	0
10	0
100	0

3.2.3.4 Tensile Meridians in Mat_72R3

The tensile or extension meridian of the failure surface for concrete is usually lower (closer to the hydrostatic at the same pressure) than the compressive meridian. According to Malvar and Simons (1996), experimental data suggest that the ratio of the tensile to compressive meridian,

herein denoted ψ , varies from about 0.5 at negative (tensile) pressures to unity at high confinements. Using equal meridians at low pressures would yield erroneous results.

Malvar et al. (1994) offer a detailed description of the meaning of ψ for different pressure ranges, as well as the definition of the tensile and pressure cutoffs, the strain rate enhancement feature, and the correction of shear modulus due to the assumption of constant Poisson's ratio.

As far as the strain rate enhancement, Table 3-7 reports input data for this function, which has been adopted from LS_DYNA user's manual (Hallquist 2009).

Table 3-7: Strain rate enhancement function

Effective strain rate (1/ms)	Shear strength enhancement
-30	9.7
-0.3	9.7
-0.1	6.72
-0.03	4.5
-0.01	3.12
-0.003	2.09
-0.001	1.45
-0.0001	1.36
-0.00001	1.28
-0.000001	1.2
-1E-07	1.13
-1E-08	1.06
0	1
3E-08	1
1E-07	1.03
0.000001	1.08
0.00001	1.14
0.0001	1.2
0.001	1.26
0.003	1.29
0.01	1.33
0.03	1.36
0.1	2.06
0.3	2.94
30	2.94

3.2.3.5 Damage Accumulation in Mat_72R3

This material model implements *shear damage accumulation* by including rate effects and by treating damage evolution differently in tension than in compression, as follows:

$$\lambda = \int_0^{\bar{\varepsilon}^p} \frac{d\bar{\varepsilon}^p}{r_f \left(1 + \frac{p}{r_f f_t}\right)^{b_1}} \quad \text{for } p \geq 0 \quad (3-25)$$

$$\lambda = \int_0^{\bar{\varepsilon}^p} \frac{d\bar{\varepsilon}^p}{r_f \left(1 + \frac{p}{r_f f_t}\right)^{b_2}} \quad \text{for } p < 0 \quad (3-26)$$

where $d\bar{\varepsilon}^p = \sqrt{\left(\frac{2}{3}\right) \varepsilon_{ij}^p \varepsilon_{ij}^p}$ is the effective plastic strain increment, r_f is a user-defined experimental rate enhancement factor (or function) from unconfined uniaxial compression tests, and b_1 and b_2 are the softening parameters explained below, also user-defined.

Additionally, Mat_72R3 accounts for *volumetric damage*. With damage accumulation as just described, if a triaxial tensile test is modeled, wherein the pressure decreases from 0 to $-f_t$ with no deviators, then no damage accumulation occurs. Parameter λ remains 0 and so does η . The equation of state reduces the pressure to $-f_t$ but keeps it at that level thereafter. To implement pressure decay after tensile failure, a volumetric damage increment is added to the deviatoric damage whenever the stress path is “close” to the triaxial tensile test path, i.e., the negative hydrostatic axis. The closeness to this path is measured by the ratio $|\sqrt{3}J_2/p|$, which, for example, is 1.5 for the biaxial tensile test. To limit the effects of this change to the paths close to the triaxial tensile path, the incremental damage is multiplied by a factor f_d given by:

$$f_d = \begin{cases} 1 - 10|\sqrt{3}J_2/p|, & 0 \leq |\sqrt{3}J_2/p| < 0.1 \\ 0, & \text{otherwise} \end{cases} \quad (3-27)$$

and the modified effective plastic strain is incremented by:

$$\Delta\lambda = b_3 f_d k_d (\varepsilon_V - \varepsilon_V^{yield}) \quad (3-28)$$

where b_3 is a user input scalar multiplier, k_d is an internal scalar multiplier, ε_V is the volumetric strain, and ε_V^{yield} is the volumetric strain at yield.

Parameter b_1 , in Equation (3-25), governs softening in compression, whereas b_2 , in Equation (3-26), has an effect on the uniaxial tensile strain softening; b_3 , in Equation (3-27), affects the triaxial tensile strain softening. These softening parameters can be determined by iteration until the value of the fracture energy, G_f , converges for a specified characteristic length, which is associated with the localization width (i.e. the width of the localization path transverse to the crack advance).

In this study, parameters b_1 , b_2 , and b_3 are taken from the values given by Mat_72R3's automatic initialization; their values are 1.60, 1.35 and 1.15 respectively.

3.2.3.6 Pressure-Volume Relationship in Mat_72R3

In LS-DYNA, this material model is used in conjunction with an equation of state (EOS_TABULATED_COMPACTION), which provides the current element pressure p as a function of the current and previous volumetric strain. In this tabulated compaction model, pressure is defined by the following formula:

$$p = C(\varepsilon_V) \quad (3-29)$$

Once the pressure is known, the stress tensor can be calculated as being a point on a movable surface that can be a yield surface or a failure surface. Function $C(\varepsilon_V)$ should be entered by the user as a series of (ε_V, p, K) sets, where K is the bulk modulus correspondent to the different $p - \varepsilon_V$ pairs.

The equation of state mentioned above, which describes the rock compaction behavior, is tabulated in Table 3-8 and plotted in Figure 3-8. Data points for this curve are obtained directly from Figure 2-8: Experimental isotropic compression of Vosges sandstone (Bésuelle et al. 2000).

Table 3-8: Equation of state (EOS_TABULATED_COMPACTIION) for MAT_72R3

Volumetric Strain	Pressure (GPa)	Bulk Modulus (GPa)
0.0	0.0	5.30
0.00143	0.002	1.07
0.00380	0.004	1.20
0.00584	0.008	2.16
0.00765	0.012	3.03
0.00903	0.017	4.21
0.01023	0.023	4.76
0.01193	0.033	6.36
0.01446	0.050	7.45
0.02385	0.130	8.69

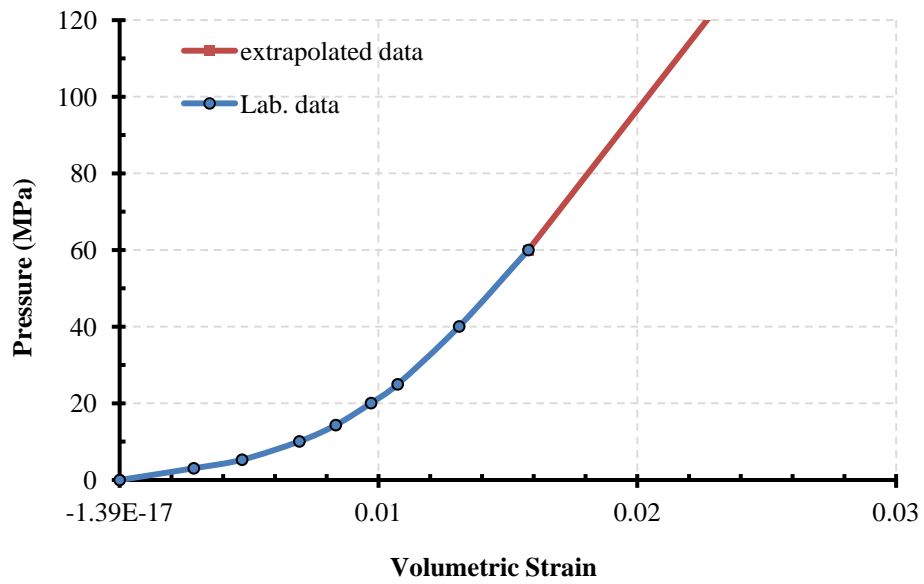


Figure 3-8: Equation of state for MAT_72R3

3.2.4 Mat_159 – Continuous Surface Cap Model

The Continuous Surface Cap Model is a visco-elastic-plastic damage model for concrete and other geologic materials developed and implemented by APTEK as a result of a research effort funded by the Federal Highway Administration (FHWA) with the aim of simulating the deformation and failure of concrete in roadside safety structures impacted by vehicles. A thorough formulation is described by Murray (2007b) and the main constitutive equations are described below.

Besides the fact that this model contemplates strain softening and modulus reduction of the material based on an isotropic damage formulation –which considers brittle and ductile damage separately– the major relevant and most beneficial attribute of this material model in simulating rock cutting is that it incorporates *element erosion* upon material failure. This denotes a dramatic advantage over the material models described before. Section 5.3 elucidates the importance of *element erosion* for this numerical modeling effort.

Mat_159 is a cap model with a smooth intersection between the shear surface and the hardening cap, as shown in Figure 3-9. In the model, the initial damage surface coincides with the yield surface and the strain rate effects are modeled with viscoplasticity.

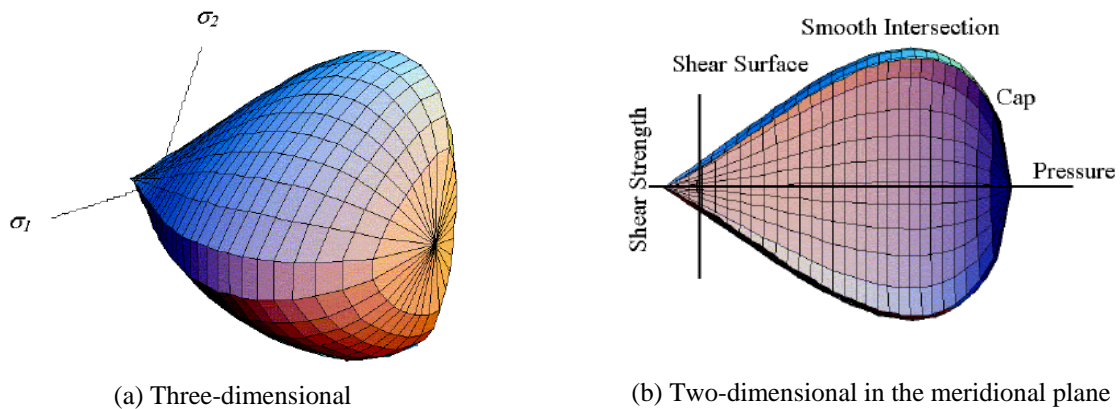


Figure 3-9: General shape of the yield surface in Mat_159 model (Murray 2007b)

The yield surface is formulated in terms of three stress invariants: I_1 is the first invariant of the stress tensor, J_2 is the second invariant of the deviatoric stress tensor, and J_3 is the third invariant of the deviatoric stress tensor. The invariants are defined in terms of the deviatoric stress tensor, S_{ij} and pressure, p , as follows:

$$I_1 = 3p \quad (3-30)$$

$$J_2 = \frac{1}{2} S_{ij} S_{ij} = \frac{1}{3} (\sigma_{eq}^2) \quad (3-31)$$

$$J_3 = \frac{1}{3} S_{ij} S_{jk} S_{ki} = \det(S_{ij}) = S_1 S_2 S_3 \quad (3-32)$$

3.2.4.1 Mat_159 Input Calibration

Mat_159 requires the specification of 45 input parameters, 22 of which were carefully calibrated by fitting the laboratory test data presented in Section 2.2. Determination of these parameters is shown in the following sections as applicable. The rest of the input parameters were estimated or taken from typical values reported by Murray in her material user's manual for the FHWA (Murray 2007b). Table 3-9 displays the values of all input parameters for Mat_159.

Table 3-9: Input Parameters for MAT_159

Control factors		Shear surface hardening	
ρ	2.0x10 ⁻⁶ kg/mm ³ (125 lb/ft ³)	N_H	0
NPLOT	1	C_H	0
INCRE	-	Cap geometry and hardening	
IRATE	1	R	0.6
ERODE	1	X_0	3.0 x10 ⁻³ GPa (435 psi)
RECOV	10.5	W	0.009
IRETRC	1	D_1	30 GPa ⁻¹ (2.0 x10 ⁻⁴ psi ⁻¹)
PRED	0	D_2	0 GPa ⁻² (0 psi ⁻²)

Stiffness

G_0	3.1 GPa	(449,617 psi)
K_0	8.75 GPa	(1,269,080 psi)

Yield surface

α	75×10^{-3} GPa	(10,878 psi)
θ	1×10^{-4}	
λ	70×10^{-3} GPa	(10,153 psi)
β	0.008×10^3 GPa ⁻¹	(5.5×10^{-5} psi ⁻¹)
α_1	68×10^{-3} GPa	(9,863 psi)
θ_1	0.02	
λ_1	65×10^{-3} GPa	(9,427 psi)
β_1	0.0078×10^3 GPa ⁻¹	(5.4×10^{-5} psi ⁻¹)
α_2	73×10^{-3} GPa	(10,588 psi)
θ_2	5×10^{-4}	
λ_2	71×10^{-3} GPa	(10,298 psi)
β_2	0.007×10^3 GPa ⁻¹	(4.8×10^{-5} psi ⁻¹)

Damage

b	100
d	0.1
G_{fc}	3.5×10^{-3} GPa (507.6 psi)
G_{ft}	3.5×10^{-5} GPa (5.076 psi)
G_{fs}	3.5×10^{-5} GPa (5.076 psi)
$pwrc$	5
$pwrt$	1
$pmod$	0

Rate effects

η_{c0}	1×10^{-4}
N_c	0.78
η_{t0}	6.0×10^{-5}
N_t	0.48
$overc$	20×10^{-3} GPa (2,901 psi)
$overt$	20×10^{-3} GPa (2,901 psi)
S_{rate}	1
$repow$	1

3.2.4.2 Plasticity Surface in Mat_159

The yield function is based on the three invariants in Equations (3-30) through (3-32) and the cap hardening parameter, κ , as follows:

$$f(I_1, J_2, J_3, \kappa) = J_2 - \mathfrak{R}^2 F_f^2 F_c \quad (3-33)$$

where F_f is the shear failure surface, F_c is the hardening cap, and \mathfrak{R} is the Rubin three-invariant reduction factor. The cap hardening parameter κ is the value of the pressure invariant at the intersection of the cap and the shear surfaces.

Trial elastic stress invariants are temporarily updated via the trial elastic stress tensor, σ^{trial} . The invariants are denoted by I_1^{trial} , J_2^{trial} , and J_3^{trial} . Elastic stress states are modeled when $f(I_1^{\text{trial}}, J_2^{\text{trial}}, J_3^{\text{trial}}, \kappa^{\text{trial}}) \leq 0$. Elastic-plastic stress states are modeled when $f(I_1^{\text{trial}}, J_2^{\text{trial}}, J_3^{\text{trial}}, \kappa^{\text{trial}}) > 0$. In this case, the plasticity algorithm returns the stress state to the yield surface in such a way that $f(I_1^{\text{p}}, J_2^{\text{p}}, J_3^{\text{p}}, \kappa^{\text{p}}) = 0$, where the p superscript denotes

inviscid. This is accomplished by enforcing the plastic consistency condition with associated flow.

Shear Failure Surface (Compressive Meridian)

The strength of concrete is modeled by the shear surface in the tensile and low confining pressure regimes. The shear surface F_f is defined along the compression meridian as:

$$F_f(I_1) = \alpha - \lambda \exp^{-\beta I_1} + \theta I_1 \tag{3-34}$$

where the values of α , β , λ , and θ are selected by fitting the model surface to strength measurements from triaxial compression (TXC) tests conducted on plain cylinders.

Using the genetic algorithm, constants α , β , λ , and θ in Equation (3-34) are estimated based on the set of laboratory triaxial tests in compression. Figure 3-10 presents the regression that best fits the shear surface along the compressive meridian.

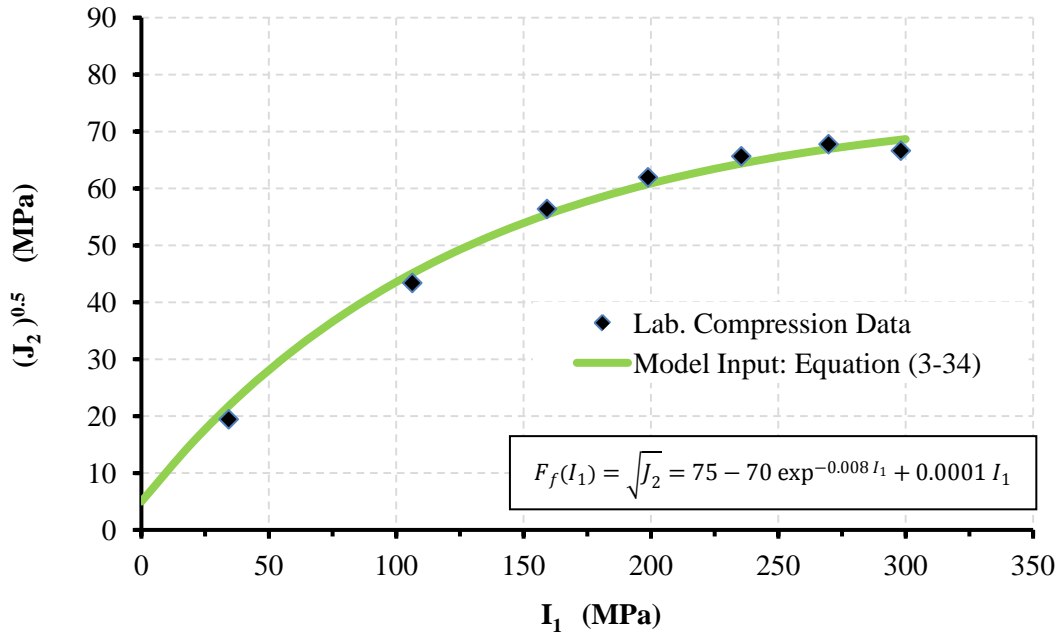


Figure 3-10: Compressive shear surface fitting by Mat_159

Rubin Scaling Function

Concrete fails at lower values of $\sqrt{3J_2}$ (principal stress difference) for triaxial extension (TXE) and shear (TOR) tests than it does for TXC tests conducted at the same pressure. The Rubin scaling function \mathfrak{R} determines the strength of concrete for any state of stress relative to the strength under TXC, via $\mathfrak{R} F_f$. Therefore, $\mathfrak{R} = Q_1$ when the strength is under TOR, and $\mathfrak{R} = Q_2$ when the strength is under TXE. The strength model for these two cases is given by:

$$Q_1 F_f = \alpha_1 - \lambda_1 \exp^{-\beta_1 I_1} + \theta_1 I_1 \quad (3-35)$$

$$Q_2 F_f = \alpha_2 - \lambda_2 \exp^{-\beta_2 I_1} + \theta_2 I_1 \quad (3-36)$$

Tensile Meridian: Similar to the compressive shear failure surface, the genetic algorithm is used to find constants α_2 , β_2 , λ_2 , and θ_2 in Equation (3-36) using the set of laboratory triaxial tests in extension. Figure 3-11 presents the regression that best fits the shear surface along the tensile meridian.

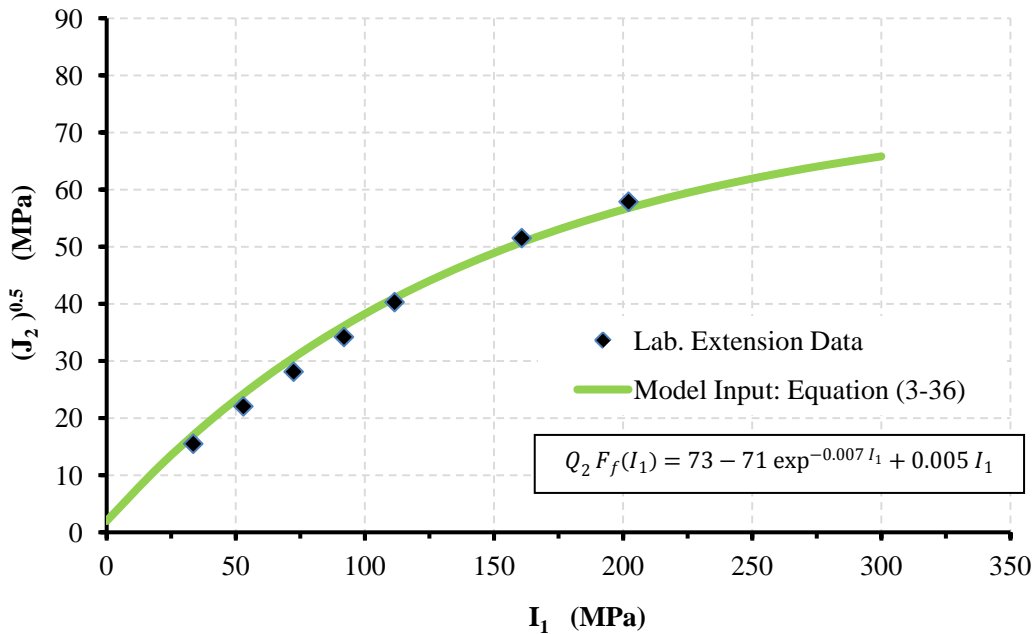


Figure 3-11: Tensile shear surface fitting by Mat_159

Shear Meridian: When enough experimental data is not available to obtain the fitting parameters that characterize the Rubin Scaling Function, the user can incorporate theoretical relationships between the strength ratios Q_1 and Q_2 , such as the Mohr-Coulomb fit (Murray 2007b).

The Mohr-Coulomb fit defines a straight line fit between the TXE and TXC states. The strength ratios are estimated based upon the following relationships:

$$Q_1 = \frac{\sqrt{3} Q_2}{1 + Q_2} \quad (3-37)$$

$$Q_2 = \frac{TXE}{TXC} \quad (3-38)$$

Q_1 and Q_2 as expressed above are independent of pressure and only apply for $I_1 = 0$. Considering the magnitude of the tensile failure envelope, TXE at $I_1 = 0$ in relation to the magnitude of the compressive failure envelope, TXC at $I_1 = 0$, Equation (3-38) results in $Q_2 = 0.9733$, which represents the average ratio of TXE over TXC. Consequently, Q_1 can be computed from Equation (3-37), giving $Q_1 = 0.8543$. Finally, by assuming a constant ratio of TOR over TXC, i.e. parallel meridians, parameters α_1 , β_1 , λ_1 , and θ_1 in Equation (3-35) are estimated through manual inspection. Figure 3-12 presents the regression that best fits the shear surface along the shear (TOR) meridian.

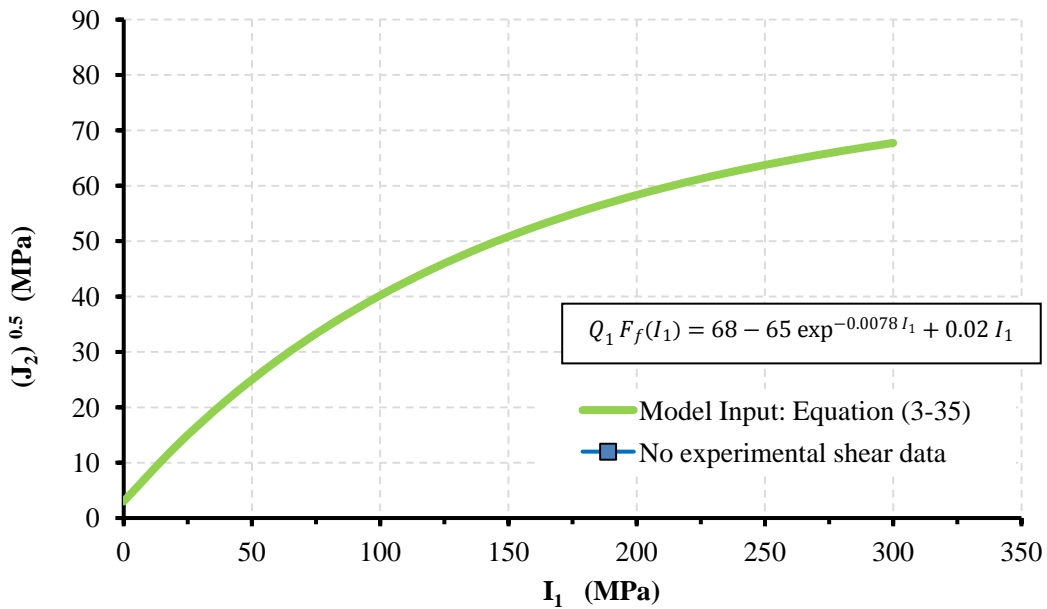


Figure 3-12: Torsion shear surface fitting by Mat_159

3.2.4.3 Cap Hardening in Mat_159

The strength of concrete is modeled by a combination of the cap and shear surfaces in the low to high confining pressure regimes. The cap is used to model plastic volume change related to pore collapse (although the pores are not explicitly modeled).

As observed in Figure 3-13(b), the isotropic hardening cap is a two-part function that is either unity or an ellipse, such that:

$$F_c(I_1, \kappa) = 1 - \frac{[I_1 - L(\kappa)][|I_1 - L(\kappa)| + I_1 - L(\kappa)]}{2[X(\kappa) - L(\kappa)]^2} \quad (3-39)$$

where $L(\kappa)$ is defined as:

$$L(\kappa) = \begin{cases} \kappa, & \kappa > \kappa_0 \\ \kappa_0, & \text{otherwise} \end{cases} \quad (3-40)$$

The equation for F_c is equal to unity for $I_1 \leq L(\kappa)$ and it describes an ellipse for $I_1 > L(\kappa)$. The intersection of the shear surface and the cap is at $I_1 = \kappa$, as denoted by the “branch point” in Figure 3-13(c). κ_0 is the value of I_1 at the *initial* intersection of the cap and shear surfaces before hardening is engaged (before the cap moves). The equation for $L(\kappa)$ restrains the cap from retracting past its initial location at κ_0 .

A simpler but less complete way of writing Equations (3-39) and (3-40) is:

$$F_c(I_1, \kappa) = \begin{cases} 1 - \frac{(I_1 - \kappa)^2}{(X(\kappa) - \kappa)^2}, & I_1 \geq \kappa \\ 1, & \text{otherwise} \end{cases} \quad (3-41)$$

The intersection of the cap with the I_1 -axis (hydrostat) is at $I_1 = X(\kappa)$, *marking the point at which pressure under hydrostatic loading would be sufficient to induce pore collapse* (Fossum and Brannon 2004).

$$X(\kappa) = L(\kappa) + R F_f(L(\kappa)) \quad (3-42)$$

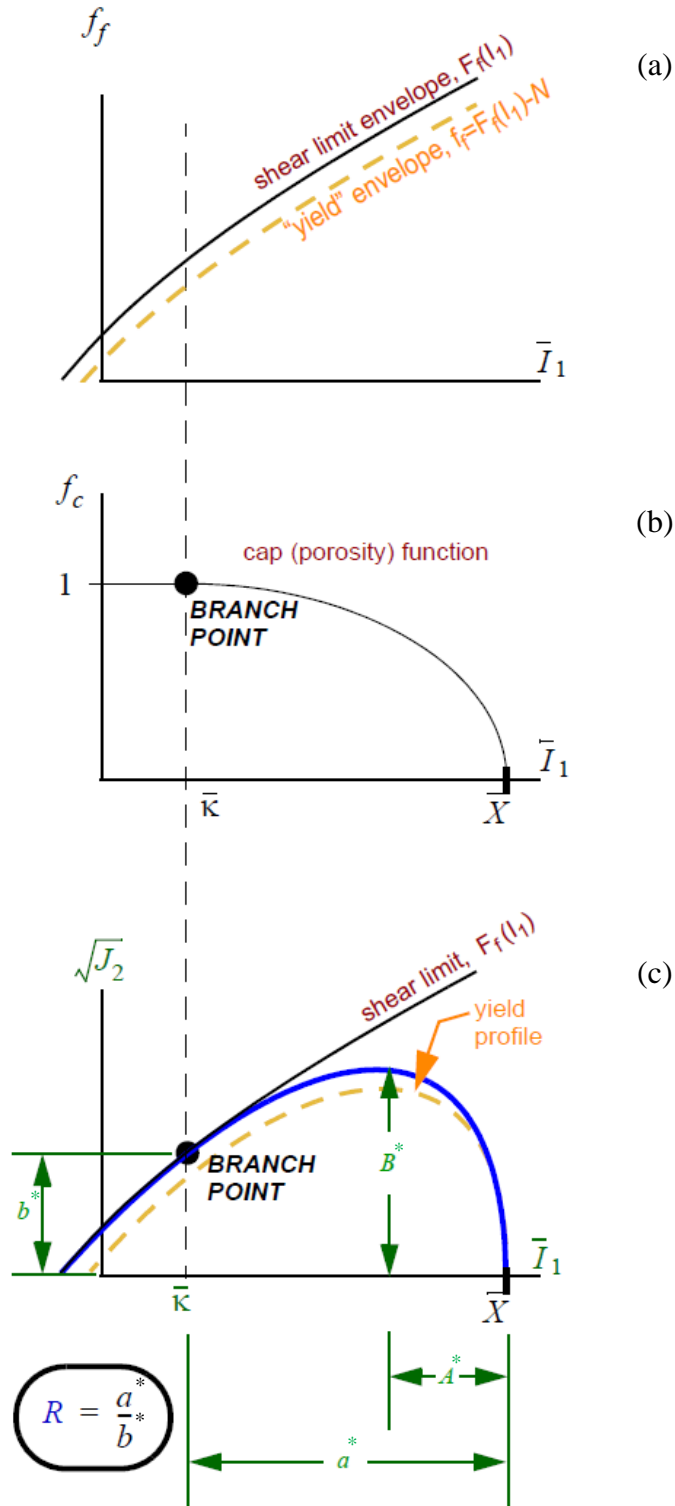


Figure 3-13: Cap curvature model (Fossum and Brannon 2004)

This intersection depends upon the cap ellipticity ratio R , which is the ratio of the ellipse's major to minor axes. As depicted in Figure 3-13(c), R can be interpreted as the ratio of the horizontal distance a^* to the vertical distance b^* of the branch point. The value of R in Mat_159 is user defined, and it is determined as explained below.

The cap moves to simulate plastic volume change. The cap expands, i.e. $X(\kappa)$ and κ increase, to simulate plastic volume compaction. The cap contracts, i.e. $X(\kappa)$ and κ decrease, to simulate plastic volume expansion, called dilation. The motion (expansion and contraction) of the cap is based upon the hardening rule:

$$\varepsilon_V^p = W(1 - \exp^{-D_1(X-X_0)-D_2(X-X_0)^2}) \quad (3-43)$$

where ε_V^p is the plastic volume strain, W is the maximum user-defined plastic volume strain, and D_1 and D_2 are model fitting parameters defined by the user, as well as X_0 , which is the initial location of the cap when $\kappa = \kappa_0$ (See Figure 3-14).

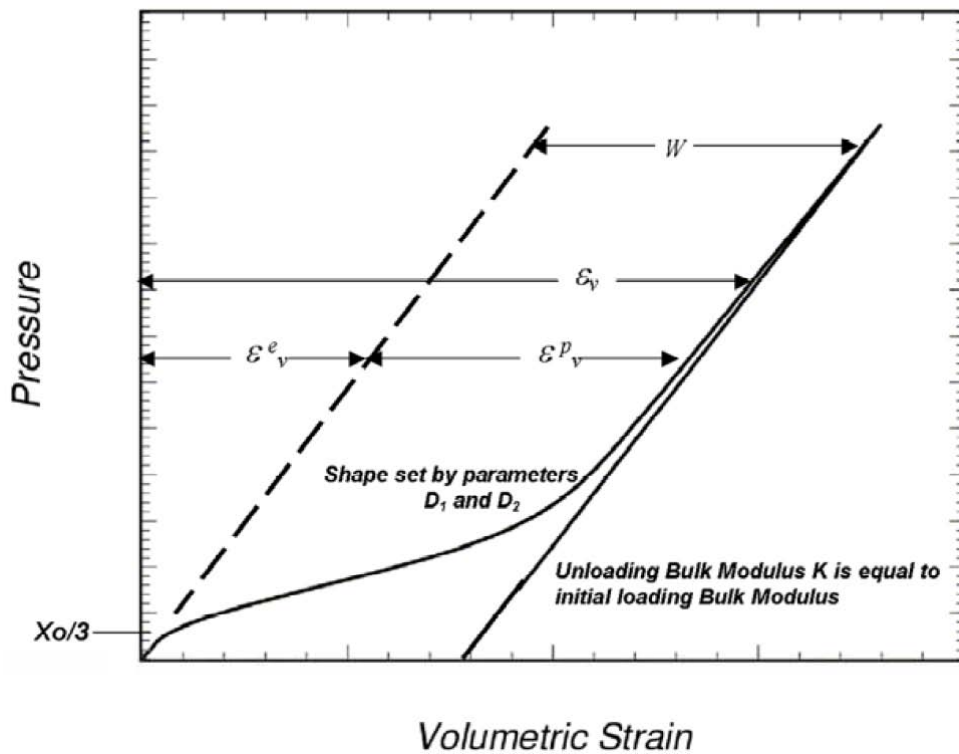


Figure 3-14: Example of parameter determination on isotropic compression curve (Murray 2007b)

The four user-defined input parameters, W , X_0 , D_1 and D_2 in Equation (3-43) are obtained from fits to the pressure-volumetric strain curve in isotropic compression, in this case study, Figure 2-8: Experimental isotropic compression of Vosges sandstone (Bésuelle et al. 2000).

A non-straightforward analysis of the model was performed to calibrate these parameters, which are determined as follows:

X_0 is the initial cap location and it is the pressure invariant (I_1) at which compaction initiates in isotropic compression, thus the curve becomes nonlinear. Based upon Figure 2-8, Vosges sandstone does not exhibit any elastic (linear) strain range, thus X_0 corresponds to the intercept of the curve at $\varepsilon_V = 0$, i.e. $p = 1.0$ MPa (145.04 psi), so $X_0 = 3.0$ MPa (435.12 psi). The non-elastic-strain behavior of Vosges sandstone can be appreciated and confirmed with the curve of Effective Stress vs. Axial Strain in Figure 2-9 at 0.1 MPa (14.5 psi) of confinement pressure. The fact that there is essentially no elastic volume change also implies that the branch point in Figure 3-13 (b and c) is initially located at $I_1 = 0$, therefore, $\kappa_0 = 0$. As a result of this, on one hand, the magnitude of a^* can be determined from Figure 3-13 (c) as:

$$a^* = X - \kappa = X_0 - \kappa_0 = X_0 = 3 \text{ MPa (435.12 psi)} \quad (3-44)$$

On the other hand, the value of b^* is determined similarly as the intercept of the shear limit function on the $\sqrt{J_2}$ -axis. Solving Equation (3-34) for $I_1 = 0$ results in $F_f(0) = \alpha - \lambda$, thus:

$$b^* = F_f(0) = \alpha - \lambda = 75 - 70 = 5 \text{ MPa (725.2 psi)} \quad (3-45)$$

According to Fossum and Brannon (2004), the ellipticity ratio, R , remains constant as hardening proceeds. Consequently, having obtained a^* and b^* , the constant input value of R for Vosges sandstone is:

$$R = \frac{a^*}{b^*} = \frac{3 \text{ MPa}}{5 \text{ MPa}} = 0.6 \quad (3-46)$$

W is the maximum plastic volume change that defines the range in volumetric strain over which the pressure-volumetric strain is nonlinear (from onset to lock-up). Based upon Figure 2-8, the input value of W for Vosges sandstone is 0.009.

Having established parameters W and X_0 , determination of D_1 and D_2 is made by manual inspection by fitting Equation (3-43) to the curve in Figure 2-8, as these two parameters describe the shape of the pressure-volumetric strain curve. Figure 3-15 presents the plot of Equation (3-43) with the selected constant values, in contrast with the experimental isotropic compression data.

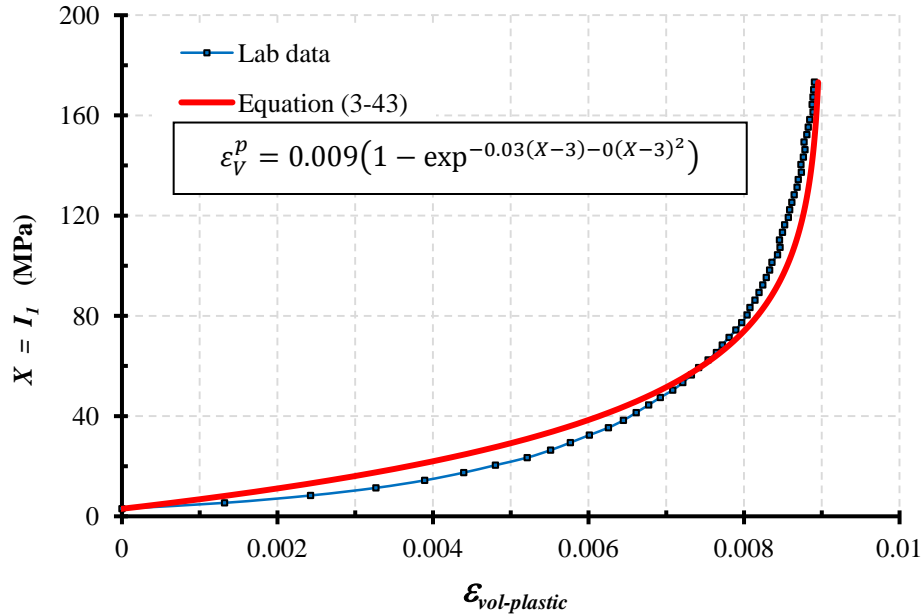


Figure 3-15: Isotropic compression curve fitting by Mat_159

3.2.4.4 Shear Hardening Surface in Mat_159

In unconfined compression, the stress-strain behavior of concrete exhibits nonlinearity and dilation prior to the peak strength. Such behavior is modeled with an initial shear yield surface, $N_H F_f$, which hardens until it coincides with the ultimate shear yield surface, F_f . Two input parameters are required. One parameter, N_H , initiates hardening by setting the location of the initial yield surface. A second parameter, C_H , determines the rate of hardening (amount of nonlinearity).

Unfortunately, during this parameterization endeavor, it was discovered that these hardening parameters do not operate properly, i.e. the material model could have a bug. The following responses were exhibited while doing sensitivity analyses to N_H and C_H :

- By default, $N_H = 1$; if this value is changed to a lower number, the maximum compressive strength is reached immediately when carrying out a 1-element uniaxial compression test, with its value being less than a hundredth of the actual material strength. The lower the value of N_H , the lower the final maximum strength achieved, and the longer the model takes to run.
- By default, $C_H = 0$; when changed to different values greater than zero, the model did not experienced any change.

As a result of the above-mentioned drawbacks, the values used in this study are the default for N_H and C_H .

3.2.4.5 Damage Accumulation in Mat_159

Concrete exhibits softening in the tensile and low to moderate compressive regimes.

$$\sigma_{ij}^D = (1 - D)\sigma_{ij}^{vp} \quad (3-47)$$

A scalar damage parameter, D , transforms the visco-plastic stress tensor without damage, σ_{ij}^{vp} , into a stress tensor with damage, σ_{ij}^D . Damage accumulation is based upon two distinct formulations, herein called *brittle* damage and *ductile* damage.

Brittle and ductile damage initiate with plasticity. This effectively means that the initial damage surface is coincident with the plastic shear surface. Therefore, a distinct damage surface or threshold is not defined by the user. Damage initiates at peak strength on the shear surface where the plastic volume strain is dilative. Damage does not initiate on the cap, where plastic volume strain is compactive.

Each strain energy term (ductile or brittle) in Equations (3-48) and (3-49) must increase in value above its previous maximum in order for damage to accumulate. When energy remains constant or decreases, damage temporarily stops accumulating. This corresponds to an expanding damage surface.

Ductile Damage

Ductile damage accumulates when the pressure, p , is compressive and an energy-type term, τ_c , exceeds the damage energy threshold, τ_{c0} , which is internally determined. Ductile damage accumulation depends upon the total strain components, ε_{ij} , as follows:

$$\tau_c = \sqrt{\frac{1}{2} \sigma_{ij} \varepsilon_{ij}} \quad (3-48)$$

The stress components, σ_{ij} , are the elasto-plastic stresses (with kinematic hardening) calculated before application of damage and rate effects.

Brittle Damage

Brittle damage accumulates when the pressure is tensile and an energy-type term, τ_t , exceeds the damage energy threshold, τ_{t0} , which is internally determined. Brittle damage accumulation depends upon the maximum principal strain, ε_{\max} , and the elastic Young's modulus, E , as follows:

$$\tau_t = \sqrt{E \varepsilon_{\max}^2} \quad (3-49)$$

Softening Function

As damage accumulates, the damage parameter D increases from an initial value of zero towards a maximum value of one, via the following formulae:

- For ductile damage ($p \geq 0$):

$$D(\tau_c) = \frac{0.999}{b} \left[\frac{1 + b}{1 + b \exp^{-a(\tau_c - \tau_{c0})}} - 1 \right] \quad (3-50)$$

- For brittle damage ($p < 0$):

$$D(\tau_t) = \frac{D_{\max}}{d} \left[\frac{1 + d}{1 + d \exp^{-c(\tau_t - \tau_{t0})}} - 1 \right] \quad (3-51)$$

The damage parameter applied to the six components of the stress corresponds to the current maximum of the brittle or ductile damage parameter. Parameters a and b in Equation (3-50), or c and d in Equation (3-51) set the shape of the softening curve plotted as stress-displacement or stress-strain. Parameters b and d should be user-defined and a and c are internally calculated. Parameter D_{\max} in Equation (3-51) is the maximum damage level that can be attained, and it is calculated internally by $D_{\max} = (\sqrt{3}J_2/I_1)^{1.5}$. The compressive softening parameter, a , may also be reduced with confinement, using the input parameter p_{mod} , by:

$$a' = a(D_{\max} + 0.001)^{p_{mod}} \quad (3-52)$$

Nevertheless, the modified moderate pressure softening parameter p_{mod} is used as suggested by (Murray 2007a), $p_{mod} = 0$.

A sensitivity analysis has been performed for parameter b , by changing its value and running a single-element unconfined compression test. Results of these simulations demonstrated that as the input value for b increased, the damage accumulation was lower, so the maximum compressive strength attained was larger. Consequently, as mentioned before, some input parameters were taken from typical values reported by Murray in her material user's manual for the FHWA (Murray 2007b). She evaluated a regulatory technique for material softening, reporting the ductile shape parameter as $b = 100$ in compression ($p > 0$), and the brittle shape parameter as $d = 0.1$.

3.2.4.6 Regulating Mesh Size Sensitivity in Mat_159

Mat_159 model maintains constant fracture energy, regardless of the element size. The fracture energy is defined here as the area under the stress-displacement curve from peak to zero strength. This is done by internally formulating the softening parameters a and c in terms of the element length, l (cube root of the element volume), the fracture energy, G_f , and the initial energy damage threshold, τ_{c0} or τ_{t0} .

The fracture energy is calculated as a function of five user-defined input parameters (G_{fc} , G_{ft} , G_{fs} , $pwrc$, pwr). The user specifies three distinct fracture energy values. These are the

fracture energy in uniaxial compression, G_{fc} , the fracture energy in uniaxial tension, G_{ft} , and the fracture energy in pure shear, G_{fs} .

By definition, the input value for G_{fc} , was calculated based upon the stress-displacement curve for Vosges sandstone, directly related to the stress-strain curve presented in Figure 2-9. The area under the unconfined compression curve from zero to peak strength is equal to 3.5 MPa-mm (20 psi-in). The other fracture energy parameters were determined following Murray's validation of the material model (Murray 2007b), such that $G_{ft} = G_{fs} = 0.01 G_{fc} = 0.035$ MPa-mm (0.2 psi-in).

The model internally selects the fracture energy from equations that interpolate between the three fracture energy values as a function of the stress state (expressed via two stress invariants). The interpolation equations depend upon the user-specified input powers $pwrc$ and pwr , as follows:

- If pressure is compressive ($p \geq 0$):

$$G_f = G_{fs} + (G_{fc} - G_{fs})trans \quad trans = \left(\frac{I_1}{\sqrt{3J_2}} \right)^{pwrc} \quad (3-53)$$

- If pressure is tensile ($p < 0$):

$$G_f = G_{fs} + (G_{ft} - G_{fs})trans \quad trans = \left(\frac{-I_1}{\sqrt{3J_2}} \right)^{pwr} \quad (3-54)$$

where the internal parameter $trans$ is limited to range between 0 and 1.

The shear-to-compression transition parameter, $pwrc$, and the shear-to-tension transition parameter, pwr , are setup as suggested by Murray (2007a) in her validation example, i.e., 5 and 1, respectively.

3.2.4.7 Visco-plastic Rate Effects in Mat_159

At each timestep, the visco-plastic algorithm interpolates between the elastic trial stress, $\sigma_{ij}^{\text{trial}}$, and the inviscid stress (without rate effects), σ_{ij}^{p} , to set the visco-plastic stress (with rate effects), σ_{ij}^{vp} by:

$$\sigma_{ij}^{\text{vp}} = (1 - \gamma)\sigma_{ij}^{\text{trial}} + \gamma \sigma_{ij}^{\text{p}} \quad (3-55)$$

$$\gamma = \frac{\Delta t / \eta}{(1 + \Delta t) / \eta} \quad (3-56)$$

This interpolation depends upon the effective fluidity coefficient, η , and the timestep size, Δt . The effective fluidity coefficient is internally calculated as a function of five user-supplied input parameters and interpolation questions:

- If pressure is compressive ($p \geq 0$):

$$\eta = \eta_s + (\eta_c - \eta_s)trans \quad trans = \left(\frac{I_1}{\sqrt{3}J_2} \right)^{pwrc} \quad (3-57)$$

- If pressure is tensile ($p < 0$):

$$\eta = \eta_s + (\eta_t - \eta_s)trans \quad trans = \left(\frac{-I_1}{\sqrt{3}J_2} \right)^{pwrt} \quad (3-58)$$

where:

$$\eta_c = \frac{\eta_{c0}}{\dot{\epsilon}^{N_c}} \quad \eta_t = \frac{\eta_{t0}}{\dot{\epsilon}^{N_t}} \quad \eta_s = S_{\text{rate}} \eta_t \quad (3-59)$$

and, where $\dot{\epsilon}$ is the effective strain rate. The input parameter values are selected based on Murray's example (Murray 2007a) as follows:

- For uniaxial compressive stress:
 - the rate effect parameter, $\eta_{c0} = 1 \times 10^{-4}$
 - the rate effect power, $N_c = 0.78$
 - the maximum overstress allowed, $overc = 20 \times 10^{-3}$ GPa (2,900 psi)
- For uniaxial tensile stress:
 - the rate effect parameter, $\eta_{t0} = 6 \times 10^{-5}$
 - the rate effect power, $N_t = 0.48$
 - the maximum overstress allowed, $overt = 20 \times 10^{-3}$ GPa (2,900 psi)
- The ratio of effective shear stress to tensile stress fluidity parameter, $S_{rate} = 1$

Mat_159 model may predict substantial rate effects at high strain rates ($\dot{\epsilon} > 100$). To limit rate effects at high strain rates, the user may input overstress limits in compression (*overc*) and in tension (*overt*) (values stated above). These input parameters limit the calculation of the fluidity parameter, η , by:

$$\text{if } E \dot{\epsilon} \eta > over \quad \text{then} \quad \eta = \frac{over}{E \dot{\epsilon}} \quad (3-60)$$

The user has the option of increasing the fracture energy as a function of effective strain rate via the *repow* input parameter by:

$$G_f^{rate} = G_f \left(1 + \frac{E \dot{\epsilon} \eta}{f'} \right)^{repow} \quad (3-61)$$

where G_f^{rate} is the fracture energy enhanced by rate effects, and f' is the yield strength before application of rate effects (which is calculated internally by the model). The term in parenthesis is greater than, or equal to one, and is the approximate ratio of the dynamic to static strength. In this study *repow* = 1.

4.0 SINGLE ELEMENT TESTS FOR MATERIAL MODEL VALIDATION

The material model evaluation is performed with one-element tests simulated to check the validity of the models via examination of the stress versus displacement behavior; namely by simulating isotropic compression tests, and triaxial compression and extension tests under different confinement pressures. The simulated tests are compared with actual laboratory data from tests on Vosges sandstone performed by Bésuelle et al. (2000) (see Section 2.2).

Through the assessment of the material models presented in Sections 4.2 to 4.5, it can be observed that Mat_111 does not characterize the triaxial response of Vosges sandstone, as good as does Mat_72R3. Since the purpose of this investigation requires a reasonable formulation that allows fracturing by means of “element erosion”, the author has to discard the good performance of Mat_72R3, while implementing Mat_159. The following chapters demonstrate how Mat_159 is superior in simulating fracturing and chip formation in rock cutting problems.

4.1 TEST SETUP

All simulations were conducted in a prismatic hexagonal solid element of 25 mm x 25 mm x 100 mm. These dimensions indicate the use of a quarter of symmetry in the vertical axis, made possible through nodal boundary conditions, as shown in Figure 4-1.

Three loading conditions are analyzed. These are the isotropic compression (or consolidation stage), the triaxial compression, and the triaxial extension at different confining pressures. Before each triaxial test, the (one-element) “sample” is subjected to isotropic load, at a constant rate of 0.2 MPa/s (29 psi/s), until it reaches the desired confining pressure. This compressive load is applied as distributed stress over the moving faces of the sample, i.e. top, front, and right segments.

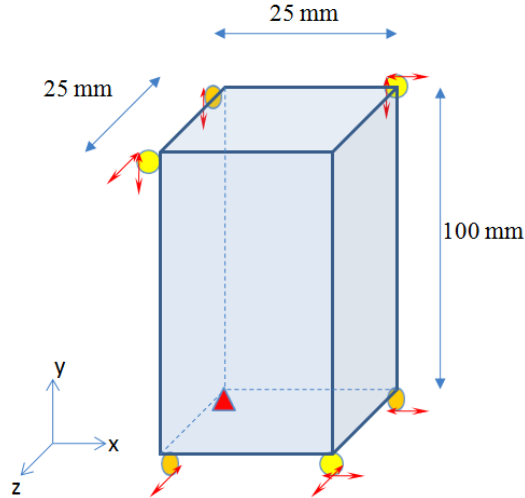


Figure 4-1: Nodal degrees of freedom in one-element tests

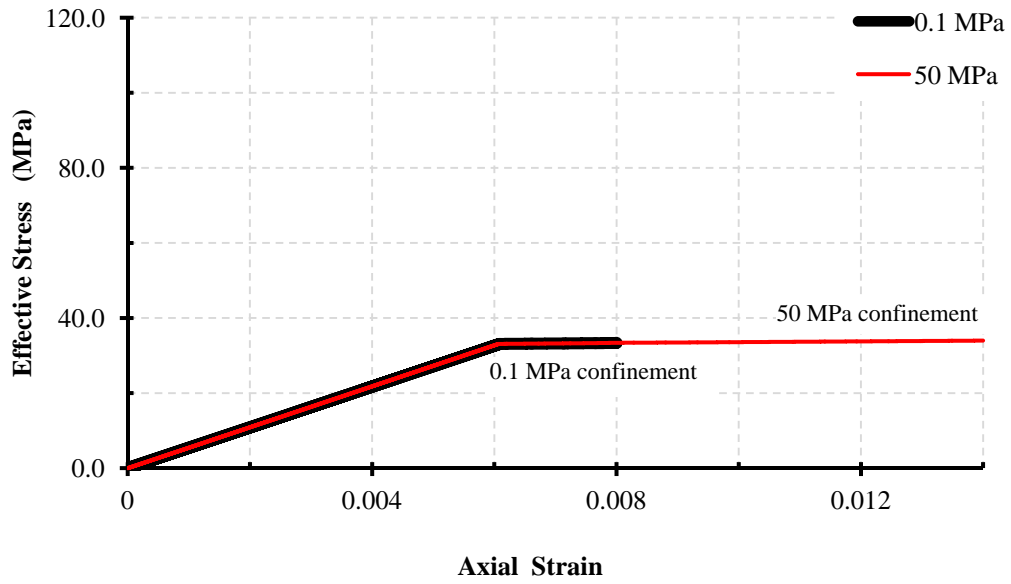
Subsequently, for each confining pressure, the sample is loaded axially in compression or tension at a strain rate of $1 \times 10^{-5} \text{ s}^{-1}$. This strain-controlled axial load is applied by means of nodal displacement (of top nodes only).

4.2 VALIDATION OF MAT_105

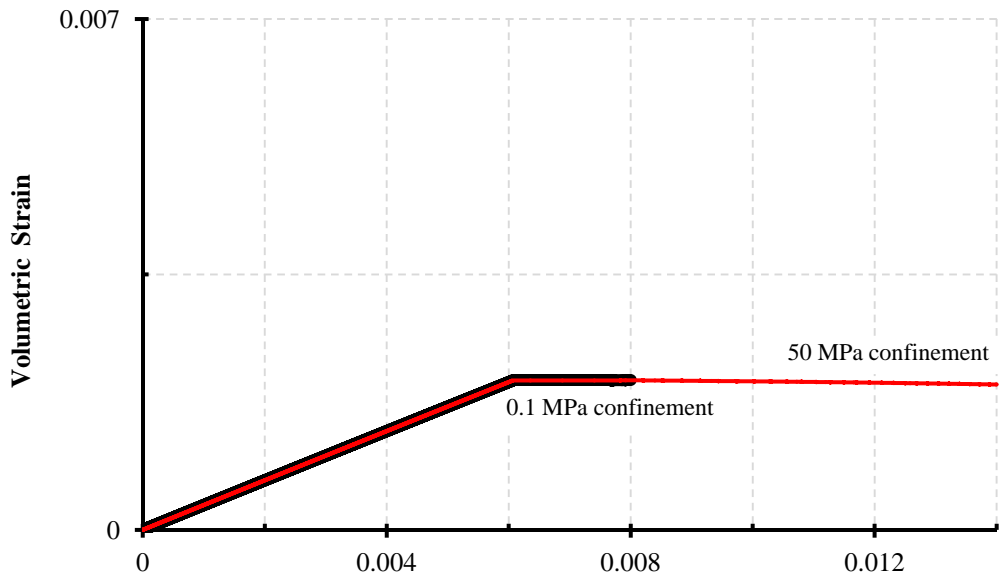
Based on the bi-linear behavior of MAT_105 and its pressure independence, it is expected that the nonlinear triaxial stress-strain response of the rock and its variable behavior with respect to pressure are not achieved. Likewise, the quasi-static and controlled nature of triaxial tests does not allow for the development of tensile damage during the simulated tests, therefore, the set of damage parameters used in this study for MAT_105 are not validated, and are just utilized as a testing means to the numerical tuning of the rock cutting simulations.

Figure 4-2 depicts the response of Mat_105 subjected to compressive triaxial load at 0.1 MPa (unconfined) and 50 MPa of confining pressure. It can be observed that Mat_105 is indifferent to the effect of the confining pressure, and this why it is meant for metal modeling, as suggested by LS-DYNA User's Manual (Hallquist 2009). The calculation of the triaxial stress state is straightforward, given the "yield strength" and the Young's elastic modulus input. As

seen in Figure 4-2(a), in the compressive tests, the value for the “yield strength” corresponded to the unconfined compressive strength of Vosges sandstone.



(a) Effective Stress vs. Axial Strain



(b) Volumetric Strain vs. Axial Strain

Figure 4-2: Simulated triaxial compression with Mat_105 under different confinement

Triaxial extension tests were also modeled with Mat_105. In this case, the “yield strength” was input as the sandstone’s tensile strength, because the material model is not capable of treating tension or compression differently. The results of these tests are identical to the compressive instance, only that failure occurs exactly at the “yield strength value” provided. With these results, it was confirmed that Mat_105 is not suitable for modeling proper rock behavior.

As far as the isotropic compression is concerned, Mat_105 maintains a constant elastic modulus throughout the consolidation phase, thus the response is perfectly linear, as is expected (see Figure 4-15). The magnitude of the volumetric strain as function of pressure is significantly less than actual Vosges sandstone, especially at lower pressures.

Although the response is not characteristic of a geomaterial, mostly due to its pressure independency, Mat_105 has been implemented in rock cutting models as a first attempt to calibrate other numerical attributes in LS-DYNA.

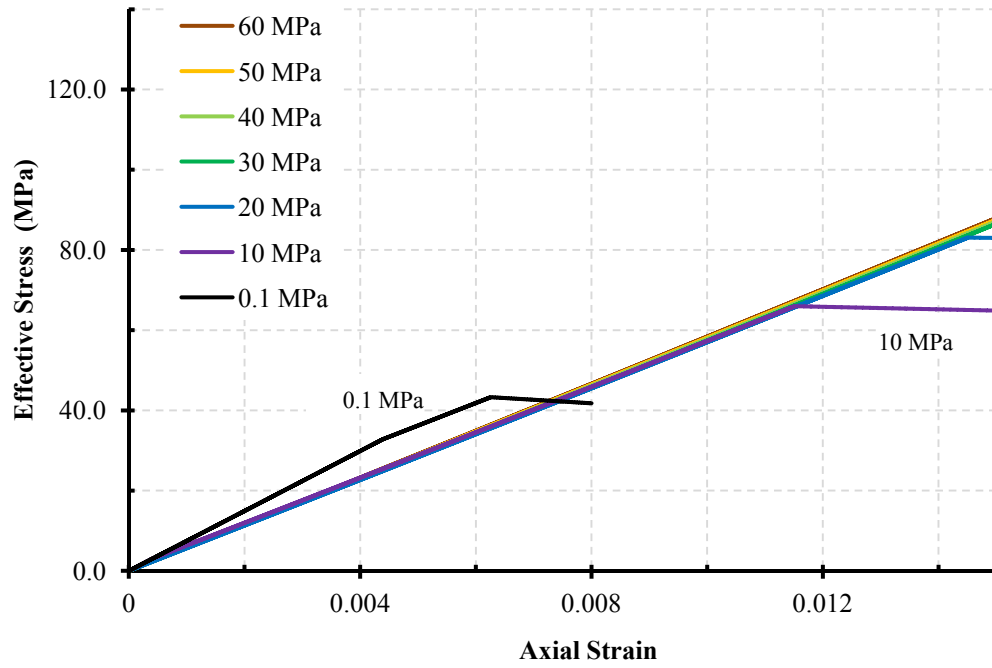
4.3 VALIDATION OF MAT_111

Johnson-Holmquist Concrete material model has been used successfully in the numerical simulation of:

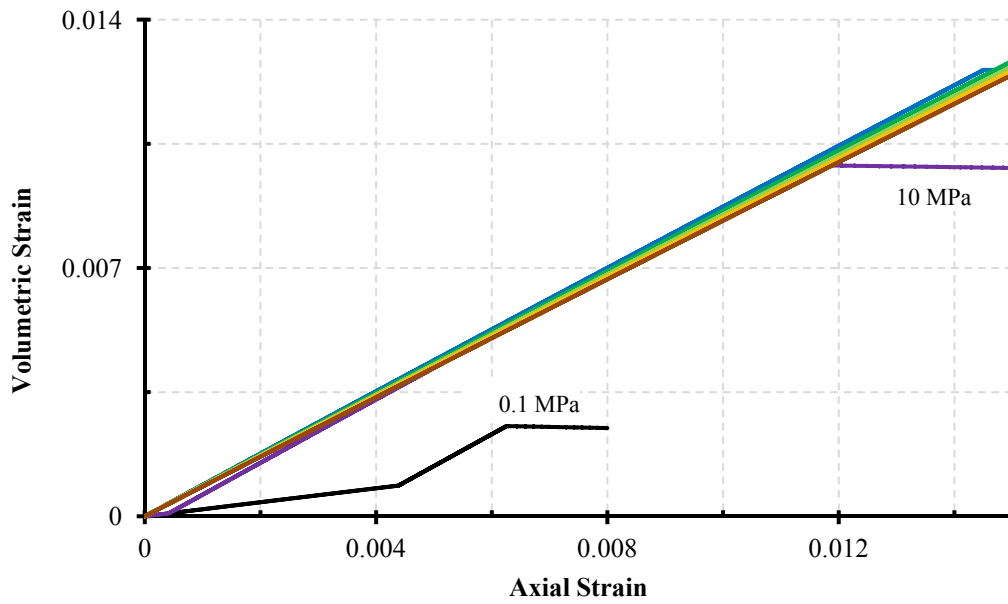
- ballistic penetrations in concrete plates (Holmquist et al. 1993);
- dynamic behavior of reinforced concrete plates under normal impact (Tai and Tang 2006a);
- response of ultra-high strength concrete to projectile impacts (Tai and Tang 2006b); and,
- concrete structures under blast loads (Du and Li 2009; Shi et al. 2007).

4.3.1 Triaxial Stress-Strain Response in Mat_111

When testing the performance of Mat_111 in confined compression tests, it revealed a bi-linear elastic-plastic response of the effective stress, reaching extremely large axial strain values corresponding to the expected maximum strength at different confining pressures (see Figure 4-3(a)). In triaxial extension, although bi-linear as well, the stress-strain data were consistent with the experimental response (see Figure 4-4(a)).

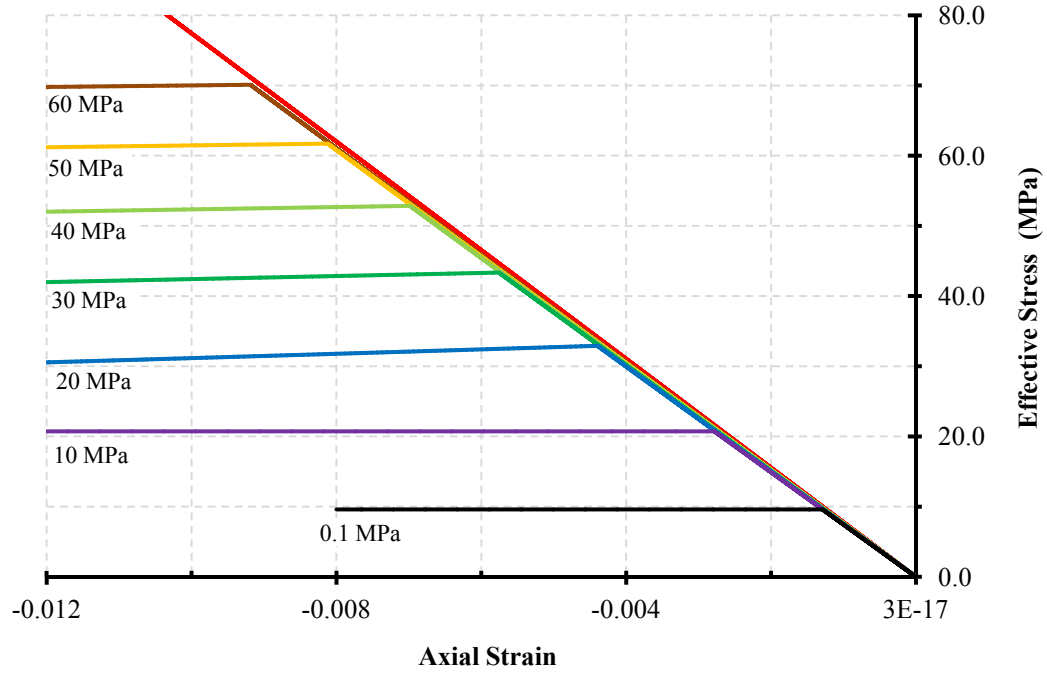


(a) Effective Stress vs. Axial Strain

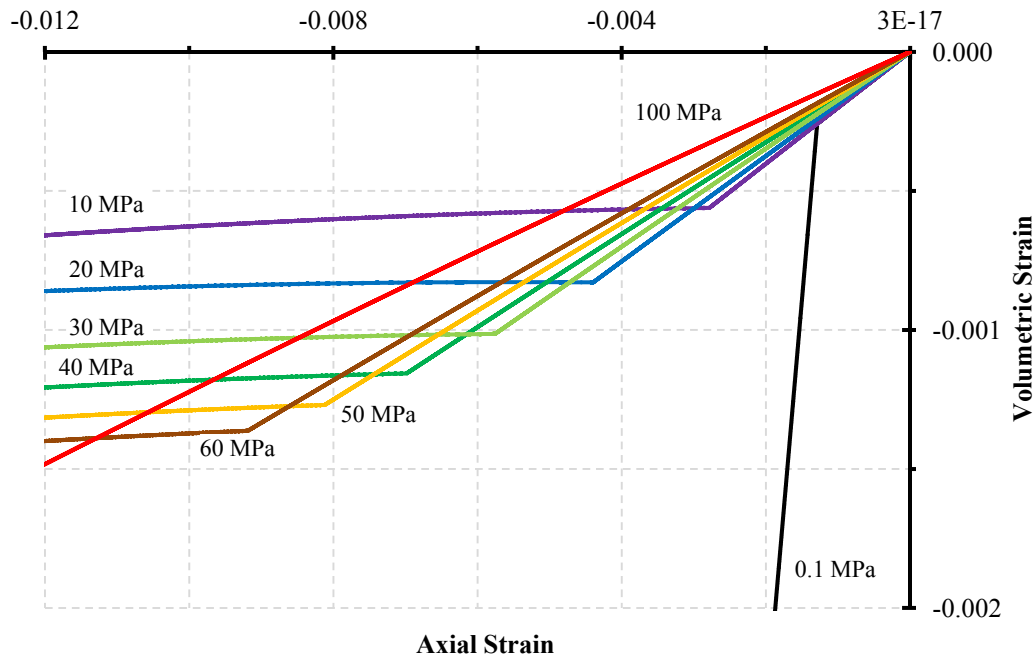


(b) Volumetric Strain vs. Axial Strain

Figure 4–3: Simulated triaxial compression with Mat_111 under different confinement



(a) Effective Stress vs. Axial Strain



(b) Volumetric Strain vs. Axial Strain

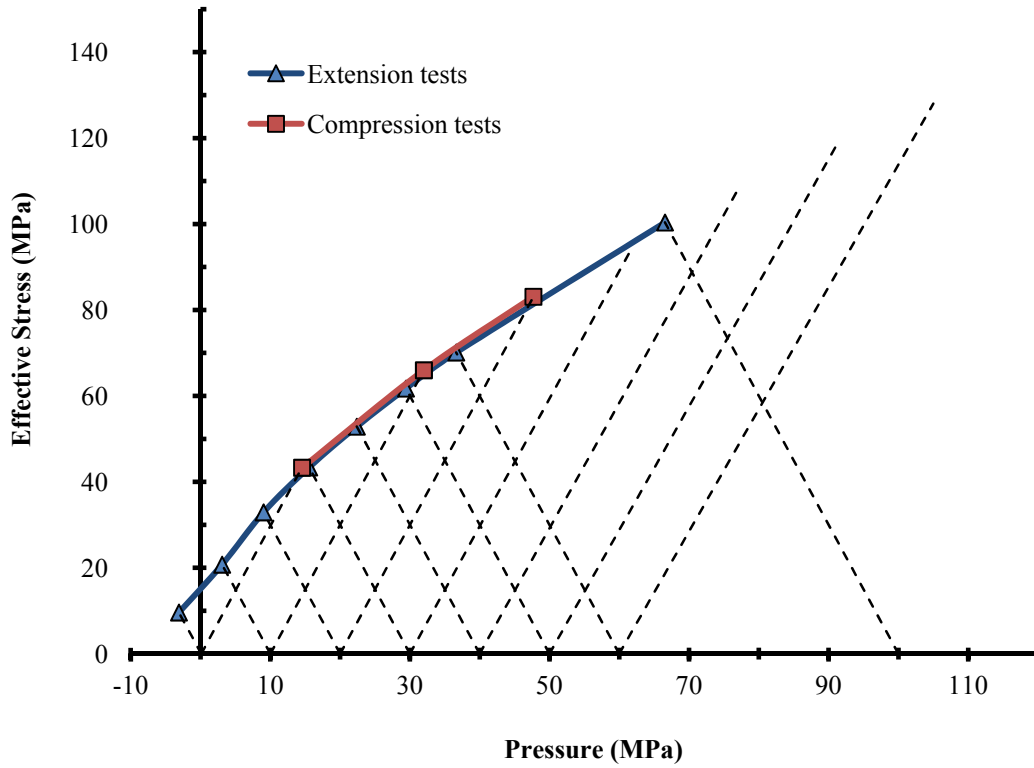
Figure 4-4: Simulated triaxial extension with Mat_111 under different confinement

In terms of the volumetric strain, the response of Mat_111 in triaxial compression failed to show the initial contraction stage (larger with larger confining pressure) followed by a dilated volume (see Figure 2-9(b)); on the contrary, the volumetric response was constantly contractive, increasing with axial strain, to very a large extent (see Figure 4-3(b)). Additionally, there seems to be no effect of the confinement, which implies no evolution of the stiffness properties (porosity) as a function of pressure. On the other hand, in triaxial extension, the material expanded linearly, although much less than the experimental tests (see Figure 4-4(b)).

As suggested above, Mat_111 lacks appropriate calculation of the volumetric strain, and this is confirmed with the isotropic compression test. Figure 4-15 shows how Mat_111 keeps a linear pressure-volumetric strain relationship, i.e. bulk modulus. Although having an initial low volume change, after 10 MPa this modulus decreases significantly with no apparent reason, and remains constant thereafter, producing very large a volume change with pressure, compared with laboratory data.

4.3.3 Strength at Failure in Mat_111

Figure 4-5 presents the failure envelopes for Mat_111 resulting upon data from each simulated triaxial test in compression and in tension. These curves are representative of the constitutive relationship in Equation (3-12) of Mat_111 (recalled below), where the effective stress is expressed as a function of pressure. The dashed lines in Figure 4-5 correspond to the stress paths during each test, from the beginning of axial loading until failure.



$$\frac{\sigma_{eff}}{f'_c} = A + B \left(\frac{p}{f'_c} \right)^N$$

Figure 4-5: Simulated strength at failure with Mat_111

4.4 VALIDATION OF MAT_72R3

In the past, the Concrete Damage Rel3 model has been used successfully for modeling:

- the behavior of standard reinforced concrete dividing walls subjected to blast loads (Malvar et al. 1997);
- penetration and perforation of concrete with projectiles (Unosson 2002);
- the loading response of concrete confined by fiber-reinforced composites (Malvar et al. 2004); and,

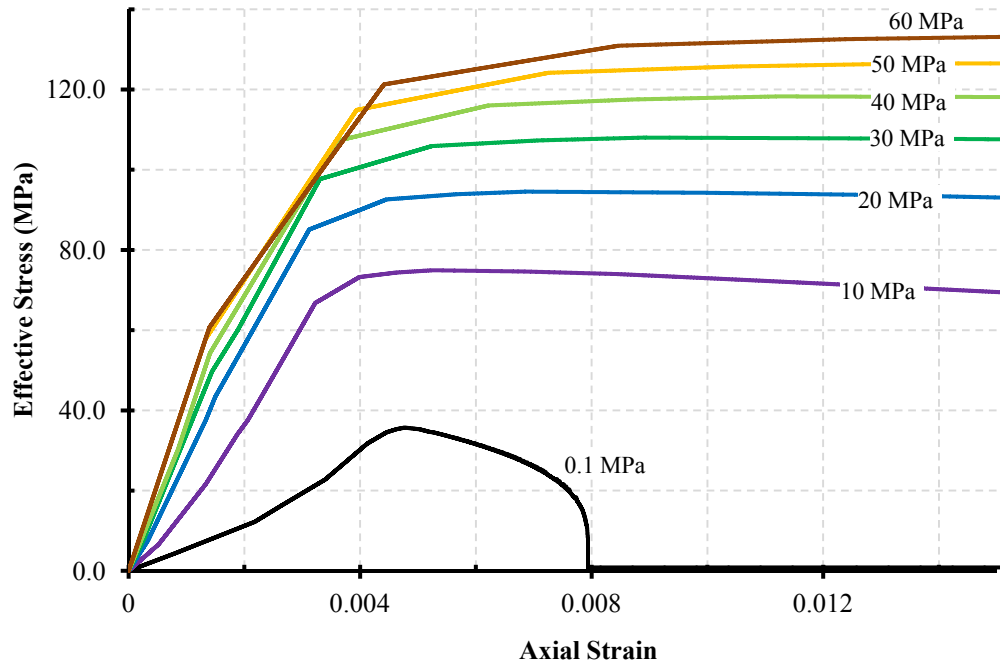
- the response of standard uniaxial, biaxial, and triaxial concrete tests in both tension and compression (Schwer and Malvar 2005).

4.4.1 Triaxial Stress-Strain Response in Mat_72R3

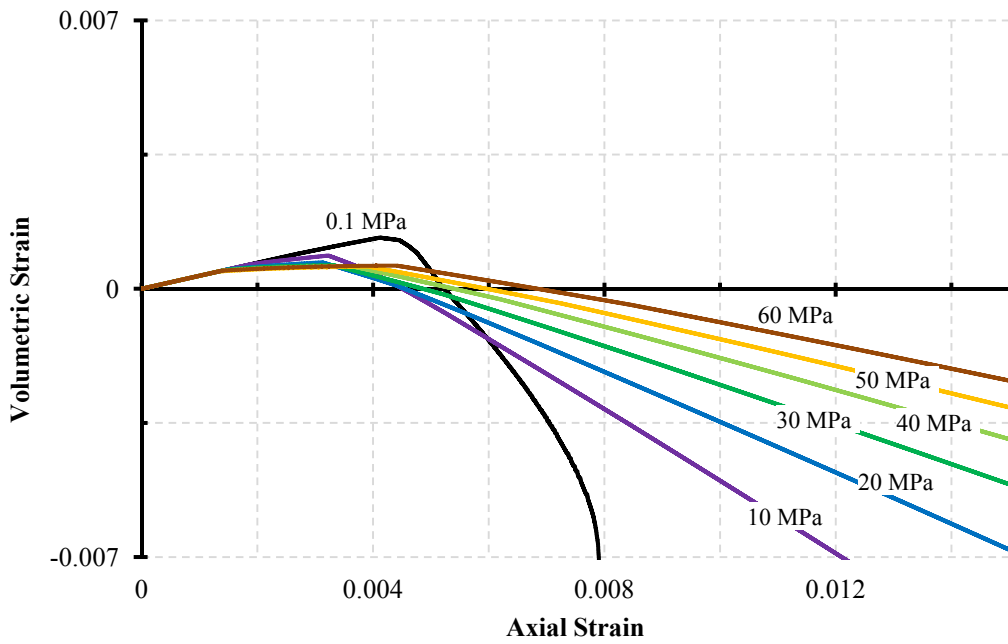
In the present study, this very complex material model has proven to be the one that best captures the nonlinear stress-strain response of Vosges sandstone in compression and tension. Except for the pressure-volumetric strain in triaxial compression, Figure 4-6 and Figure 4-7 show excellent correlation of the simulated stress-strain characterization with the laboratory tests. Figure 4-6(a) reveals a shortcoming in the computation of the volumetric strain, attributed perhaps to the constant increase in the Poisson's ratio of the material, internally modified by the code based on input data.

As mentioned in the calibration Section 3.2.2.1, Mat_72R3 requires the input of an equation of state that relates the volumetric strain of the rock with pressure, therefore, the isotropic compression curve of the simulated material perfectly agrees with experimental data, as can be observed in Figure 4-15.

Unfortunately, when implementing this material model in the simulation of rock cutting, the outcome is not acceptable. Although Mat_72R3 provides a satisfactory agreement of the stress-strain response of Vosges sandstone with experimental data (under controlled conditions), it does not comprise a built-in element erosion formulation. It has been confirmed that even with the possibility of adding a user-supplied element erosion criterion, the rock does not behave in a realistic way (see Section 5.3.2). This fact makes Mat_72R3 limited to applications where fracturing is not expected. Section 5.3.2 illustrates the negative effect produced by inconsistent element erosion criteria.

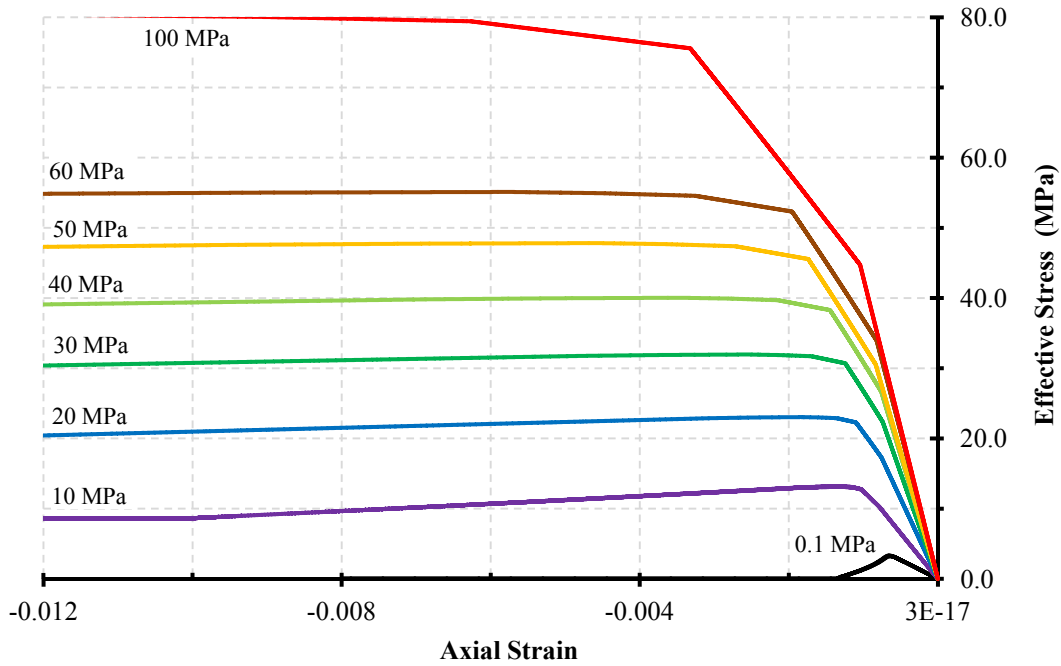


(a) Effective Stress vs. Axial Strain

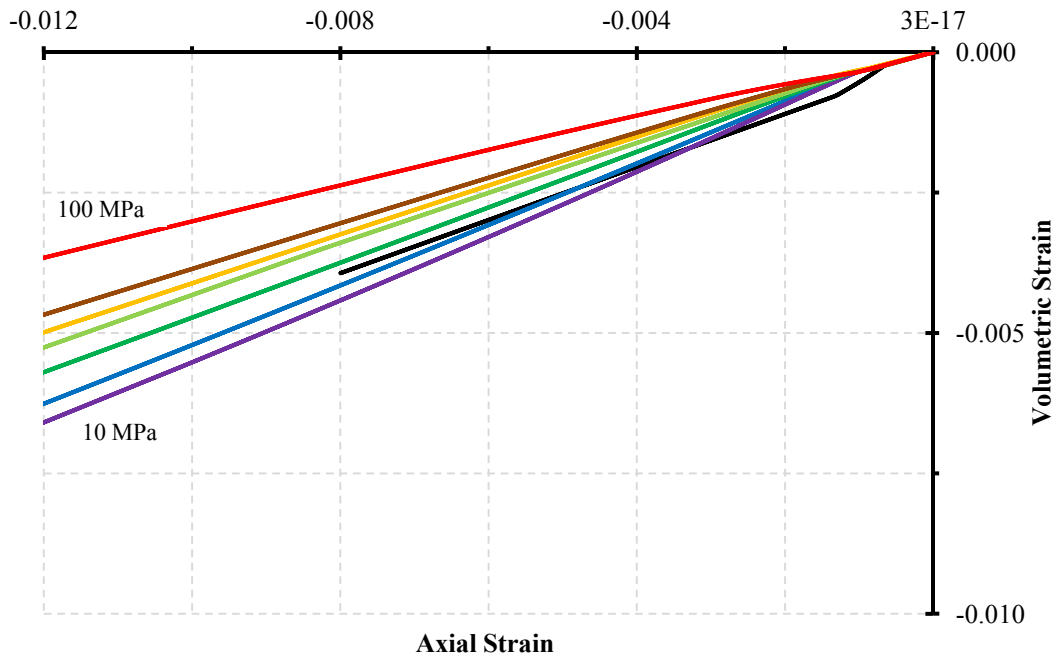


(b) Volumetric Strain vs. Axial Strain

Figure 4-6: Simulated triaxial compression with Mat_72R3 under different confinement



(a) Effective Stress vs. Axial Strain

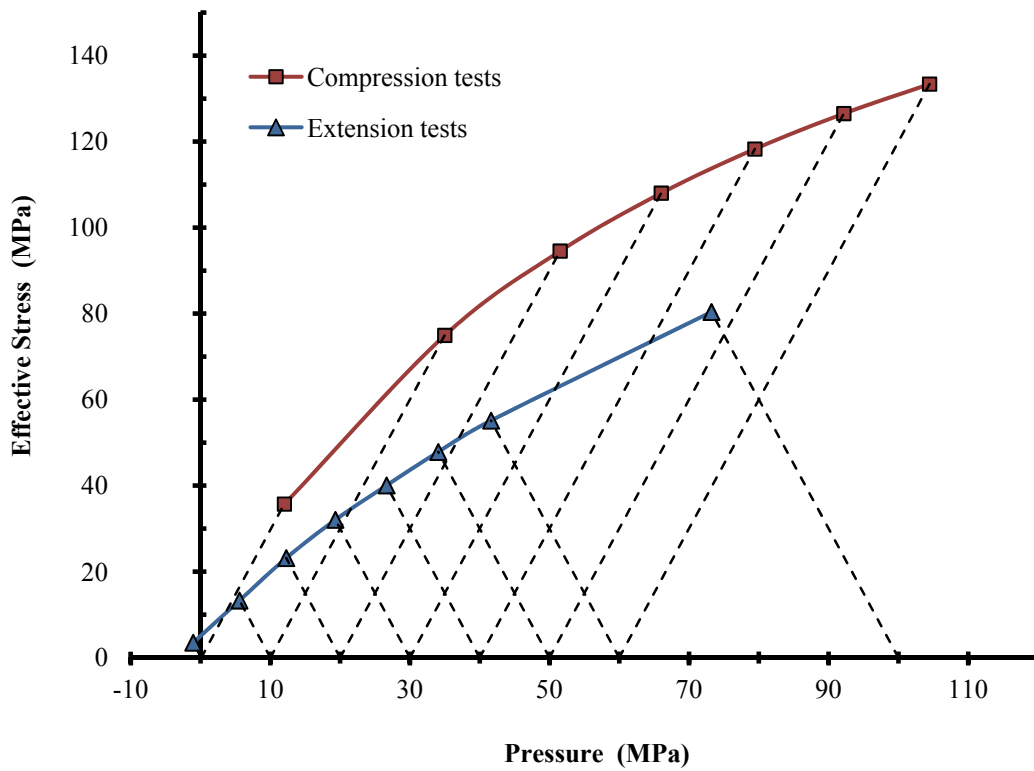


(b) Volumetric Strain vs. Axial Strain

Figure 4–7: Simulated triaxial extension with Mat_72R3 under different confinement

4.4.2 Strength at Failure in Mat_72R3

Figure 4-8 presents the failure envelopes for Mat_72R3 resulting upon data from each simulated triaxial test in compression and in tension. These curves are representative of the constitutive relationship in Equation (3-17) of Mat_72R3 (recalled below), where the effective stress is expressed as a function of pressure. The dashed lines in Figure 4-8 correspond to the stress paths during each test, from the beginning of axial loading until failure.



$$\Delta\sigma_m = a_0 + \frac{p}{a_1 + a_2 \cdot p}$$

Figure 4-8: Simulated strength at failure with Mat_72R3

4.5 VALIDATION OF MAT_159

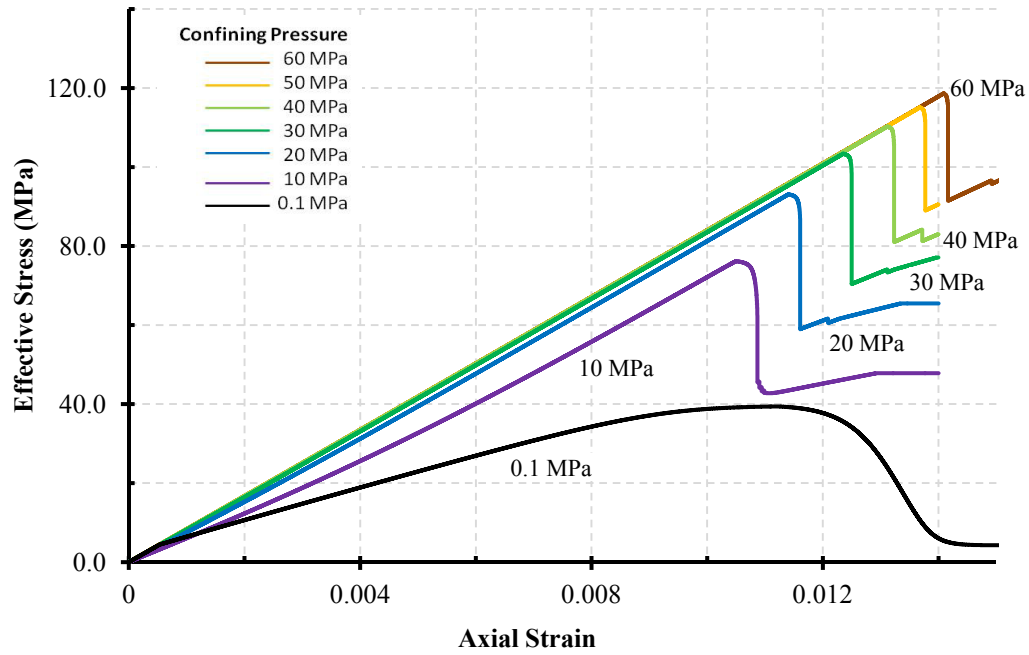
The Continuous Surface Cap Model is perhaps the most robust material model in LS-DYNA in regards to geomaterial constitutive laws. It is fundamentally based on Sandia Geomaterial Model (Fossum and Brannon 2004) and was developed and implemented for the Federal Highway Administration in LS-DYNA as a means for research on concrete used in roadside safety structures when involved in a collision with motor vehicles (Murray 2007b).

After a rigorous and lengthy effort to analyze the performance of Mat_159 and to calibrate its input parameters, the final set of established input parameters for this material model showed the most realistic behavior under different loading conditions. Although some formulation problems were encountered (as described in Section 4.5.2), the rock-cutting simulations presented in Chapters 6.0, 7.0, and 8.0 are based upon this calibrated and validated values.

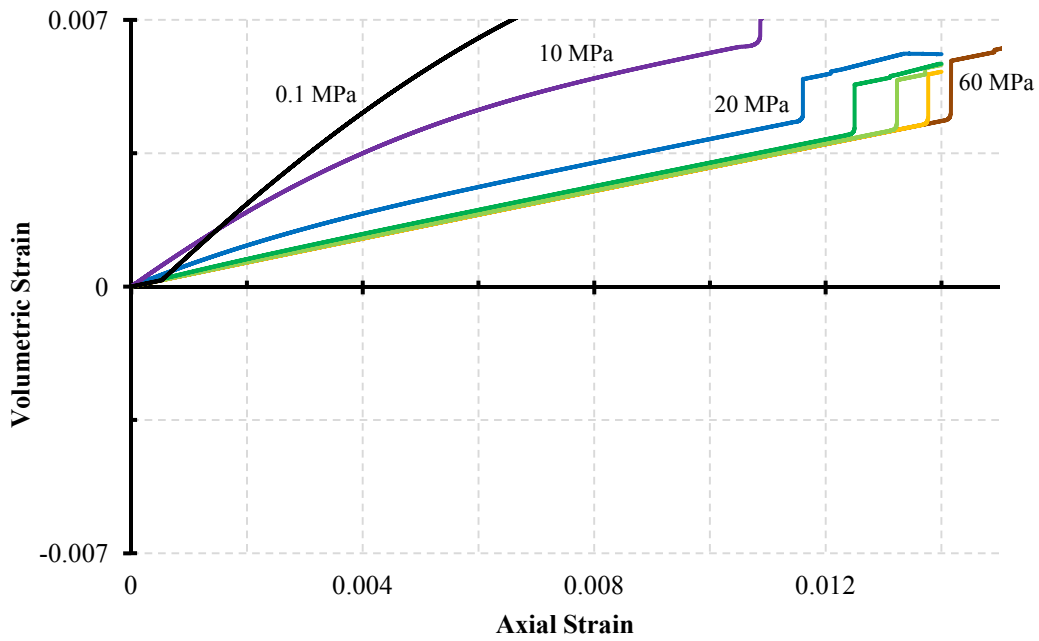
4.5.1 Triaxial Stress-Strain Response in Mat_159

As mentioned in Section 3.2.4.4, the material model parameters that could describe the natural nonlinearity of Vosges sandstone –before reaching the peak strength– are not functional. Therefore, as shown in Figure 4-9(b), there is no sign of hardening (dilation), and the shape of the stress-strain curves does not exhibit pronounced roundness before failure for confining pressures larger than 20 MPa (2,900 psi) in the triaxial compressive tests. Furthermore, this behavior is even more characteristic of the triaxial extension simulation results (see Figure 4-10), where all the loading moduli seem to have the same constant value, and the magnitude of the dilative (volumetric) strain is significantly lower and more erratic than expected.

Despite this drawback, the material model characterizes favorably the failure envelope in compression for Vosges sandstone. This is considered of greater connotation, due to the nature of the rock-cutting simulations, where the highly dynamic mechanics of the problem rely heavily on the plastic, post-failure response of the rock material, as a function of pressure.

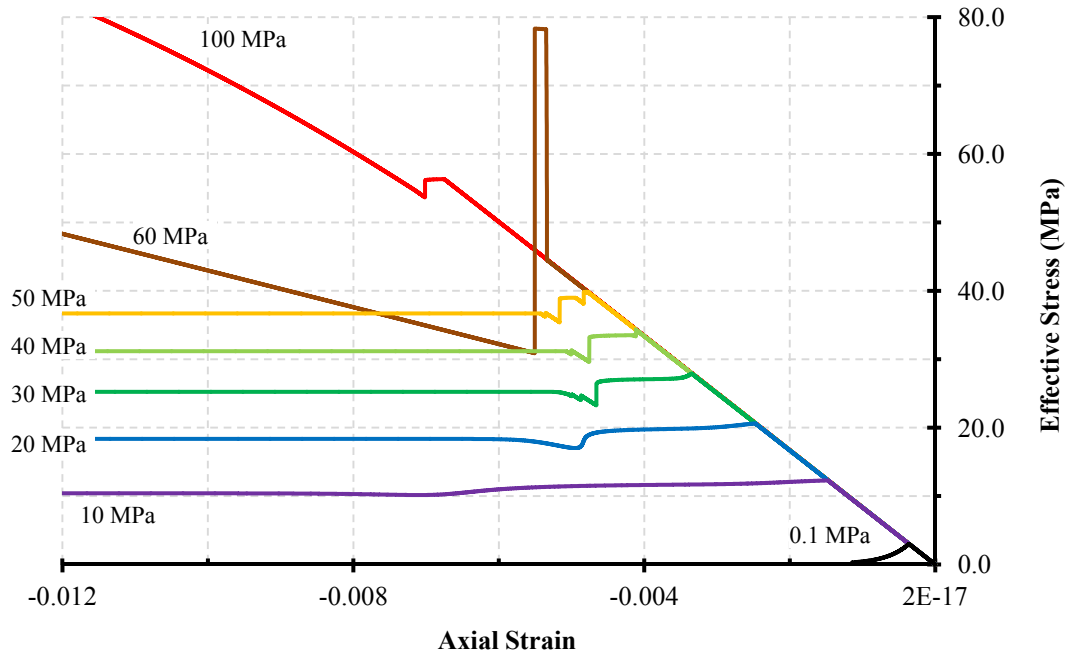


(a) Effective Stress vs. Axial Strain

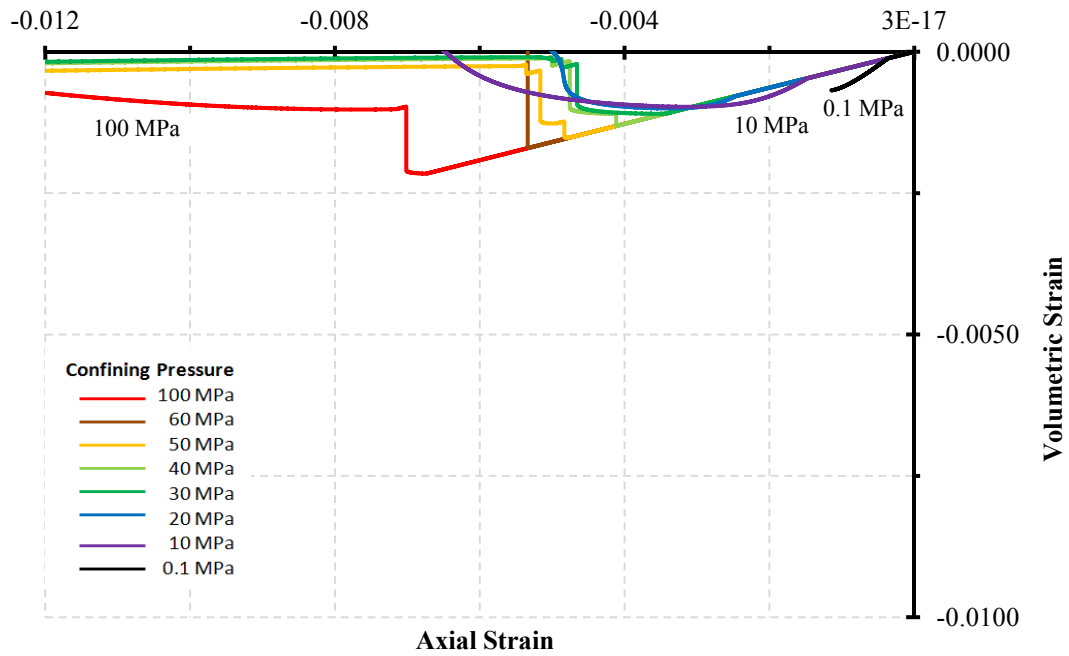


(b) Volumetric Strain vs. Axial Strain

Figure 4–9: Simulated triaxial compression with Mat_159 under different confinement



(a) Effective Stress vs. Axial Strain



(b) Volumetric Strain vs. Axial Strain

Figure 4-10: Simulated triaxial extension with Mat_159 under different confinement

4.5.2 Strength at Failure in Mat_159

Based upon the definition of the compression failure surface (meridian) in Equation (3-34), as well as the failure surface in shear and tension described by Equations (3-35) and (3-36), respectively, the results from triaxial test simulations in compression, tension and shear should look like the following example (Murray 2007b):

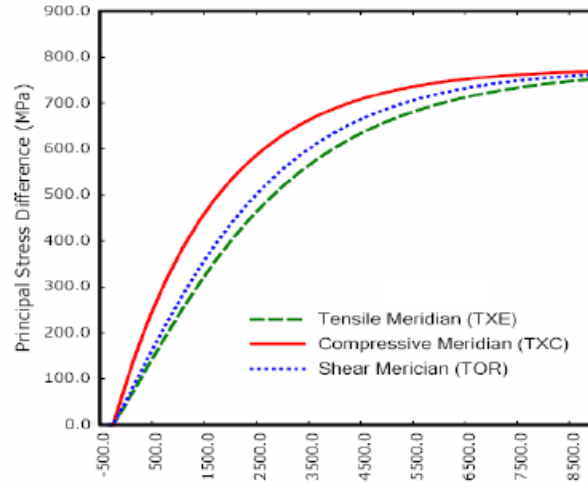


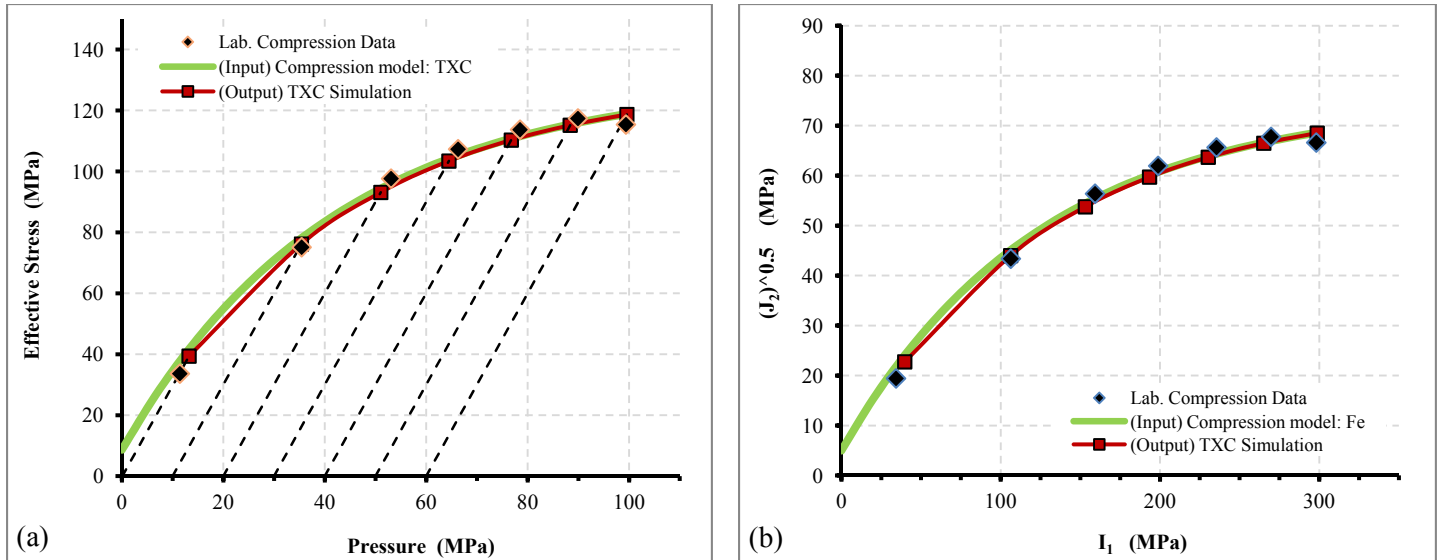
Figure 4-11: Example plots of the failure surfaces of LS-DYNA Model 159 in the meridian plane

Although in triaxial compression (TXC) the material performed perfectly (see Figure 4-12), unfortunately, when modeling triaxial extension (TXE) tests at different confining pressures, the maximum strength at failure in each test was produced too soon. In other words, the maximum failure envelope in extension, as seen in Figure 4-14, is too low compared to tensile meridian depicted in Figure 4-11.

As illustrated in Figure 4-13, the simulated failure envelope in extension has presumably been calculated just by using a constant value of $Q_2 = 0.5$ in the formulation of the tensile meridian (see Figure 3-11), instead of using the actual variable function for this failure envelope.

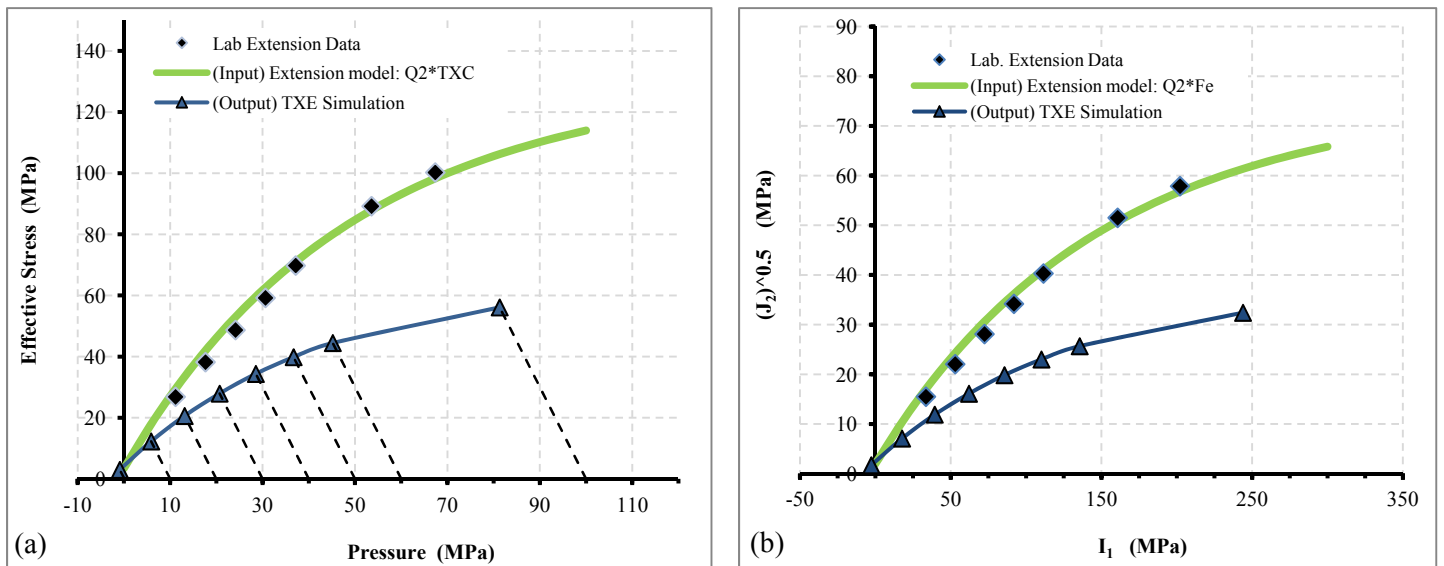
According to the *User's manual for LSDYNA concrete material model 159* (Murray 2007b), “the shape of the yield surface in the deviatoric plane transitions with pressure from triangular, to irregular hexagonal, to circular.” “Currently, the eight input parameters, which define Q_1 and Q_2 [in Equations (3-35) and (3-36)], set the shape of the three-invariant yield surface when the pressure is compressive, but not when the pressure is tensile. When the

pressure is tensile, the model automatically sets $Q_1 = 0.5774$ and $Q_2 = 0.5$. These values simulate a triangular yield surface in the deviatoric plane, and cannot be overwritten by the user. With the triangular yield surface, the strengths attained in uniaxial, biaxial, and triaxial tensile stress simulations are approximately equal.”



Proportional plots as $\Delta\sigma = \sqrt{3J_2}$ and $p = \frac{I_1}{3}$

Figure 4-12: Failure envelope in triaxial compression



Proportional plots as $\Delta\sigma = \sqrt{3J_2}$ and $p = \frac{I_1}{3}$

Figure 4-13: Failure envelope in triaxial extension

Although the theoretical model described above states that the value of Q_2 will only be a constant value of 0.5 when pressure is negative, it is evident that the current model in LS-DYNA version 9.71 release 4 maintains $Q_2 = 0.5$ during the simulation of any stress state where $\sigma_3 > \sigma_1$, regardless of the sign of the pressure value. Conversely, it was observed that once the calibrated material reached the yield meridian while in extension mode, it continued to raise its resistance upon decreasing the vertical stress, leading to a much larger critical strength associated with plastic deformation. This phenomenon was distinct at large confining pressures (i.e. $p \geq 100$ MPa). Due to the ambiguity as to when the maximum strength is attained when $\sigma_3 > \sigma_1$, the validity of the simulated element erosion during the rock cutting is guaranteed by defining the additional erosion criterion of $\varepsilon_I = 0.05$ (see Section 5.3.3).

Since this validation study did not include the simulation of torsion tests (failure in direct shear), the performance of Equation (3-35) and Q_I were not corroborated.

Figure 4-14 presents the failure envelopes for Mat_159 resulting upon data from each simulated triaxial test in compression and in tension. These curves are representative of the constitutive relationship in Equation (3-34) of Mat_159 (recalled below), where the effective stress is expressed as a function of pressure. The dashed lines in Figure 4-14 correspond to the stress paths during each test, from the beginning of axial loading until failure.

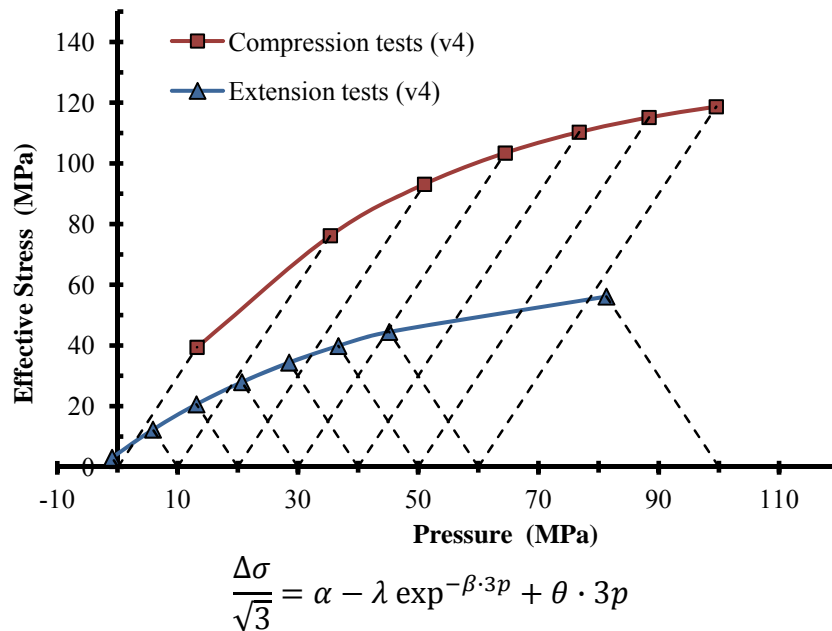


Figure 4-14: Simulated strength at failure with Mat_159

4.6 COMPARISON OF TEST RESULTS: LABORATORY VS. SIMULATION

Figure 4-15 illustrates the simulated pressure-volumetric strain response of all the material models analyzed in contrast with actual laboratory data. Similarly, in the following sections, Figure 4-16 through 4-20 display the experimental triaxial response of Vosges sandstone in comparison to the simulated response of Mat_111, Mat_72R3 and Mat_159. The later charts have been previously presented in greater size and detail in Sections 4.3, 4.4 and 4.5.

4.6.2 Isotropic Compression

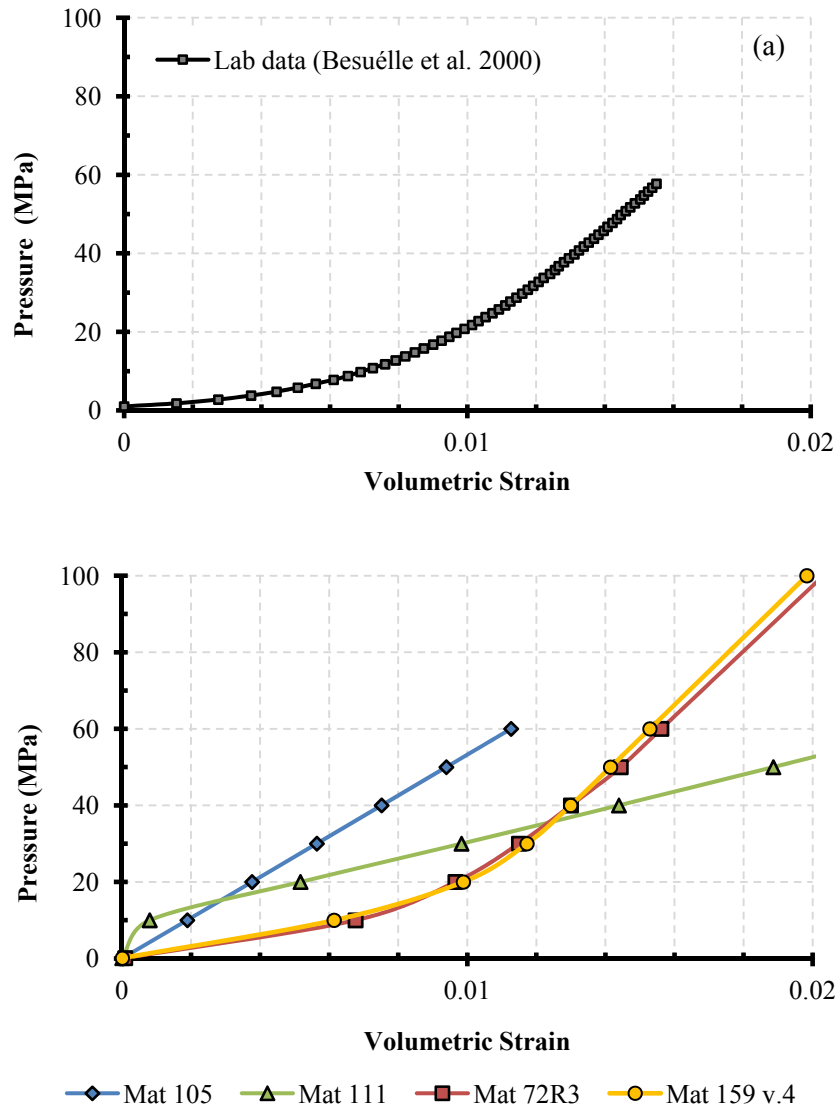


Figure 4-15: Pressure vs. Volume strain - Comparison between experimental and simulated results

4.6.2 Triaxial Compression

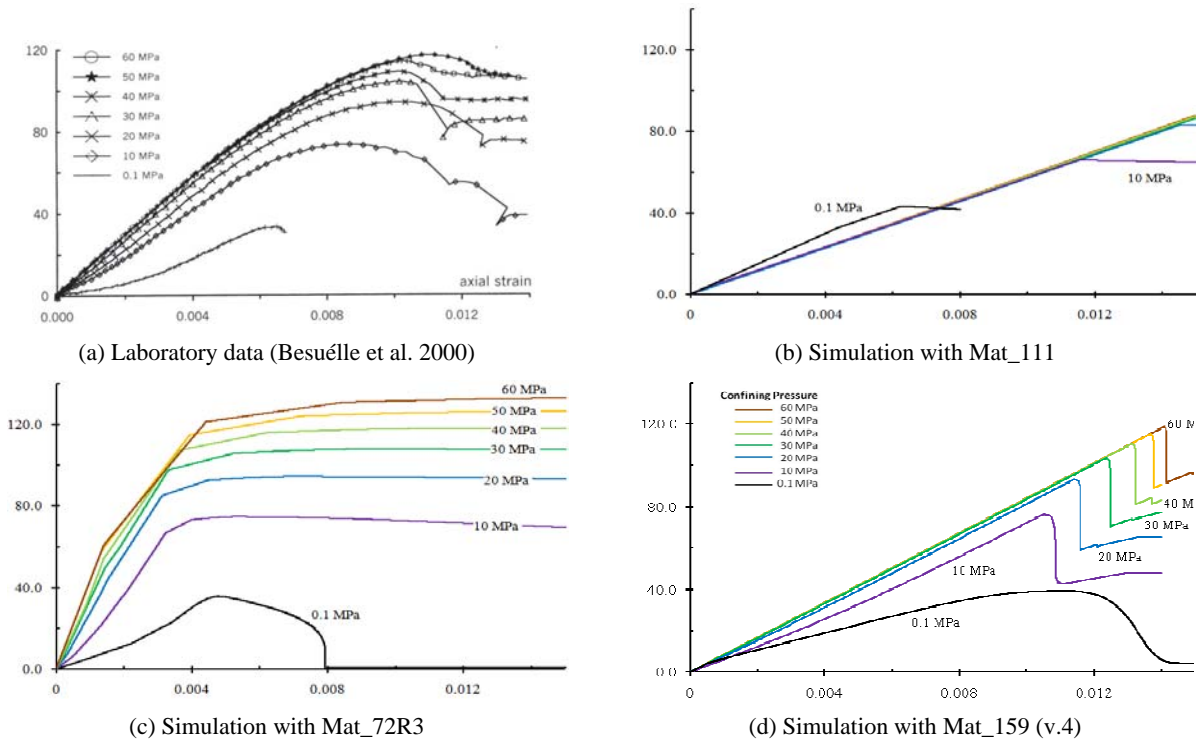


Figure 4-16: TXC Effective stress (MPa) vs. axial strain - Comparison of experimental and simulated results

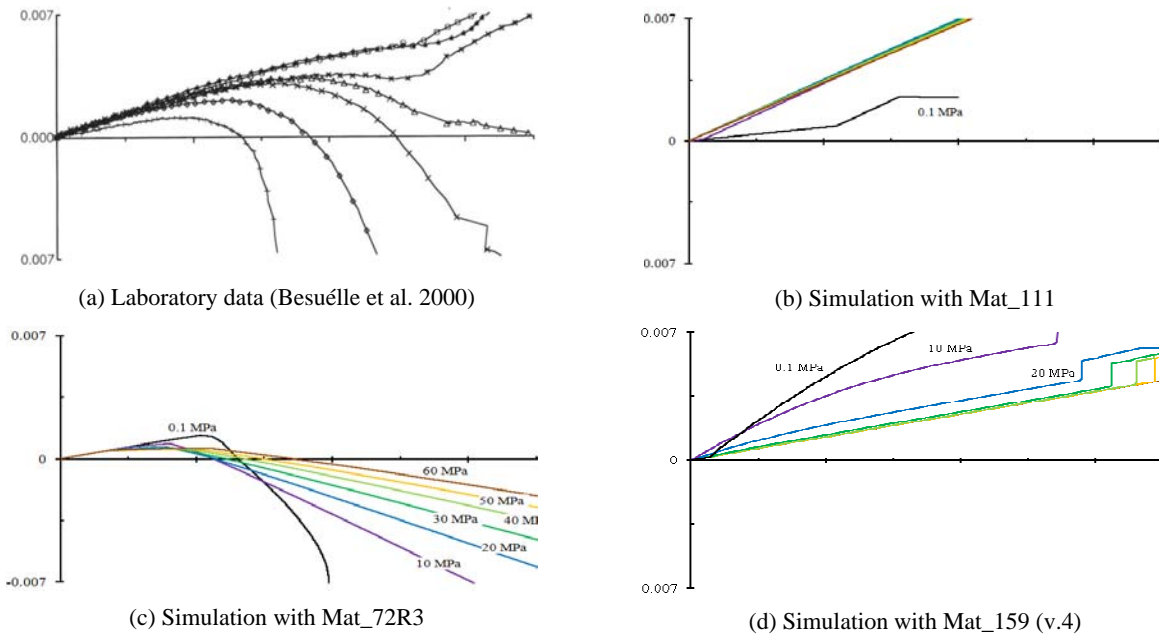


Figure 4-17: TXC Volume strain vs. axial strain - Comparison of experimental and simulated results

4.6.3 Triaxial Extension

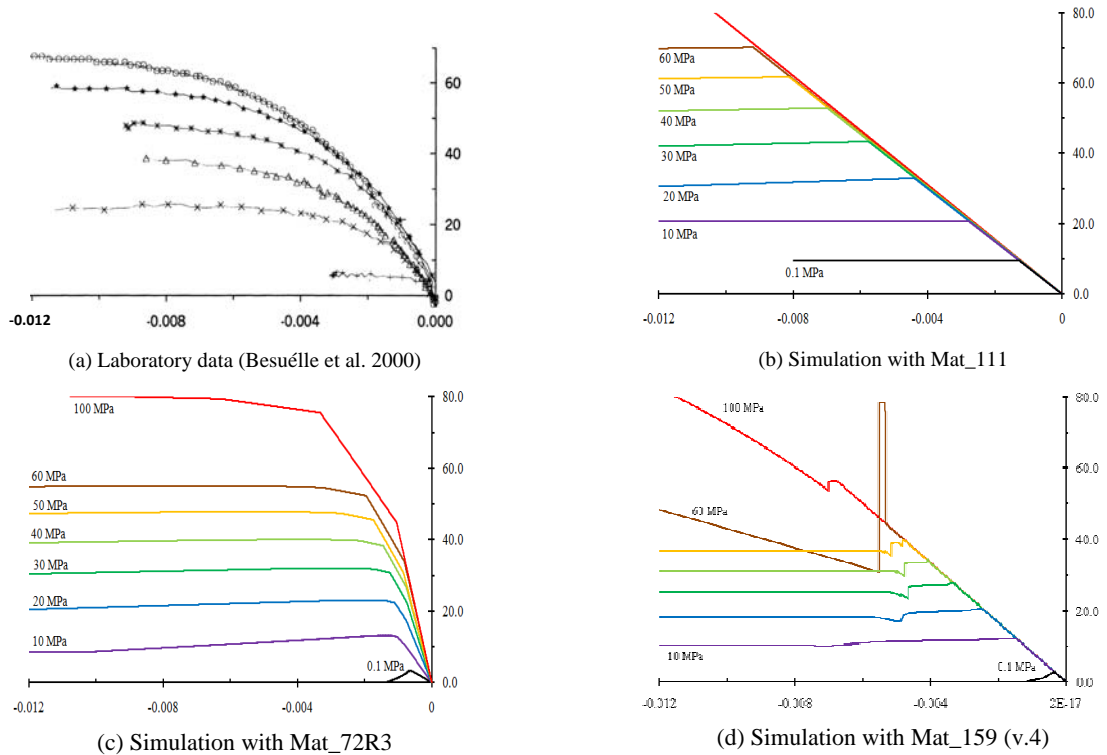


Figure 4-18: TXE Effective stress (MPa) vs. axial strain - Comparison of experimental and simulated results

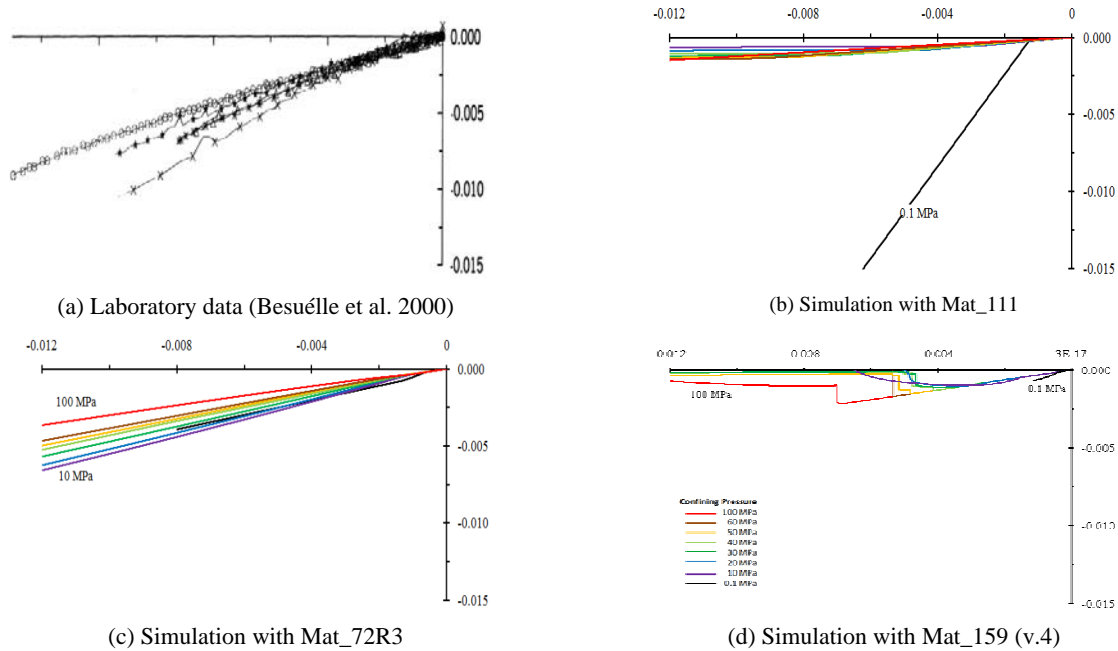


Figure 4-19: TXE Volume strain vs. axial strain - Comparison of experimental and simulated results

4.6.4 Failure Envelope

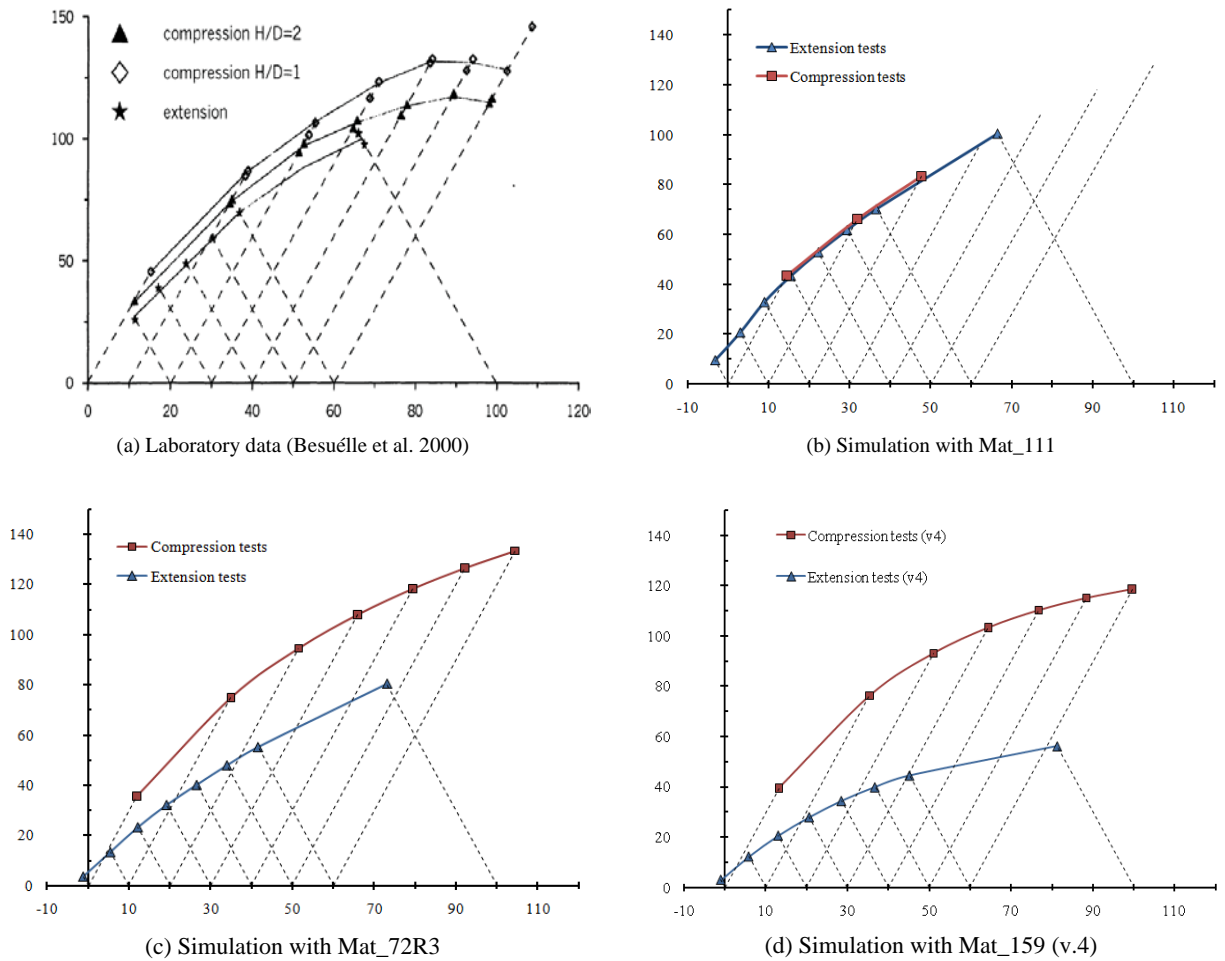


Figure 4-20: Effective stress (MPa) vs. Pressure (MPa) - Comparison of experimental and simulated results

Despite some shortcomings of the volumetric strain response of Mat_159 in the compression and extension triaxial tests –as shown in the previous figures–, overall, this material model is the most suitable material in LS-DYNA for the rock-cutting simulations in this research study; not only due to the robust theoretical model, but also due to its unique incorporation of element erosion upon material constitutive damage, which allows the simulation of realistic rock fracturing and fragmentation.

5.0 CALIBRATION OF THE ROCK CUTTING MODEL

An important component of the proposed research initiative includes the critical implementation of several key features offered by LS-DYNA, which are described in the following sections.

5.1 THE ROCK DOMAIN

5.1.1 Mesh Sensitivity

Depending on the application, the finite element domain representing the model in question is determinant in the final resolution of the stress-strain state. In this particular case, where the initiation and propagation of cracks is the main interest, the mesh definition plays a major role. Two basic characteristic of the mesh are relevant in obtaining good results: 1) the element size, and 2) the element type.

One of the most important implementations in these cutting simulations is the use of *element erosion* upon failure (see Section 5.3); therefore, the eroded surface of the rock, as well as the path that a crack may follow should be as realistic (not uniform) as possible. To achieve this, the smallest, non-cubic element would be ideal; however, it is vital to avoid an excessive number of elements in the domain and its associated long run time. The element size in these simulations was selected based upon the actual particle size in Vosges Sandstone, i.e. between 0.15 mm and 0.45 mm (Bésuelle et al. 2000). The finer established mesh, located at the top of the rock samples where cutting takes place, is formed by elements of 0.14 mm in average size. In this way, the concept of continuum may be disputable.

In LS-DYNA the default and perhaps mostly used solid element type is the hexahedron constant-stress element, due to its one-integration point efficiency. This element type was used

extensively during the course of this investigation, leading to the conclusion that its orthogonal shape makes it impossible to replicate the heterogeneity of the particle assembly in a rock. As a result, the 1-integration-point tetrahedron element is found to serve this purpose in a better manner. The influence of the different element types in the crack propagation process can be compared in Figure 5-1.

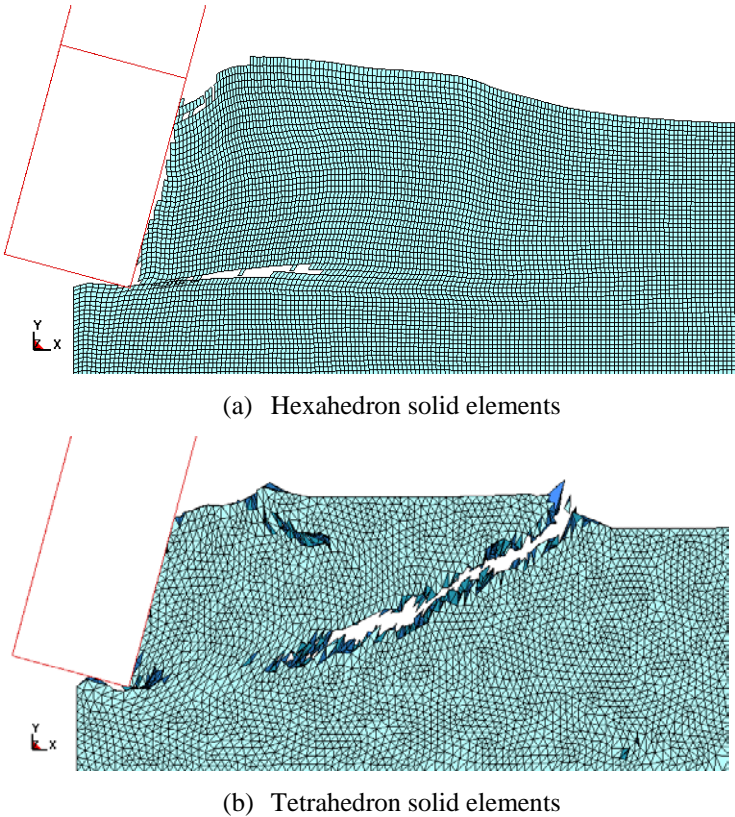


Figure 5-1: Different element types evaluated in rock cutting

5.1.2 Rock Specimen Geometry

The size of the finite element models follow the premise by Richard et al. (1998) that the cutting force from the experiments should be averaged over a distance of at least one order of magnitude larger than the depth of cut, d ; therefore, the minimum horizontal dimension, l , of the numerical models is consistent with the ratio $l/d \geq 10$.

Moreover, for each independent laboratory test simulated, as described in, and 8.0, the three-dimensional FE models represent the actual geometry of the tested specimens of rock in such a way that the simulation results are not affected by the boundary conditions of the model (see Section 5.1.3). The deep and shallow scratch tests performed by Richard (1999) (see Section 2.1.1) are run in prismatic samples or slabs of rock of 10 mm in thickness, thus even a deep cut (e.g. 3.6 mm deep) could be considered to behave as in plane strain mode. Chapter 6.0 presents the model geometry and simulation results of these scratch tests.

Chapter 7.0 and 8.0 portray the simulations of rock cutting in a “groove” based upon additional experimental tests by Richard (1999) and Kaitkay and Lei (2005). Richard wanted to study the influence of the cutter width especially considering the creation of side walls along the groove. Kaitkay and Lei ran experiments of rock cutting with a circular-shape cutter under hydrostatic pressure. In both cases, the rock samples are subjected to a three-dimensional stress loading –in contrast to the plane strain conditions of the scratching tests in rock slabs. Therefore, the rock models for these simulations employ larger domains, but still follow the principles of generating finite elements as small as the grain particles comprising the rock, (see Section 5.1.1).

It is important to highlight that regardless of the depth of cut, the finite elements being cut should have a consistent size as noted above. This fact significantly affects the behavior of the fracture mode, being either ductile or brittle. In other words, in order to compare numerical simulations results from different depths and widths of cut, the element sizes (or the particle sizes in the case of the Discrete Element Method) must have the same dimensional characteristics.

5.1.3 Boundary Conditions

When simulating rock cutting on slabs, the plane strain condition is provided by means of nodal constraints so that the front and rear faces act as symmetry planes. Table 5-1 reports the configuration of the nodal degrees of freedom of rock and cutter nodes. In both, deep and shallow cut simulations, the following boundary conditions apply.

These same nodal constraints apply to the rock models for groove cutting. The plane strain condition does not apply in these cases because of the size of the rock samples. Yet, this

size is large enough so the boundary effect does not interfere with the stress state distributions from the cutting test.

Table 5-1: Nodal degrees of freedom in FE models

		Degree of freedom (1 = fixed, 0 = free)					
		Translational			Rotational		
		X	Y	Z	X	Y	Z
Rock nodes	bottom surface	0	1	0	1	0	1
	right and left side surfaces	1	0	0	0	1	1
	front and rear surfaces	0	0	1	1	1	0
	top surface	0	0	0	0	0	0
Cutter nodes	All nodes	0	1	1	1	1	1

In addition, surfaces on the bottom, right, and left sides of the rock part are treated as “non-reflective boundaries”, which allow stress waves to be dissipated instead of being reflected, thus there is no such boundary effect affecting the stress distribution near the edges of the model. This non-reflecting boundary condition in LS-DYNA is based on the wave propagation concept that the stress is proportional to the velocity. The following are the characteristics of the method:

$$\sigma = \rho cv \quad (5-1)$$

where ρ is the element mass density, $c = \sqrt{E/\rho}$ = stress wave speed, and v = velocity.

Stress can be written in terms of a force f_d such that:

$$f_d = \sigma A = [(\sqrt{E\rho})v]A \quad (5-2)$$

where A is the area of the element face on the non-reflecting boundaries.

Equation (5-2) is essentially a viscous damping force described by:

$$f_d = d_c v \quad (5-3)$$

where the damping constant, d_c , is equivalent to $d_c = A\sqrt{E\rho}$. Accordingly, a non-reflecting boundary is constructed by adding viscous damping to the boundary.

Lastly, prior to starting the rock cutting transient analysis, gravity load –i.e., $g = 9.81 \text{ m/s}^2$ (32.2 ft/s²) – is applied to the rock piece through an initial dynamic relaxation stage (see Section 5.4.2.1 for details).

5.2 CONTACT FORMULATION

Contact treatment forms an integral part of many large-deformation problems. Accurate modeling of contact interfaces between bodies is crucial to the prediction capability of the finite element simulations. In LS-DYNA, a contact is defined by identifying what locations (parts, part sets, segment sets, and/or node sets) are to be checked for potential penetration of a slave node through a master segment. A search for penetrations is made every time step.

In this particular simulation problem, two different contact models must be implemented: one that treats the cutter-rock interface and a separate one that treats the rock-rock interface. The latter becomes necessary due to the newly exposed rock surfaces after *element erosion* (see Section 5.3). *Element erosion* leads to the initiation of cracks and potential rock chips that would eventually be detached and would get in contact with any solid surface in an arbitrary way.

5.2.1 Cutter-Rock Contact

During the course of this work, an extensive assessment of numerous parameters related to contact models has been performed. Among all the types of contact formulations available in LS-DYNA, the following were analyzed for treating the cutter-rock contact:

- Eroding nodes to surface,
- Eroding surface to surface, and,
- Eroding single surface.

It was observed that cutting forces on the cutter were greatly sensitive to the type of contact model used, and to their input parameters. Treatment of slave and master stiffness for the removal of penetrations was the most influential factor and did not allow for a consistent calculation of contact force. For this reason, it was eventually decided that the best cutter-rock contact behavior was provided by using a rigid wall embodying the cutter, because it is assumed non-deformable, which makes the contact calculation more efficient.

According to LS-DYNA, a RIGIDWALL is used for treating deformable nodes against “rigid” geometric surfaces. The analytical equations defining the geometry of the surface are used in the contact calculations. This is an improvement over the usual segmented surface as represented by a mesh (Bala 2001). It is very important to note that a constraint-based approach

(see Section 5.2.1.1) is used herein to calculate the forces that resist penetration, however, when treating the cutter with a rigid wall, the simplification stated in Section 5.2.1.2 is implemented.

The prism analytical shape of the RIGIDWALL algorithm has been selected to act as the cutter. In order to minimize computational time, slave nodes from the rock are defined using a “box”, which encompasses only a set of nodes in the upper portion of the rock, where the cutting action takes place. Only the nodes within this box will be checked for penetration. Figure 5-2 portrays the setup of the rigid wall prism and the box surrounding the upper portion of a rock sample.

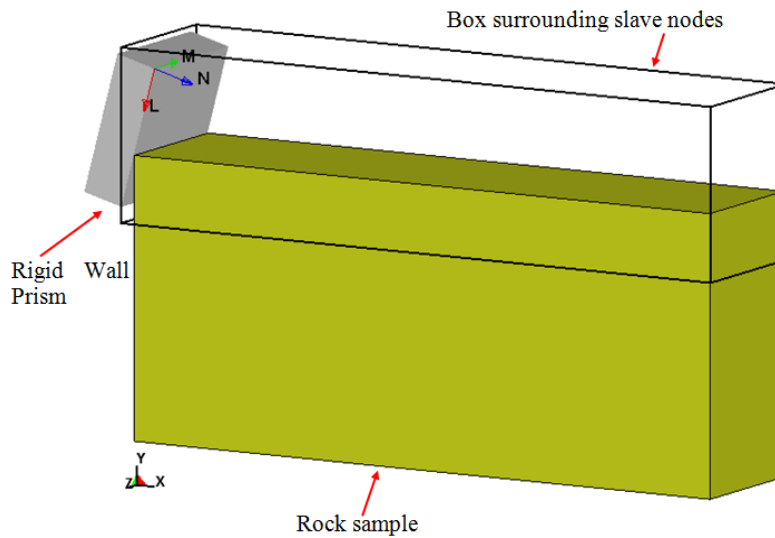


Figure 5-2: Rigid-wall-prism and its node-checking box

5.2.1.1 Constraint Contact Formulation

The constraint algorithm implemented in LS-DYNA is based on the predictor-corrector algorithm developed by Taylor and Flanagan (1989). The biggest advantage of this contact model is that interface nodes remain on or very close to the surface they are in contact with. Furthermore, elastic vibrations that can occur in penalty formulations are insignificant with the constraint technique. The problem related to finding good penalty constants for the contact is totally avoided by this approach.

At every timestep, t_n , the contact algorithm must first predict accelerations, velocities, and displacements for the next timestep t_{n+1} . LS-DYNA obtains these predictors (i.e., $\ddot{\mathbf{u}}_{t_{n+1}}^{pred}$, $\dot{\mathbf{u}}_{t_{n+1}}^{pred}$, $\mathbf{u}_{t_{n+1}}^{pred}$) from its explicit integration routine, assuming that no contact occurs. During

timestep t_n , the nodal accelerations must be corrected for any changes in the traction boundary conditions, i.e., changes in acceleration due to surface contact determined from the displacement prediction for time t_{n+1} (i.e., $\mathbf{u}_{t_{n+1}}^{pred}$).

To ensure that two surfaces do not interpenetrate, any penetrating slave node and its associated master surface must have accelerations applied to negate the predicted penetration. First, the penetration force of each slave node at time t_n is calculated by:

$$\mathbf{f}_{S_p,t_n} = \frac{m_S \delta_{t_{n+1}}^{pred}}{\Delta t_n^2} \hat{\mathbf{n}} \quad (5-4)$$

in which m_S is the mass of the slave node (denoted by subscript S), δ is the penetration distance on the predictor configuration, Δt_n is the current timestep size, and $\hat{\mathbf{n}}$ is the master surface normal unit vector.

Next, this force is balanced to the master nodes (denoted by subscript M) using a linear interpolation function $N_{SM}(\eta, \xi)$ across the contact surface where η and ξ correspond to the point of contact of the node with the surface.

$$m_{SM} = N_{SM} m_S \quad (5-5)$$

$$\mathbf{f}_{SM,t_n} = N_{SM} \mathbf{f}_{S_p,t_n} \quad (5-6)$$

Once this is complete, the contributions from the slave nodes contacting the master node (denoted by subscript SM) are summed, and virtual work is used to generate the normal (denoted by subscript \mathbf{n}) acceleration correction for the master nodes:

$$\ddot{\mathbf{u}}_{M,\mathbf{n}}^c = \frac{\sum_S \mathbf{f}_{SM,t_n}}{(m_M + \sum_S m_{SM})} \quad (5-7)$$

where m_M is the mass of the particular master node. The correction for the slave node is then calculated using master nodes response. For the particular case of a rectangular contact master surface (i.e. the cutter), $M = 4$:

$$\ddot{\mathbf{u}}_{S,n}^c = \sum_{M=1}^4 N_{MS} \ddot{\mathbf{u}}_{M,n}^c - \left(\frac{\mathbf{f}_{Sp,t_n}}{m_S} \right) \quad (5-8)$$

This corrections are in turn used to get the final accelerations in the absence of friction for the slave and master nodes, at timestep t_n :

$$\ddot{\mathbf{u}}_{S,t_n} = \ddot{\mathbf{u}}_{S,t_{n+1}}^{pred} + \ddot{\mathbf{u}}_{S,n}^c \quad (5-9)$$

$$\ddot{\mathbf{u}}_{M,t_n} = \ddot{\mathbf{u}}_{M,t_{n+1}}^{pred} + \ddot{\mathbf{u}}_{M,n}^c \quad (5-10)$$

Friction Treatment in Constraint Contact

A Coulomb friction model is also adopted by LS-DYNA from (Taylor and Flanagan 1989). Friction forces are handled by a velocity dependent model, in which they resist the relative in-plane motion of the contacting surfaces. The relative velocity, $\dot{\mathbf{u}}_{t_n}^{rel}$, between the slave node and the corresponding master surface at timestep t_n is predicted by:

$$\dot{\mathbf{u}}_{t_n}^{rel} = \dot{\mathbf{u}}_{S,t_{n+1}}^{pred} - \sum_{M=1}^4 N_{MS} \dot{\mathbf{u}}_{M,t_{n+1}}^{pred} \quad (5-11)$$

where $\dot{\mathbf{u}}_{S,t_{n+1}}^{pred}$ and $\dot{\mathbf{u}}_{M,t_{n+1}}^{pred}$ are the predicted velocities for the slave node and master nodes, respectively. From this, the relative tangential velocity, $\dot{\mathbf{u}}_{t_n-t}^{rel}$, its magnitude $v_{t_n-t}^{rel}$, and the tangential unit vector $\hat{\mathbf{t}}$ can be found by:

$$\dot{\mathbf{u}}_{t_n-t}^{rel} = \dot{\mathbf{u}}_{t_n}^{rel} - (\hat{\mathbf{n}} \cdot \dot{\mathbf{u}}_{t_n}^{rel}) \hat{\mathbf{n}} \quad (5-12)$$

$$v_{t_n-t}^{rel} = \sqrt{\dot{\mathbf{u}}_{t_n-t}^{rel} \cdot \dot{\mathbf{u}}_{t_n-t}^{rel}} \quad (5-13)$$

$$\hat{\mathbf{t}} = \frac{\dot{\mathbf{u}}_{t_n-t}^{rel}}{v_{t_n-t}^{rel}} \quad (5-14)$$

Similar to the treatment of penetration, a tangential contact force –defined as a fraction of the force that must be applied to the slave node to cancel its relative motion– is given by:

$$f_{S_{tan},t_n} = \frac{m_S v_{t_n-t}^{rel}}{\Delta t_n} \quad (5-15)$$

An additional acceleration correction for the slave node is then calculated by:

$$\ddot{\mathbf{u}}_{S,t}^c = -\min\left(\left(\mu \ddot{\mathbf{u}}_{S,n}^c\right) \cdot \hat{\mathbf{n}} \ , \ \frac{v_{t_n-t}^{rel}}{\Delta t_n}\right) \quad (5-16)$$

where μ is the friction coefficient at the contact interface.

Finally, the corrected accelerations in Equations (5-9) and (5-10) are re-defined as follows:

$$\ddot{\mathbf{u}}_{S,t_n} = \ddot{\mathbf{u}}_{S,t_{n+1}}^{pred} + \ddot{\mathbf{u}}_{S,n}^c + \ddot{\mathbf{u}}_{S,t}^c \hat{\mathbf{t}} \quad (5-17)$$

$$\ddot{\mathbf{u}}_{M,t_n} = \ddot{\mathbf{u}}_{M,t_{n+1}}^{pred} + \ddot{\mathbf{u}}_{M,n}^c - \left(N_{SM} \frac{m_S}{m_M} \ddot{\mathbf{u}}_{S,t}^c \hat{\mathbf{t}}\right) \quad (5-18)$$

5.2.1.2 Rigid Wall Contact Simplification

The advantage of the constraint method is that it always guarantees the slave nodes to lie on the positive side of the master surface, i.e. no penetration permitted. Nevertheless, when the method is applied to treat the contact between a rigid wall and a deformable node, it does not conserve momentum or energy. The penetrating node is first moved back onto the surface of the rigid wall, and then its velocity and acceleration normal to the wall are immediately reset to zero:

$$\dot{\mathbf{u}}_{S,t_n} = \dot{\mathbf{u}}_{S,t_{n+1}}^{pred} - (\hat{\mathbf{n}} \cdot \dot{\mathbf{u}}_{S,t_{n+1}}^{pred}) \hat{\mathbf{n}} \quad (5-19)$$

$$\dot{\mathbf{u}}_{S,t_n} = \dot{\mathbf{u}}_{S,t_{n+1}}^{pred} - (\hat{\mathbf{n}} \cdot \dot{\mathbf{u}}_{S,t_{n+1}}^{pred}) \hat{\mathbf{n}} \quad (5-20)$$

This procedure for stopping nodes represents a perfectly plastic impact resulting in an irreversible energy loss.

5.2.2 Rock-Rock Contact

When simulating the fragmentation process in rock cutting in FEM, it is necessary to define a separate contact model to handle the rock-rock interaction because newly exposed rock surfaces after *element erosion* (see Section 5.3) will be present.

The “Eroding Single Surface” contact model is employed to treat the rock-rock interface because it allows the contact surface to be updated as exterior elements are removed. The slave surface is typically defined as a set of parts. No master surface is defined. Contact is considered between all the parts in the slave set, including self-contact of each part (in this case, only the rock part is included). The Eroding-Single-Surface contact model in this particular study is defined through a penalty formulation to calculate the contact force. This penalty force is dependent on a penalty stiffness value, and a *segment-based* approach (see Section 5.2.2.2) has been chosen to calculate the force.

5.2.2.1 Penalty Contact Formulation

In line with the theoretical manual of LS-DYNA (Hallquist 2006), when applying the penalty method, each slave node is checked for penetration through the master surface at every timestep (cycle). In this study, the *bucket-sorting* algorithm for detecting penetrations is established. It divides the target surface into cubes (buckets), and the contacting nodes or segments can contact any segment of the target surface in the same bucket or adjacent buckets. A number of 25 cycles between bucket-sort contact searches has been specified.

If the slave node does not penetrate, nothing is done. If it does penetrate, a normal interface force, f_{Sp} , is applied between the slave node and its contact point:

$$f_{Sp} = k_M \delta \quad (5-21)$$

where k_M is the stiffness factor for the master segment (see Section 5.2.2.2) and δ is the amount of normal penetration through the master segment ($\Delta 1$ or $\Delta 2$ in Figure 5-3). This can be thought of as the addition of an interface spring.

f_{Sp} is then resolved in a local coordinate system embedded at the master element (contact point) to determine the normal and shear components. The sliding resistance is then computed using the friction parameters of the master segment and the normal force component as shown in Figure 5-3.

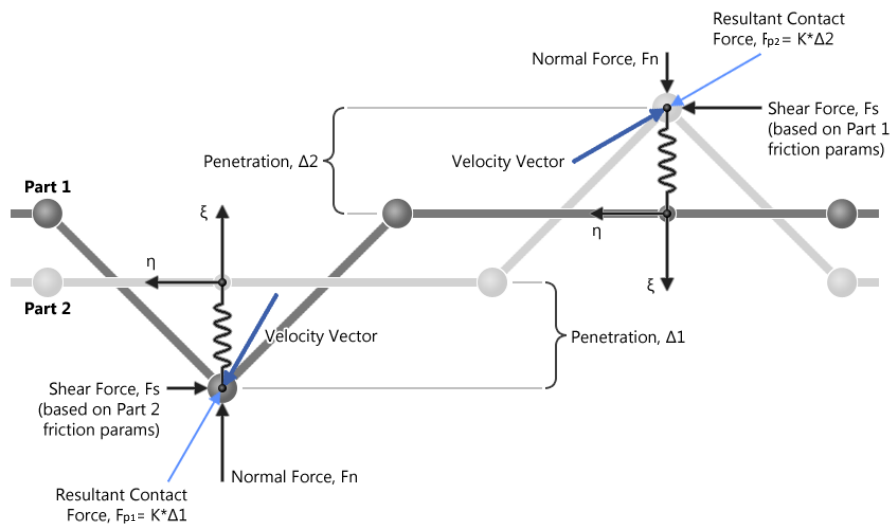


Figure 5-3: Penetration removal process (Bala 2006)

5.2.2.2 Contact Stiffness Calculation

LS-DYNA provides two methods of calculating the stiffness factor (or spring stiffness); these are the Penalty-based approach and the Soft Constraint (or Segment)-based approach.

The penalty-based approach is the most typical and the default in LS-DYNA; it uses the size of the contact segment and its material properties to determine the contact spring stiffness. This method was analyzed during the course of this investigation, and it was found that since it depends on the actual material bulk modulus, instabilities were caused while simulating the rock

cutting process. As the rock stiffness moduli are decreased during plastic deformation, the stiffness factor no longer works effectively, and the contact eventually breaks down causing undesirable penetration. Consequently, the segment-based penalty formulation is employed to calculate the contact stiffness.

Segment-based Approach for Contact Stiffness

With the segment-based contact algorithm, contact between segments is employed rather than using the common node-to-segment treatment. When two 4-noded segments come into contact, forces are applied to eight nodes to resist segment penetration. This treatment has the effect of distributing forces more realistically. The contact stiffness factor for the master segment is calculated by:

$$k_M = \frac{1}{2} SLSFAC \cdot SFS \cdot \left(\frac{m_1 m_2}{m_1 + m_2} \right) \left(\frac{1}{\Delta t} \right)^2 \quad (5-22)$$

where: *SLSFAC* is a scale factor for sliding interface penalties. (*SLSFAC* = 0.1)

SFS is a scale factor for slave penalty stiffness. (*SFS* = 1.0)

*m*₁ and *m*₂ are the segment masses (=1/2 element mass).

Δt is automatically set to the initial solution timestep size, which is updated only if the solution timestep grows by more than 5%.

5.2.2.3 Calibration of Penalty Contact Parameters

As a result of an extensive trial-and-error process, the following input parameters for the Penalty Contact Formulation have been calibrated, and their values greatly affect the performance of the contact model for the rock simulated.

The frictional coefficient at the rock-rock interface is assumed to be dependent on the relative velocity $v_{t_n-t}^{rel}$ of the surfaces in contact:

$$\mu_c = FD + (FS - FD)e^{-DC|v_{t_n-t}^{rel}|} \quad (5-23)$$

where *FS* = 0.6 = Static coefficient of friction

FD = 0.4 = Dynamic coefficient of friction

DC = 20 = Exponential decay coefficient

Additionally, the validated contact parameters listed in Table 5-2 are critical:

Table 5-2: Calibrated input parameters for Penalty Contact

Parameter	Value	Meaning
<i>XPENE</i>	4.0	Contact surface maximum penetration check multiplier.
<i>PENCHEK</i>	2	Flag for small penetration in contact search. If the slave node penetrates more than the segment's (shortest diagonal · <i>XPENE</i> / 20), the penetration is ignored and the slave node is set free.
<i>EROSOP</i>	1	Flag for storage allocation so that eroding contact can occur.
<i>BSORT</i>	25	Number of cycles between bucket sorts.
<i>FRCFRQ</i>	2	Number of cycles between contact force updates.
<i>ENMASS</i>	1	Flag for treatment of the mass of eroded nodes in contact. Eroding nodes of solid elements are retained and continue to be active in contact calculation. This option affects the contact where nodes are removed after surrounding elements fail.

5.3 CRACK INITIATION AND FRAGMENT FORMATION

Without knowing a priori the direction and trajectory of cracks during the rock cutting process, the success of the FEM simulation is dependent upon the implementation of *element erosion* in order to produce fragmentation of the rock piece.

Depending on the state of stress, erosion of elements could sequentially take place either at the front of the cutter –mainly due to the material compressive failure (crushing)– or throughout a failure surface, representing a crack.

When the simulated crack propagates to a free surface, or when it joins other cracks, a chip of rock may be formed and chipped out from the rock continuum piece. Thereafter, independent chips continue to behave according to the rock's constitutive material model. The calculation of contact remains active between these chips and the cutter, as well as among chips and rock piece, thus they have the potential to break further.

5.3.1 Element Erosion

In general, the “added” *element erosion* technique in LS-DYNA removes elements from the simulation once an element satisfies the user-supplied criteria. Since many of the material constitutive models do not allow failure together with erosion in their formulation, this added option provides a means for including erosion in these models. This option can also be applied to constitutive models with other failure/erosion criteria. Table 5-3 provides the details of the erosion criteria available in LS-DYNA, which are independent of the material model to which they can be added in a one-by-one basis.

Although this capability of LS-DYNA is very useful when using material models whose performance could be “controlled” by the user, its application becomes limited when trying to simulate the most-likely-spontaneous behavior of geomaterials.

In addition, no general guidelines exist for selecting such criteria. During the course of this investigation, it has been found that the response of the overall rock-cutting simulation is very sensitive to the value of the erosion parameter selected (see Section 5.3.2); therefore, the selection of the right parameter, among the ones available (see Table 5-3), is a trial-and-error task.

The ideal element erosion technique is one that follows the constitutive law of the material, hence is able to erode elements once the material has failed upon different loading conditions. In other words, the material model has to be able to incorporate element erosion in its formulation. From the set of robust concrete/geomaterial models available in LS-DYNA, it was ultimately found that Mat_159 fulfills this necessity.

5.3.1.1 Treatment of the Mass of Eroded Elements

The fact that elements are deleted from the finite element model is commonly thought as an infringement of the basic modeling principle of conservation of mass. Fortunately, LS-DYNA provides a mechanism to circumvent this violation. It is important to note that within the definition of contact controls (see Section 5.2.2.3), the parameter ENMASS equals 1, which works by retaining the mass of the eroded nodes in the calculation, and keeping them active in contact. Consequently, the overall energy calculation of the system is not affected, as its mass is not reduced.

Table 5-3: Erosion criteria available in LS-DYNA

Parameter	Erosion Criterion	Meaning
p_{\max}	$p \geq p_{\max}$	p is the pressure (positive in compression), and p_{\max} is the maximum pressure for erosion.
ε_{\min}	$\varepsilon_3 \leq \varepsilon_{\min}$	ε_3 is the minimum principal strain (negative in compression), and ε_{\min} is the minimum principal strain for erosion.
p_{\min}	$p \leq p_{\min}$	p is the pressure (positive in compression), and p_{\min} is the minimum pressure for erosion.
σ_{\max}	$\sigma_1 \geq \sigma_{\max}$	σ_1 is the maximum principal stress (positive in tension), and $\sigma_{1_{\max}}$ is the maximum principal stress for erosion.
$\overline{\sigma}_{\max}$	$\sqrt{\frac{3}{2} \sigma_{ij}' \sigma_{ij}'} \geq \overline{\sigma}_{\max}$	σ_{ij}' are the deviatoric stress components and $\overline{\sigma}_{\max}$ is the equivalent stress for erosion.
ε_{\max}	$\varepsilon_1 \geq \varepsilon_{\max}$	ε_1 is the maximum principal strain (positive in tension), and ε_{\max} is the maximum principal strain for erosion.
γ_{\max}	$\gamma_1 \geq \gamma_{\max}$	γ_1 is the maximum shear strain = $(\varepsilon_1 - \varepsilon_3)/2$, and γ_{\max} is the shear strain for erosion.
NCS	-	Number of failure conditions to satisfy before element erosion occurs.

5.3.2 Sensitivity Analysis of “Added” Erosion Criteria

Since Mat_72R3 proved to be a rational material model characterizing the triaxial response of Vosges Sandstone (see Sections 4.6.1 through 4.6.4) in compression and tension, it was used to carry out a parametric study of the element erosion criteria available in LS-DYNA, while simulating scratching tests on rock (see Section 2.1). The added erosion criteria evaluated during this study are listed in Table 5-4; these include shear strain γ_{\max} , maximum principal strain $\varepsilon_{1\max}$ (tension), and minimum principal strain, $\varepsilon_{3\min}$ (compression). Depending on the case analyzed, one or two criteria are to be satisfied before an element is deleted from the simulation.

For illustration purposes, Figure 5-4 compares the first six cases proposed in Table 5-4. This figure illustrates the rock deformation and fracturing in response to different erosion criteria in Mat_72R3, after the cutter has advanced 2.4 mm (0.1 in) at time 4.8 ms. Color contours are values of von-Mises or equivalent stress (red corresponds to a maximum value of 0.1 GPa (14,500 psi)). It can be seen how sensitive the material is to these erosion criteria, and how poor

the rock performs using Mat_72R3. In order to initiate a crack and propagate it, the elements are subjected to very high, irrational strain values.

Table 5-4: Erosion criteria analyzed

Simulation Name	A $\gamma >$	B $\epsilon_1 >$	C $\epsilon_3 <$
A_0.3	0.3		
A_0.5	0.5		
A_0.8	0.8		
B_0.5		0.5	
B_0.7		0.7	
B_0.8		0.8	
AB_0.5	0.5	0.5	
BC_0.5		0.5	-0.5
BC_0.8		0.8	-0.8
BC_0.5_0.8		0.5	-0.8
BC_0.8_0.5		0.8	-0.5

It was observed that values smaller than 0.3 (30%) of any of the strains analyzed, produced a very quick element erosion, resembling crushing of the material. For this reason, no crack could be developed throughout the simulation, thus values larger than 0.3 were tried and evaluated.

The deformation of the rock in all cases shown in Figure 5-4 is found to be irrational because it experiences extremely large plastic deformation before breaking (i.e. is not brittle), so the model configuration is not useful. Lower values of erosion criteria could minimize this effect, however, that would lead into a pure crushing failure mode without crack propagation.

It can be concluded that the “added” erosion method is very subjective and may lead to inappropriate stress-strain conditions. As mentioned in Section 5.3.1, the ideal element erosion technique is one that follows the constitutive law of the material, hence is able to erode elements once the material has failed upon different loading conditions. In other words, the material model has to be able to incorporate element erosion in its formulation. From the set of robust concrete/geomaterial models available in LS-DYNA, it was ultimately found that Mat_159 fulfills this necessity.

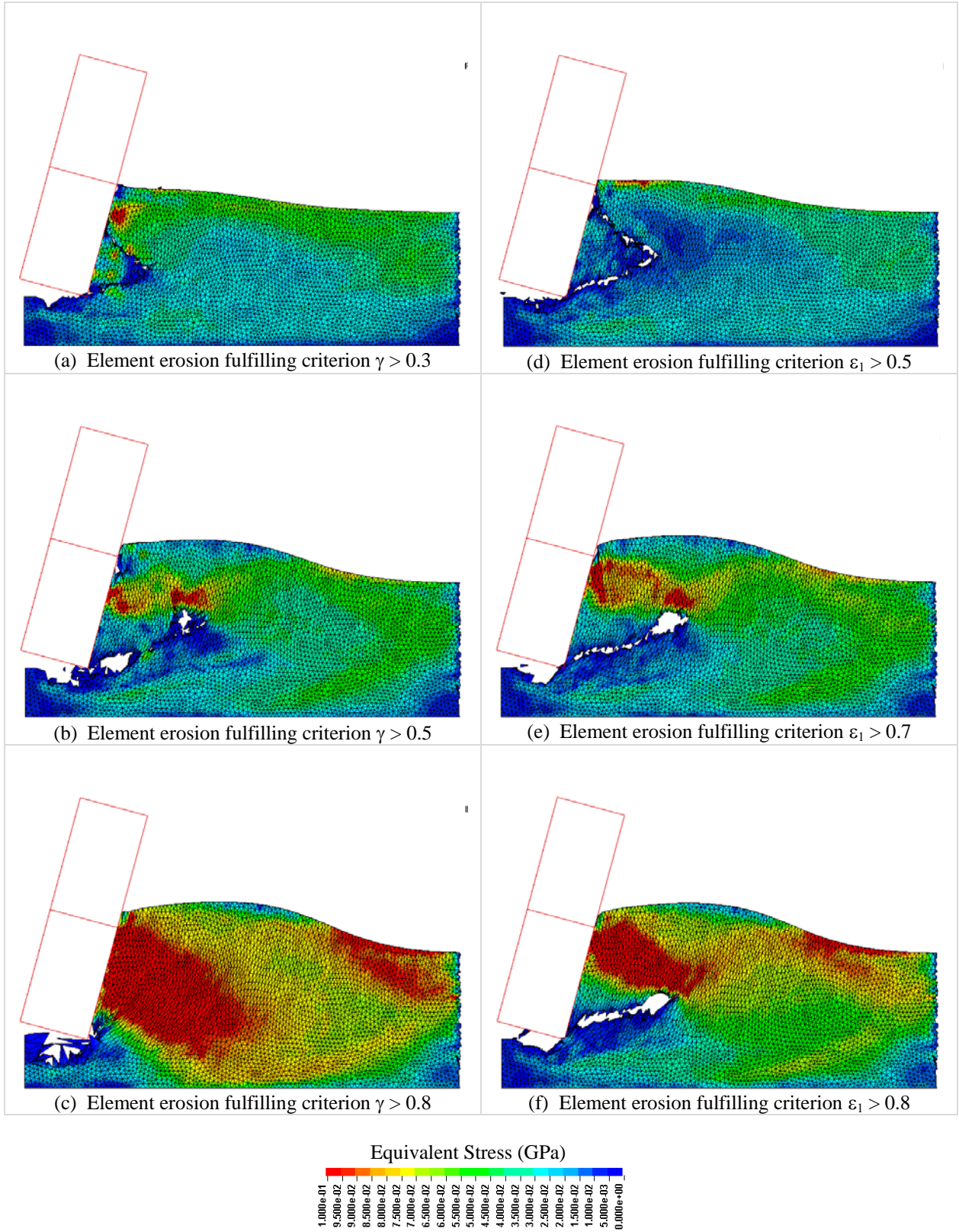


Figure 5-4: Erosion criteria sensitivity analysis on Mat_72R3 – Color fringe of Equivalent stress

5.3.3 Sensitivity Analysis of Erosion Criteria in Mat_159

As mentioned in Section 3.2.4, Mat_159 automatically enables element erosion when the element loses all strength and stiffness as the damage parameter approaches a value of 1.0. To prevent computational difficulties with very low stiffness, element erosion is available as a user option. An element erodes when the damage variable D is greater than 0.99 and, simultaneously, the maximum principal strain, $\varepsilon_{1\text{-erosion}}$, is greater than a user-supplied input value, ERODE, minus 1.

This automatic –and rational– erosion capability of Mat_159 makes this material model the most appropriate to use in the simulation of rock cutting with FEM, using LS-DYNA.

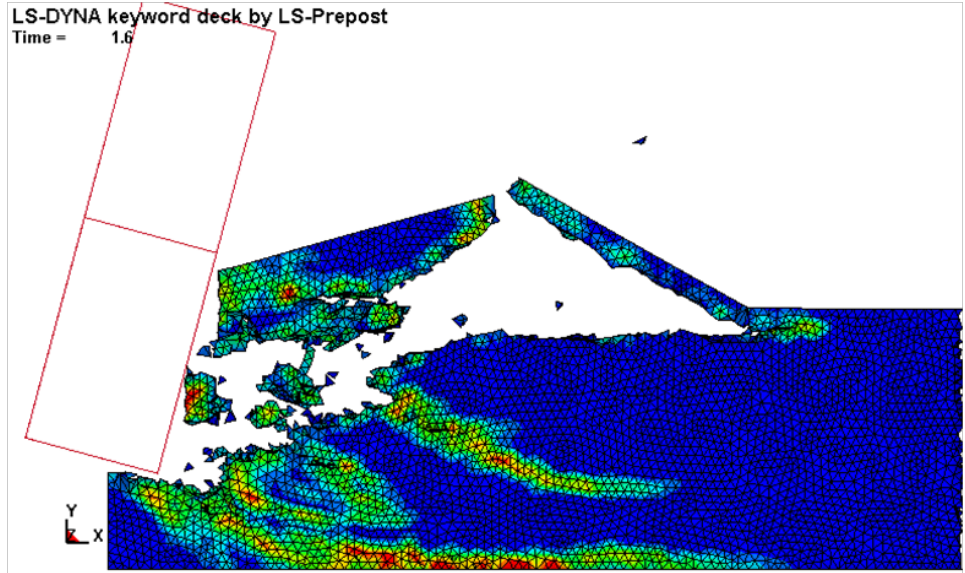
A sensitivity analysis has been completed to determine the value of ERODE that best suits the model so it replicates the laboratory tests of rock cutting. $\text{ERODE} = 1 + \varepsilon_{1\text{-erosion}}$, where $\varepsilon_{1\text{-erosion}}$ is the threshold of maximum principal strain in an element in order for it to be eroded from the simulation. Mat_159 allows the user to include $\varepsilon_{1\text{-erosion}}$ together with the built-in damage magnitude calculation, both that would determine the element erosion. Values of 0%, 5%, and 10% of $\varepsilon_{1\text{-erosion}}$ were attempted and compared. The benchmark for comparison of the results presented in this section is found in Section 2.1.1.1, Deep Cut Experiments. In addition, a video of the actual rock scratching experiment in the laboratory is examined and used for comparison.

Figures Figure 5-5, Figure 5-6 and Figure 5-7 display the performance of input parameter ERODE equal to 1.00, 1.05, and 1.10 respectively, during the simulation of rock cutting. They illustrate the rock deformation and fracturing after the cutter has advanced 0.8 and 7.6 mm (0.03 and 0.3 in). Color contours are values of accumulated damage (red corresponds to a maximum value of 0.7).

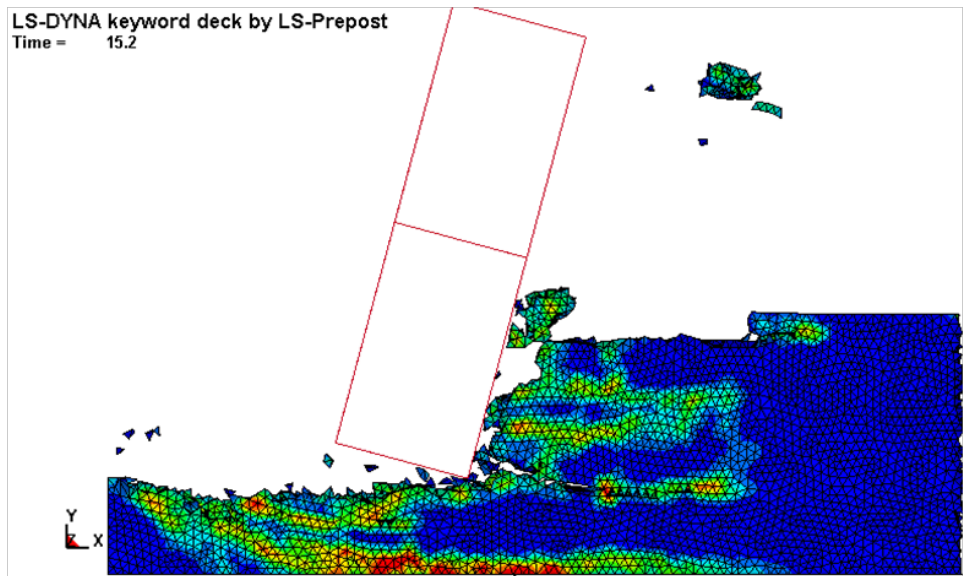
It can be observed that as the value of $\varepsilon_{1\text{-erosion}}$ increases, the accumulated damage increases as well. Furthermore, increasing the value of $\varepsilon_{1\text{-erosion}}$ implies that the rock is subjected to larger deformation before breaking. This produces a larger energy release when cutting, thus fragmentation occurs more abruptly, being evident by larger fragments chipped away from the rock sample.

Figure 5-8 shows the time history of the accumulated amount of volume being eroded from the rock, and Figure 5-9 shows the time history of the horizontal cutting force, both for the three cases evaluated. These figures accurately validate the abovementioned observations.

After intensive sensitivity analyses of this parameter combined with others (as explained in Section 5.4.2), and using an improved set of input values for the Mat_159, it can be concluded that the value of ERODE that provides the most reasonable fragmentation mode is ERODE = 1.05.



(a) Cutter travel distance, $l = 0.8$ mm at time $t = 1.6$ ms



(b) Cutter travel distance, $l = 7.6$ mm at time $t = 15.2$ ms

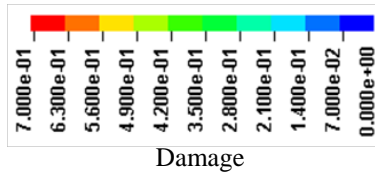
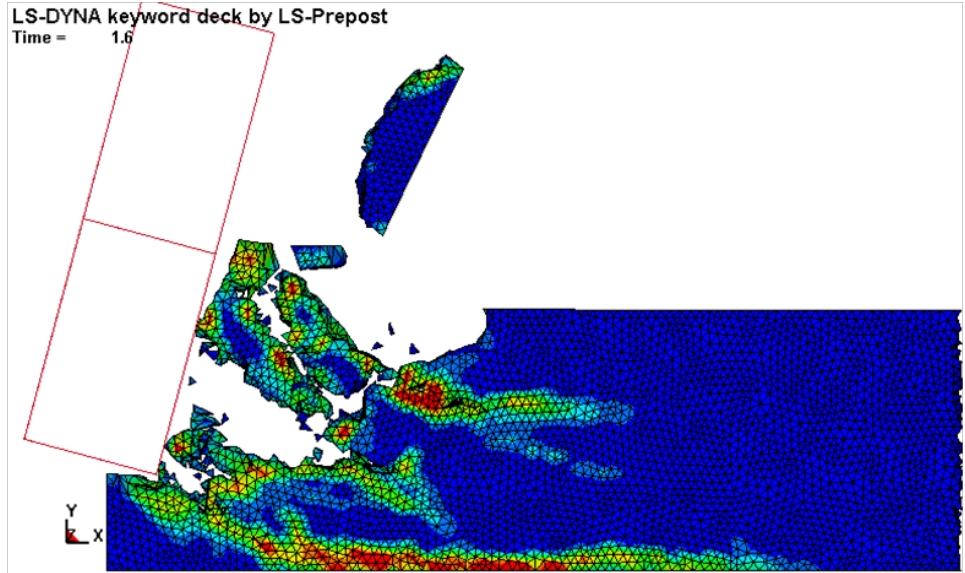
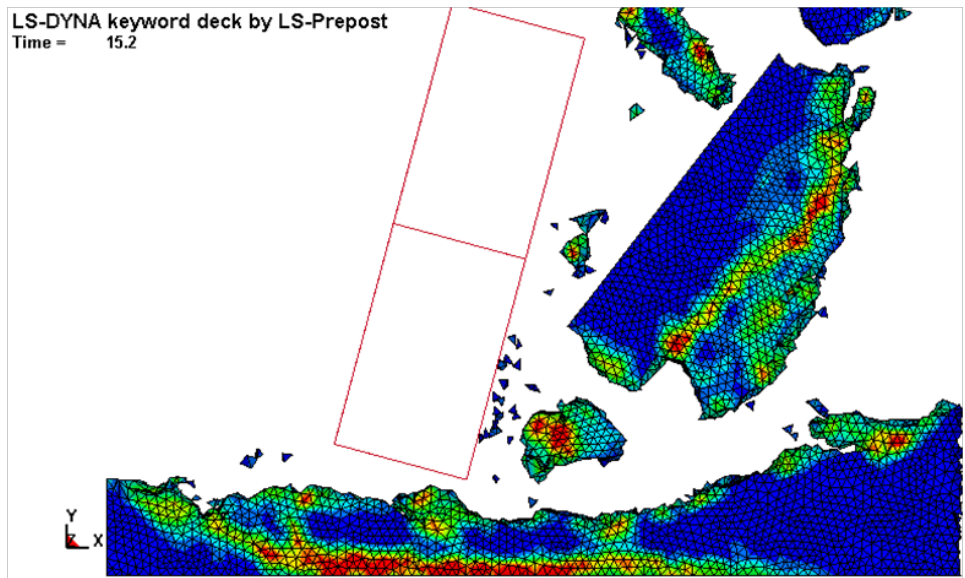


Figure 5-5: Erosion criterion in Mat_159, ERODE = 1.00 – Color fringe of *Damage* value



(a) Cutter travel distance, $l = 0.8$ mm at time $t = 1.6$ ms



(b) Cutter travel distance, $l = 7.6$ mm at time $t = 15.2$ ms

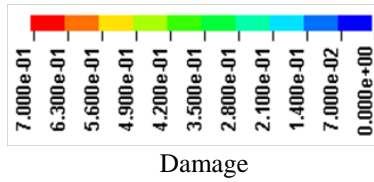
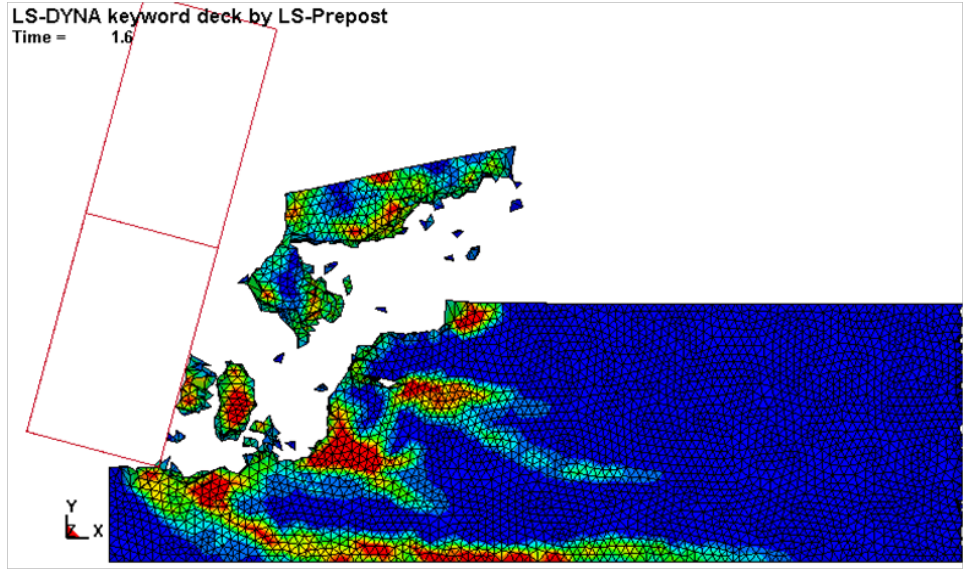
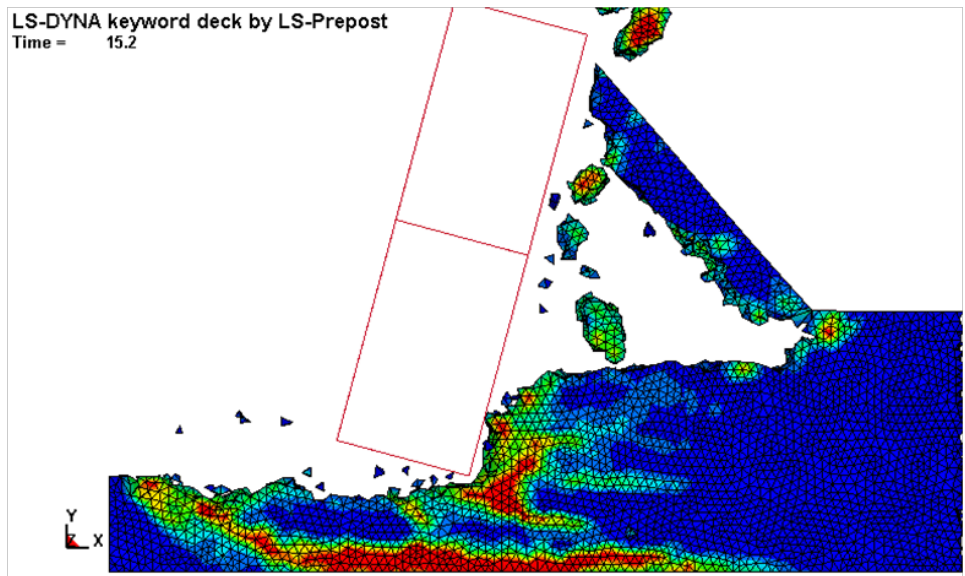


Figure 5-6: Erosion criterion in Mat_159, ERODE = 1.05 – Color fringe of *Damage* value



(a) Cutter travel distance, $l = 0.8$ mm at time $t = 1.6$ ms



(b) Cutter travel distance, $l = 7.6$ mm at time $t = 15.2$ ms

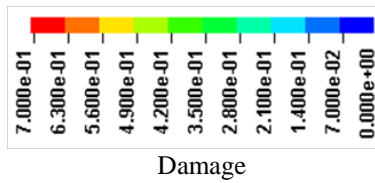
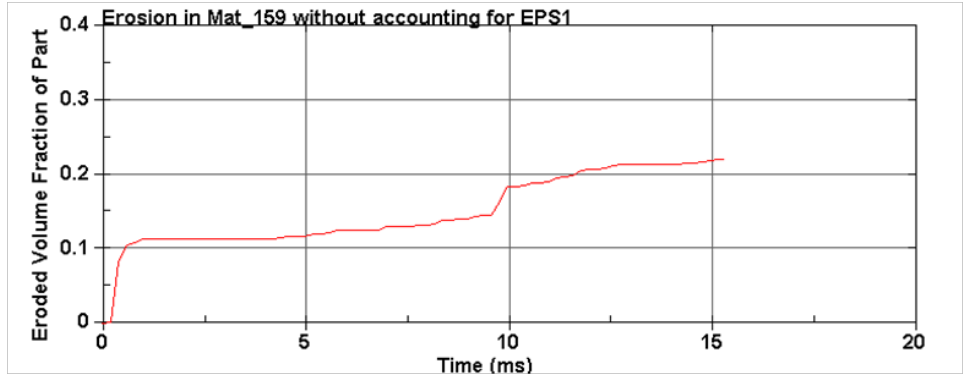
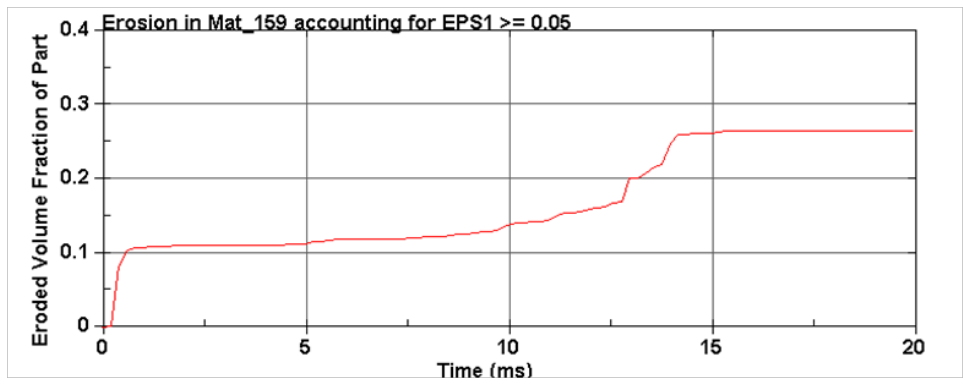


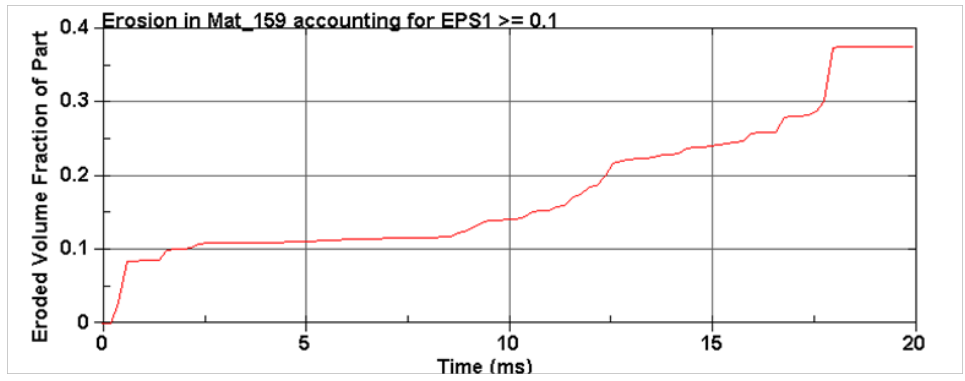
Figure 5-7: Erosion criterion in Mat_159, ERODE = 1.10 – Color fringe of *Damage* value



(a) ERODE = 1.00

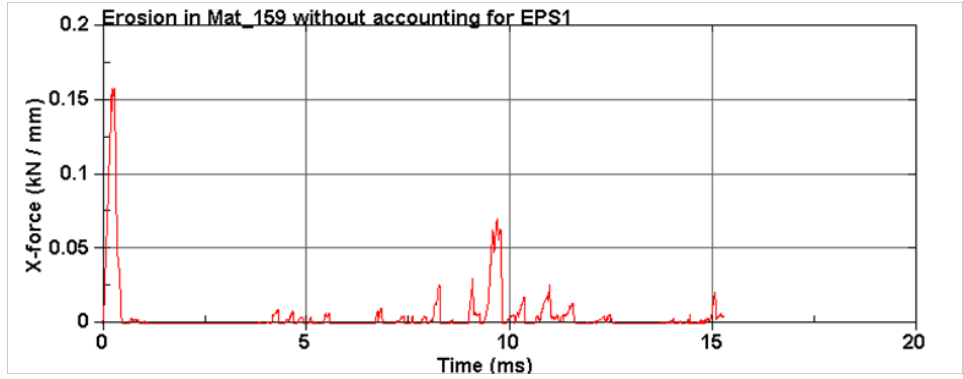


(b) ERODE = 1.05

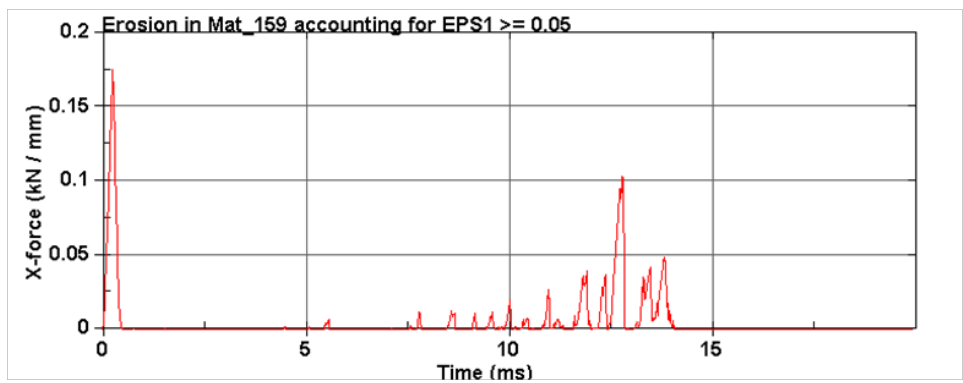


(c) ERODE = 1.10

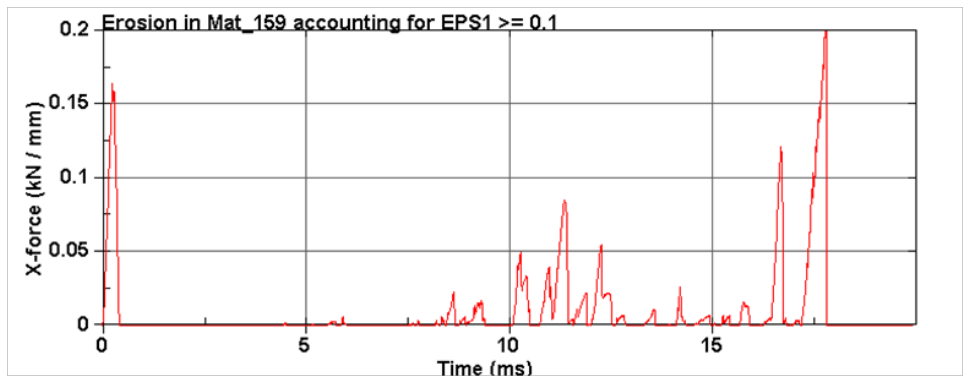
Figure 5-8: Eroded volume fraction from rock piece during cutting simulation in Mat_159



(a) ERODE = 1.00



(b) ERODE = 1.05



(c) ERODE = 1.10

Figure 5-9: Horizontal force during erosion criteria assessment in Mat_159

5.4 ANALYSIS OF FORCES FROM SIMULATIONS

5.4.1 Force Signal Filtering and Calibration

Due to the nature of the solution implemented, i.e. *element erosion* (see Section 5.3), it is expected that the simulated forces show frequent drops to zero as the elements in front of the cutter are deleted and a loss of contact takes place between the rock piece and the cutter. Consequently, the shape of the force plot from the simulations would lack correspondence with the shape of the laboratory measurements, while the magnitude of the peak forces could agree.

In order to be able to compare quantitatively the results from the simulations, a sound filtering procedure has to be implemented on the recorded simulated forces. Taking into account that the computer simulation is capable of sampling the force values with a time interval as short as the timestep size (e.g. 1.0215×10^{-8} s), it would be easy to treat the data so that the right amount of computed force points are compared to the experimental data. Table 5-5 compares the data acquisition characteristics for both the laboratory scratching tests (see Section 2.1.1) and the numerical simulations of the rock-cutting tests. Based on these values it is clear that the simulation force signals are not only capturing 8 times more events occurring at a scale smaller than the rock grain size (i.e., 0.15–0.45 mm (0.006-0.018 in)), but they are also getting a higher fluctuation of the force magnitude due to fictitious phenomena associated with the numerical erosion implementation. Section 5.4.1.1 reviews the data-filtering technique found to be appropriate for this specific modeling application.

Table 5-5: Characteristics of the force time history in the lab experiments and simulations

	Lab. Scratching Tests	FEM Simulations
Cutting velocity	4×10^{-3} m/s	4 m/s
Data acquisition frequency	100 Hz	800,000 Hz
Measurement time interval	1×10^{-2} s	1.25×10^{-6} s
Sampling rate	25 points/mm	200 points/mm
Measurement length (spatial resolution)	0.04 mm	0.005 mm

Once the simulation force has been filtered and an average force has been estimated (see Section 5.4.1.2), the viability of the numerical model could be assessed quantitatively, not only by comparing with the laboratory results, but also with calculated force values from analytical solutions (see Chapter 9.0).

5.4.1.1 Butterworth Filter on Simulation Force Signal

Curves can be filtered to remove high frequency noise. The technique is typically applied to acceleration or force traces. LS-Prepost is the post processing package for LS-DYNA's output, and it offers four filtering options to attenuate output data. These are: the standard SAE filter, the FIR 100 (Finite Impulse Response) filter, the raised cosine filter, and the Butterworth filter. After studying these filters capabilities, it was found that the Butterworth filtered the cutting force output data satisfactorily, in order to be compared with the force time series measured in the laboratory tests.

All filtering options require the curves to have a constant time increment between points. This will generally be the case in for the LS-DYNA time history results. Typically, the time increment should be at least 10 times the cut-off frequency.

The Butterworth filter is designed to have a frequency response which is as flat as mathematically possible in the pass band. It is a low pass filter with two input variables: order and cut-off frequency. The order of the filter controls the roll-off rate, i.e. higher orders (roll-off rates) attenuate the results more quickly. On the other hand, the cut-off frequency is the frequency at which the magnitude of the signals is halved by the filter. The lower the frequency, the less noise passes through, and any peaks in the signal tend to get reduced in magnitude.

With careful analysis of the force time history characteristics, listed in Table 5-5, it was established that the cut-off frequency using the Butterworth filter of LS-Prepost should be 1 kHz, which is equivalent to 1 Hz filtering frequency on the lab data.

5.4.1.2 Force Signal Calibration: Experiment vs. Simulation

Having the force signals from the shallow-cut and deep-cut scratching tests as point of reference (see Section 2.1.1), it is possible to compare and validate the quality of the force output from the LS-DYNA simulations.

After applying the Butterworth filter to the horizontal cutting force output signal, with a cut-off frequency of 1 kHz, the shape of the force profiles for the shallow-cut and deep-cut simulation compare very well with the background trends of the experimental force series. Figure 5-10 and Figure 5-11 illustrate both profiles side by side for the shallow-cut and deep-cut respectively. In the simulation output plots, the red series correspond to the original signal, and the blue series correspond to the filtered data.

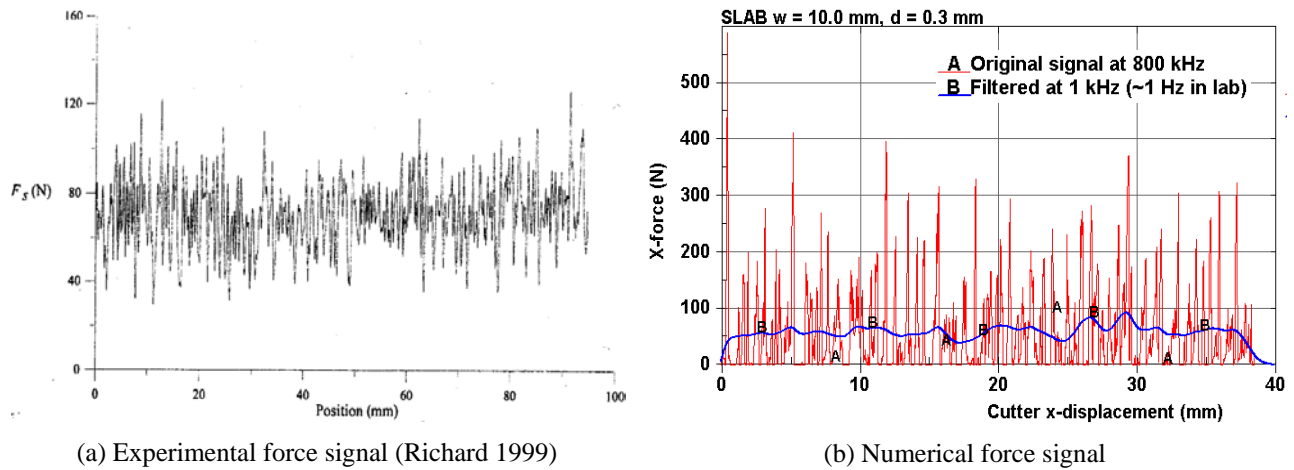


Figure 5-10: Validation of force signals from 0.3-mm shallow-cut

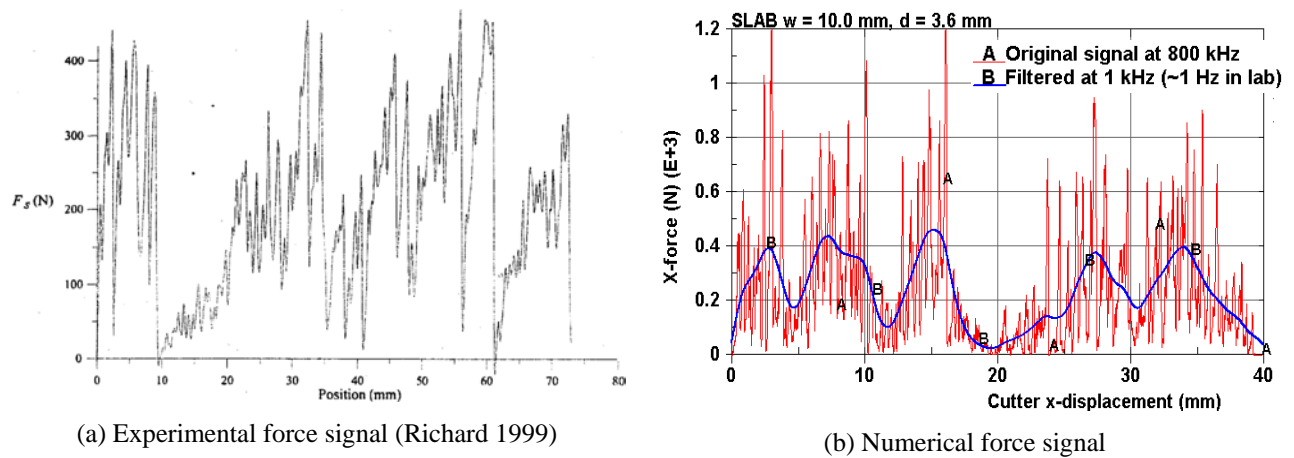


Figure 5-11: Validation of force signals from 3.6-mm shallow-cut

In agreement with Richard’s findings (1999), the force fluctuation increases with the depth of cut. Furthermore, in order to find the most representative value of the average force for each test, it is opportune to follow his analysis for the determination of this value, which will help us compare and validate the results in a quantitative basis. Richard states that when cutting in the ductile mode –i.e. at a shallow depth less than the critical depth, where only damage of the rock (crushing) and a plastic flow of particles occurs– the *mean force* is the relevant output parameter of the test. Conversely, when cutting in the brittle regime –i.e. a deep cut where cracks and fragmentation of the rock takes place– the peaks of the force signal seem to be more adapted to characterize this failure mode, thus an *average of the peak forces* is the output value to consider. To evaluate this average, only the peak values located above the mean value are isolated and taken into consideration.

To ensure the validity of the filtering technique used, it is important to note that the mean force calculated from the filtered simulated force history yielded the same results as the force obtained from the “external work” LS-DYNA output from each run.

After the filter is passed through the simulated force signal in question, the above-mentioned criteria are applied and a quantitative value of the force is obtained with the aim of comparing with the experimental value. In this way, it is possible to corroborate the viability of the rock-cutting simulation results and the filtering technique employed to treat the output force data. Figure 5-12 and Figure 5-13 include a comparison of the mean forces from the laboratory (reported by Richard (1999)) and the simulation for shallow cut and deep cut, respectively.

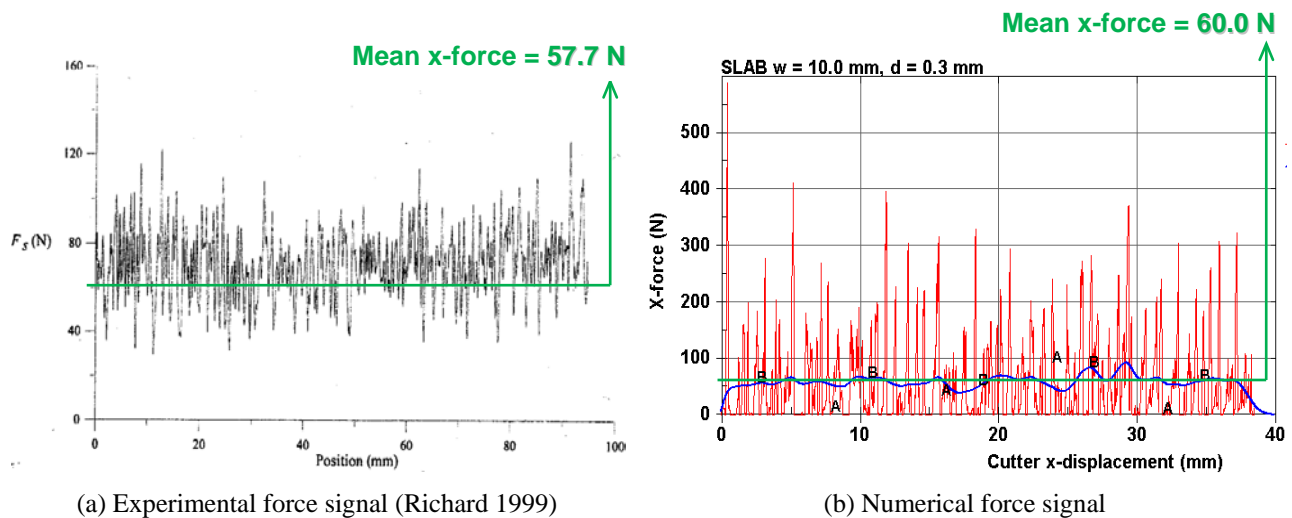


Figure 5-12: Validation of force magnitude from 0.3-mm shallow-cut

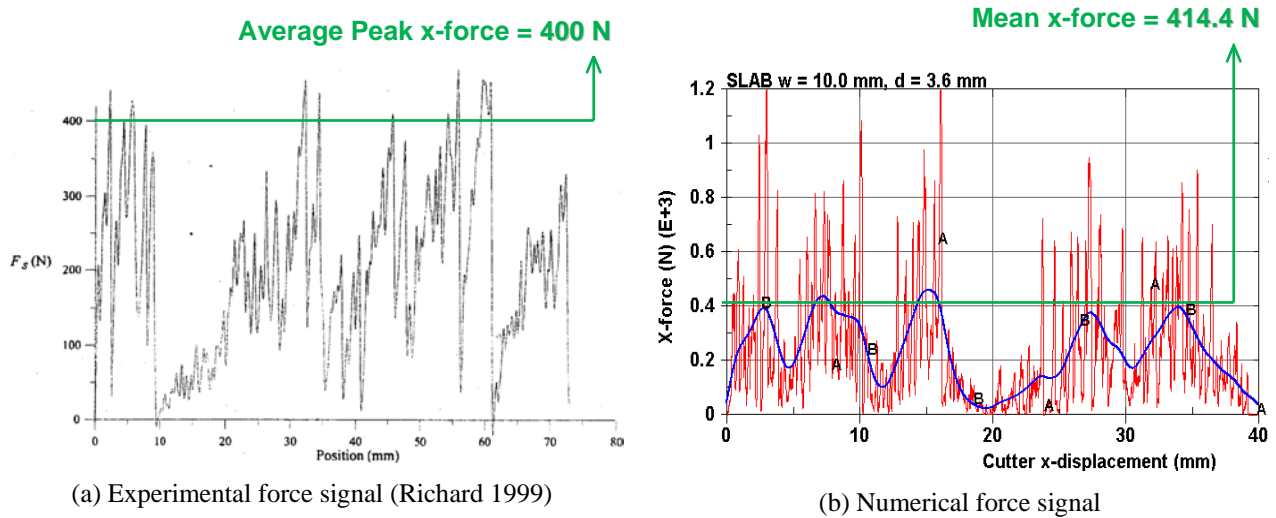


Figure 5-13: Validation of force magnitude from 3.6-mm deep-cut

5.4.2 Factors Affecting Resulting Cutting Forces and Chip Formation

The calculated results of the finite element models –such as stresses, deformations, and thus forces– are particularly sensitive to user defined factors associated with the dynamic nature of the rock-cutting simulations. Throughout the development of the optimum FEM model for rock cutting, hundreds of simulations were run as part of several parametric studies searching for the proper material model parameters, and the proper numerical control parameters. The most influential non-material-related factors affecting the results of this study were found to be the cutting velocity, the numerical damping properties of the rock material, and the size and shape of the elements comprising the rock piece.

In addition to the above-mentioned factors related to the physics of the problem, several input parameters within LS-DYNA material models are significantly dominant in the results of the simulations. It is very important to carry out a thorough calibration of the input values in order to simulate the rock material behavior as realistic as possible. That is essentially one of the main objectives of this research effort, and it is portrayed throughout Chapters 3.0, 4.0, and 5.0.

Another significant aspect that affects the rock cutting force output from the simulations is the *element erosion* parameter, as described in Section 5.3.1. The element erosion user input value for Mat_159 is limited to an additional criterion, i.e. the tensile strain magnitude, to be

fulfilled together with the element damage value, which is calculated internally by the code. Although Section 5.3.3 illustrates three different cases for this user-defined parameter, further sensitivity was carried out in combination with other parameters. Before acquiring the best understanding of the behavior of Mat_159 and thus its input parameters, a range of sensitivity analyses were performed based on the variation of dominant factors such as the damage threshold input, ERODE, and the moduli recovery input, RECOV (see Section 5.4.2.3 for details). Results from these simulations helped in establishing the final set of input values appropriate for this rock-cutting modeling effort, as seen in Figure 5-5 through Figure 5-7 for the erosion parameter calibration and Figure 5-24 through Figure 5-29 for stiffness recovery parameter calibration.

Once Mat_159 was ultimately calibrated and perfected, 28 different simulations of the same scratch test case (i.e., 3.6-mm (0.142 in) deep cut) that were run as a result of combining variable parameters like damping, erosion criteria, and moduli recovery, as well as of changing boundary conditions such as the lateral constraint of the rock piece, and the cutting velocity. Table 5-6 lists these 28 combinations, from which one was eventually selected to be the one that yielded the best results. Circled numbers are the simulation ID numbers. Comparison of these simulated cases with the actual laboratory test was made on a qualitative basis –based upon the fracturing/cracking mode, chip formation, and shape of the force signal– as well as on a quantitative basis –with the averaged horizontal cutting force magnitude.

The set of inputs that produced the best rock-cutting simulation include:

- Both external faces of the rock piece are constrained in the Z-direction (thus plane strain is fulfilled)
- Cutting velocity = 4 m/s (13.12 ft/s) –in contrast with 4×10^{-3} m/s in the lab–
- System damping constant = 1×10^{-8} (Essentially no numerical damping)
- RECOV = 10.5 for Mat_159 (Moduli partially recovered based on pressure and sign of volumetric strain)
- ERODE = 1.05 for Mat_159

The following subsections exemplify the effect of the most relevant factors within this sensitivity analysis, i.e., the system damping constant, the cutting velocity, and value of the stiffness recovery parameter, RECOV.

Table 5-6: Combinatory of critical input parameters for sensitivity analysis

		All surface nodes constrained in Z-dir			Only front face with constrained nodes in Z-dir		
		Additional ϵ_1 criterion for Erosion			Additional ϵ_1 criterion for Erosion		
System Damping constant		0%	5%	10%	0%	5%	10%
v = 0.5 m/s	default: critical = $2*\omega_{min}$	☐ ①			☐ ⑪		
	0.1						
	0.05						
	0.01						
	0.001						
	0.0001	☐ ②	☐ ③A ● ③B	☐ ④			
	1.00E-08						
v = 2 m/s	default: critical = $2*\omega_{min}$				☐ ⑫		
	0.1				☐ ⑬		
	0.05				☐ ⑭		
	0.01				☐ ⑮	☐ ⑯	☐ ⑰
	0.001				☐ ⑱	☐ ⑲	☐ ⑳
	0.0001		☐ ⑤A ● ⑤B	☐ ⑥	☐ ㉑	☐ ㉒	☐ ㉓
	1.00E-08		☐ ⑦A ● ⑦B				
v = 4 m/s	default: critical = $2*\omega_{min}$						
	0.1						
	0.05						
	0.01						
	0.001						
	0.0001		☐ ⑧A ● ⑧B				
	1.00E-08		☐ ⑨A ● ⑨B	☐ ⑩			

☐ parameter RECOV = 10.5 (Moduli is partially recovered based on pressure sign and vol. strain)

● parameter RECOV = 1 (Moduli is not recovered after damaged)

5.4.2.1 System Damping

As mentioned in Section 5.1.3, part of the boundary conditions of the developed models in this research accounts for a gravity-application stage prior to start the cutting (transient) simulation. During the *dynamic relaxation* phase (for initialization), LS-DYNA applies a static load, i.e. the gravitational load defined by the author, and the calculation begins and executes with damping incorporated in the update of the displacement field. LS-DYNA's starting point is the dynamic equilibrium equation, Equation (1-13), with the addition of a damping term, at the n^{th} timestep t_n :

$$\mathbf{M} \ddot{\mathbf{u}}_{t_n} + \mathbf{C} \dot{\mathbf{u}}_{t_n} + \mathbf{Q}_{t_n}(\mathbf{u}_{t_n}) = 0 \quad (5-24)$$

$$Q_{t_n}(\mathbf{u}_{t_n}) = \mathbf{f}_{ext,t_n} - \int_V \mathbf{B}^T \boldsymbol{\sigma}_{t_n} dV \quad (5-25)$$

where we recall that \mathbf{M} is the mass matrix, \mathbf{C} is the damping matrix, $\ddot{\mathbf{u}}_{t_n}$ is the acceleration, $\dot{\mathbf{u}}_{t_n}$ is the velocity, and \mathbf{u}_{t_n} is the displacement vector.

Based on the central difference scheme, for $\dot{\mathbf{u}}_{t_n}$ we can assume an averaged value of

$$\dot{\mathbf{u}}_{t_n} = \frac{1}{2} \left(\dot{\mathbf{u}}_{t_{n+\frac{1}{2}}} + \dot{\mathbf{u}}_{t_{n-\frac{1}{2}}} \right) \quad (5-26)$$

Furthermore, as a starting procedure for the quasi-static solution, LS-DYNA imposes $\dot{\mathbf{u}}_{t_0} = 0$ and $\mathbf{u}_{t_0} = 0$, thus $\dot{\mathbf{u}}_{t_{0+\frac{1}{2}}} = \dot{\mathbf{u}}_{t_{0-\frac{1}{2}}}$. Consequently, the velocity at timestep $t_{0+\frac{1}{2}}$ is

$$\dot{\mathbf{u}}_{t_{0+\frac{1}{2}}} = -\frac{1}{2} \Delta t_0 \mathbf{M}^{-1} Q_{t_0} \quad (5-27)$$

At this point of the calculation, a damping coefficient must be selected to obtain convergence to the static solution in minimal time. The best estimate for damping values is based on the frequencies of the structure (Hallquist 2006). One choice is to focus on an optimal damping parameter, so that the dynamic relaxation is nothing else but a critically damped system

$$C = C_{critical} = 2 \omega_{min} m \quad (5-28)$$

where m is the nodal mass. The problem here is finding the dominant eigenvalue (natural frequency) in the structure related to the “pseudo-dynamic” behavior of the structure. As the exact estimate would be rather costly and not fit into the explicit algorithm, an estimate must be used. The automatic estimate of the minimum eigenvalue of the structure is calculated based on Papadrakakis’ paper as described in LS-DYNA’s Theory Manual (Hallquist 2006).

If the automatic estimate for ω_{min} is not used, LS-DYNA’s default method to apply damping during the dynamic relaxation phase includes an input damping factor η (defaulted to 0.995), such that

$$\dot{\mathbf{u}}_{t_{n+\frac{1}{2}}} = \eta \dot{\mathbf{u}}_{t_{n-\frac{1}{2}}} + \ddot{\mathbf{u}}_{t_n} \Delta t_n \quad (5-29)$$

The relaxation process continues until a convergence criterion based on global kinetic energy is met, i.e. convergence is assumed if

$$E_k < cvtol \cdot E_k^{max} \quad (5-30)$$

where *cvtol* is the convergence tolerance (defaulted to 0.001). The kinetic energy excludes any rigid body component. Initial velocities assigned in the input are stored during the relaxation. Once convergence is attained the velocity field is initialized to the input values.

Mass Weighted Damping

With mass weighted damping, the damping force in Equation (5-24) is simplified into

$$F_{t_n}^{damp} = \mathbf{C} \dot{\mathbf{u}}_{t_n} = D_s m \dot{\mathbf{u}}_{t_n} \quad (5-31)$$

As can be seen from Figure 5-14 and as discussed above, the best damping constant for the system is usually some value approaching the critical damping factor for the lowest frequency mode of interest; therefore, LS-DYNA recommends the use of $D_s = 2 \omega_{min}$.

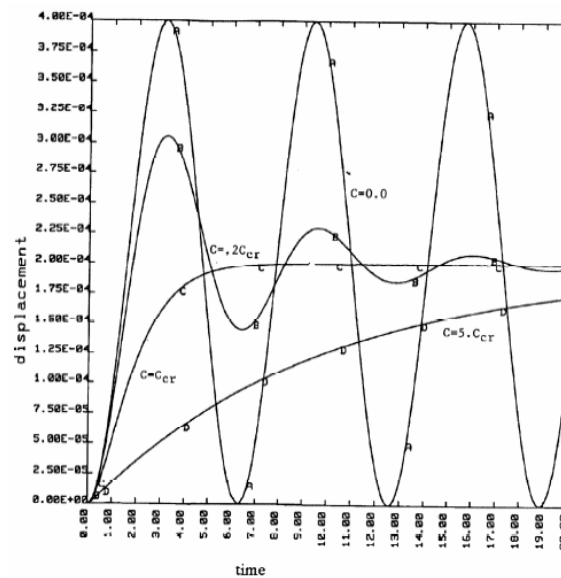


Figure 5-14: Effect of damping coefficients applied to a 1-degree-of-freedom oscillator (Hallquist 2006)

One expects that the application of a mass weighted damping factor to the system provides resistance against disturbance motion (as in the rock-cutting dynamic problem), and eventually this motion subsides until a state of quasi-static deformation is reached due to frictional losses and spreading of shock waves. These shock waves can be represented as mechanical waves of finite amplitude and are initiated when the material undergoes a fast compression. The rock-piece medium is comprised of material points, which are forced away from their equilibrium position as the disturbance propagates through the material. In this order of ideas, the use of a system damping coefficient should be able to considerably affect the resulting cutting forces, as the internal element vibration and thus the kinetic energy of the system is supposed to decrease.

Commonly, researchers dealing with numerical modeling of rock cutting (or associated problems) make use and describe the application of a system damping factor to attenuate out-of-balance (non-contact-related) forces behind a shock front. Some instances include investigations on fracture initiation, growth and effect of stress field (McKinnon and Garrido 1998), numerical modeling of indentation and scratch problems (Cheng 1996), combination of discrete element and finite element methods for dynamic analysis of geomechanical problems (Oñate and Rojek 2004), and discrete element modeling of rock cutting (Rojek 2007). Although these research groups implement global damping factors into their rock cutting simulations, they do not specify the effect that such a parameter has on their results.

In the present work, the influence of the system damping constant, D_s , is studied by varying its value as shown in Table 5-6. As a quantitative measure of the simulation results, the average peak force from all the cases has been compiled in Table 5-7 (see Section 5.4.1 for details on the force averaging method). Surprisingly, there seems to be no dramatic variation in the force magnitude due to the application of damping coefficients of different value. There is only a slightly decrease in the average cutting force, as the damping coefficient is reduced. This trend is illustrated in Figure 5-15, where the results from runs 12 through 23 are plotted. This group of runs encompasses all those that had one of the rock slab faces not constrained, and a cutting velocity of 2 m/s (6.56 ft/s). These include also the variation of the erosion criterion value. It can be seen that for simulations with $ERODE = 1.0$, the effect of the damping coefficient is negligible, whereas for $ERODE = 1.05$ and 1.10 the influence is notorious, being somewhat stronger for $ERODE = 1.05$.

Table 5-7: Final sensitivity analysis: Resultant cutting forces

		All surface nodes constrained in Z-dir			Only front face with constrained nodes in Z-dir			Average Peak Force (N) for a 10-mm wide rock slab
		Additional ϵ_1 criterion for Erosion			Additional ϵ_1 criterion for Erosion			
		0%	5%	10%	0%	5%	10%	
		RECOV			RECOV			
	System Damping constant	10.5	10.5	1	10.5	10.5	10.5	
v = 0.5 m/s	default: critical = $2 \cdot \omega_{min}$	418.26 ①				-- ⑪		
	0.1							
	0.05							
	0.01							
	0.001							
	0.0001	402.5 ②	325.68 ③A	347.72 ③B	406.91 ④			
	1.00E-08							
v = 2 m/s	default: critical = $2 \cdot \omega_{min}$					343.36 ⑫		
	0.1					336.62 ⑬		
	0.05					334.96 ⑭		
	0.01					346.25 ⑮	370.31 ⑯	363.78 ⑰
	0.001					330.24 ⑱	346.56 ⑲	354.48 ⑳
	0.0001		373.98 ⑤A	369.25 ⑤B	418.62 ⑥	-- ⑳	307.51 ㉑	331.86 ㉒
	1.00E-08		373.19 ⑦A	341.68 ⑦B				
v = 4 m/s	default: critical = $2 \cdot \omega_{min}$							
	0.1							
	0.05							
	0.01							
	0.001							
	0.0001		447.05 ⑧A	348.73 ⑧B				
	1.00E-08		414.41 ⑨A	368.23 ⑨B	393.2 ⑩			

Not enough data

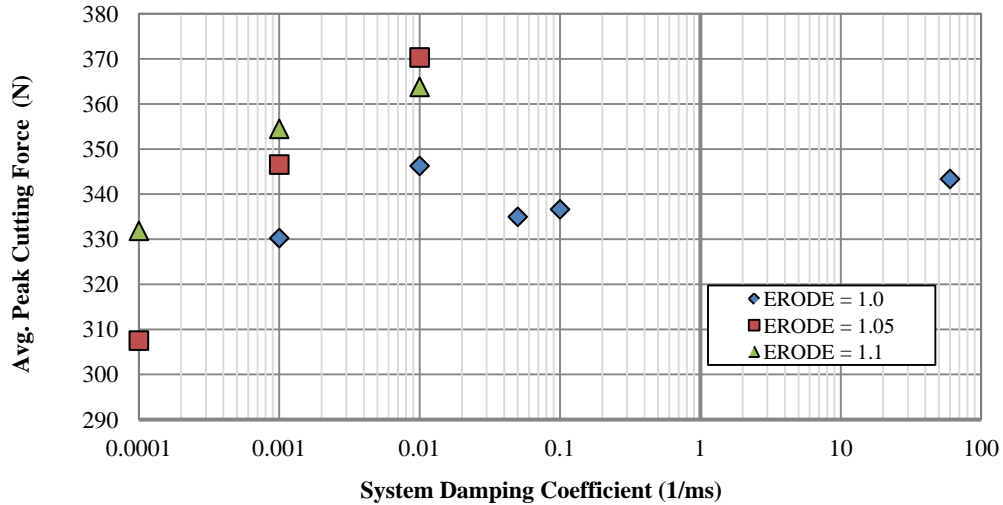


Figure 5-15: Effect of damping coefficients on simulated horizontal cutting forces

As far as the quality of the force signal, Figure 5-16 presents the raw data and the filtered time history of cutting forces for runs 12 through 23. Based on these, it is possible to validate the statement that the cutting force is not importantly affected by the damping coefficient. This can as well be corroborated by the illustrations of the fracturing modes in all the analyzed rock-cutting cases. Figure 5-17 depicts the element damage value (with damage equal or greater than 50% in red) at a certain stage of each of the runs, where the creation of cracks and the potential formation of chips are expected once a red line (thin red zone) is propagated through the rock.

Within the damage contour plots, in general, for a crack to start at the cutter edge and propagate to the surface, thus a chip is formed and separated, there should not be a concentration red elements at the cutting face. Damaged elements at the cutter front represent elements that are being crushed before a crack is propagated forward. It is arguable that some of these cases reflect a good fracturing mode, however, the optimal simulation, in agreement with the experimental scratching tests, should develop more chips than the runs shown in Figure 5-17.

In addition, it is expected that the peak forces are more spaced apart (about the same distance as the cutting depth, i.e. 3.6 mm), because this is an indication of chip formation. Therefore, due to the magnitude of the forces, and the quality of the fragmentation process, runs 12 through 23 do not have the best model configuration to validate the experimental tests.

It is then demonstrated that a fixed boundary condition on all rock piece faces, with non-reflective characteristics works best in this rock cutting modeling. This assures that a plane strain condition (with constant behavior in the z-direction) is met.

Only front face with constrained nodes in Z-dir

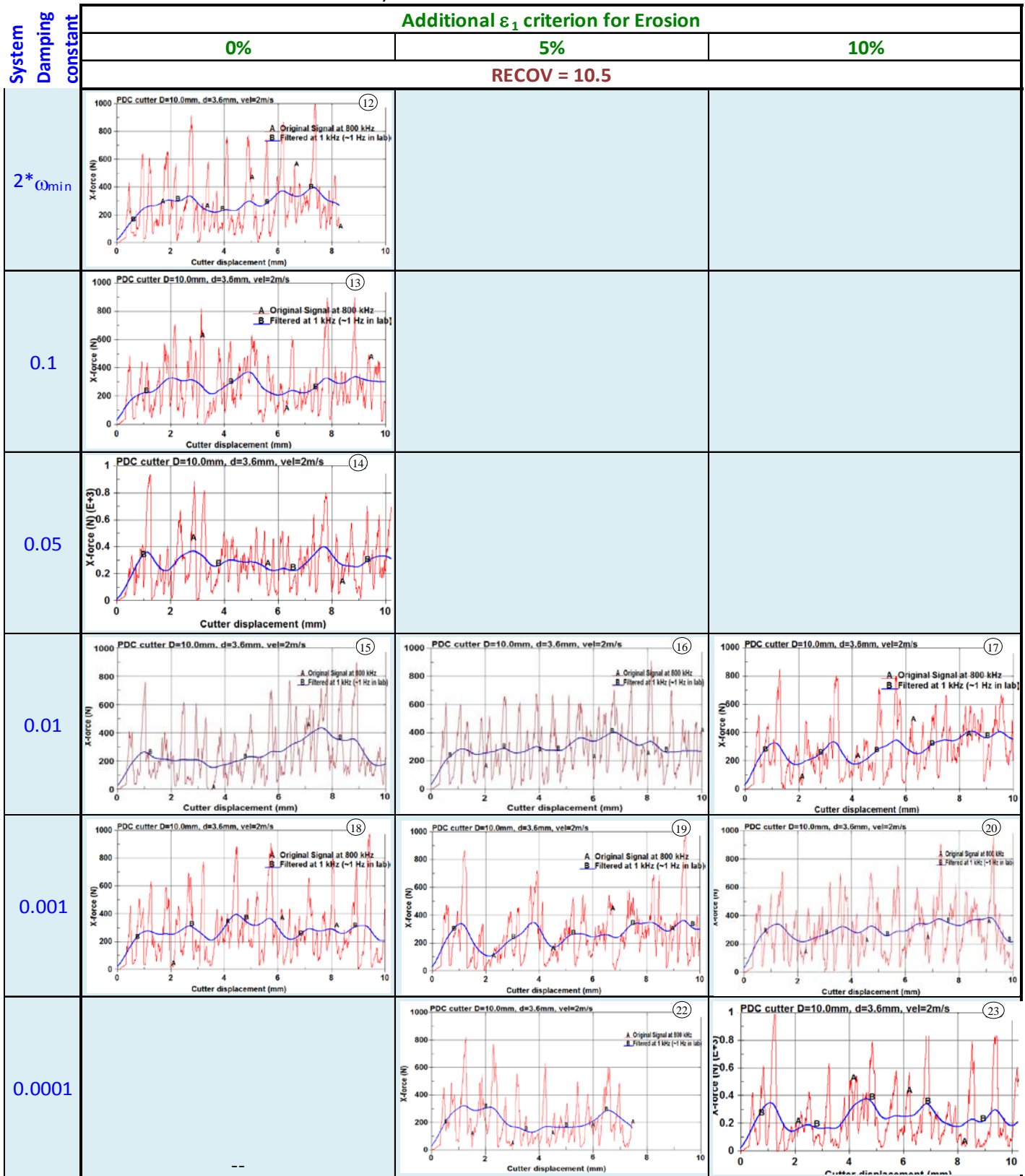


Figure 5-16: Damping sensitivity in deep-cut simulation: Force signals

Only front face with constrained nodes in Z-dir

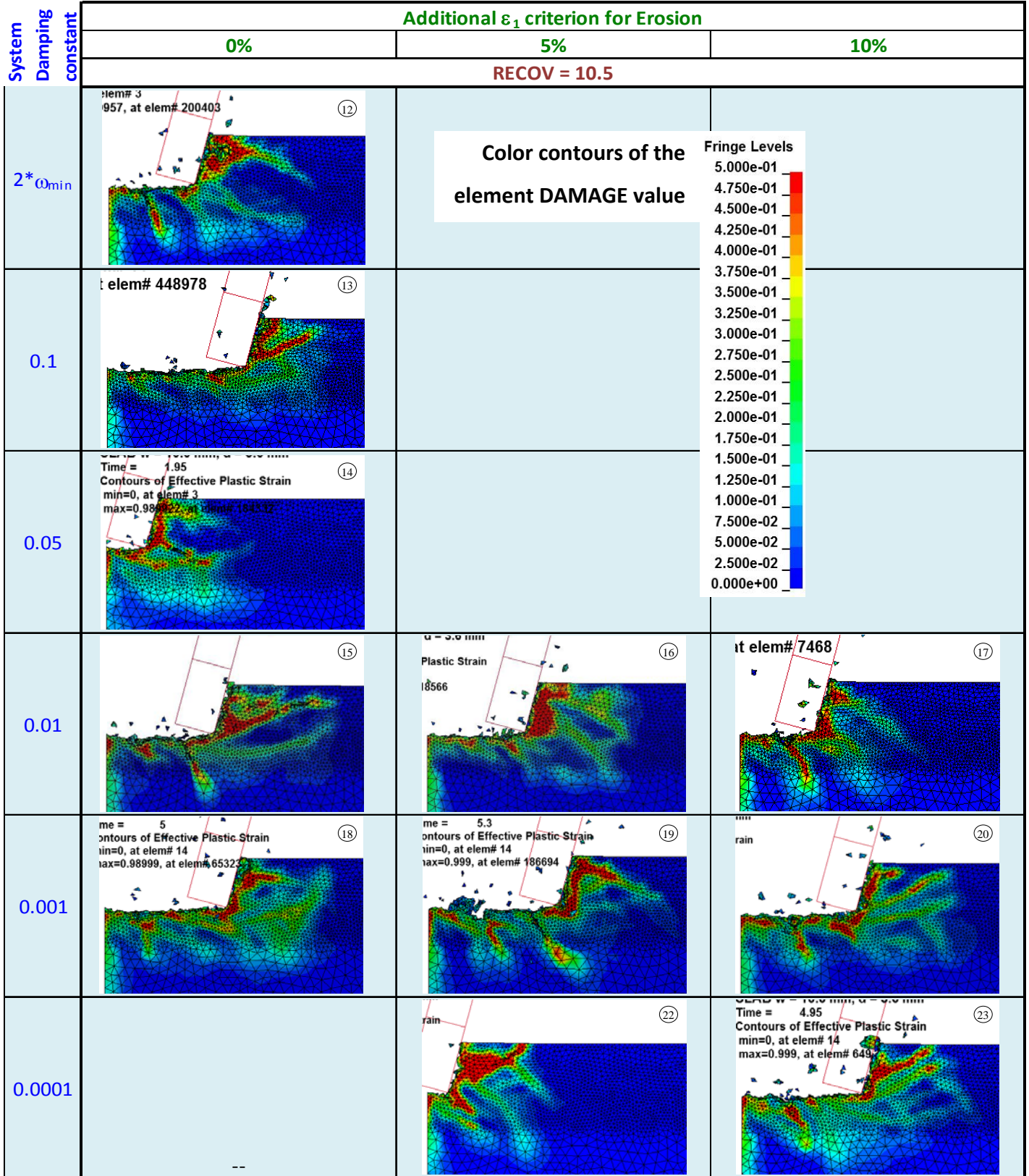


Figure 5-17: Damping sensitivity in deep-cut simulation: Chip formation

5.4.2.2 Cutting Velocity

The velocity of the cutting tool in numerical simulations is a critical feature of the model as it can drastically change the results when implementing rock materials that are strain / load rate sensitive and have a non-linear behavior. It is also important due to the transient nature of the problem, where the dynamics of the model should resemble the real physical situation.

Although there are no findings in the literature of numerical modeling of rock cutting reporting any effect of the tool velocity on the cutting forces, some researchers have accounted for the influence of the cutter velocity on numerical models of ceramic and granular material, as well as on rock specimens in the experimental setting. The observations are followed by a wide-range of conclusions; from direct proportionality to independence between the cutting velocity and forces.

Nouguier et al. (2000) checked the influence of the cutting velocity on the mean force when pushing granular material simulated with a DEM computer code. At a high velocity –i.e. 0.5 m/s, as compared to 0.02 m/s– they observed a dynamic regime where the granular material intermittently got loose from the tool, a fact revealed by the force vanishing at some moments. They also observed that when increasing the cutting velocity, a certain fluidization of the free surface manifested by its larger void ratio. Their simulation results led them to conclude that the mean force increases quadratically with the cutting velocity.

Furthermore, El-Wardany et al. (2009)) simulated the process of green machining fragile ceramic compacts with FEM modeling. They state that the “hydrostatic pressure in the workpiece is mainly controlled by speed and tooltip radius. The increase in the hydrostatic pressure reduces the [detrimental] crack initiation, which indicates that higher speed and lower tooltip radius are recommended” for this manufacturing process.

In contrast, as far as experimental rock cutting, Germy et al. (2009) indicate that the forces on single cutter tests depend on the depth of cut but not on the cutting velocity, at least in the range suitable to field conditions. They also describe steady-state kinematically controlled experiments of rock drilling with bit forces depending on the rate of penetration and on the bit angular velocity, only through their ratio, i.e., on the depth of cut, which suggests that the force is rate-independent.

This study includes the sensitivity analysis of the cutter force to the cutting velocity, by varying its value as listed in Table 5-6. As a quantitative measure of the simulation results, the average peak force from all the cases has been compiled in Table 5-7 (see Section 5.4.1 for details on the force averaging method). In contrast to the findings described in the previous section, and due to the fragmentation mode observed, only the models in the sub-group of “All surface nodes constrained in the Z-direction” with an ERODE value of 1.05 are displayed in this section and used to draw the conclusions on the effect of the velocity on the horizontal cutting force.

As shown in Figure 5-18, with the exception of run 8B, there is a clear trend of the mean force increasing with the magnitude of the cutting velocity. Although run 8B presents a lower mean force, this can be the result of the lack of simulation time (fewer data), and in reality, this particular case could have a larger value of force reflected by the time history illustrated in Figure 5-19. It can be seen in this figure that with larger velocity, the peaks of the forces are more spaced apart. It also shows that the forces tend to drop lower after peaks when the velocity is higher. This fact validates the statement of Nougquier et al. (2000) mentioned above regarding the loss of contact between the material being cut and the tool, and that the force is proportional to the velocity.

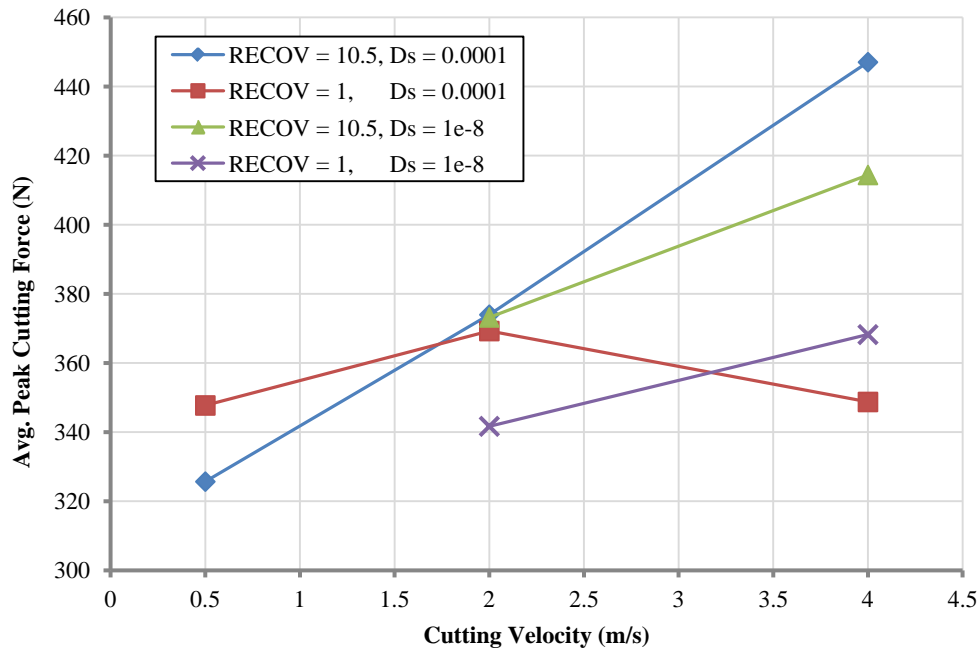


Figure 5-18: Effect of cutting velocity on horizontal cutting forces from deep-cut simulation

All surface nodes constrained in Z-dir

Additional ϵ_1 criterion for Erosion = 5%

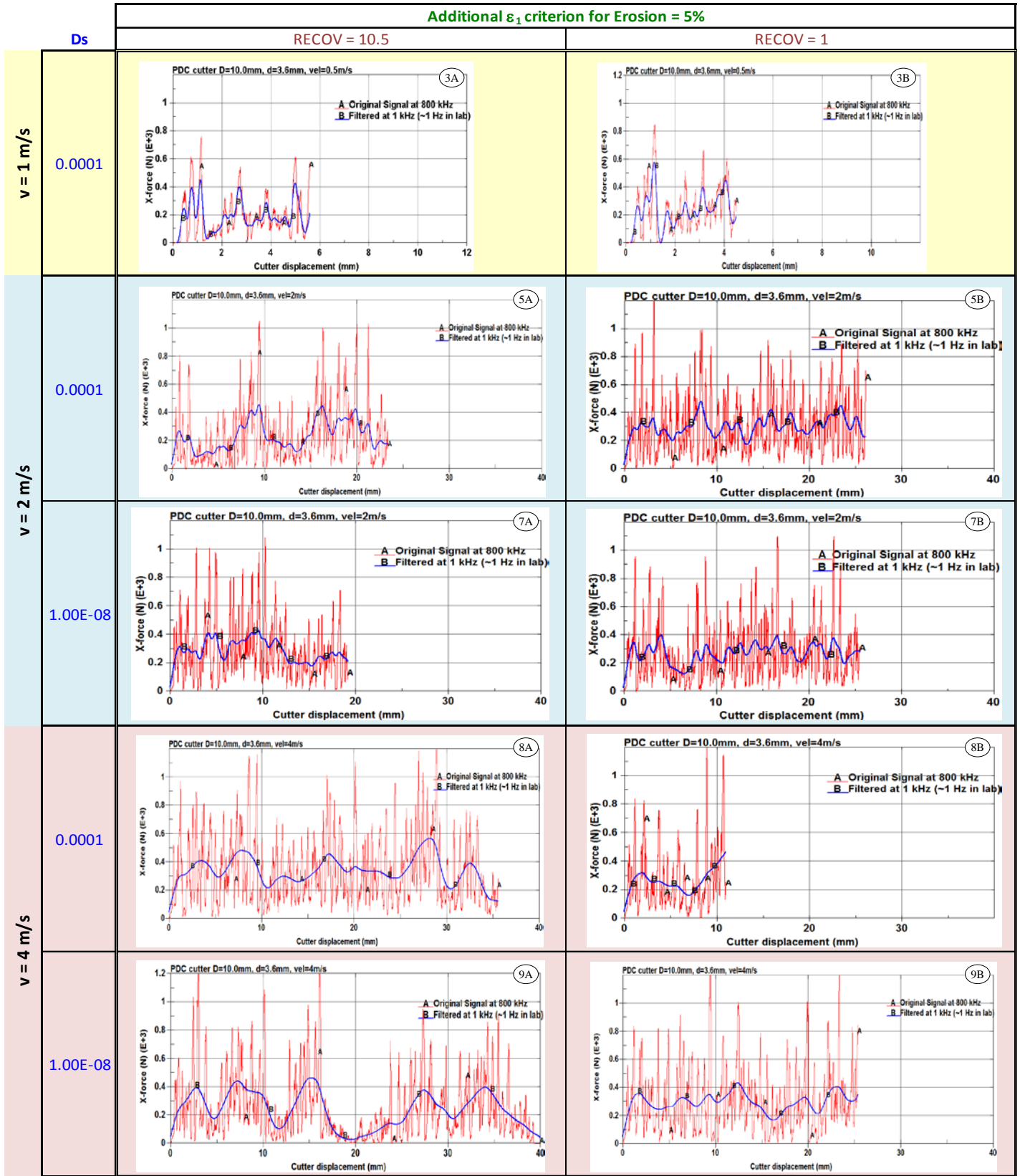


Figure 5-19: Cutting velocity and RECOV sensitivity in deep-cut simulation: Force signals

All surface nodes constrained in Z-dir

Additional ϵ_1 criterion for Erosion = 5%

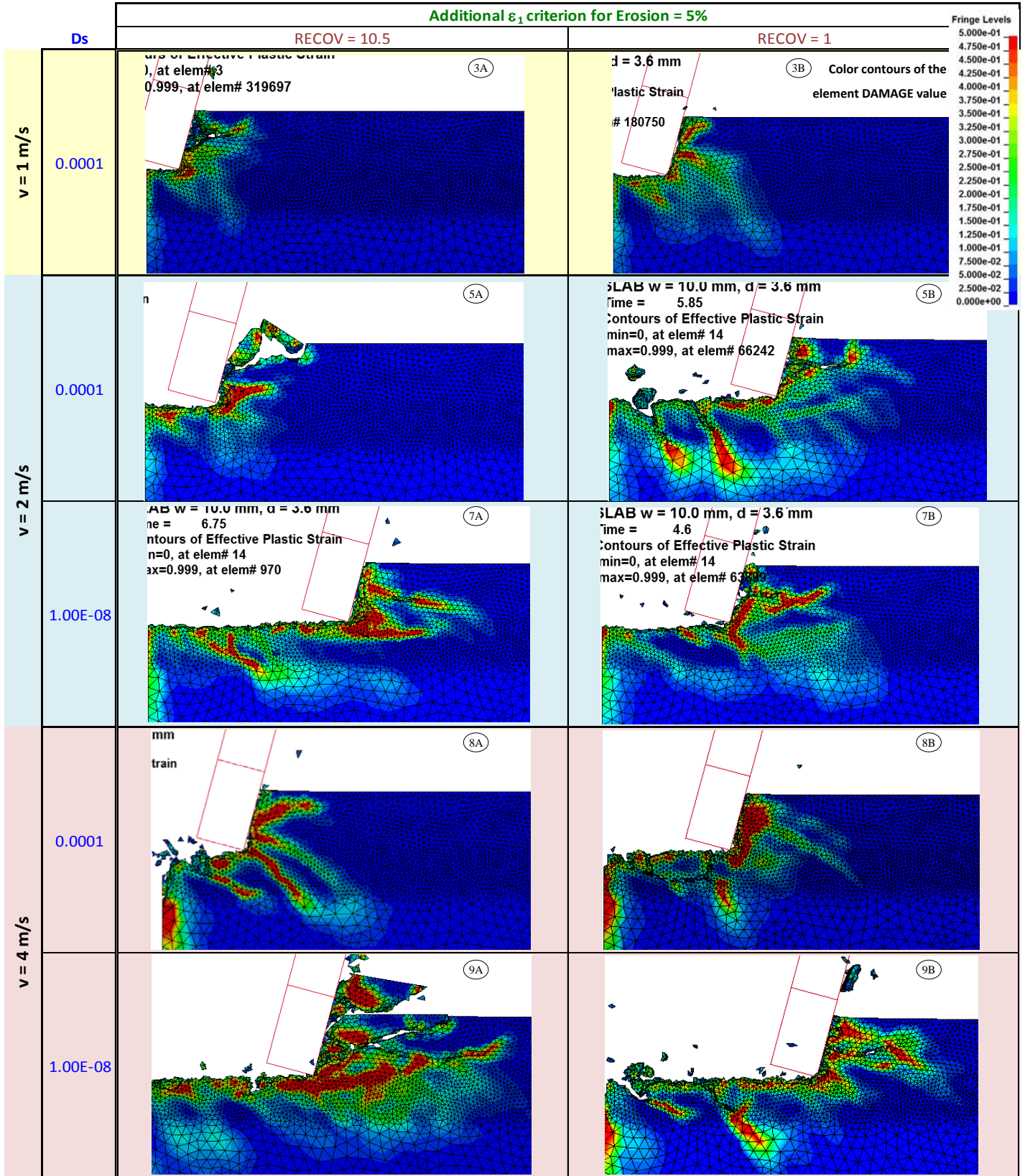


Figure 5-20: Cutting velocity and RECOV sensitivity in deep-cut simulation: Chip formation

On the other hand, although the deep-cut simulation results seem to contradict the claim made by Germy et al. (2009) regarding the independence of the cutting force from the velocity, Figure 5-21 shows that there is indeed a point where the horizontal cutting force converges to a value and is not affected by larger velocities. The simulation results plotted in Figure 5-21 belong to the velocity sensitivity analysis performed at a shallow depth of cut, i.e. 0.3 mm (0.012 in) on a 10-mm (0.4 in) wide rock slab.

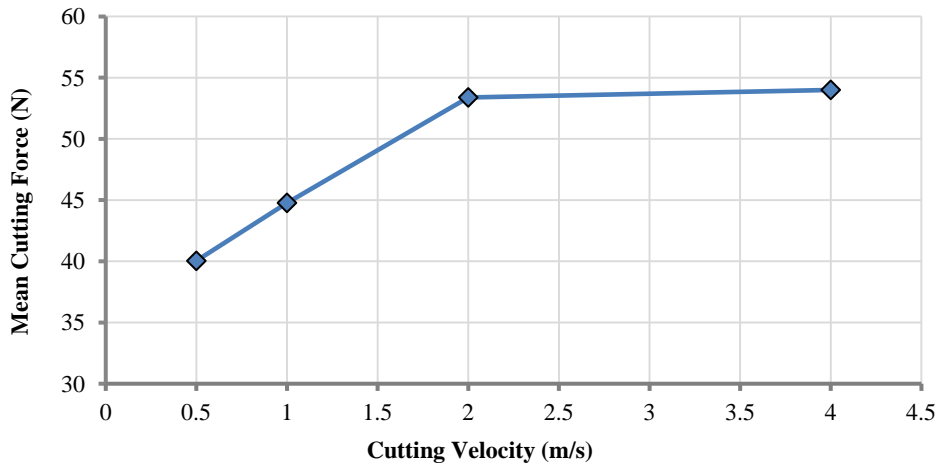


Figure 5-21: Effect of cutting velocity on horizontal cutting forces from shallow-cut simulation

Obtaining a relatively constant force after the 2 m/s (6.6 ft/s) velocity in the shallow-cut scenario led the author to choose the velocity of 4 m/s (13.1 ft/s) as the appropriate value to carry out all the rock cutting simulations that wanted to be compared with experimental scratching tests at an actual speed of 4 mm/s (0.16 in/s). In addition to the good results obtained at this cutting speed, there is a tremendous benefit as far as computational time.

This selection is supported also by the quality of the force signals in the deep and shallow cut simulations (see Figure 5-19 and Figure 5-22 respectively), and moreover by the fragmentation process revealed by the cases run at 4 m/s (13.1 ft/s). It can be appreciated in Figure 5-20 how the crack propagation and eventual chip formation is more predominant amongst the runs with the largest velocity, especially those with the lowest value of the system damping parameter (i.e. $D_s = 1 \times 10^{-8} \text{ ms}^{-1}$).

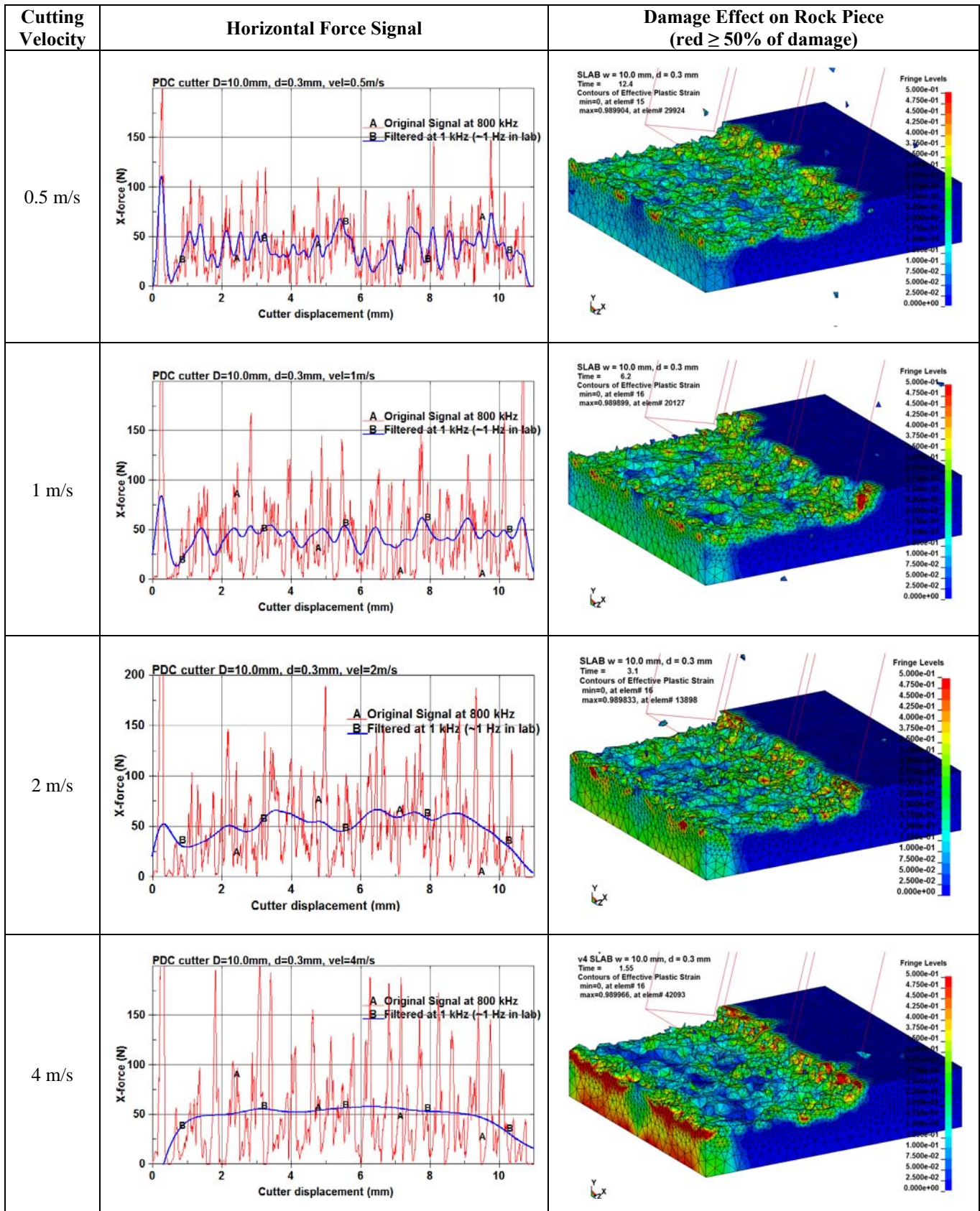


Figure 5-22: Cutting velocity sensitivity in shallow-cut simulations

5.4.2.3 Damage Recovery

Parameter RECOV is thought to be a determinant characteristic of Mat_159 material model, because it is responsible of tracking the damage parameters and controlling their behavior. Due to the nature of the material model implemented for this research, this feature has significant implications as shown below.

As part of Mat_159's formulation, and as explained in the *User's Manual for LS-DYNA Concrete Material Model 159* (Murray 2007b), the damage parameters in Equation (3-50) and (3-51) are tracked as follows:

- a) The ductile damage parameter, $D(\tau_c)$ increases in value whenever the ductile damage formulation is active (i.e., when pressure is compressive) and τ_c exceeds the current damage threshold. The value of the ductile damage never decreases, even temporarily.
- b) The brittle damage parameter, $D(\tau_t)$ increases in value whenever the brittle damage formulation is active (i.e., when pressure is tensile) and τ_t exceeds the current damage threshold. When inactive, $D(\tau_t)$ is temporarily set equal to zero in order to *model stiffness recovery with crack closing*. In other words, brittle damage drops to zero (i.e., stiffness is recovered) when the pressure switches from tensile to compressive. The maximum value of $D(\tau_t)$ is recovered when the brittle formulation becomes active again.

The input parameter RECOV is user-specified to control the stiffness recovery. Is it by default zero, which means that 100% of stiffness and strength is recovered when pressure becomes compressive. A value of 1 would provide no recovery of stiffness and strength; hence, brittle damage remains at its maximum level. Partial recovery is modeled for values of RECOV between 0 and 1. Its implementation considers one of the following two optional conditions:

- c) Input value between 0 and 1. A recovery percentage –corresponding to the RECOV value– is based upon the sign of the pressure invariant only (compressive to be active), thus RECOV works according to criteria a) or b) above.
- d) Input value between 10 and 11. A recovery percentage –corresponding to $\text{RECOV} = \text{RECOV} - 10$ – is based upon the sign of both the pressure and volumetric strain (compressive to be active). A flag is set to request the volumetric strain check.

Equation (5-32) and Figure 5-23 describe how RECOV controls the moduli behavior:

$$D(\tau_t) = \text{RECOV} \cdot D(\tau_t) \quad (5-32)$$

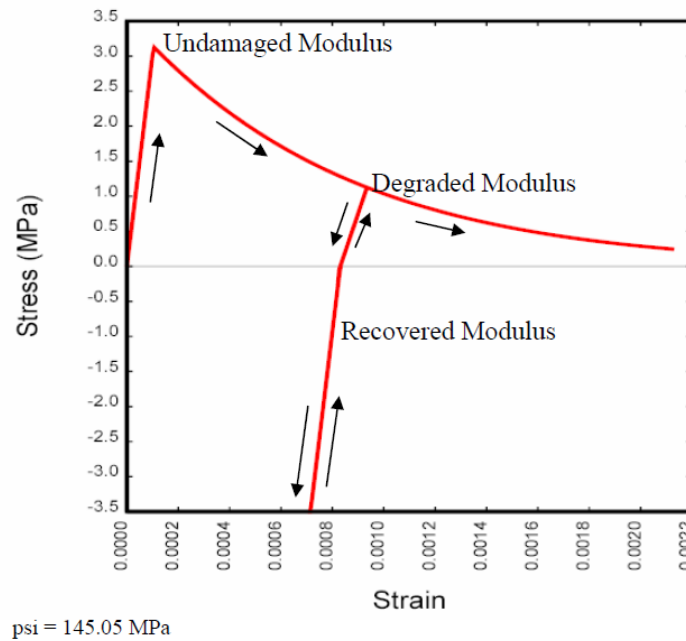


Figure 5-23: Modulus degradation with strength -example for concrete under cyclic loading (Murray 2007a)

During the beginning stages of this parametric study, it was intuitively thought that in order to simulate a clear generation of cracks and subsequent rock chips while cutting, it was necessary to maintain the brittle damage condition at its maximum, thus $\text{RECOV} = 1$ and consequently the stiffness was not recovered. However, this configuration of the model did not yield the best results, as compared to other values of RECOV . Figure 5-24 through Figure 5-29 depict the outcome of 6 simulations upon the variation of the RECOV value as 0, 0.5, 1, 10, 10.5, and 11 respectively. This group of runs corresponds to a limited rock size version of the 3.6-mm (0.142-in) deep cut, at a speed of 0.5 m/s. Each of the Figure 5-24 through Figure 5-29 contains a sequence of cutting illustrations at 3 different fixed times of the simulation, such as 0.4 ms, 2.8 ms, and 13.8 ms, as well as the time history of horizontal cutting force. It is important to note that the quality of the force signals is not the best, as the material model used herein was not completely calibrated at that moment. However, these runs serve as a means to **visualize** the influence of the RECOV parameter. Although not completely evident from this graphic record, the most appropriate fragmentation mode was provided by the case with $\text{RECOV} = 10.5$.

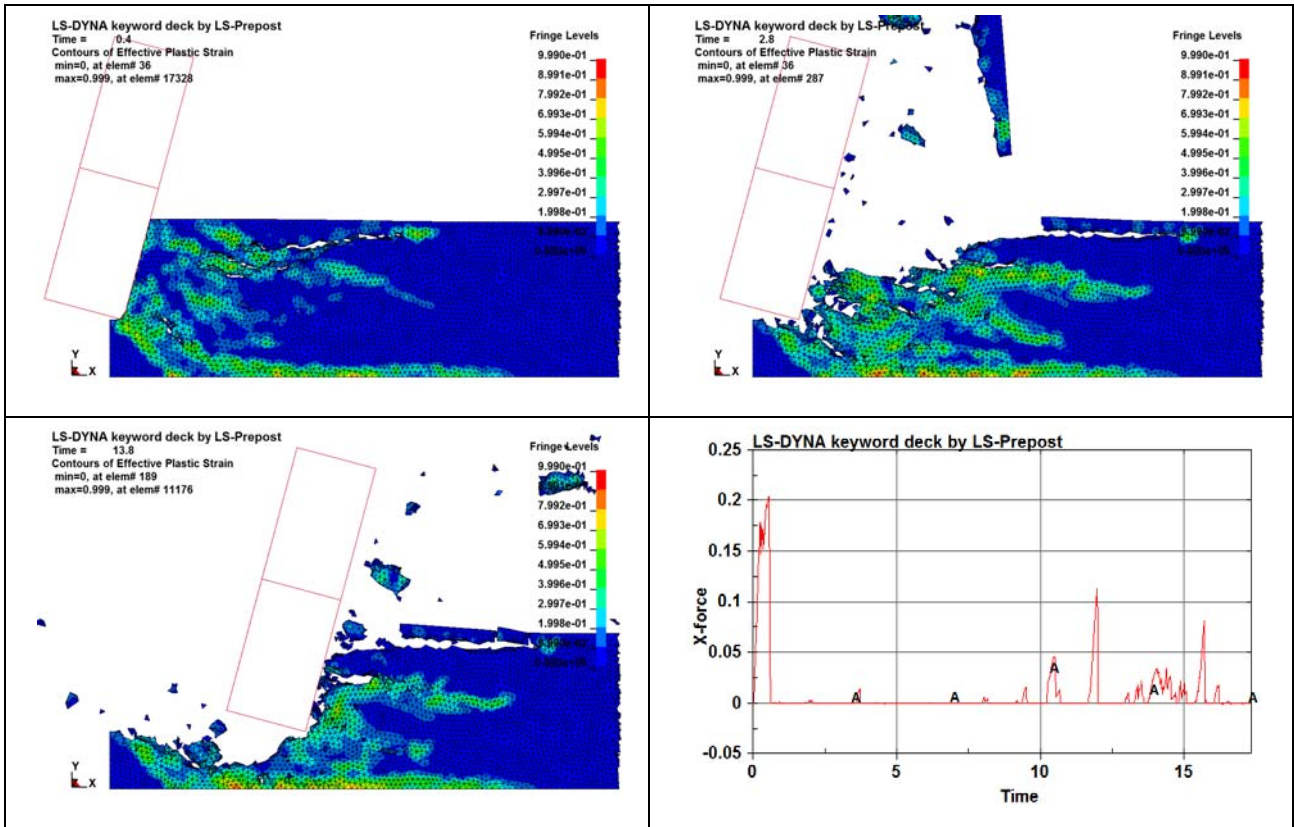


Figure 5-24: Preliminary simulation of 3.6-mm deep rock cut with RECOV = 0

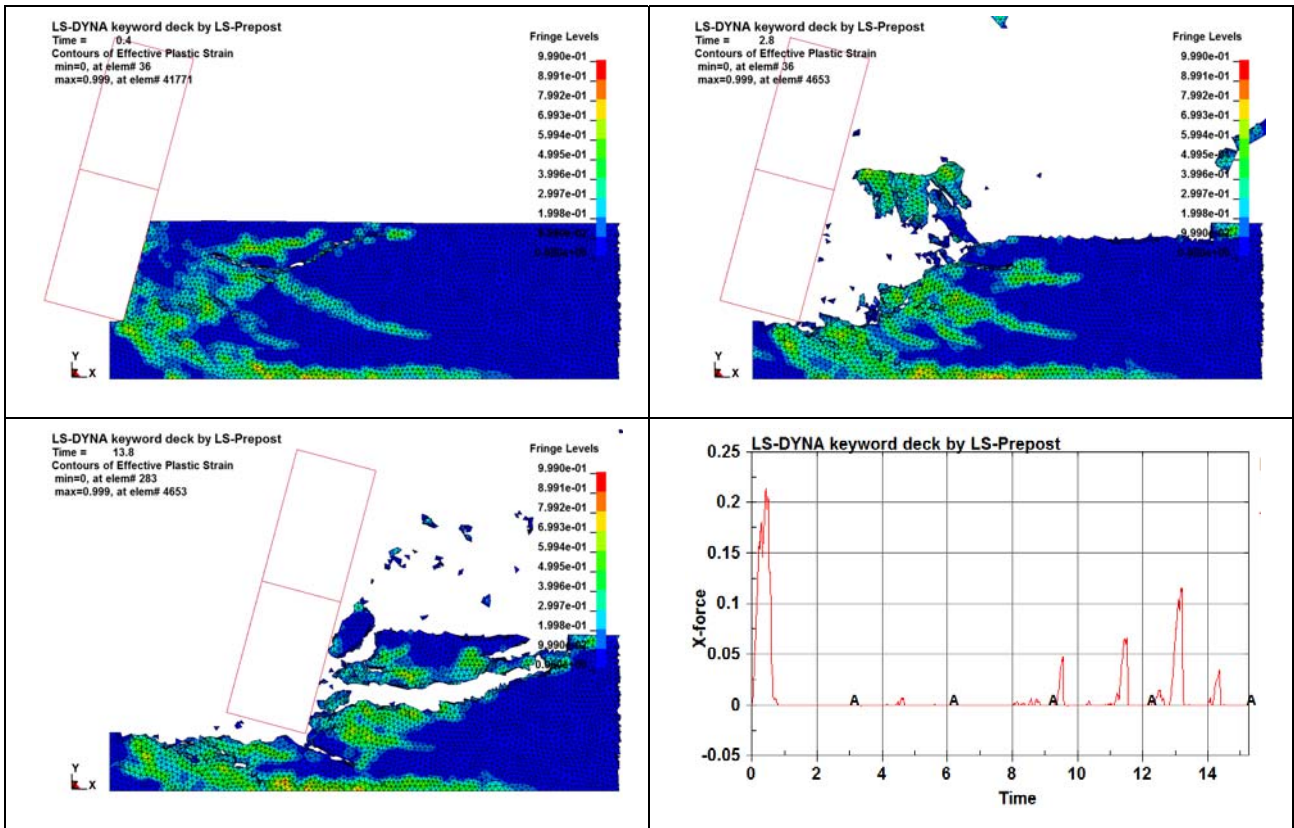


Figure 5-25: Preliminary simulation of 3.6-mm deep rock cut with RECOV = 0.5

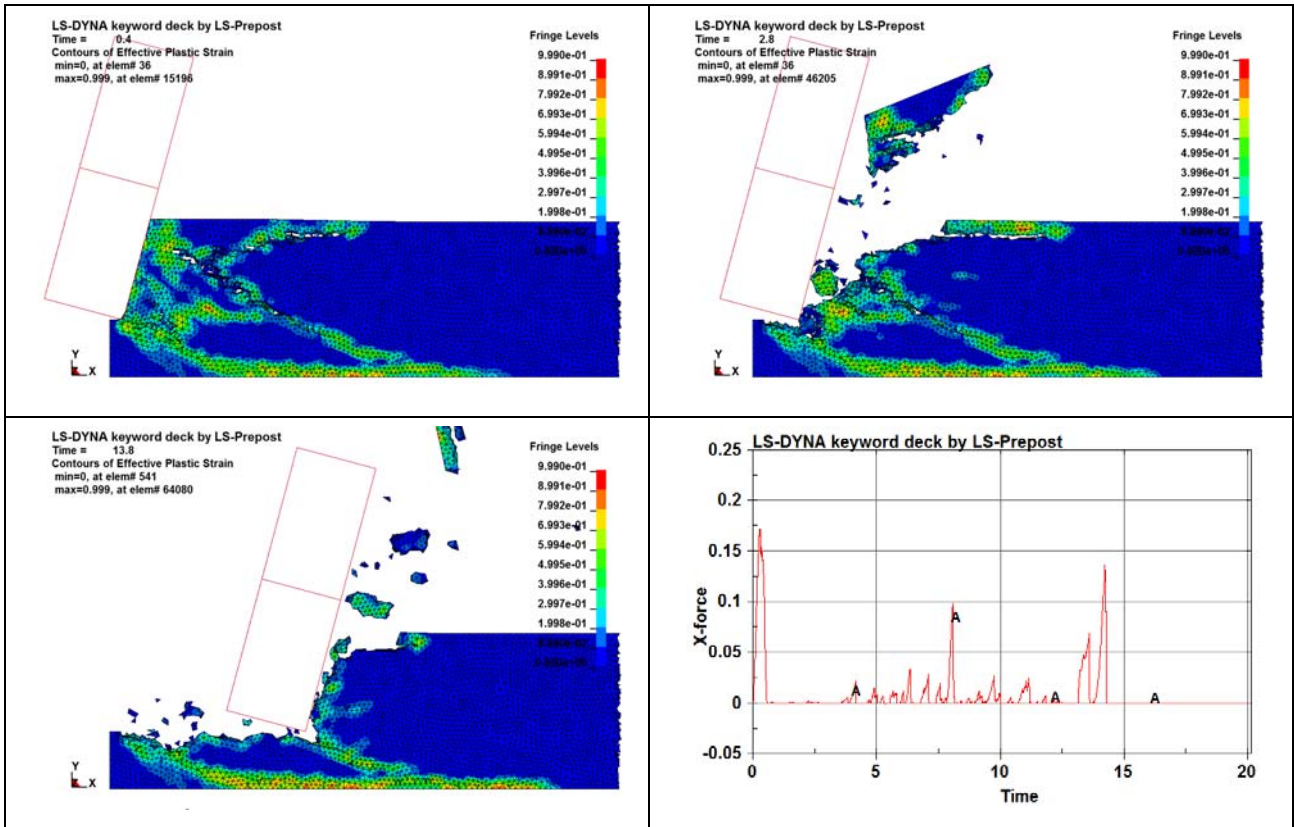


Figure 5-26: Preliminary simulation of 3.6-mm deep rock cut with RECOV = 1

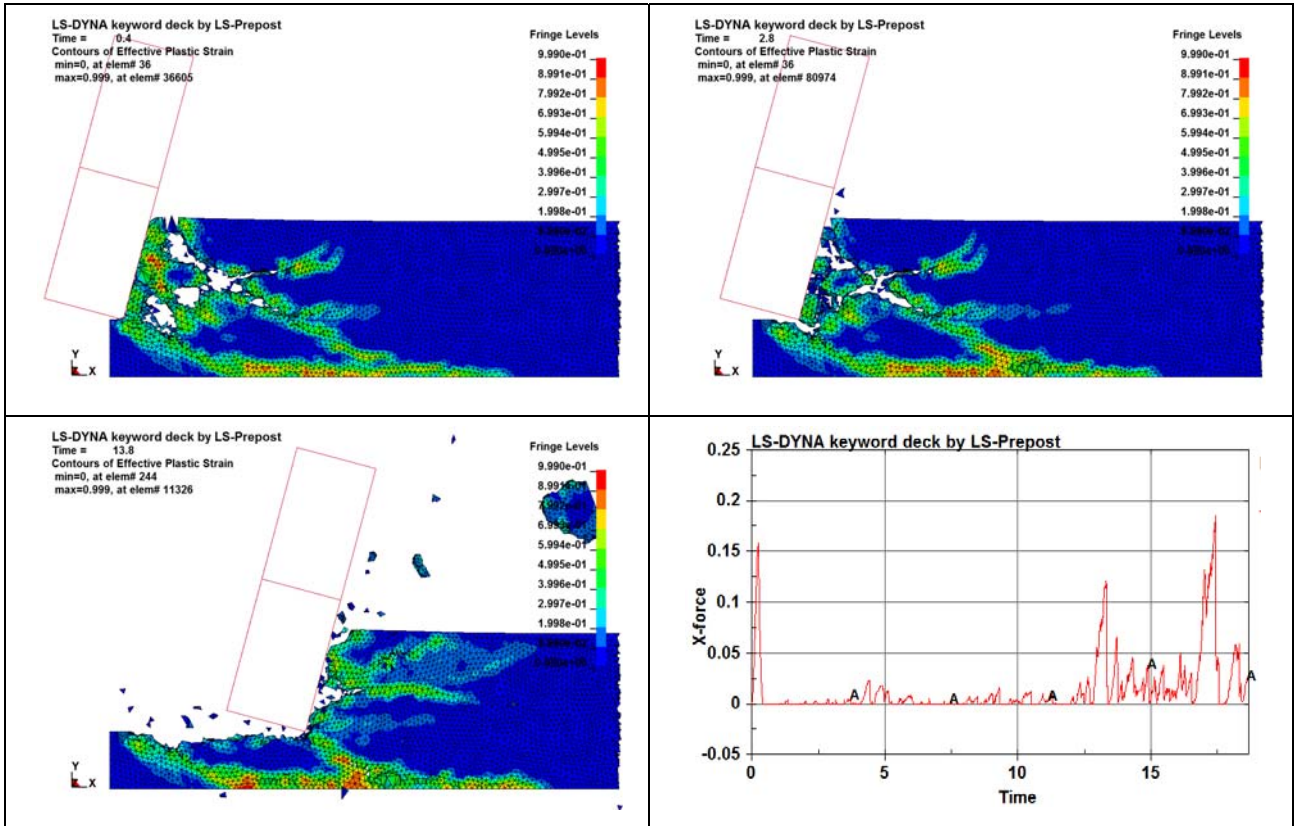


Figure 5-27: Preliminary simulation of 3.6-mm deep rock cut with RECOV = 10

Theoretically in the case of $RECOV = 10.5$, the rock recovers half of its stiffness modulus and strength once its elements are damaged to some degree (less than 99%, otherwise elements are eroded) through tension and subsequently compressed. This imitates the process of an almost-developed crack which is compressed back and still provides some strength upon loading.

With the material model fully calibrated, runs denominated with letters A and B in Table 5-6 were intended to reveal the influence of the $RECOV$ parameter with values 10.5 and 1. Figure 5-18 not only shows the effect of the cutting velocity on the mean force of each run, but it also exposes the effect of $RECOV$ on the cutting force. For runs with $D_s = 1 \times 10^{-8} \text{ ms}^{-1}$, there is a marked tendency of getting larger mean values of force with $RECOV = 10.5$.

As a matter of fact, simulation 9A –with additional erosion criterion $\varepsilon_1 = 5\%$, cutting velocity of 4 m/s (13.1 ft/s), system damping coefficient $D_s = 1 \times 10^{-8} \text{ ms}^{-1}$, and $RECOV = 10.5$ – results in the closest value of mean peak horizontal force to the experimental results by Richard (1999). For the deep-cut scratch test in Vosges Sandstone, the simulated mean peak force of 414.41 N (93.16 lbf) compares very well with the reported experimental force of 400 N (30.0 lbf).

In addition to the quantitative validation obtained, Figure 5-19 and Figure 5-20 present the force signals and fracturing process images, respectively, for rock cutting cases at different velocities, with a couple of different damping coefficients, and additionally, the two columns in each figure compare the variation in $RECOV$ value, from 10.5 to 1. Evidently run 9A exhibits the best quality in force signal and fragmentation mode output. This is shown in detail in Section 6.1.

Due to the successful validation through the different aspects described in this and former sub-sections, the configuration of run 9A is selected as the baseline for future simulations of rock cutting in LS-DINA –as mentioned in page 123.

6.0 NUMERICAL SIMULATION OF CUTTING ON ROCK SLABS

This chapter presents the numerical simulation of the scratch tests performed by Richard (1999). Not only the models resemble the rock fragmentation seen in the laboratory, but the resulting cutting forces can be successfully validated by comparing with the experimental measurements. The rock material simulated herein corresponds to Vosges sandstone modeled with Mat_159, following all the considerations explained in Section 3.2.4 and Chapter 5.0. The same rock slab model is used to simulate scratching tests at a depth of 0.3, 0.6, 0.8, 1.0, 1.4, 2.0, and 3.6 mm (0.012, 0.024, 0.031, 0.04, 0.055, 0.079 and 0.14 in).

Sections 6.2.1 and 6.2.2 illustrate in detail a time series of the simulation of deep cut (i.e. 3.6 mm) and shallow cut (i.e. 0.3 mm) tests, respectively, in par with pictures of the laboratory tests on Berea Sandstone. This remarkable achievement helps verify the robustness of the numerical models developed. The last section in this chapter provides a quantitative assessment of the model by comparing the obtained specific energy from the simulations and from the experiments.

6.1 MODEL GEOMETRY

6.1.1 Rock Specimen Geometry

The level of damage experienced in the shallow cut –less than 1.5 mm in depth– remains very close to the surface, so practically, the numerical rock mesh could be limited to a thickness of only 10 times the cutting depth to guarantee no boundary influence over the element stresses in the cut zone. Nevertheless, the deep-cut model imposes a great challenge associated with the large number of elements and the need to maintain element sizes as small as the actual particle

sizes in these sandstones, throughout the area where the fragmentation takes place. Figure 6-1 shows the geometry of the numerical domain used for all the slab cut simulations regardless of the depth of cut. Only half of the actual slab thickness is modeled in order to save on computational time; however, the cutting forces reported are adequately proportioned to the full thickness. A fine mesh with average element size of 0.18 mm (0.007 in) forms the top of the sample, while a coarse mesh with average element size of 1.1 mm (0.04 in) is distributed throughout the rest of the rock piece. The total number of nodes is 81,276 and total number of elements is 454,870.

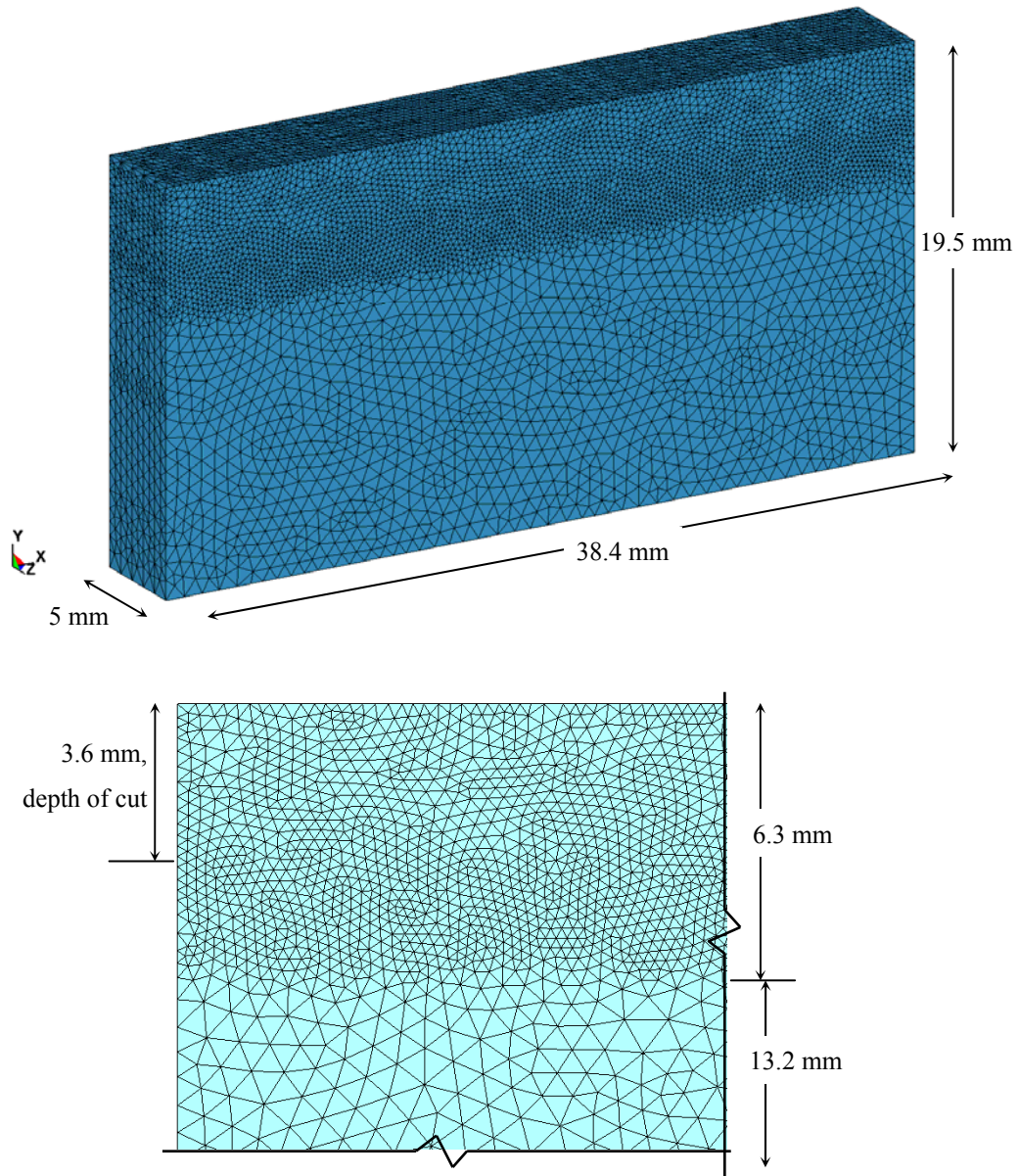


Figure 6-1: Rock model geometry for slab cuts

6.1.2 Cutter Geometry

Since the contact model implemented between the cutter and the rock is RIGIDWALL (see Section 5.2.1.2), as its name implies, the cutter is characterized by rigid body. This simplifies the model of the cutter as there is no need for element discretization throughout its volume, but instead, a simple 1-solid- element body is all takes to simulate the PDC cutter.

The only dimension requiring a specific definition is the width of the cutter. It has to be greater than the rock slab width to guarantee full contact along the cutting front. The other dimensions of the cutter are selected arbitrarily. Figure 6-4 shows the geometry of the cutter model used for all the slab cut simulations regardless of the depth of cut. It is tilted 15 degrees forward (negative rake angle), such as the experimental configuration. Only half of the actual slab thickness is modeled in order to save on computational time; however, the cutting forces reported have been adequately proportioned to the full thickness.

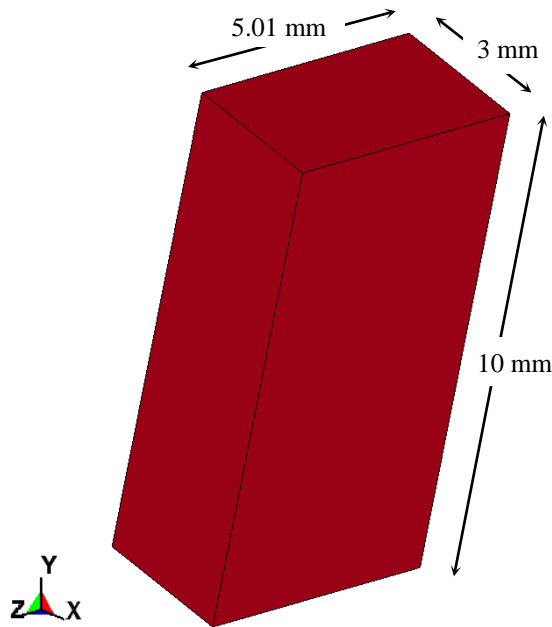


Figure 6-2: Cutter geometry for slab cuts

6.2 SIMULATION OUTPUT

6.2.1 Deep Cut Simulation Output

First, Figure 6-3 depicts the horizontal force signal –original and filtered– from the simulation of cutting Vosges Sandstone at a depth of 3.6 mm. On this plot, selected stages of the simulation are indicated with small red letters in parenthesis. This sequence of stages is presented in Table 6-1. The selected images correspond to various instances of the rock experiencing different loading conditions over time. A brief account of the potential mechanisms found at each stage is described in Table 6-1. The color contours seen throughout the rock model correspond to the maximum element damage, with red being equal or larger than 50% and blue equal to zero. Elements are eroded once the element damage value is greater than 99%.

Moreover, a good comparison of the simulated horizontal force history and magnitude with that measured in the laboratory can be appreciated in Section 5.4.1.2.

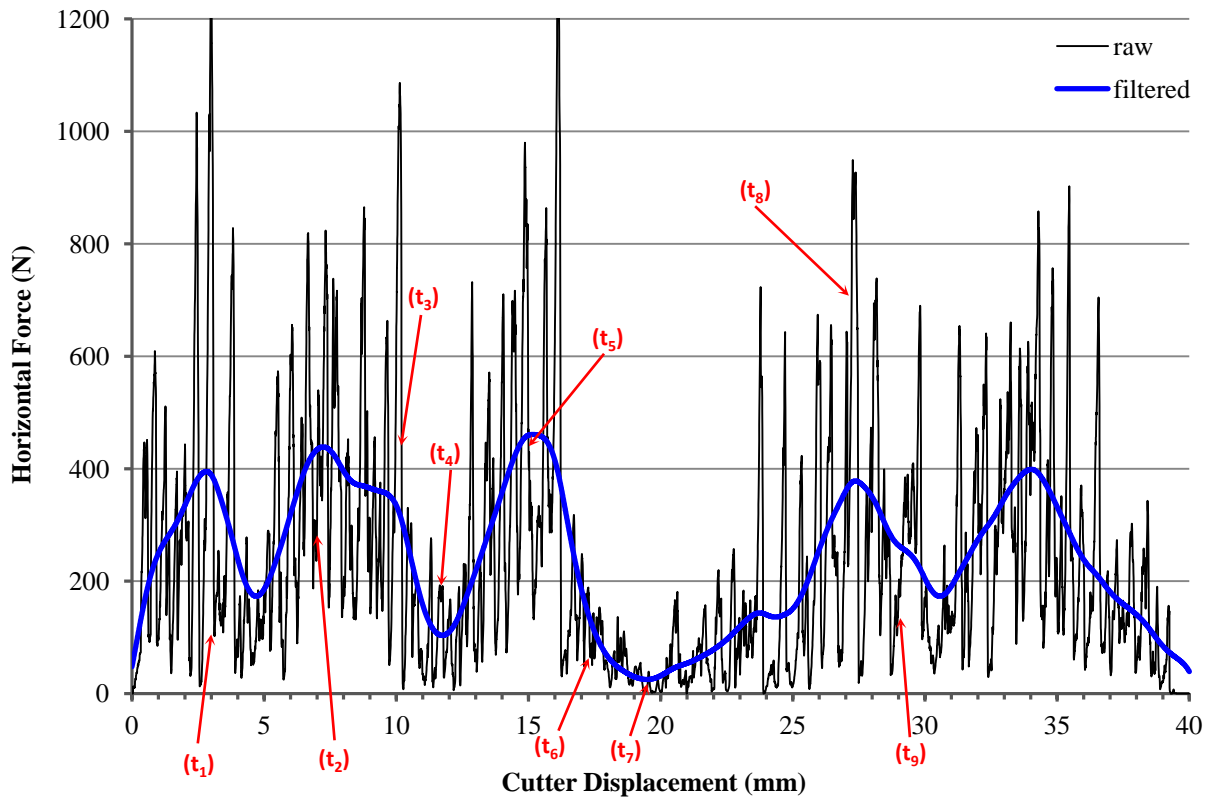


Figure 6-3: Horizontal force during simulation of Vosges Sandstone cutting (3.6-mm deep)

Table 6-1: Simulated cutting sequence on Vosges Sandstone at a depth of 3.6 mm (damage contours)

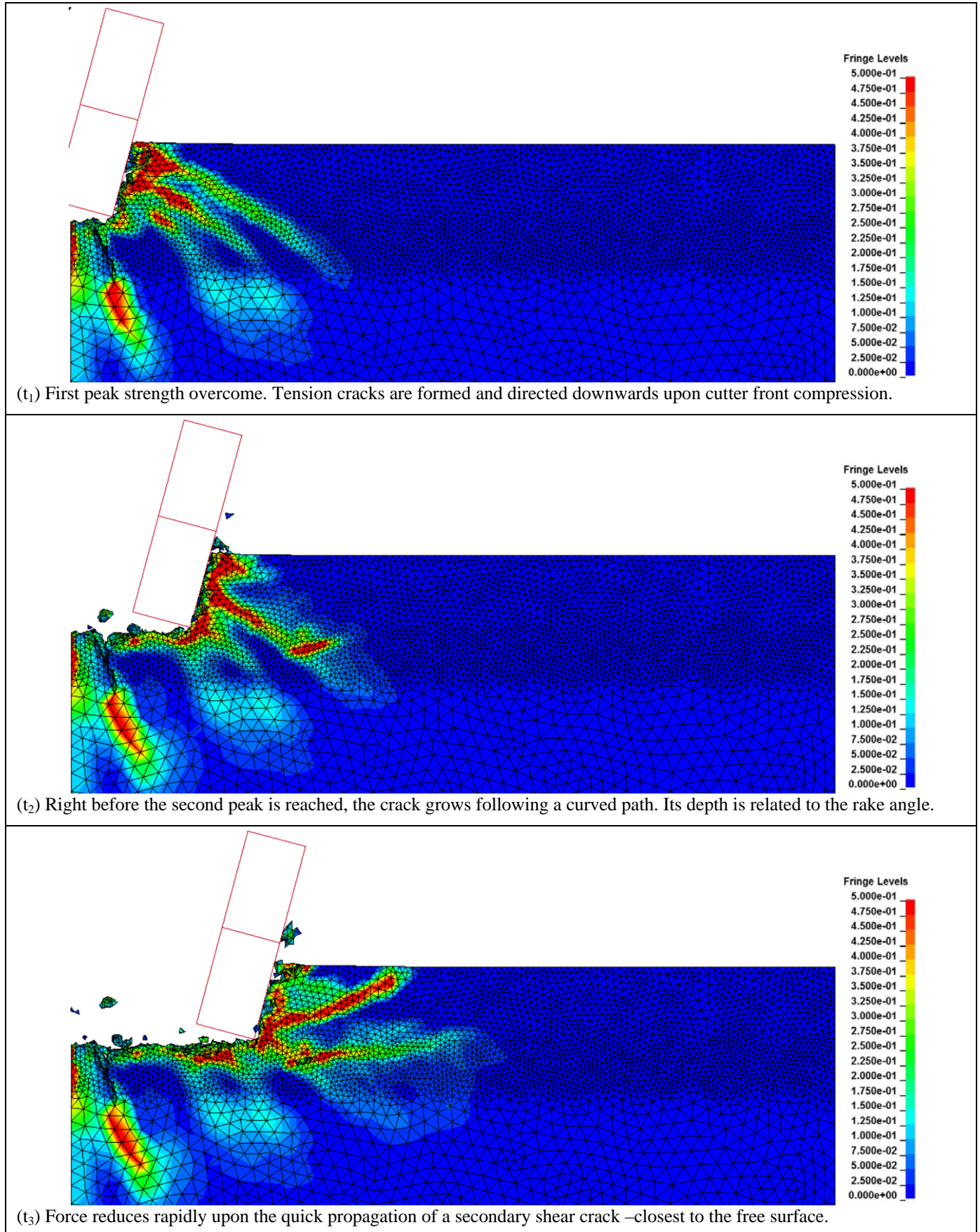
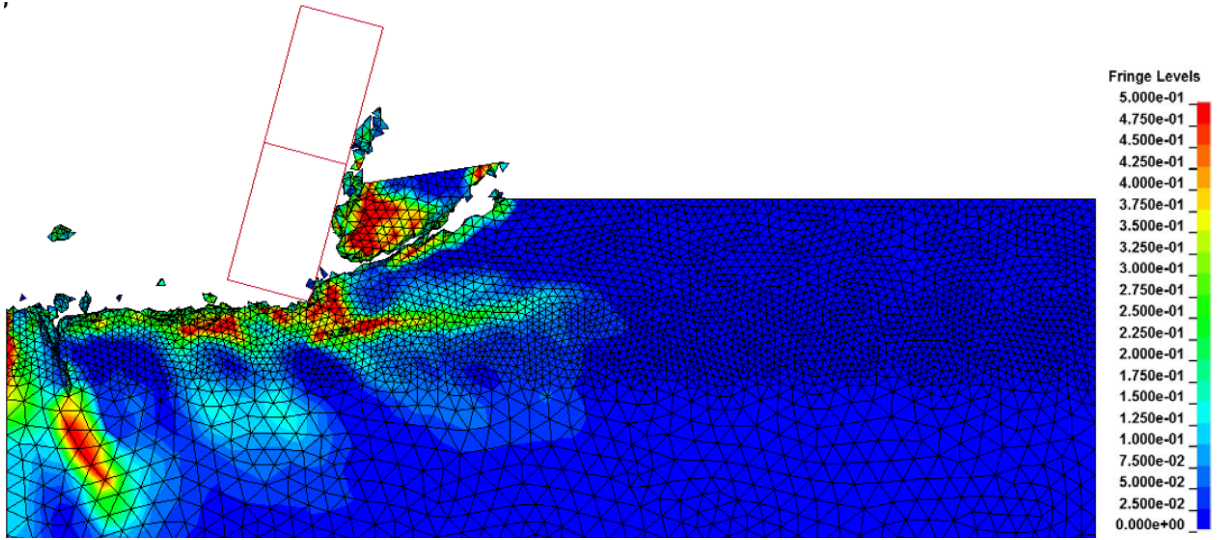
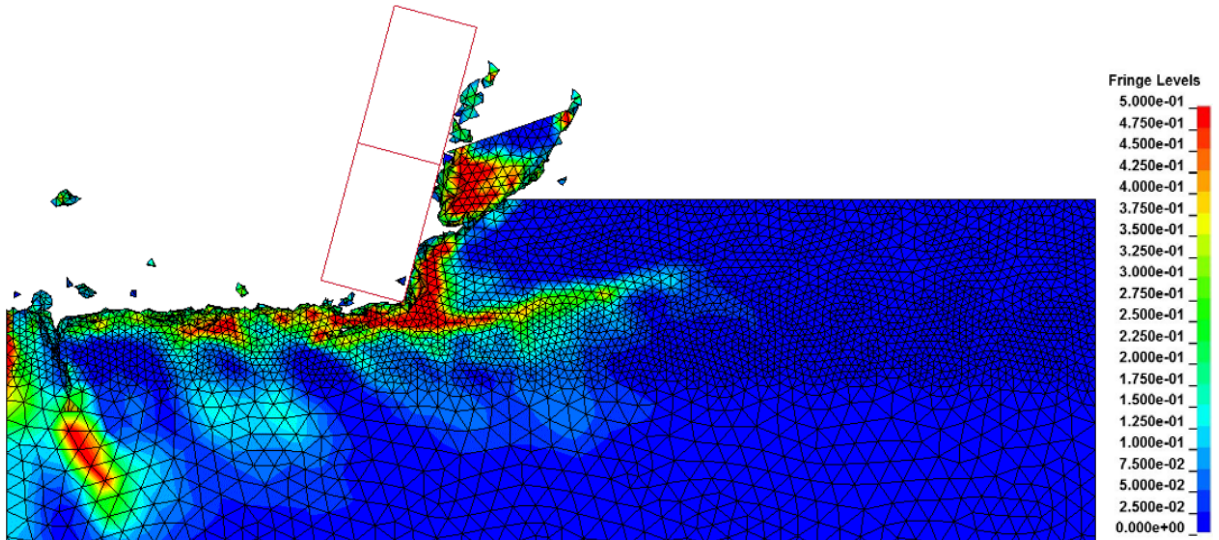


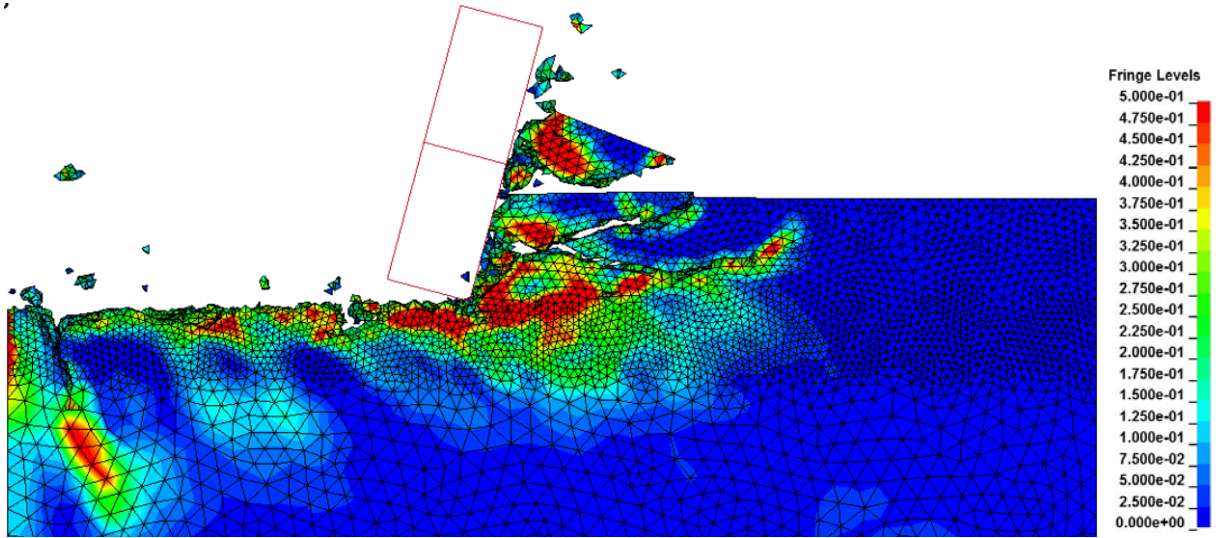
Table 6-1 (continued)



(t₄) First rock fragment separates and cutting face area in contact with cutter is reduces significantly; so does the force.

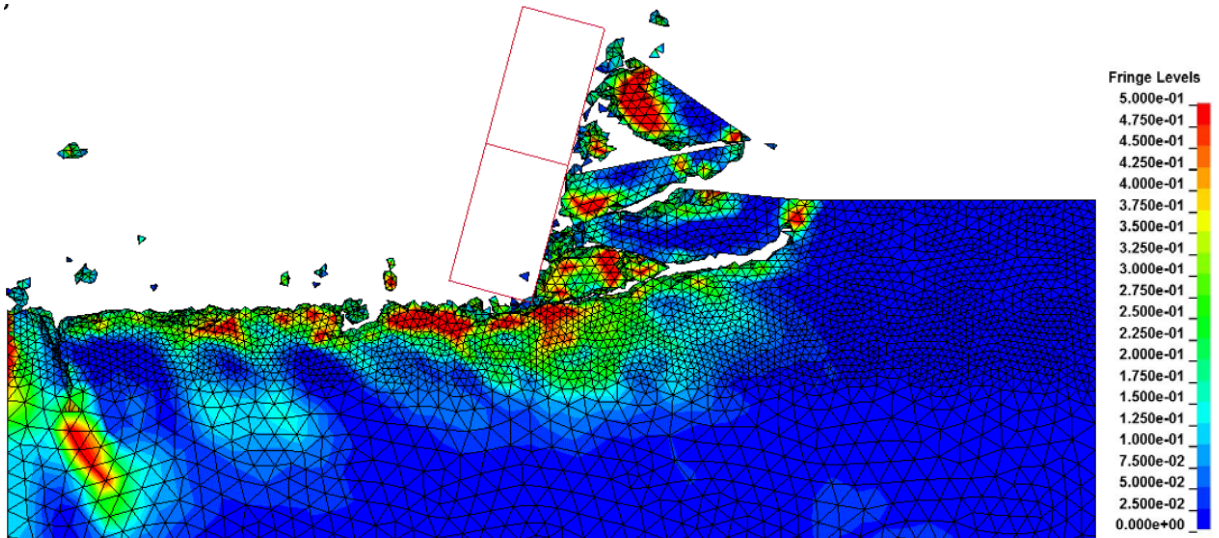


(t₅) Force accumulates again and reaches a maximum while crushing some front material. Tension at the tip creates new crack.

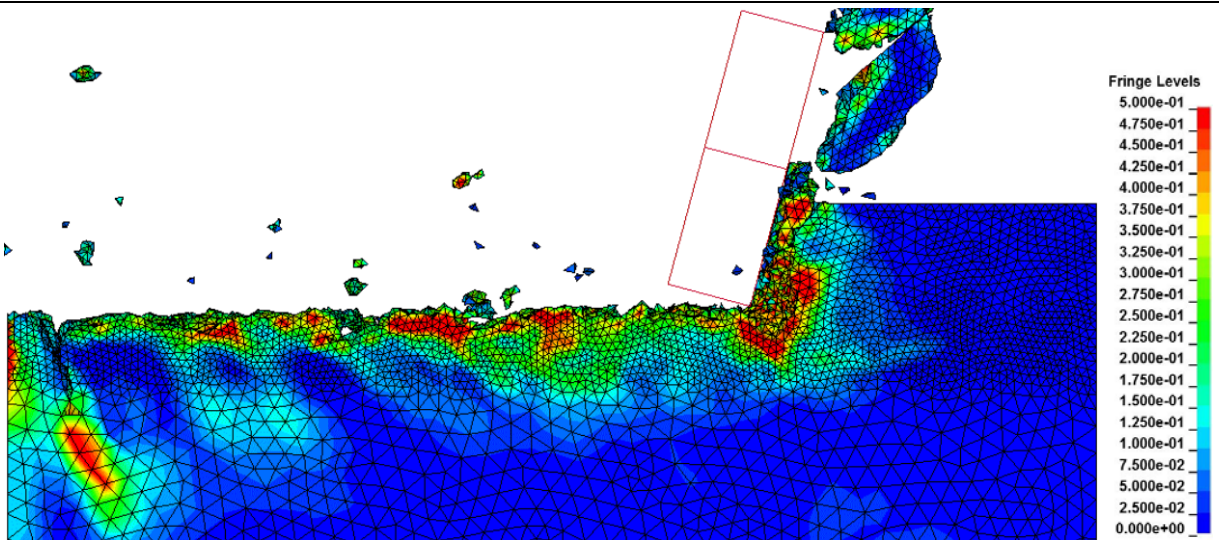


(t₆) Multiple interconnected tension cracks initiate upon the large stress concentration after (t₅).

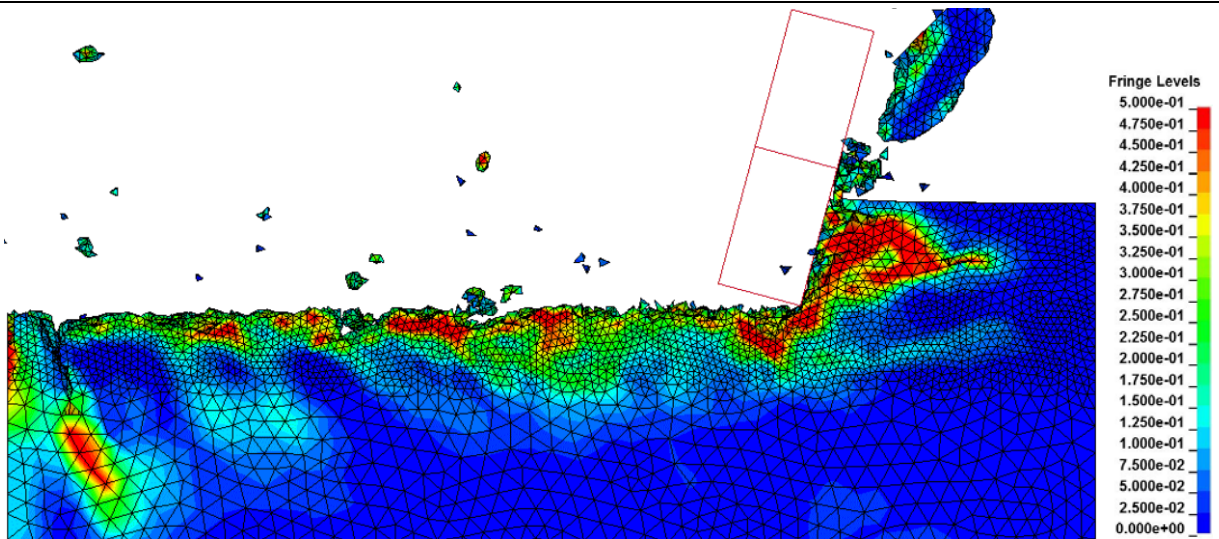
Table 6-1: (continued)



(t₇) The force drops to a minimum as the cracks reach the free surface and chips are eventually sheared off the rock.



(t₈) As the front material is potentially more degraded, it gets crushed in front of the cutter, until stronger material is met.



(t₉) Again, compression at the front eventually creates tension cracks propagated forward. Cutting cycle may re-start at (t₁).

In addition to the very realistic fragmentation process observed during the simulation of Vosges Sandstone cutting at 3.6 mm of depth (presented above), cutting of Berea Sandstone (with material properties slightly different) at a depth of 4 mm (0.16 in) has been simulated and compared with the physical scratching experiment. Figure 6-4 allows us to appreciate a sequence of stages where different fracturing forms are observed in the simulation, and can be suitably corroborated by snapshots from the experimental test. Among the random combination of failure mechanisms found during the rock cutting process, the following instances were selected and validated with laboratory images:

- Figure 6-4 (a, a*): As the material is compressed horizontally, superficial cracks can be created due to tension in the direction perpendicular to cutting.
- Figure 6-4 (b, b*): Once the small fragments in front of the cutter are chipped away, the cutter loses contact with the material ahead, causing the forces to drop.
- Figure 6-4 (c, c*): Large fragments result from deep shear failure and are pushed in front of the cutter.
- Figure 6-4 (d, d*): Cracks propagated longitudinally ahead of the cutter can produce big sharp fragments.
- Figure 6-4 (e, e*): Despite small fragments getting caught between the cutter and the rock, a shear crack may be initiated and may grow toward the free surface.

6.2.2 Shallow Cut Simulation Output

The time history of the simulated horizontal cutting force at a depth of 0.3 mm for Vosges Sandstone is plotted in Figure 6-5. Three stages of the simulation are indicated with small red letters in parenthesis on the force plot and displayed in Figure 6-6. The color contours seen throughout the rock model correspond to the maximum element damage, with red being equal or larger than 50% and blue equal to zero. Elements are eroded once the element damage value is greater than 99%.

As it is expected, the failure mechanism involves only crushing of particles (elements), in this case simulated by element removal. This is the reason why the force plot reflects frequent drops to zero, as the cutter loses contact with the crushed material ahead.

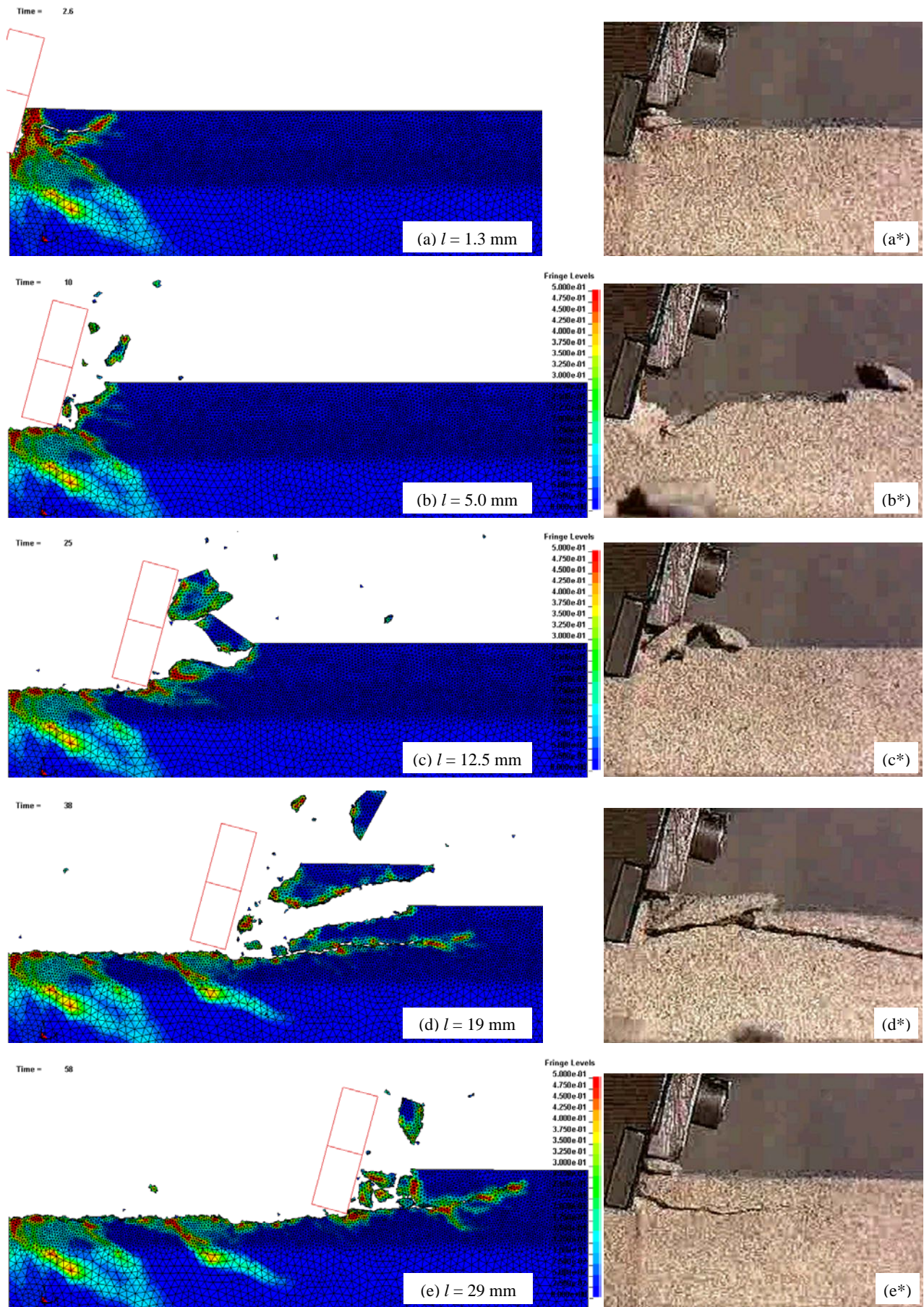


Figure 6-4: Cutting sequence on Berea Sandstone at 4-mm deep. LEFT: Simulation, RIGHT: Laboratory

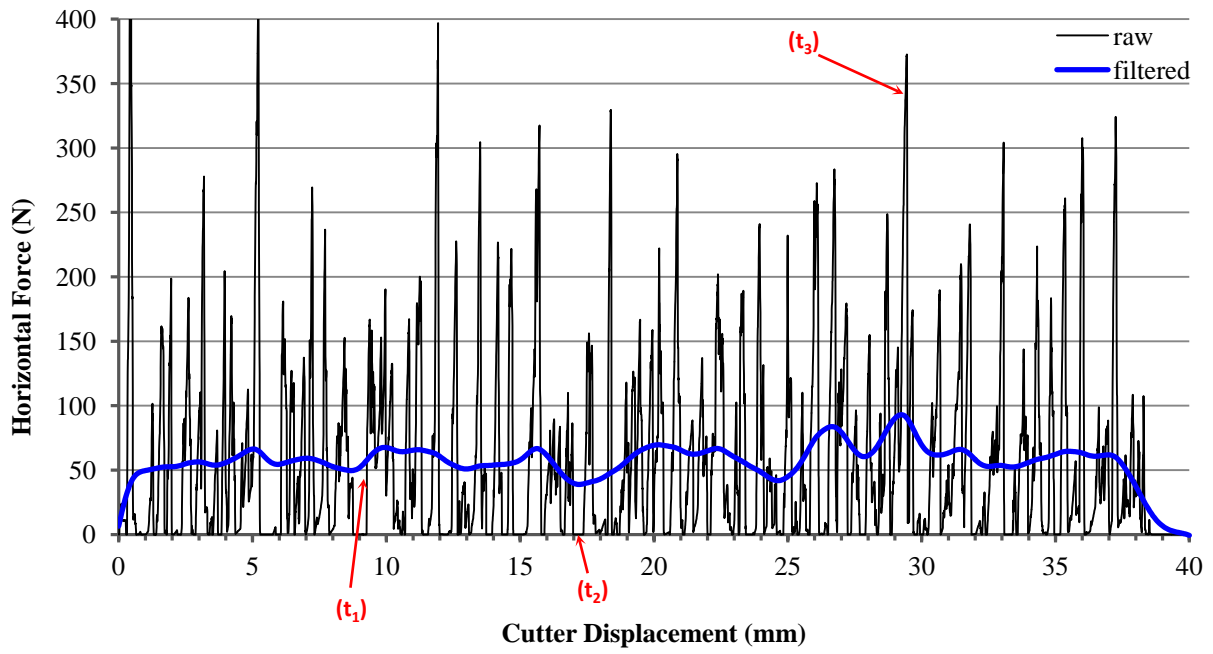


Figure 6-5: Horizontal force during simulation of Vosges Sandstone cutting (0.3-mm deep)

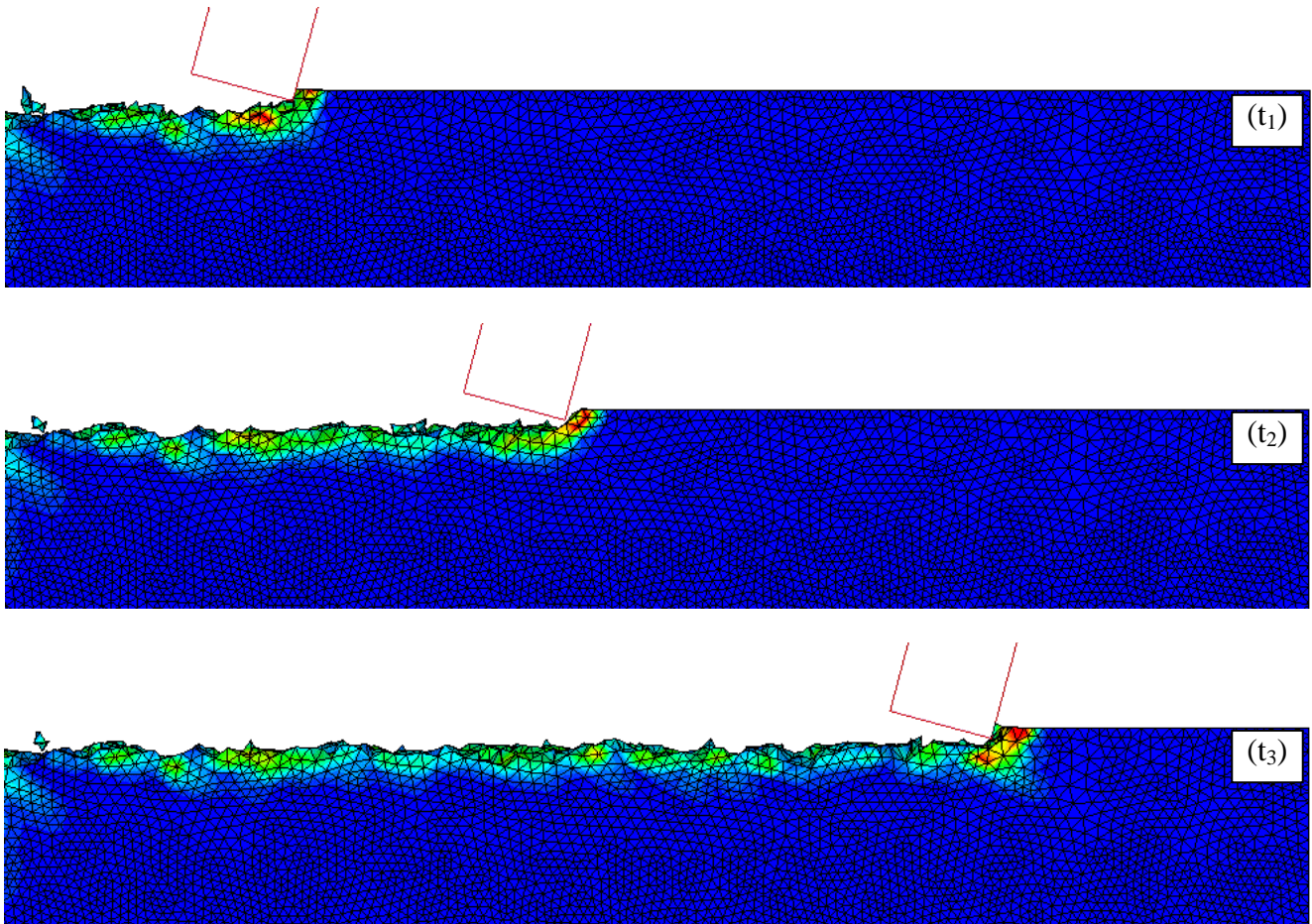


Figure 6-6: Simulated cutting sequence on Vosges Sandstone at a depth of 0.3 mm

This persistent drop to zero makes the simulated and laboratory force signals look different (as seen in Section 5.4.1.2). Nevertheless, after applying the filtering technique to the output data, as explained in Section 5.4.1, the filtered time series as well as the averaged force magnitude can be compared satisfactorily with the experimental results.

In addition to the ductile failure mode observed during the simulation of Vosges Sandstone cutting at 0.3 mm of depth (presented above), cutting of Berea Sandstone (with material properties slightly different) at a depth of 0.3 mm (0.012 in) has been simulated and compared with the physical scratching experiment. Figure 6-7 shows a sequence of three stages where the continuous ductile damage of the rock surface is observed, and can be suitably corroborated by snapshots from the experimental test.

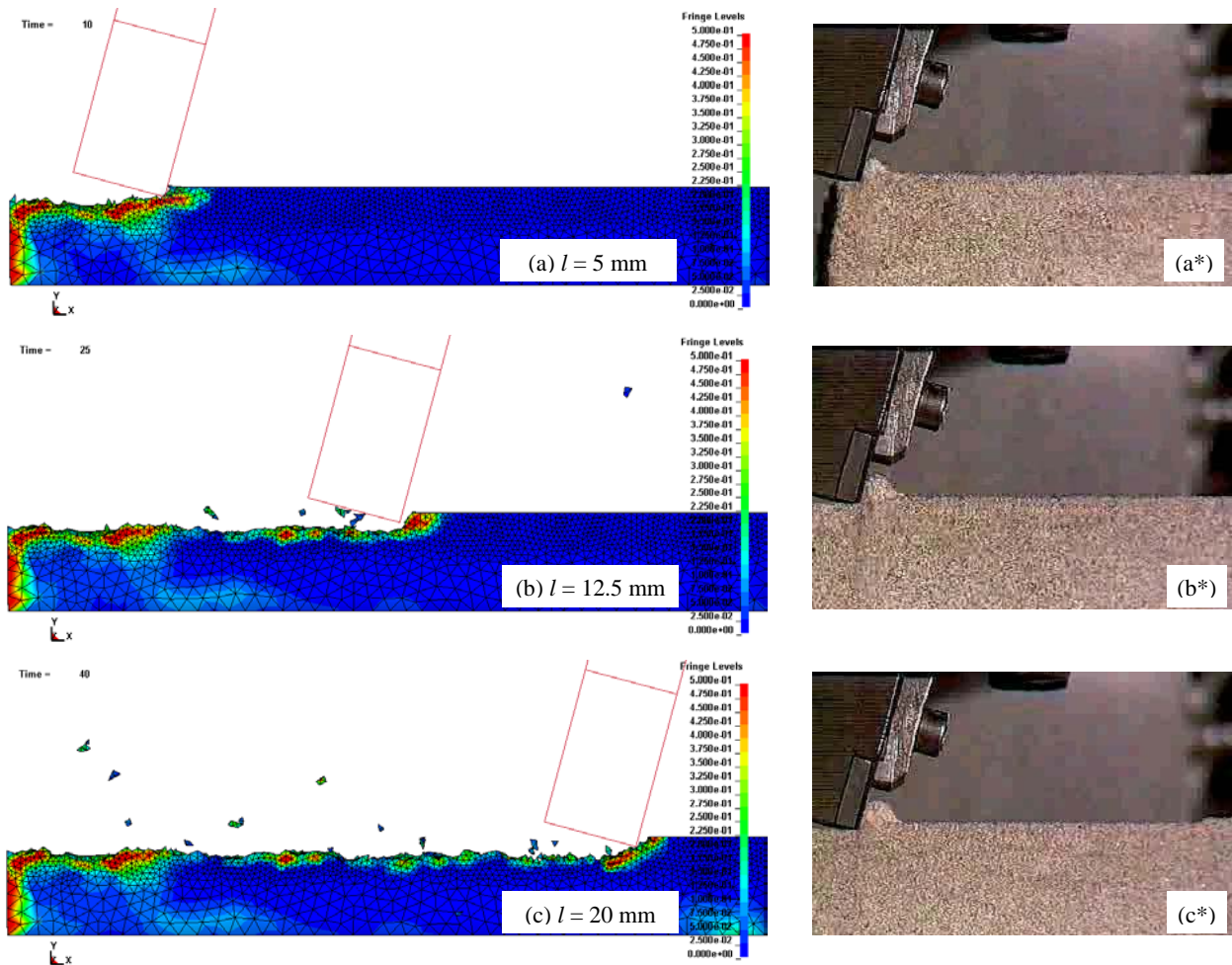


Figure 6-7: Cutting sequence on Berea Sandstone at 0.3-mm deep. LEFT: Simulation, RIGHT: Laboratory

6.2.3 The Effect of Cutting Depth on the Force

The resulting horizontal cutting force signals and their filtered series for different depths of cut are tabulated in Table 6-2. As discussed in Section 5.4.1.2, once the original force signals from the simulation have been filtered, for cutting tests considered shallow (in ductile failure mode), the mean force value is computed simply by averaging all the filtered data. On the other hand, based on the suggested procedure by Richard (1999), for cutting tests considered deep (in brittle failure mode), the mean force is obtained by averaging only the data greater than the mean. It is important to note that the mean peak force for simulated deep cuts in the present work is calculated slightly different. Only the peak values above the mean of the filtered forces are considered in the average.

Figure 6-8 combines laboratory data reported by Richard et al. (1998) and simulation data from this study. The original plot has been used by Richard et al. to describe the transition from ductile to brittle failure mode in relationship with the depth of cut. For Vosges Sandstone, he identifies a critical depth of cut of 1.5 mm (0.06 in) at which the behavior of the braking mechanism evolves from ductile to brittle. This transition is particularly characterized by the first appearance of small chips, and consequently the first peak signals in the force history.

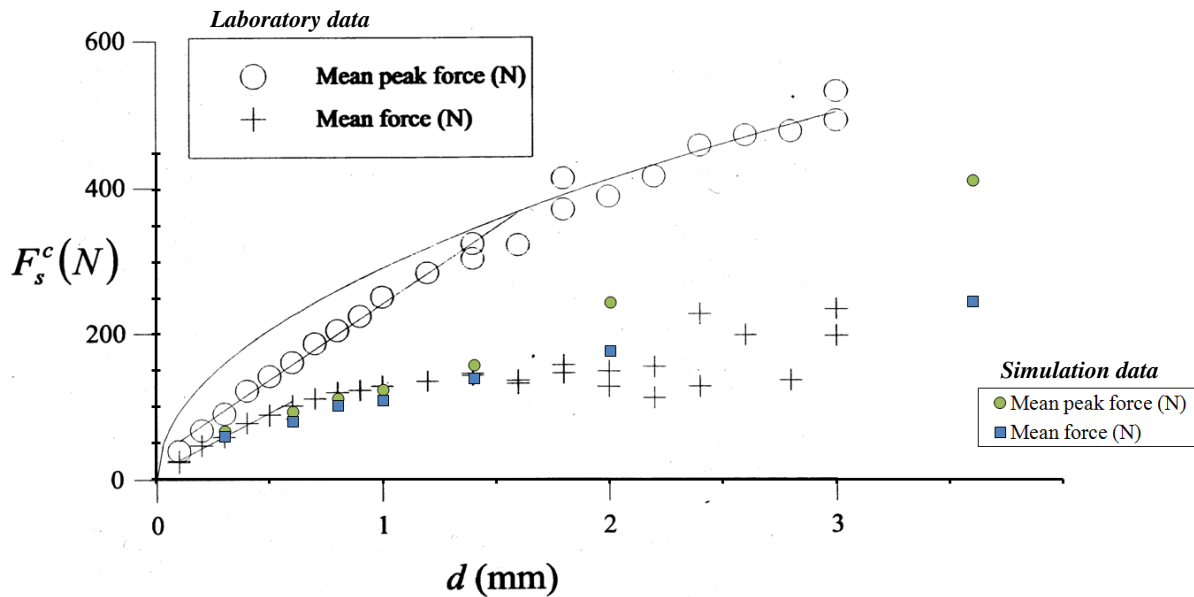


Figure 6-8: Slab horizontal cutting force as a function of depth. Laboratory vs. Simulation **

** Original plot by Richard et al. (1998) with superimposed simulation data from this study.

Table 6-2: Horizontal force signals at different cutting depths for slab cut simulations

d (mm)	Horizontal Force (N) vs. Cutter displacement (mm)	Mean Force (N)	Mean Peak Force (N)
0.3		60.0	67.3
0.6		80.4	94.2
0.8		102.6	112.1
1.0		109.8	124.1
1.4		140.2	158.3
2.0		178.6	245.2
3.6		246.4	414.4

It can be observed in Figure 6-8 that the mean and mean peak force data points from the simulation are relatively close to the mean values from the laboratory up to a depth of 1 mm (0.04 in). It can be claimed that both of these forces from the simulation follow a linear trend during the ductile failure mode, such as Richard states. With a cutting depth larger than 1 mm, however, the discrepancy between the experimental and numerical forces starts to increase gradually.

In addition, when focusing on the brittle mode, the mean peak data from the simulations follow a steeper linear trend, in contrast with the non-linear variation of the force in relation with the cutting depth reported by Richard –which eventually becomes a horizontal asymptote. Figure 6-9 presents the information of the linear regression that best fits the ductile and brittle modes (separately) for the mean peak forces, and the polynomial regression that best represents the mean force values over all the simulations.

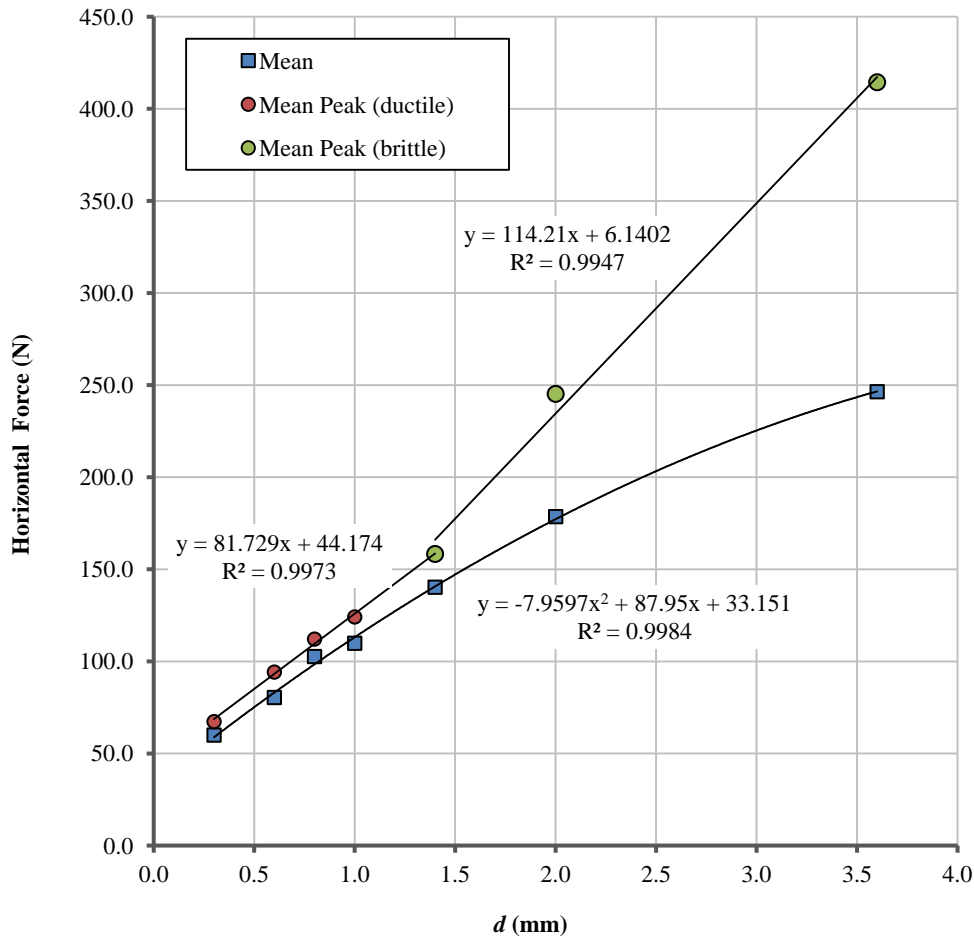


Figure 6-9: The effect of cutting depth on the slab-cut simulation forces

Although the tendency of the force in the brittle mode differs between Richard's laboratory results and the numerical simulations, the latter agree with several authors who have obtained the same upward trend of the mean peak cutting force (using sharp cutters in the laboratory) while increasing the depth of cut in the brittle regime. Among them are Glowka (1987), Garcia-Garavito (1998), Wise et al. (2002), Kaitkay and Lei (2005), and Bilgin et al. (2006).

This study has also demonstrated that there could be a cutting depth at which the fracture mode transitions from ductile to brittle, i.e., $d > 1.4$ mm (0.055 in), as seen in Table 6-2 and Figure 6-9. Nonetheless, from the simulated results, it can be claimed that such a transition is experienced gradually rather than at a definite critical depth. This statement can be further validated throughout the next section.

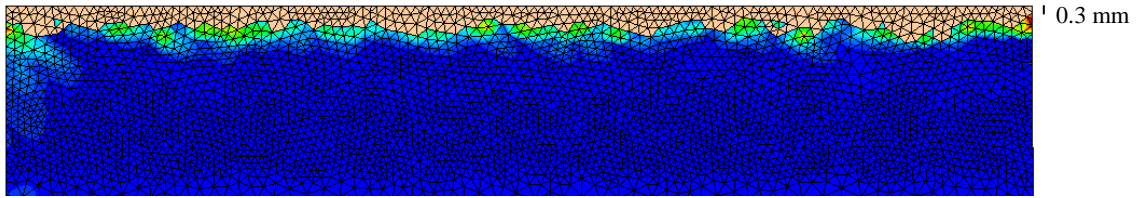
6.3 EROSION ANALYSIS FOR SLAB CUT SIMULATIONS

One of LS-DYNA's useful outputs available is the percentage of rock that has been eroded during each run. Additionally, a clear representation of this measure is provided by displaying the elements that have been "eroded" from the model. These eroded elements are considered as being "crushed" upon reaching maximum strength and strain criteria, and help in visualizing the gradual evolution of the fracturing mechanism, from ductile to brittle. Figure 6-10 portrays the rock models from each slab cut simulation with the elements that have been eroded –colored in light or dark brown– once the cutter has passed through. The remaining rock elements show the maximum damage value reached. The color contours of maximum damage range from blue for zero damage, to red for damage equal or greater than 50%.

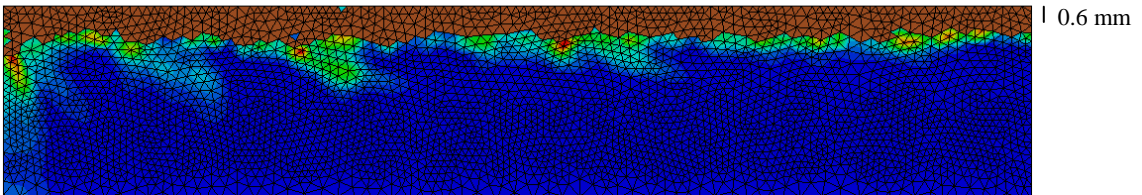
It can be seen in this group of illustrations that as the depth of cut increases, the exposed rock surface becomes more erratic, and the rock elements more damaged. Also, although it is not so evident in this set of images, the rock chips detached from the specimen become larger in size and more abundant as the cut is deeper.

As far as the actual volume fraction of rock that is eroded from the model, this measurement is plotted against the cutter displacement and shown in Figure 6-11 for all the slab cut simulations. It can be seen how the eroded volume pattern gradually changes from a quasi-straight line for a cutting depth of 0.3 mm, to a more rippled line for a depth of 2.0 mm, to a very bumpy line for a depth of 3.6 mm.

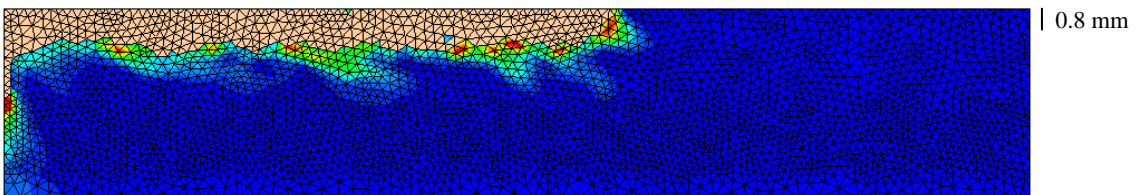
SLAB $w = 10.0$ mm, $d = 0.3$ mm



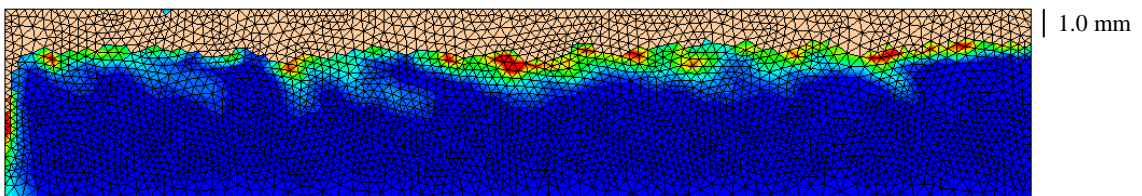
SLAB $w = 10.0$ mm, $d = 0.6$ mm



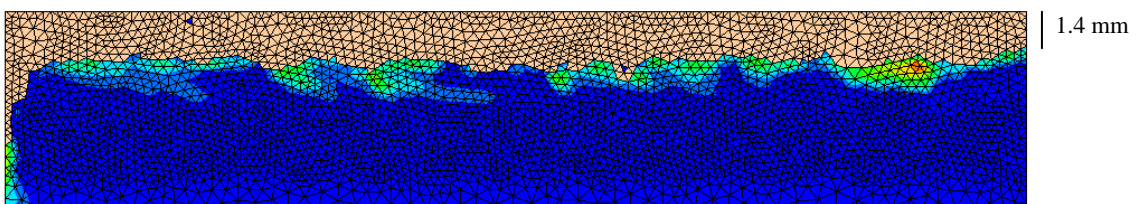
SLAB $w = 10.0$ mm, $d = 0.8$ mm



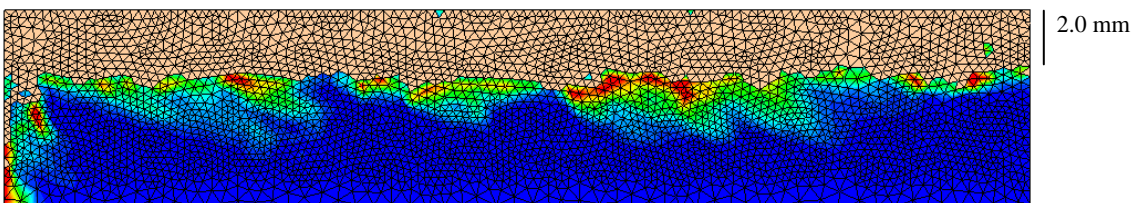
SLAB $w = 10.0$ mm, $d = 1.0$ mm



SLAB $w = 10.0$ mm, $d = 1.4$ mm



SLAB $w = 10.0$ mm, $d = 2.0$ mm



SLAB $w = 10.0$ mm, $d = 3.6$ mm

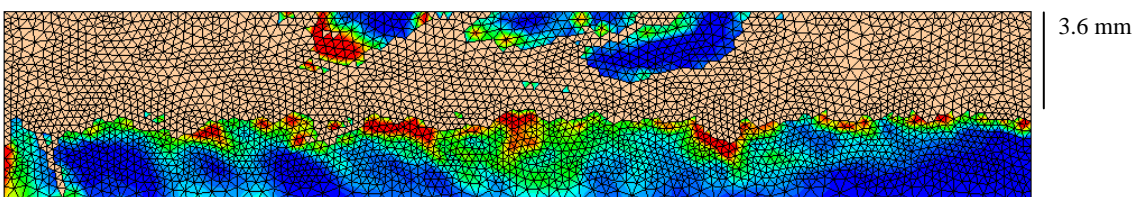


Figure 6-10: Visualization of eroded elements in slab-cut simulations

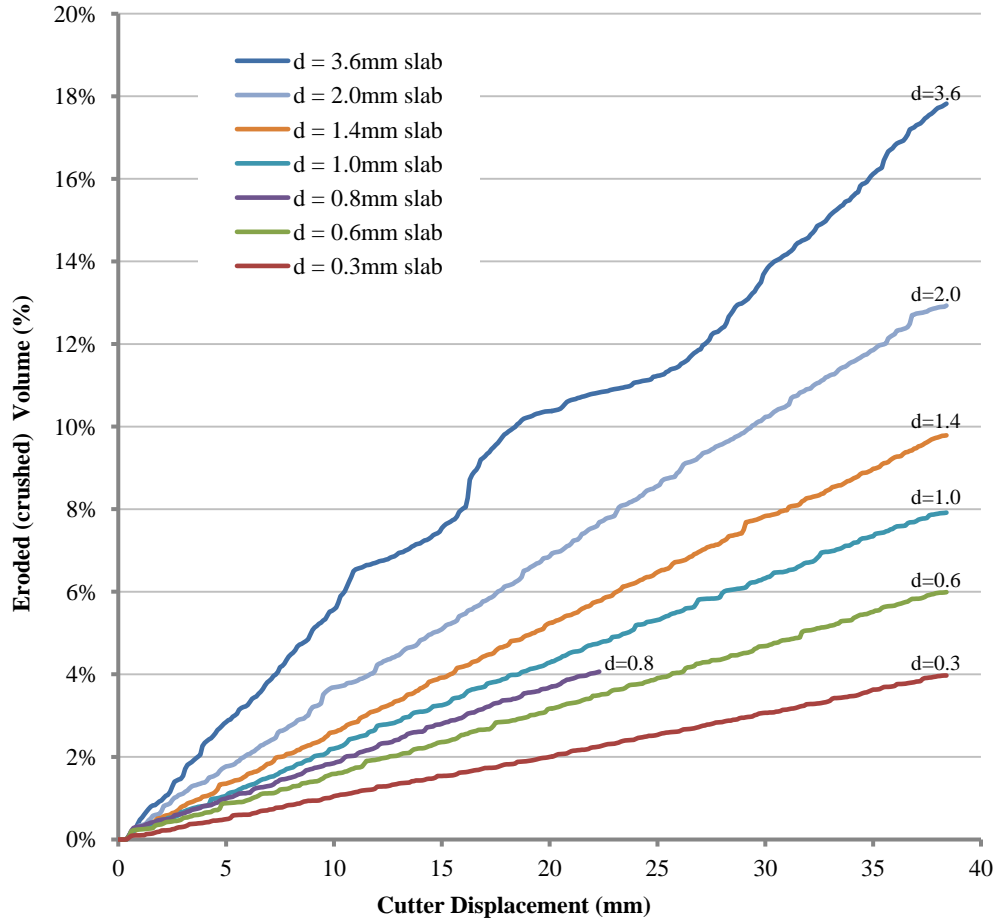


Figure 6-11: Eroded volume fraction during each slab-cut simulation

In order to quantify the amount of rock material that gets crushed with respect to the nominal amount (depth) of material intended to be cut during each slab cut simulation, the following parameters are introduced:

$$V^{crushed} = EVF_{max} \times V_0 \quad (6-1)$$

$$A^{crushed} = \frac{V^{crushed}}{l_{max}} \quad (6-2)$$

$$d^{crushed} = \frac{A^{crushed}}{w} \quad (6-3)$$

$$d_{slab}^* = \frac{d^{crushed}}{d} \times 100\% \quad (6-4)$$

where $V^{crushed}$ is the maximum volume of rock that has been eroded from the model after the cutter has passed, EVF_{max} is the maximum eroded volume fraction, V_0 is the rock sample initial volume, $A^{crushed}$ is the averaged cross-sectional area considered crushed, $d^{crushed}$ is the averaged rock depth considered crushed, and d_{slab}^* is an index that represents the percentage of crushed rock material with respect to the intended depth of cut, d .

Both variables in Equations (6-3) and (6-4) have been graphed in Figure 6-12 against the fixed cutting depth in each simulated case. Focusing on the primary y-axis, it is evident that all the values of $d^{crushed}$, except for the one corresponding to $d = 3.6$ mm, are located to the right of the 1-to-1 dashed line (in blue). This means that the actual crushed depth –once the cutter passes– is greater than the fixed depth that was intended to be cut. The percentage of actual crushed material with respect to the intended depth of cut is plotted on the secondary y-axis.

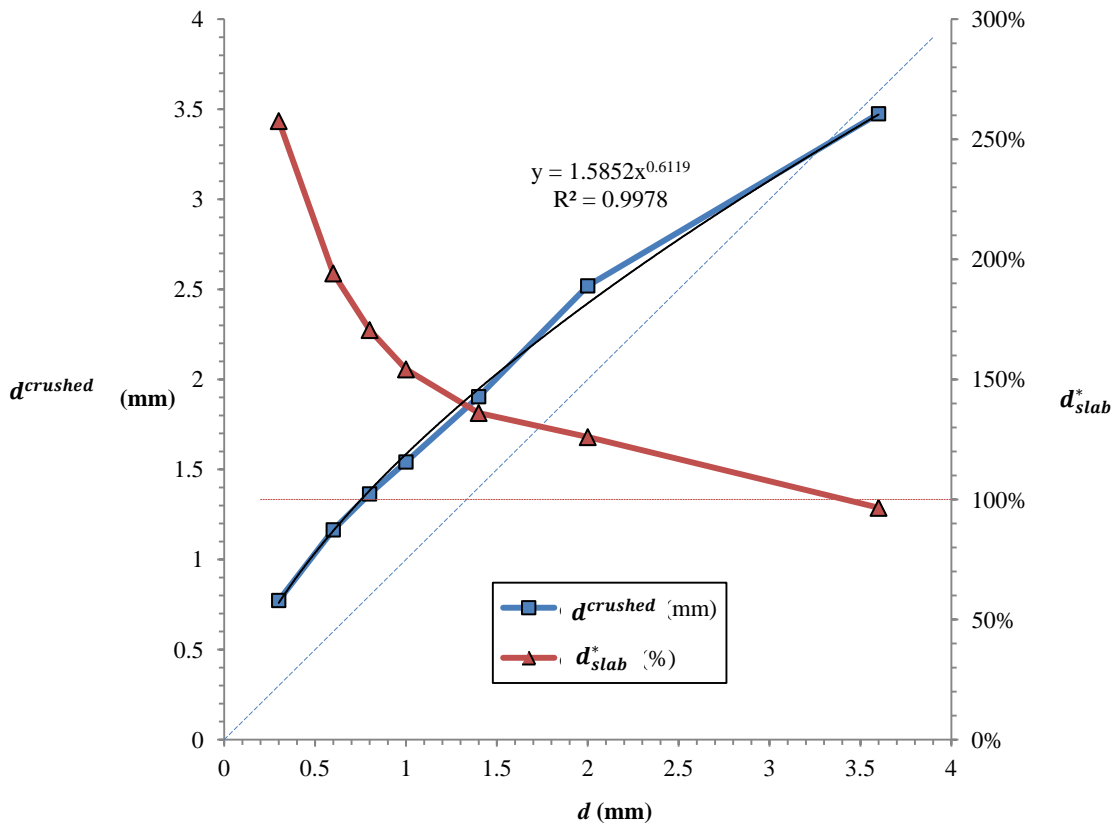


Figure 6-12: Measurement of crushed material for slab cut simulations

Likewise, focusing on left-hand y-axis, it can be seen that all the values of d_{slab}^* , except for the one corresponding to $d = 3.6$ mm, fall above the 100% dotted line (in red). This is the numerical representation of what is illustrated in Figure 6-11. For all slab-cut images, the amount of eroded material always seems to go lower than the level of the fixed cutter depth –shown to scale on the far right end of each model.

The case of $d = 3.6$ mm in particular (and also, in less proportion, the case of $d = 2$ mm) exhibits lower values of $d^{crushed}$ –and correspondingly d_{slab}^* – because of the presence of detached solid rock fragments whose volume is being left out this calculation. This behavior is expected to occur in the brittle failure mode scenarios. The larger the depth of cut, the less material should be eroded, and instead, should be chipped away in the form of independent rock fragments.

Overall, the calculation of $d^{crushed}$ and d_{slab}^* is found to be a useful measure to confirm the observations in Section 6.2.3. It has been discussed that based upon the cutting force as a function of depth, the numerical models result in a gradual transition from ductile to brittle fracture mode. Figure 6-12 not only displays soft curves for $d^{crushed}$ and d_{slab}^* , but is also shows the regression that best fits the $d^{crushed}$ data. It is a power function with an outstanding coefficient of correlation equal to 0.9978. These model output parameters are considered to be reliable, not only due to the robustness of the numerical model, but also because the elements that comprise the rock model have an average size of 0.18 mm (0.007 in) while the real Vosges Sandstone particle sizes range from 0.15 mm (0.006 in) to 0.45 mm (0.018 in).

Ultimately, $d^{crushed}$ and d_{slab}^* as defined in this section, will aid in the calculation of a *true* specific energy (as seen in Section 6.4) and will be used as a standard way to compare the results from additional numerical simulations of rock cutting under different conditions (as seen in Sections 7.4 and 8.3).

6.4 SPECIFIC ENERGY IN ROCK CUTTING

6.4.1 Background on Specific Energy

Within the framework of the ultimate goals of the NETL towards the subject of borehole drilling in rock environments under extreme conditions –as presented in the introductory chapter of this work– it is essential to understand how to obtain an optimum rate of penetration (ROP) in order to lower the costs of drilling, maximize the efficiency, and improve safety of the operations.

The optimum ROP is directly related to the minimum specific energy attained while cutting, because this is a measure of cutting efficiency. Specific energy within the context of rock cutting is a synonym of *energy density*, which is defined as the amount of energy consumed in cutting a unit volume of rock.

Detournay and Defourny (1992) in their paper introduce the concept of *Intrinsic Specific Energy*, ε , and define it as the proportionality factor between the averaged horizontal cutting force and the cross-sectional area of rock being cut. They emphasize that the word *intrinsic* refers to the pure cutting action (with a sharp cutter), and use ε conveniently with units of stress (i.e. MPa) instead of units of specific energy (i.e. J/cm³), as these two are numerically identical.

According to Richard et al. (1998), the intrinsic specific energy parameter should be calculated only for rock cutting scenarios characterized by the ductile failure mode, i.e., at shallow depths. For the case of rock cutting in the brittle regime, the mean cutting force “evolves non-linearly with the depth of cut, thus the specific energy is found smaller than the intrinsic specific energy.” (Richard et al. 2010)

6.4.2 Specific Energy for Slab Cutting Simulations

Being aware of the great difference between the nominal (intended) depth of cut, d , and the actual crushed depth, $d^{crushed}$, it is important that the latter is used in the calculation of the specific energy for the slab cutting simulations in this study. As the shallow cut simulations (i.e., $0.3 \text{ mm} < d < 1.4 \text{ mm}$) do not produce any chipping and indeed behave in a ductile regime, it is

definite that the quantity provided by $d^{crushed}$ is equivalent to 100 % of rock volume crushed. As a result, the specific energy for the simulated slab cut runs is defined as:

$$\epsilon = \frac{F_{mean}}{A^{crushed}} = \frac{F_{mean}}{w \times d^{crushed}} \quad (6-5)$$

where w is the fixed width of the rock slab, equal to 10 mm (0.4 in).

Table 6-3 summarizes the values of actual crushed depth, mean horizontal cutting force and specific energy for the slab cut simulations in ductile regime. It can be seen how the value of specific energy has a very small variation as a function of cutting depth –having an average of 7.33 MPa (1,064 psi) and a standard deviation of only 0.34 MPa (49 psi)– which can satisfactorily confirm that the value of ϵ can be interpreted as having an association with the material strength, as suggested by Richard et al. (1998). They indicate that there is a range of depth of cut that is characterized by a constant intrinsic specific energy, and that scratching should ideally take place in this range.

Table 6-3: Output parameters for slab cut simulations in the ductile regime

Nominal Depth of Cut		$d^{crushed}$		F_{mean}		ϵ	
(mm)	(in)	(mm)	(in)	(N)	(lbf)	(MPa)	(psi)
0.3	0.012	0.77	0.030	59.97	13.48	7.76	1,125
0.6	0.024	1.16	0.046	80.37	18.07	6.90	1,001
0.8	0.031	1.36	0.054	102.60	23.06	7.52	1,091
1.0	0.039	1.54	0.061	109.82	24.69	7.12	1,033
1.4	0.055	1.90	0.075	140.24	31.53	7.36	1,068
Average						7.33	1,064

The specific energy results from the above table will be further analyzed together with a larger set of results from groove cutting cases in the following chapter.

7.0 NUMERICAL SIMULATION OF GROOVE CUTTING IN ROCK

In order to further verify the soundness of the numerical model developed throughout this research effort, a set of rock cutting simulations has been carried out mimicking the groove cutting experiments performed by Richard (1999) on Vosges Sandstone.

The objective of this series of tests was exploring the influence of the cutter width for a groove with four sharp cutters of different widths: 2.56 mm (0.1 in), 5 mm (0.197 in), 10 mm (0.394 in) and 15 mm (0.59 in). Throughout this chapter a comparison of the experimental and the numerical simulation results is presented and discussed.

Sixteen cases of the groove cut tests are simulated varying the depth of cut four times for each cutter width studied. The cutting depths used for this part of the study are 0.3, 0.6, 0.8, and 1.0 mm (0.012, 0.024, 0.031, 0.04 in), which ensure the material failure mode falls within the ductile regime. The rock material simulated herein corresponds to Vosges sandstone modeled with Mat_159, following all the considerations explained in Section 3.2.4 and Chapter 5.0.

To facilitate the understanding of the effect of the groove edges on the resulting cutting forces, empirical equations of the cutting force are derived from the two-dimensional and three-dimensional test results as a function of the cutting dimensions. These 2 models are eventually integrated into a more generalized formula, which characterizes the numerical results.

7.1 MODEL GEOMETRY

7.1.1 Rock Specimen Geometry

As the simulations conducted herein do not represent brittle fragmentation, the rock models do not require a great dimension in the vertical direction; however, as these cases are

aimed at investigating the effect of the cutter width in the groove cutting, then the width of the rock specimen must be considerably larger than the slab rock samples (i.e. truly three-dimensional).

Like the rock model for the slab cut simulations, the rock models prepared for groove cutting consist of an upper fine mesh where cutting takes place, and a lower coarser mesh that guarantee no boundary effects from the bottom on the elements' behavior upon the cutting load. The width of the rock model for each case is similarly defined wide enough so that there are no boundary effects from the side edges. Moreover, only half of the actual sample thickness is modeled in order to save on computational time; yet, the cutting forces reported are adequately proportioned to the full thickness. In this regards, (half of) the groove is cut along the longitudinal (x-axis) edge of the rock model, and the results are interpreted by mirroring the model with respect to the xy-plane highlighted in Figure 7-1.

Figure 7-1 displays the variable dimensions established for the groove cut specimens, and Table 7-1 lists the variables' value for each one of the cases simulated. The table also includes and the average element size in the fine zone, the total number of elements and total number of nodes in each model.

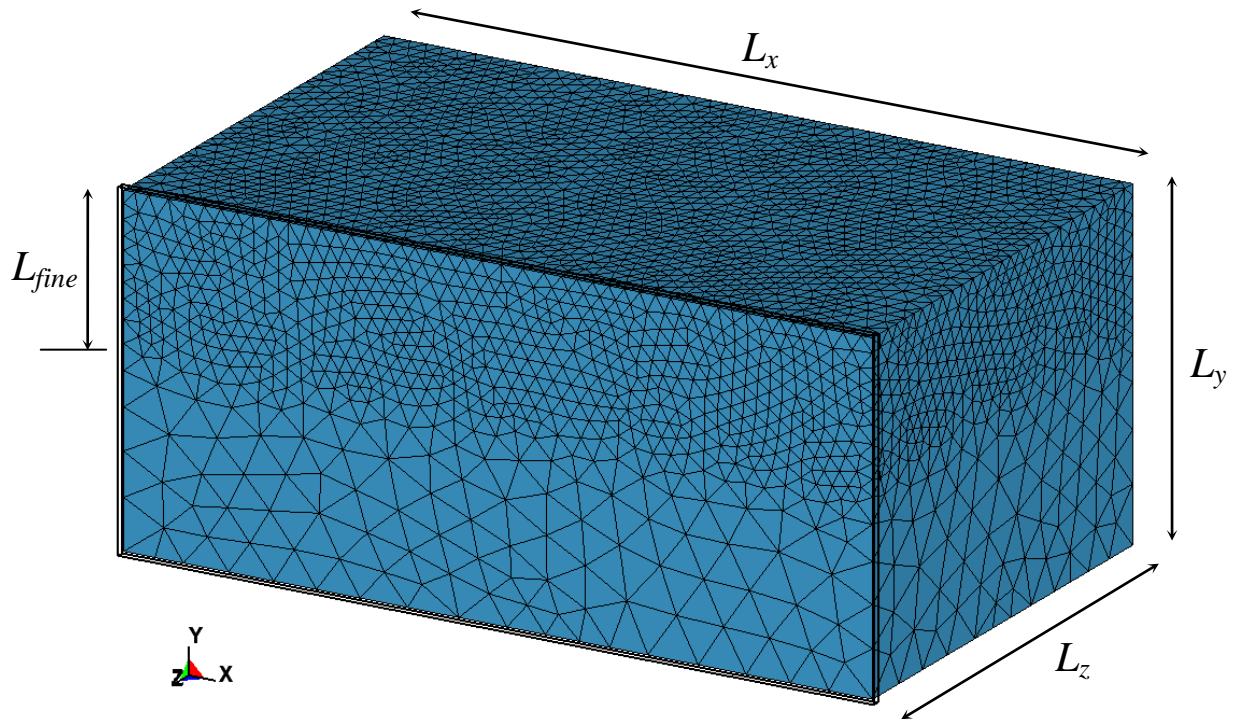


Figure 7-1: Rock model geometry for groove cuts

Table 7-1: Dimensional information of the groove cut rock models

Model ID	w (mm)	d (mm)	L_x (mm)	L_y (mm)	L_z (mm)	L_{fine} (mm)	Avg. element size (fine zone) (mm)	Total Number of Nodes	Total Number of Elements
d1w1	2.56	0.3	10.8	2.3	3.28	1.0	0.145	6,159	31,185
d2w1	2.56	0.6	10.8	3.6	4.28	1.5	0.145	11,657	61,750
d3w1	2.56	0.8	10.8	4.8	5.28	2.0	0.145	14,522	77,889
d4w1	2.56	1	10.8	6.0	6.28	2.5	0.144	29,641	165,030
d1w2	5	0.3	10.8	2.3	4.50	1.0	0.144	7,796	39,503
d2w2	5	0.6	10.8	3.6	5.50	1.5	0.145	15,393	83,092
d3w2	5	0.8	10.8	4.8	6.50	2.0	0.142	20,598	112,616
d4w2	5	1	10.8	6.0	7.50	2.5	0.144	32,752	181,250
d1w3	10	0.3	10.8	2.3	7.00	1.0	0.144	10,589	53,661
d2w3	10	0.6	10.8	3.6	8.00	1.5	0.144	19,010	101,824
d3w3	10	0.8	10.8	4.8	9.00	2.0	0.143	23,636	112,501
d4w3	10	1	10.8	6.0	10.00	2.5	0.142	51,237	290,082
d1w4	15	0.3	10.8	2.3	9.50	1.0	0.142	14,282	72,891
d2w4	15	0.6	10.8	3.6	10.50	1.5	0.142	21,921	117,497
d3w4	15	0.8	10.8	4.8	11.50	2.0	0.143	24,020	129,371
d4w4	15	1	10.8	6.0	12.50	2.5	0.140	52,960	294,779

Model ID	w (in)	d (in)	L_x (in)	L_y (in)	L_z (in)	L_{fine} (in)	Avg. element size (fine zone) (in)	Total Number of Nodes	Total Number of Elements
d1w1	0.10	0.01	0.425	0.091	0.129	0.039	0.0057	6,159	31,185
d2w1	0.10	0.02	0.425	0.142	0.169	0.059	0.0057	11,657	61,750
d3w1	0.10	0.03	0.425	0.189	0.208	0.079	0.0057	14,522	77,889
d4w1	0.10	0.04	0.425	0.236	0.247	0.098	0.0057	29,641	165,030
d1w2	0.20	0.01	0.425	0.091	0.177	0.039	0.0057	7,796	39,503
d2w2	0.20	0.02	0.425	0.142	0.217	0.059	0.0057	15,393	83,092
d3w2	0.20	0.03	0.425	0.189	0.256	0.079	0.0056	20,598	112,616
d4w2	0.20	0.04	0.425	0.236	0.295	0.098	0.0057	32,752	181,250
d1w3	0.39	0.01	0.425	0.091	0.276	0.039	0.0057	10,589	53,661
d2w3	0.39	0.02	0.425	0.142	0.315	0.059	0.0057	19,010	101,824
d3w3	0.39	0.03	0.425	0.189	0.354	0.079	0.0056	23,636	112,501
d4w3	0.39	0.04	0.425	0.236	0.394	0.098	0.0056	51,237	290,082
d1w4	0.59	0.01	0.425	0.091	0.374	0.039	0.0056	14,282	72,891
d2w4	0.59	0.02	0.425	0.142	0.413	0.059	0.0056	21,921	117,497
d3w4	0.59	0.03	0.425	0.189	0.453	0.079	0.0056	24,020	129,371
d4w4	0.59	0.04	0.425	0.236	0.492	0.098	0.0055	52,960	294,779

7.1.2 Cutter Geometry

The cutter geometry for groove cutting simulations follows the same premises described in Section 6.1.2. The only difference lies in the variation of the cutter width (in the y-direction) for each case. The actual dimension of the cutter model width is established as one half of that tabulated in Table 7-1 under the w dimension.

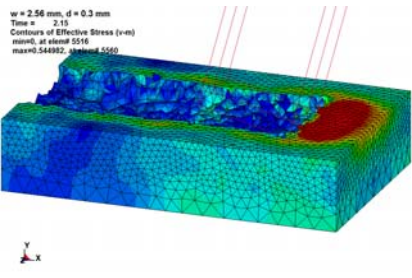
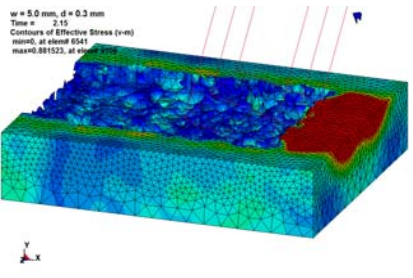
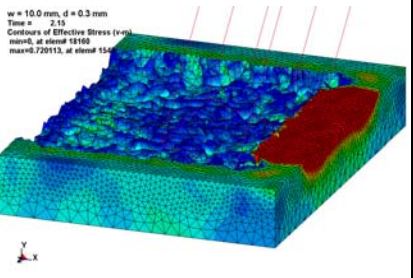
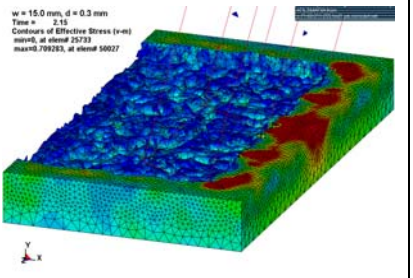
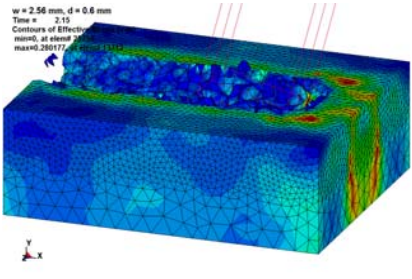
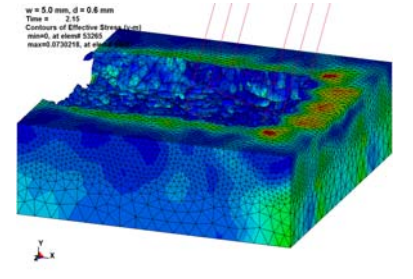
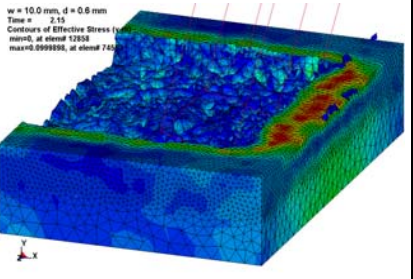
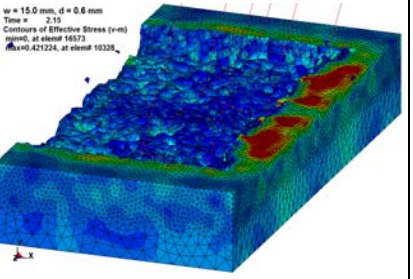
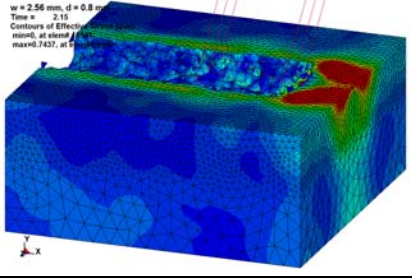
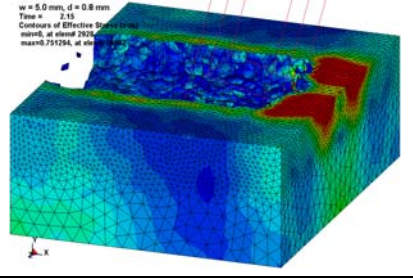
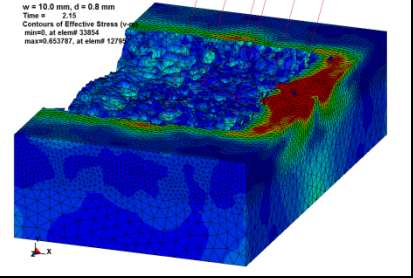
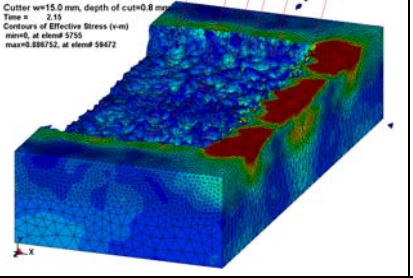
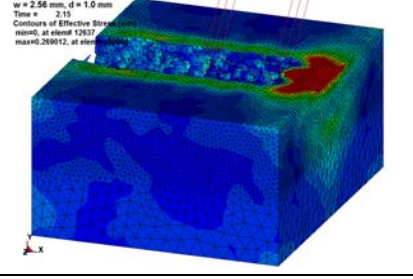
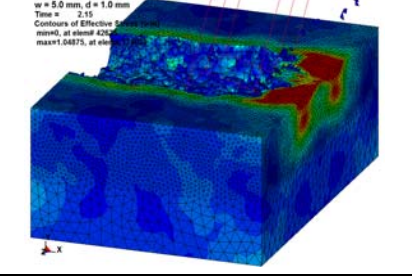
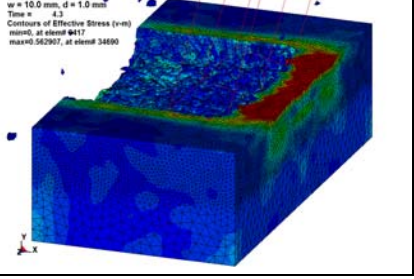
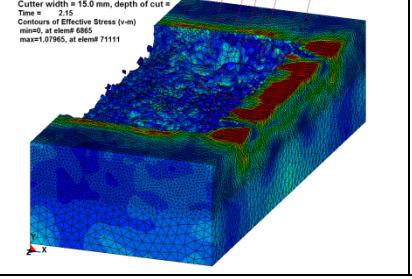
7.2 GROOVE CUT SIMULATION OUTPUT

As it is expected for all the groove cut cases simulated, the failure mechanism exhibited is purely ductile, thus all elements in front of the cutter get crushed (eroded) as it passes through. The behavior of these cutting models resembles the one described in Section 6.2.2 for the shallow cut of rock slabs. What can be observed herein is the effect of cutting side walls along the cutting length.

7.2.1 Stresses Caused by Different Groove Size

Table 7-2 displays the effective stress (Von-mises) distribution in each case's rock specimen at the same instance in time. These illustrations allow us to compare the impact of the groove size on the tested rock model. The color contours of effective stress range from a magnitude of 0 MPa in blue, to 10 MPa or greater in red. Although the effect of the cutting depth is not clearly appreciated, it is indeed evident when comparing these images at the same scale that the stressed zone along the groove edge in the y-direction is irrespective of the nominal cutter width and the nominal depth of cut. For example, for all cases with $d = 1.0\text{mm}$ (0.04 in), the stressed zone on each side of the groove extends approximately 0.73 mm (0.028 in) in the y-direction. The same stressed zone size can actually be measured on most of the models, provided they have some boundary elements still in blue.

Table 7-2: Effective Stress (contours) when cutter displacement is 8.6 mm in all groove cutting cases

Nominal Width of Cutter, w						
$w1 = 2.56 \text{ mm}$	$w2 = 5 \text{ mm}$	$w3 = 10 \text{ mm}$	$w4 = 15 \text{ mm}$			
<p>$w = 2.56 \text{ mm}$, $d = 0.3 \text{ mm}$ Time = 2.15 Contours of Effective Stress (v-m) min=0, at element 5516 max=0.54492, at element 5560</p> 	<p>$w = 5.0 \text{ mm}$, $d = 0.3 \text{ mm}$ Time = 2.15 Contours of Effective Stress (v-m) min=0, at element 5341 max=0.881523, at element 5341</p> 	<p>$w = 10.0 \text{ mm}$, $d = 0.3 \text{ mm}$ Time = 2.15 Contours of Effective Stress (v-m) min=0, at element 15160 max=0.720113, at element 15160</p> 	<p>$w = 15.0 \text{ mm}$, $d = 0.3 \text{ mm}$ Time = 2.15 Contours of Effective Stress (v-m) min=0, at element 15733 max=0.794293, at element 50027</p> 	$d1 = 0.3 \text{ mm}$	Nominal Depth of Cut, d	
<p>$w = 2.56 \text{ mm}$, $d = 0.6 \text{ mm}$ Time = 2.15 Contours of Effective Stress (v-m) min=0, at element 13111 max=0.260177, at element 13111</p> 	<p>$w = 5.0 \text{ mm}$, $d = 0.6 \text{ mm}$ Time = 2.15 Contours of Effective Stress (v-m) min=0, at element 53265 max=0.8730216, at element 53265</p> 	<p>$w = 10.0 \text{ mm}$, $d = 0.6 \text{ mm}$ Time = 2.15 Contours of Effective Stress (v-m) min=0, at element 12858 max=0.999898, at element 7401</p> 	<p>$w = 15.0 \text{ mm}$, $d = 0.6 \text{ mm}$ Time = 2.15 Contours of Effective Stress (v-m) min=0, at element 16573 max=0.421224, at element 16326</p> 			$d2 = 0.6 \text{ mm}$
<p>$w = 2.56 \text{ mm}$, $d = 0.8 \text{ mm}$ Time = 2.15 Contours of Effective Stress (v-m) min=0, at element 12637 max=0.7437, at element 12637</p> 	<p>$w = 5.0 \text{ mm}$, $d = 0.8 \text{ mm}$ Time = 2.15 Contours of Effective Stress (v-m) min=0, at element 2924 max=0.75284, at element 2924</p> 	<p>$w = 10.0 \text{ mm}$, $d = 0.8 \text{ mm}$ Time = 2.15 Contours of Effective Stress (v-m) min=0, at element 33854 max=0.833787, at element 12770</p> 	<p>Cutter $w=15.0 \text{ mm}$, depth of cut=0.8 mm Time = 2.15 Contours of Effective Stress (v-m) min=0, at element 5755 max=0.888752, at element 58472</p> 			$d3 = 0.8 \text{ mm}$
<p>$w = 2.56 \text{ mm}$, $d = 1.0 \text{ mm}$ Time = 2.15 Contours of Effective Stress (v-m) min=0, at element 12637 max=0.26012, at element 12637</p> 	<p>$w = 5.0 \text{ mm}$, $d = 1.0 \text{ mm}$ Time = 2.15 Contours of Effective Stress (v-m) min=0, at element 4216 max=1.04875, at element 4216</p> 	<p>$w = 10.0 \text{ mm}$, $d = 1.0 \text{ mm}$ Time = 4.3 Contours of Effective Stress (v-m) min=0, at element 9417 max=0.562967, at element 34890</p> 	<p>Cutter width = 15.0 mm, depth of cut = 1.0 mm Time = 2.15 Contours of Effective Stress (v-m) min=0, at element 6865 max=1.07965, at element 71111</p> 			$d4 = 1.0 \text{ mm}$

7.2.2 The Effect of Groove Size on the Horizontal Cutting Force

The resulting cutting force signals and their corresponding filtered series for different depths of cut and different cutter widths are tabulated in Table 7-3. As discussed in Section 5.4.1.2, once the original force signals from the simulation have been filtered, for cutting tests considered shallow (in ductile failure mode), the mean force value is computed simply by averaging the filtered data. The mean value of the cutting force for each case is also reported on this table.

Furthermore, Figure 7-2 presents a summary of the simulation forces for groove cutting tests as a function of cutting depth, for each of the cutting widths selected, and compares it with the same summary from Richard's laboratory results. Although it is evident that there is a discrepancy in the magnitude of the forces between the numerical and experimental results, particularly larger as the cutting depth increases, there is a good agreement in that the trend is essentially linear in most of the cases. For $w = 2.56$ mm, both the simulations and the laboratory tests are characterized better by a curvature (2nd order polynomial) that might eventually converge to the lineal pattern of the other sets with larger d .

Figure 7-2(a) shows the linear regression equations and coefficients of correlation for each set of runs, with an excellent relationship between the cutting force and the groove nominal dimensions when w is greater than 2.56 mm. By normalizing these linear equations with respect to their corresponding w , it is possible to obtain a general expression for the mean cutting force as a function of the groove size, as follows:

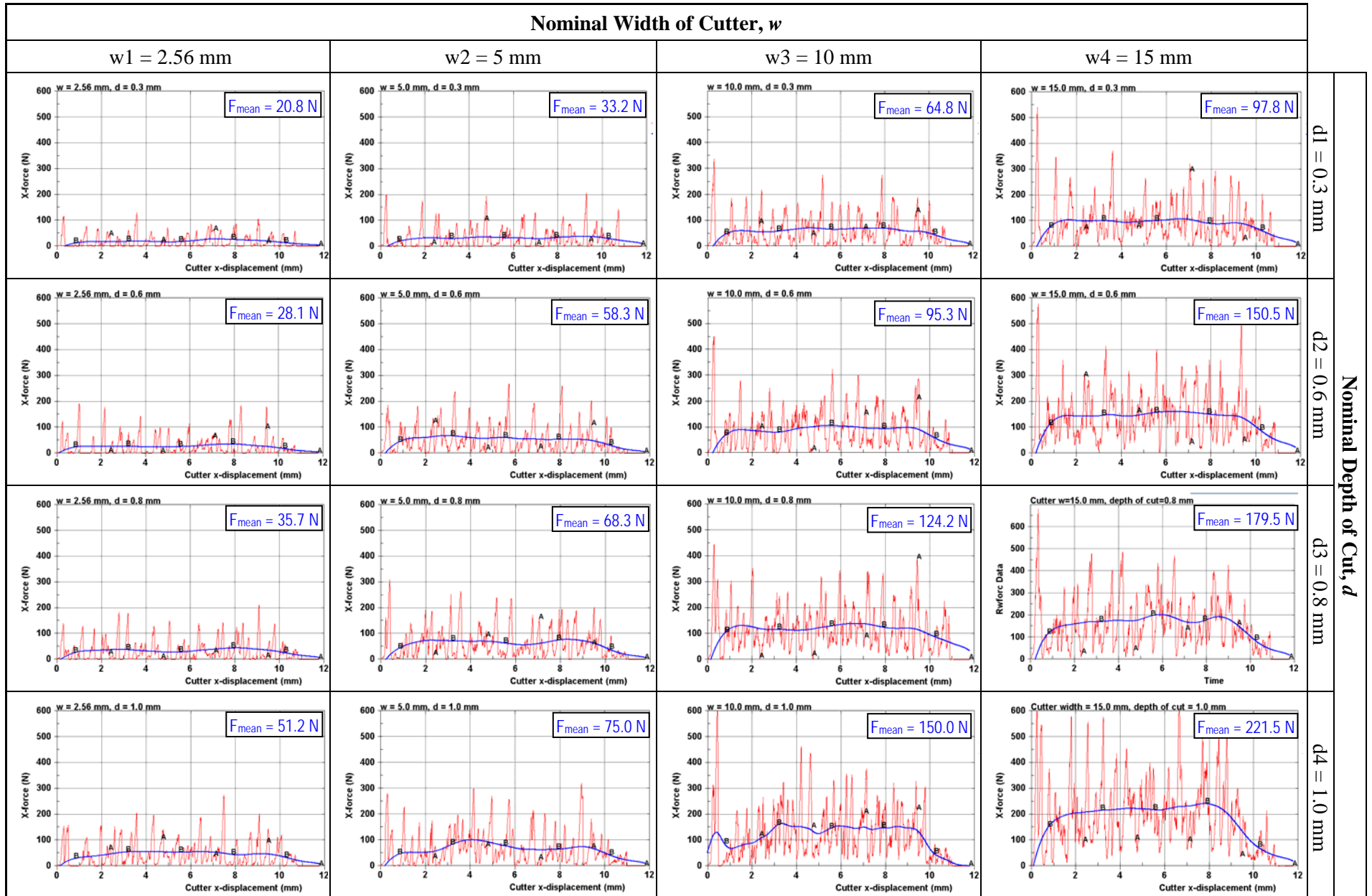
$$F_{mean} = (A_f \cdot d + B_f)w \quad (7-1)$$

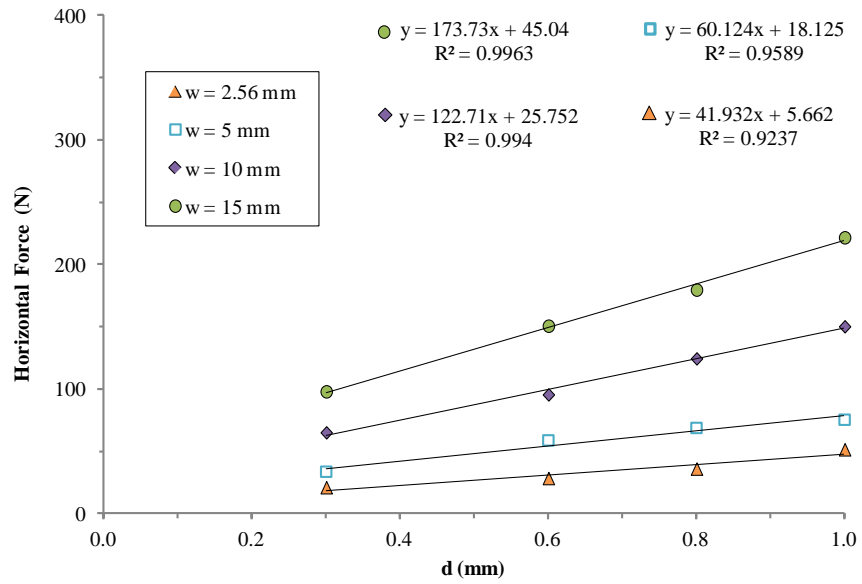
where A_f and B_f are the averaged coefficients from the linear regression equations (for $w > 2.56$ mm) in Figure 7-2(a). Determination of these coefficients is abridged in Table 7-4. As a result, the groove horizontal cutting force from these (initial) set of simulations can be expressed as:

$$F_{mean} = (11.96 \cdot d + 3.07)w \quad (\text{N}) \quad (7-2)$$

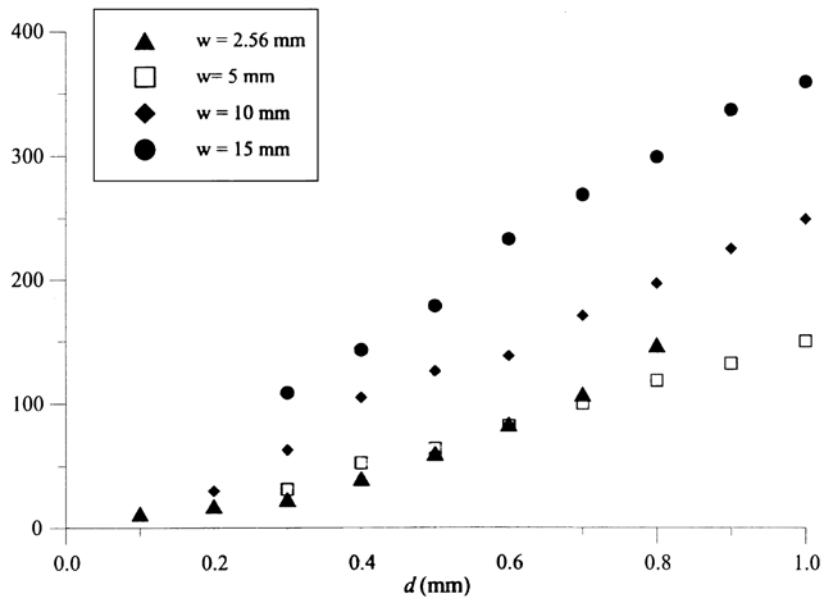
where d and w are used in millimeters.

Table 7-3: Horizontal force signals at different cutting depths and widths for groove cut simulations





(a) Numerical Simulation Results



(b) Laboratory Results (Richard 1999)

Figure 7-2: Groove cutting force as a function of depth. (a) Simulation vs. (b) Laboratory

Table 7-4: Coefficient determination for F_{mean} expression as a function of groove size

	w2 = 5 mm	w3 = 10 mm	w4 = 15 mm
Linear regression	$F = 60.12d + 18.13$	$F = 122.71d + 25.75$	$F = 173.73d + 45.04$
Normalized function	$\frac{F}{w} = 12.02d + 3.63$	$\frac{F}{w} = 12.27d + 2.58$	$\frac{F}{w} = 11.58d + 3.00$
Coefficient A_f	$A_{f2} = 12.02$ (N/mm)	$A_{f3} = 12.27$ (N/mm)	$A_{f4} = 11.58$ (N/mm)
	$A_{f-avg} = 11.96$ (N/mm)		
Coefficient B_f	$B_{f2} = 3.63$ (N)	$B_{f3} = 2.58$ (N)	$B_{f4} = 3.0$ (N)
	$B_{f-avg} = 3.07$ (N)		

7.3 EROSION ANALYSIS FOR GROOVE CUT SIMULATIONS

Following the same logic explained in Section 6.3, it is important to analyze the “actual” volume extracted during a cutting test in contrast to the “nominal” volume intended to be taken by the cutter dimensions, especially in the three-dimensional case of groove cutting.

Figure 7-3 through Figure 7-6 depict the rock models from each groove cut simulation with the elements that have been eroded –colored in dark brown– once the cutter has passed through. The remaining rock elements show the maximum damage value reached. The color contours of maximum damage range from blue for zero damage, to red for damage equal or greater than 50%. The rock model for each case contains a series of measurements shown in the picture: the white lines correspond to the nominal dimensions of the cutter, i.e., intended depth, d , and width, w , of cut; and the yellow lines represent the average actual depth, $d^{crushed}$, and average actual width $w^{crushed}$ extracted by the cutter from the groove.

The values of $d^{crushed}$ and $w^{crushed}$ are iteratively estimated and marked on each case’s picture of “eroded elements” based upon the computed value of $A^{crushed}$ for all groove cut simulations. The averaged cross-sectional area considered crushed, $A^{crushed}$, is calculated with Equation (6-2), which makes use of the *eroded volume fraction* history output from each run.

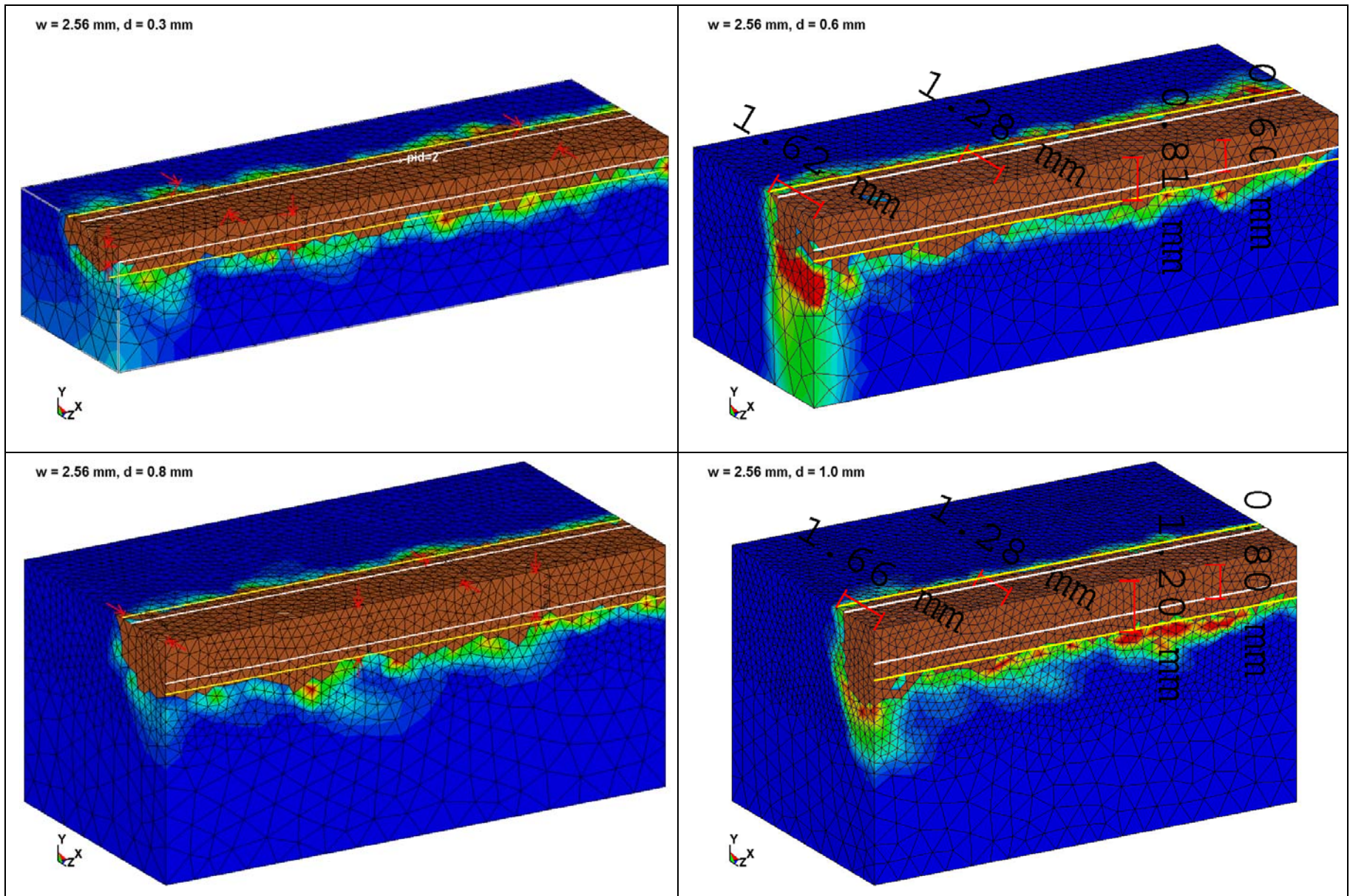


Figure 7-3: Visualization of deleted elements in groove-cut simulations: $w = 2.56$ mm, $d =$ variable (half model shown)

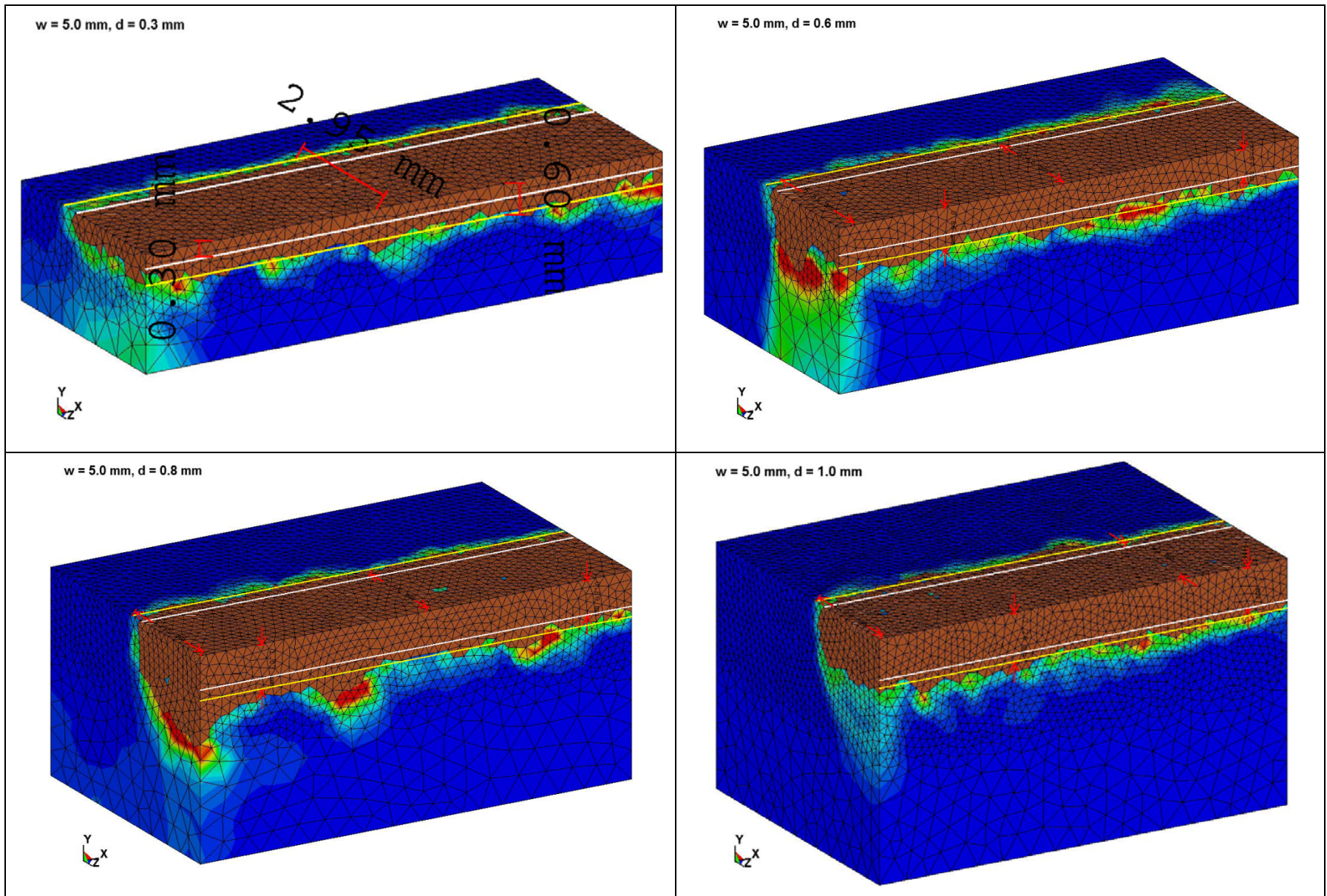


Figure 7-4: Visualization of deleted elements in groove-cut simulations: $w = 5$ mm, $d =$ variable (half model shown)

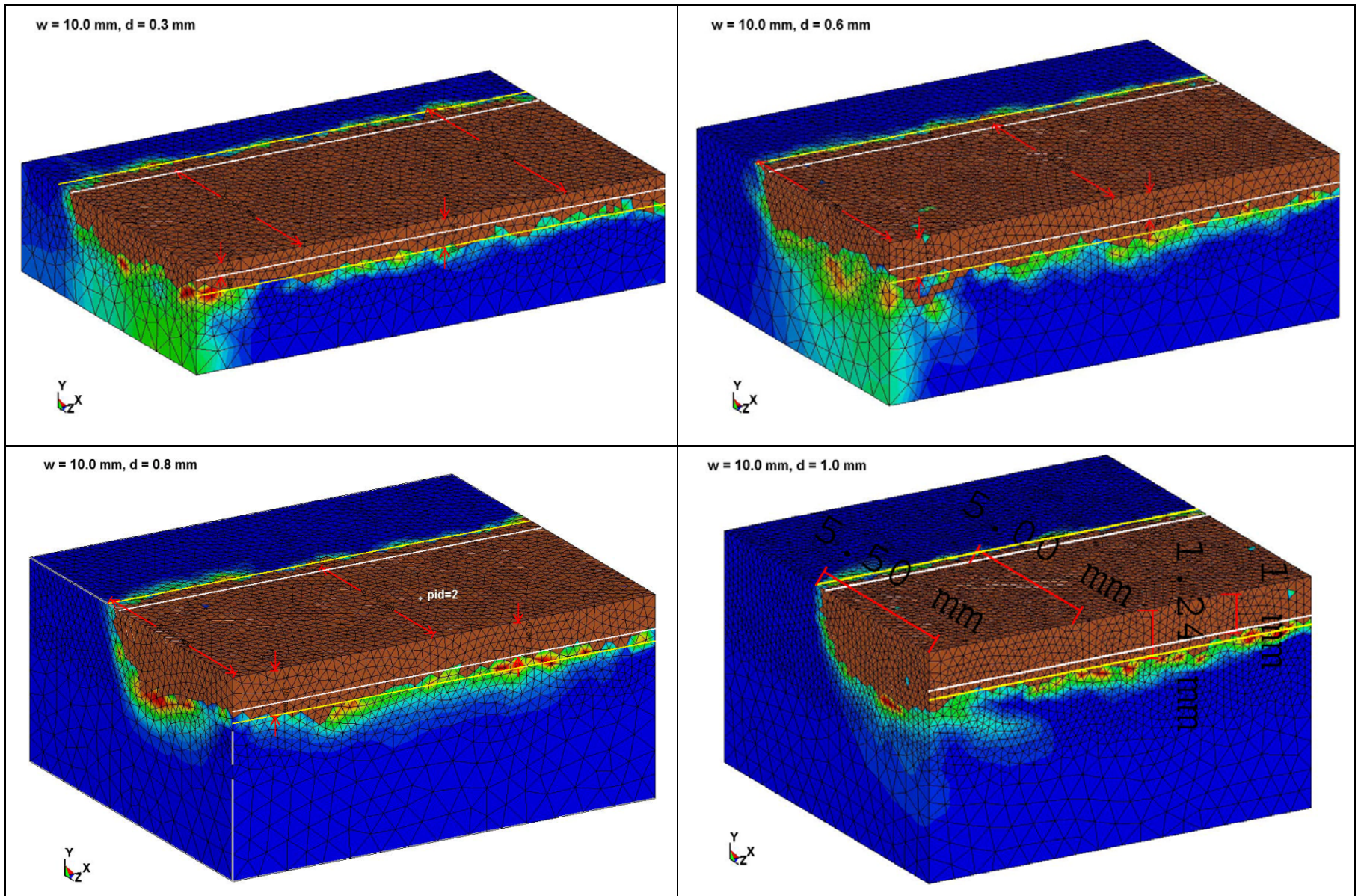


Figure 7-5: Visualization of deleted elements in groove-cut simulations: $w = 10$ mm, $d =$ variable (half model shown)

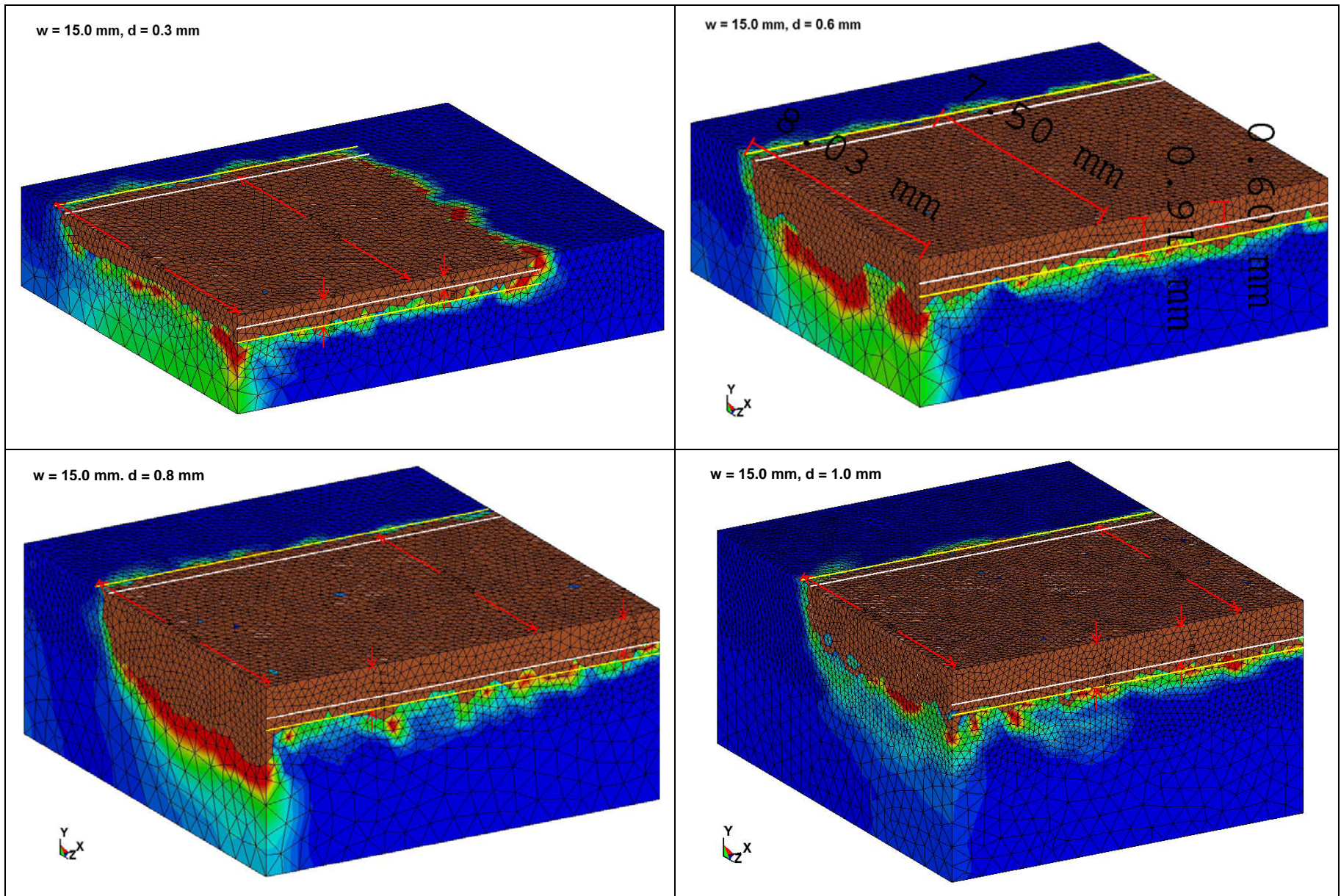


Figure 7-6: Visualization of deleted elements in groove-cut simulations: $w = 15$ mm, $d =$ variable (half model shown)

Like in the analysis of the slab cut simulations, three geometric indices are introduced here to quantify the amount of rock material that gets crushed. They relate the actual depth, width and area being crushed within a groove to its corresponding nominal dimension. These are:

$$d_{groove}^* = \frac{d^{crushed}}{d} \times 100\% \quad (7-3)$$

$$w_{groove}^* = \frac{w^{crushed}}{w} \times 100\% \quad (7-4)$$

$$A_{groove}^* = \frac{A^{crushed}}{A} \times 100\% \quad (7-5)$$

Figure 7-7 through Figure 7-9 show the plot of these quantities against nominal values in the simulated groove cut tests. Together with the visualization of the eroded elements within each groove's geometry, these graphs provide valuable information that indicates the occurrence of certain patterns that are not so straight forward.

It is clear from Figure 7-7(a) that by staying within the ductile failure mode range (i.e. shallow depths, less than 1.4 mm for Vosges Sandstone) the relationship between the nominal depth of cut and its corresponding actual eroded depth is perfectly linear. This linear behavior is independent of the width of cut. This figure also shows that by increasing the width of the cutter, the actual depth of cut slightly increases. This behavior is evidently less perceptible as the nominal depth of cut gets larger, as seen in Figure 7-7(b).

Figure 7-8 illustrates the values of actual crushed width (in magnitude and percentage) against the nominal width of cut. Although the four graphs in this figure seem identical, each one of them corresponds to a different cutting depth. There is no doubt that varying the cutter depth has practically no effect in the amount of actual eroded width. It can be observed that this lateral dimension is actually not too far from the 1-to-1 line, or the 100% line in relation to the nominal width, whereas the depth of cut indeed shows a significantly greater variation.

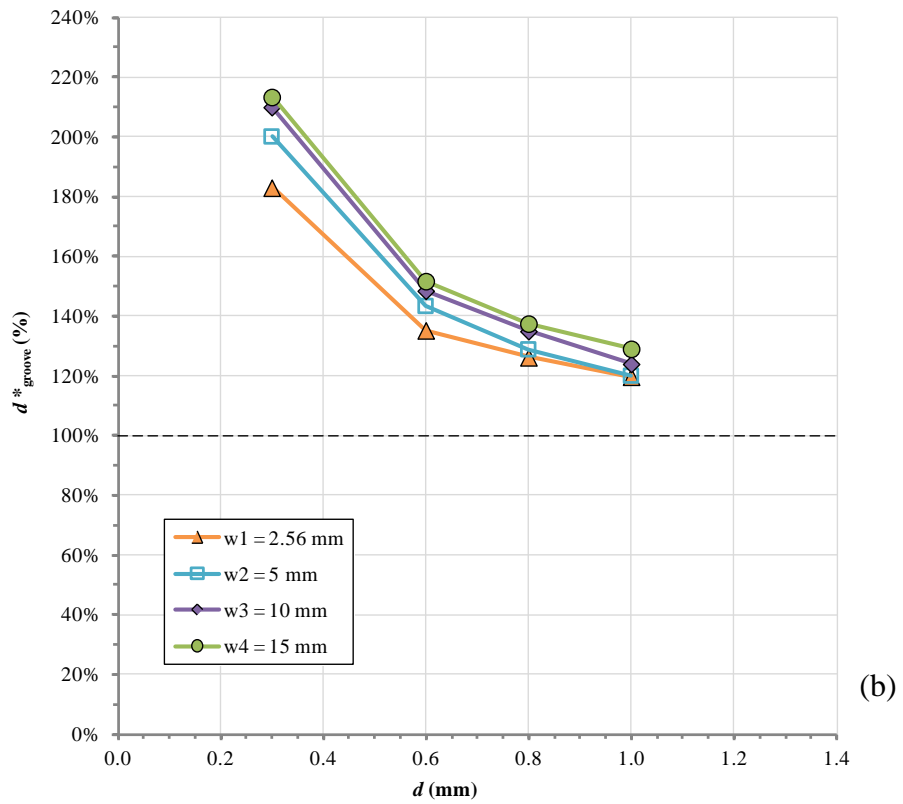
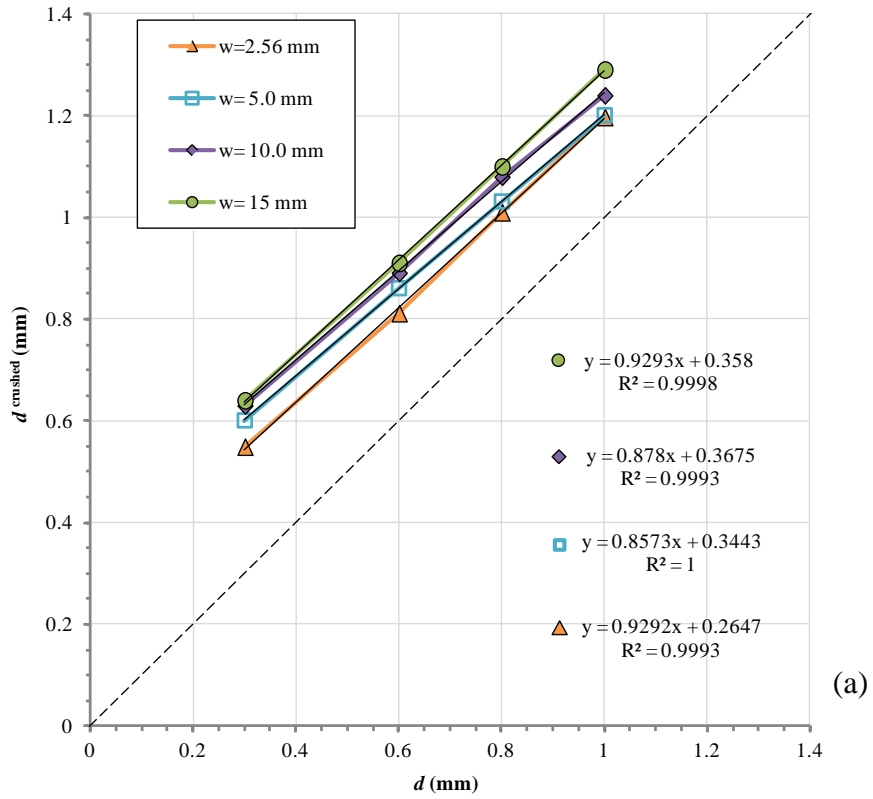


Figure 7-7: Measurement of crushed material with respect to nominal depth in groove cut simulations

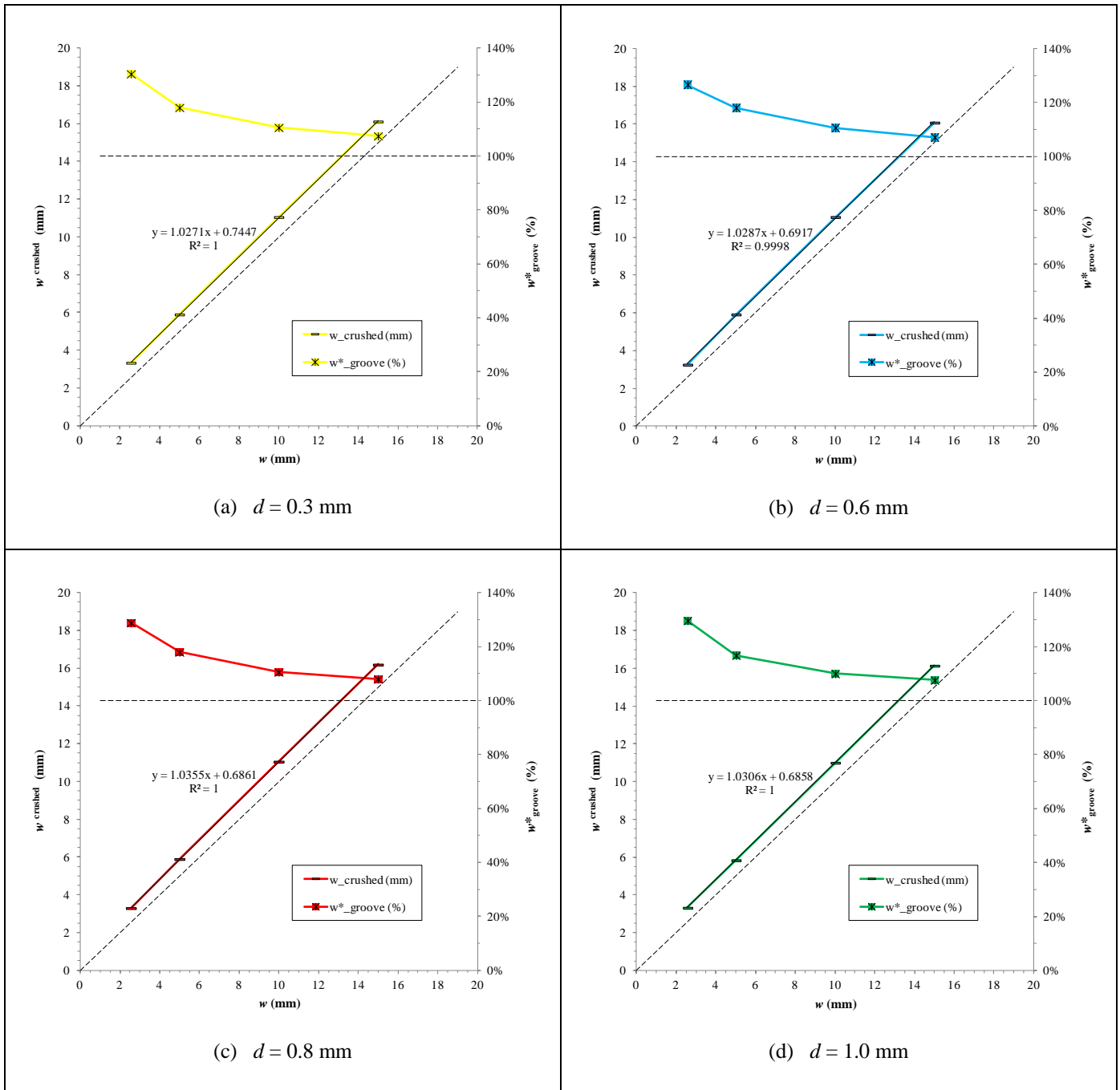


Figure 7-8: Measurement of crushed material with respect to nominal width in groove cut simulations

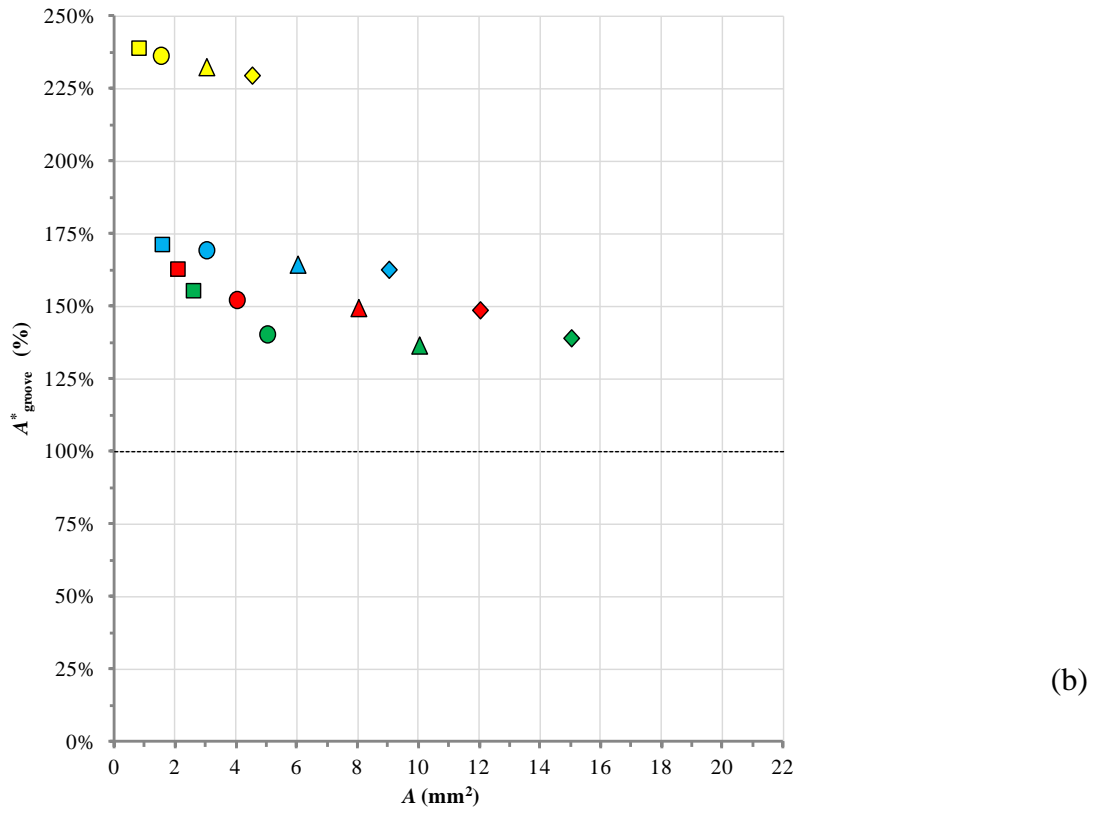
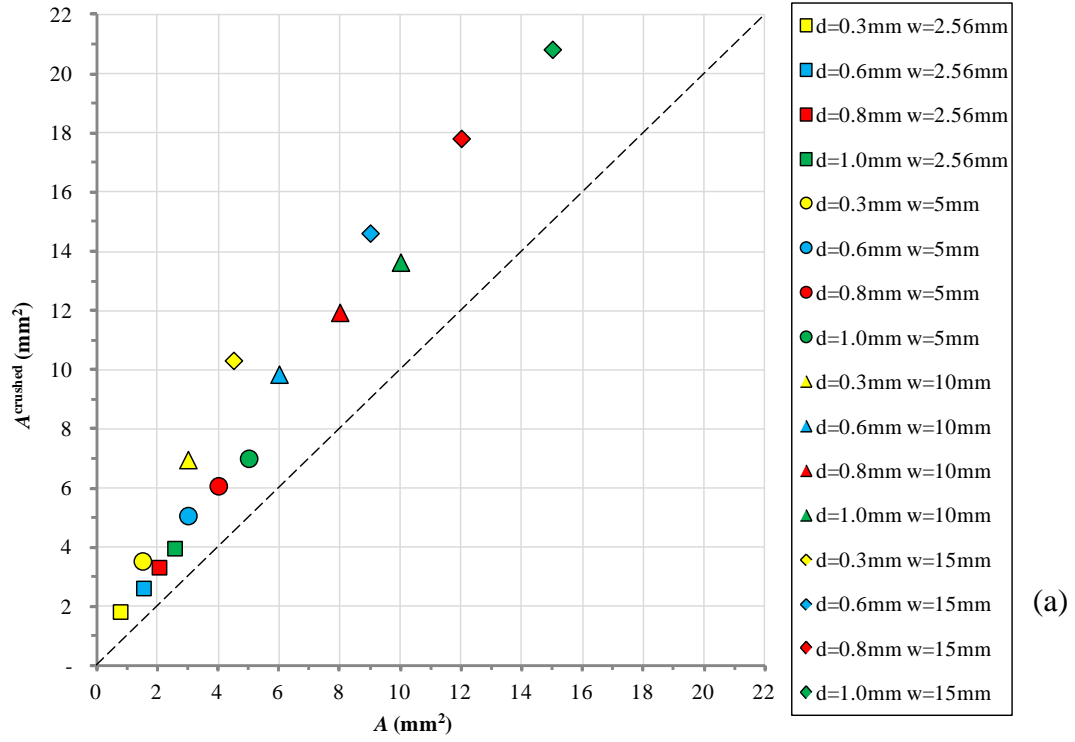


Figure 7-9: Measurement of crushed material with respect to nominal area in groove cut simulations

Taking advantage of the linear regressions presented in Figure 7-7(a) and Figure 7-8 for each set of runs, and following a similar procedure as the one summarized in Table 7-4, a couple of expressions are derived so that they characterize the actual amount of material eroded as a function of the nominal cutter dimensions during the groove cutting of Vosges Sandstone in the ductile regime.

$$d^{crushed} = 0.8985 d + 0.2402 w^{0.169} \quad (N) \quad (7-6)$$

$$w^{crushed} = 1.03 w + 0.702 \quad (N) \quad (7-7)$$

If order to identify the effect that these trends have in the actual area of cut, which will ultimately define the specific energy required to cut through a groove in rock, the data points in Figure 7-7 and Figure 7-8 have been compiled in Figure 7-9 in the form of *area*.

Overall, groove cuts with the smallest value of d (i.e. 0.3 mm) show the largest impact in the actual eroded material amount in relation to their nominal size, as reflected by the steepest trend of the yellow data points in Figure 7-9(a) and the highest percentages in Figure 7-9(b). On the other hand, larger nominal cutter sizes not only show a proportional reduced effect on the actual crushed area, but the trends also imply a convergence point where the minimum area crushed lies in the vicinity of 135% of the nominal area, which is seen for cutter widths greater than 5 mm and depths of cut greater than 0.8 mm.

7.4 SPECIFIC ENERGY IN GROOVE CUTTING

Following the same line of thought as described in Section 6.4 for the slab cutting simulations, the actual crushed area, $A^{crushed}$, as defined in Section 7.3 is used to calculate the specific energy for the groove cutting simulations in this study. Equation (6-5); is re- defined as:

$$\epsilon = \frac{F_{mean}}{A^{crushed}} = \frac{F_{mean}}{w^{crushed} \times d^{crushed}} \quad (7-8)$$

Table 7-5 summarizes the values of dimensions, mean horizontal cutting force and specific energy for the groove cut simulations in ductile regime.

Table 7-5: Output parameters for groove cut simulations in the ductile regime

Model ID	w (mm)	d (mm)	A (mm ²)	w^{crushed} (mm)	d^{crushed} (mm)	A^{crushed} (mm ²)	F_{mean} (N)	ϵ (MPa)
d1w1	2.56	0.3	0.77	3.34	0.55	1.84	20.77	11.31
d2w1	2.56	0.6	1.54	3.24	0.81	2.62	28.13	10.72
d3w1	2.56	0.8	2.05	3.30	1.01	3.33	35.74	10.72
d4w1	2.56	1	2.56	3.32	1.20	3.98	51.22	12.86
d1w2	5	0.3	1.5	5.90	0.60	3.54	33.18	9.37
d2w2	5	0.6	3.0	5.90	0.86	5.07	58.35	11.50
d3w2	5	0.8	4.0	5.90	1.03	6.08	68.35	11.25
d4w2	5	1	5.0	5.84	1.20	7.01	74.95	10.70
d1w3	10	0.3	3.0	11.06	0.63	6.97	64.82	9.30
d2w3	10	0.6	6.0	11.06	0.89	9.85	95.29	9.67
d3w3	10	0.8	8.0	11.06	1.08	11.94	124.21	10.40
d4w3	10	1	10.0	11.00	1.24	13.64	150.00	11.00
d1w4	15	0.3	4.5	16.12	0.64	10.32	97.76	9.48
d2w4	15	0.6	9.0	16.06	0.91	14.61	150.49	10.30
d3w4	15	0.8	12.0	16.20	1.17	18.97	179.49	9.46
d4w4	15	1	15.0	16.14	1.29	20.82	221.48	10.64
Average								10.54
Standard Deviation								0.96

Model ID	w (in)	d (in)	A (in ²)	w^{crushed} (in)	d^{crushed} (in)	A^{crushed} (in ²)	F_{mean} (lbf)	ϵ (psi)
d1w1	0.10	0.01	1.2E-03	0.131	0.022	2.85E-03	4.67	1639.8
d2w1	0.10	0.02	2.4E-03	0.128	0.032	4.07E-03	6.32	1554.7
d3w1	0.10	0.03	3.2E-03	0.130	0.040	5.17E-03	8.03	1555.2
d4w1	0.10	0.04	4.0E-03	0.131	0.047	6.18E-03	11.52	1864.8
d1w2	0.20	0.01	2.3E-03	0.232	0.024	5.49E-03	7.46	1359.6
d2w2	0.20	0.02	4.7E-03	0.232	0.034	7.86E-03	13.12	1667.8
d3w2	0.20	0.03	6.2E-03	0.232	0.041	9.42E-03	15.36	1631.2
d4w2	0.20	0.04	7.8E-03	0.230	0.047	1.09E-02	16.85	1551.2
d1w3	0.39	0.01	4.7E-03	0.435	0.025	1.08E-02	14.57	1349.2
d2w3	0.39	0.02	9.3E-03	0.435	0.035	1.53E-02	21.42	1402.4
d3w3	0.39	0.03	1.2E-02	0.435	0.043	1.85E-02	27.92	1508.2
d4w3	0.39	0.04	1.6E-02	0.433	0.049	2.11E-02	33.72	1595.0
d1w4	0.59	0.01	7.0E-03	0.635	0.025	1.60E-02	21.98	1374.3
d2w4	0.59	0.02	1.4E-02	0.632	0.036	2.27E-02	33.83	1493.5
d3w4	0.59	0.03	1.9E-02	0.638	0.046	2.94E-02	40.35	1372.3
d4w4	0.59	0.04	2.3E-02	0.635	0.051	3.23E-02	49.79	1542.9
Average								1528.9
Standard Deviation								138.7

Just as happened with the slab cutting cases of the present study, it can be seen in Figure 7-10(a) how the value of specific energy has a very small variation as a function of the cut area –having an average of 10.54 MPa (1,529 psi) and a standard deviation of 0.96 MPa (139 psi)– which can satisfactorily confirm that the value of ε can be interpreted as having an association with the material strength, as suggested by Richard et al. (1998). They indicate that there is a range of depth of cut that is characterized by a constant intrinsic specific energy, and that scratching should ideally take place in this range.

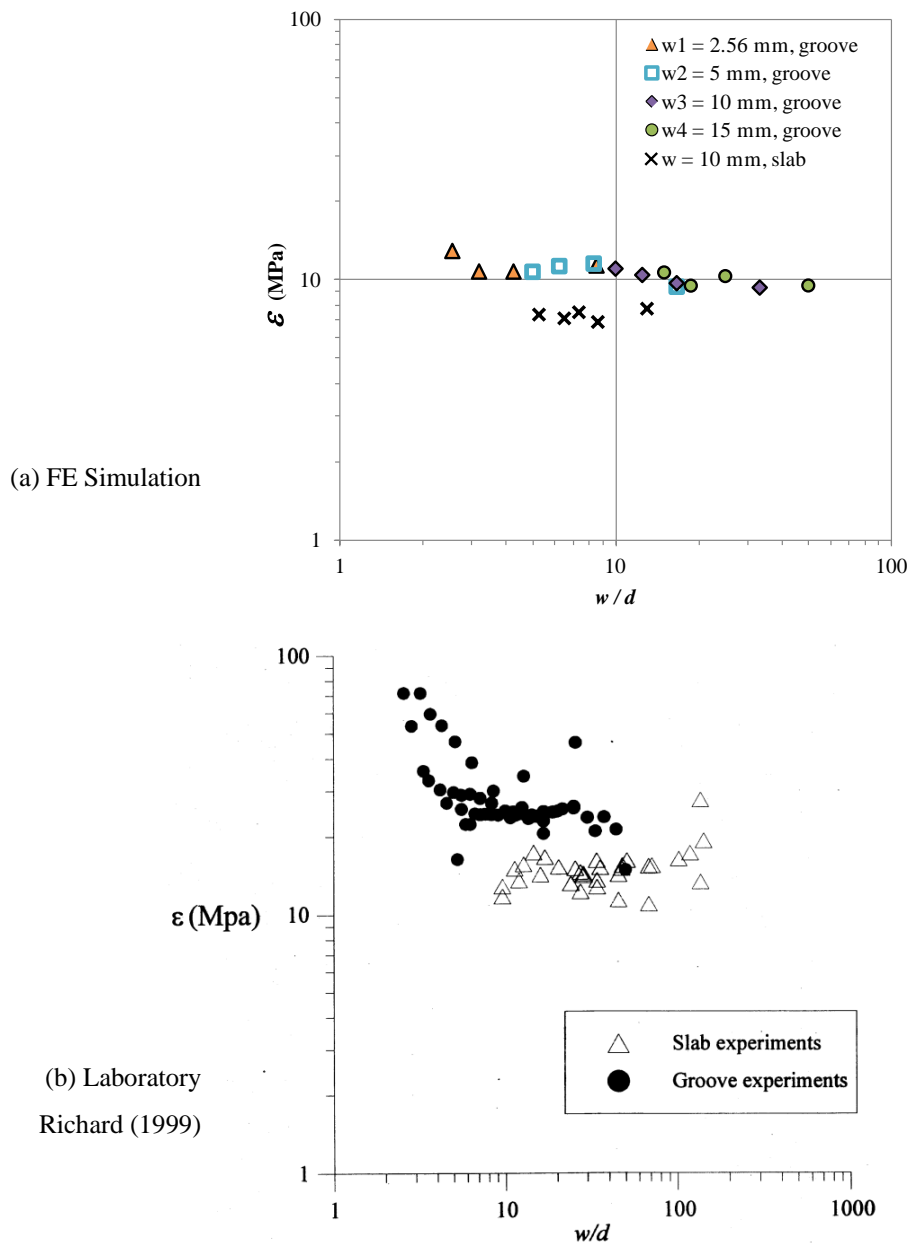


Figure 7-10: Specific energy as a function of w/d ratio: Simulation vs. Lab

It is apparent that the magnitude of the specific energy reported by Richard (1999) and shown in Figure 7-10(b) is greater than the specific energy obtained by the numerical simulations. The same situation is reflected in the comparison of groove cutting forces in Figure 7-2; however, this is significantly less obvious in the case for the slab cutting forces compared in Figure 6-8. Particularly within the ductile regime, the simulation forces compare well with the forces from slab cutting experiments. Since all the slab-cutting experiments are run on the same rock specimen (according to the sample preparation description provided in Richard's Master's thesis), it is likely that when doing groove cutting experiments, numerous external factors affect the outcome of the tests. The repeatability of the results has a low probability of occurrence when multiple rock specimens are tested and when human error plays a role.

Furthermore, it is believed that although the calibration efforts during this investigation have been vast, it would be necessary to expand the suit of rock materials modeled in order to have a stronger foundation for accurate prediction of force values. Nevertheless, the contributions made through the numerical models in the present work have been superlative as far as reproducing the rock behavior under numerous loading conditions, including the never-seen modeled fracture propagation and chip formation. More importantly, these features help to understand the entire physical phenomena that takes place during the rock cutting process, and consequently could aid in achieving a cost-effective means to develop optimum PDC drill bits under extreme conditions.

7.5 EDGE EFFECT IN GROOVE CUTTING

The graph shown in Figure 7-10(a), relating the specific energy and w/d ratio for the numerical simulations, is presented in logarithmic scale for comparison purposes; however, if one would like to focus on a potential trend of these values, it would be convenient to plot the same graph in linear scale as shown in Figure 7-11.

In agreement with Richard's findings, these results suggest that there is a three-dimensional effect which could be identifiable when the ratio w/d is less than 10. With w/d greater than 10, the groove-cut data have a tendency to converge asymptotically to the specific energy obtained for the slab-cut simulations, which would be the minimum value for this specific

rock type. This implies that when $d \rightarrow 0$, the groove-cut force with essentially no sides, would yield the same result as the slab-cut force, for a given width of cut.

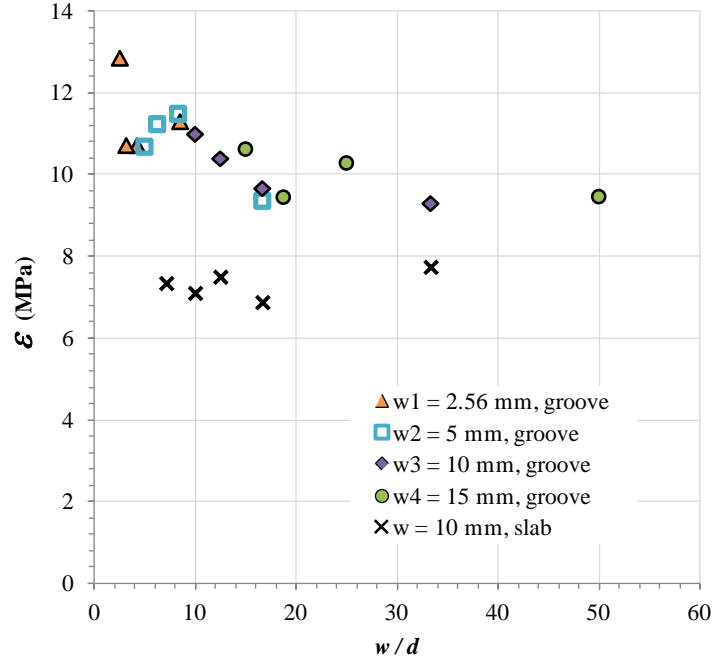


Figure 7-11: Specific energy as a function of w/d ratio in FE simulations

The previous statement could be verified by using the expressions (regressions) derived for both slab-cut and groove-cut forces as function of the cutter nominal dimensions –in the ductile regime. Recalling the regression for slab-cut mean forces from Figure 6-9, the corresponding normalized force with respect to the 10-mm cutter width is:

$$\frac{F_{slab}}{w} = \frac{1}{10}(-7.96 d^2 + 87.95 d + 33.15) \quad (7-9)$$

Conversely, for groove-cut mean forces, Equation (7-2) can be re-written as:

$$\frac{F_{groove}}{w} = 11.96 d + 3.07 \quad (7-10)$$

where the units for both of the expressions above are Newton / millimeter.

Based upon the hypothesis that Equations (7-9) and (7-10) should result in the same value when evaluating $d \rightarrow 0$, it is convenient to average the independent constant in both equations (i.e. specifically 3.315 and 3.07) and fixing it to a value of 3.2 in order to adjust the regressions that characterize the slab-cut and groove-cut forces. As a result, after going back to the data plots that yielded these two regressions, and forcing the intercept to be at $F_{mean} / w = 3.2$, the tuned expressions are:

$$\frac{F_{slab}}{w} = \frac{1}{10}(-8.28 d^2 + 89.38 d + 32) \quad (7-11)$$

$$\frac{F_{groove}}{w} = 11.83 d + 3.2 \quad (7-12)$$

Graphing Equations (7-11) and (7-12) simultaneously provides a better representation of the effect of the vertical sides when cutting a groove in rock.

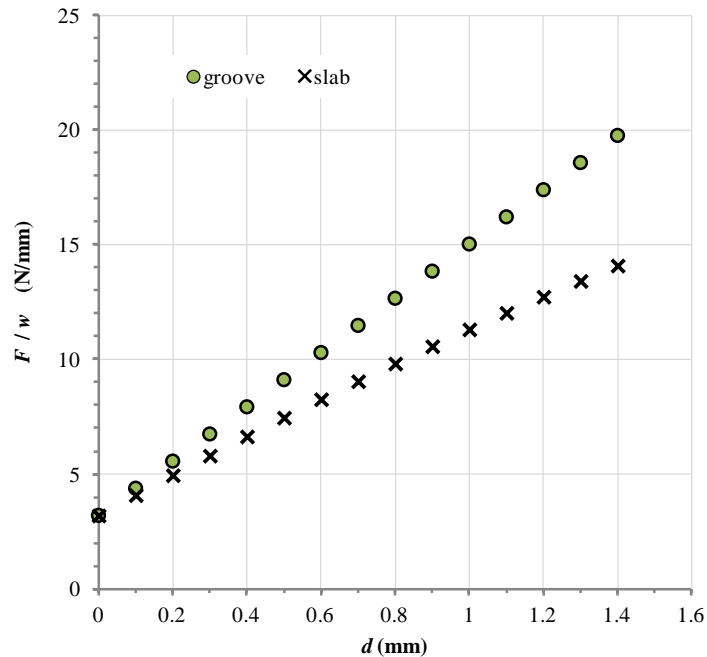


Figure 7-12: Variation of normalized forces in slab and groove cutting as a function of depth

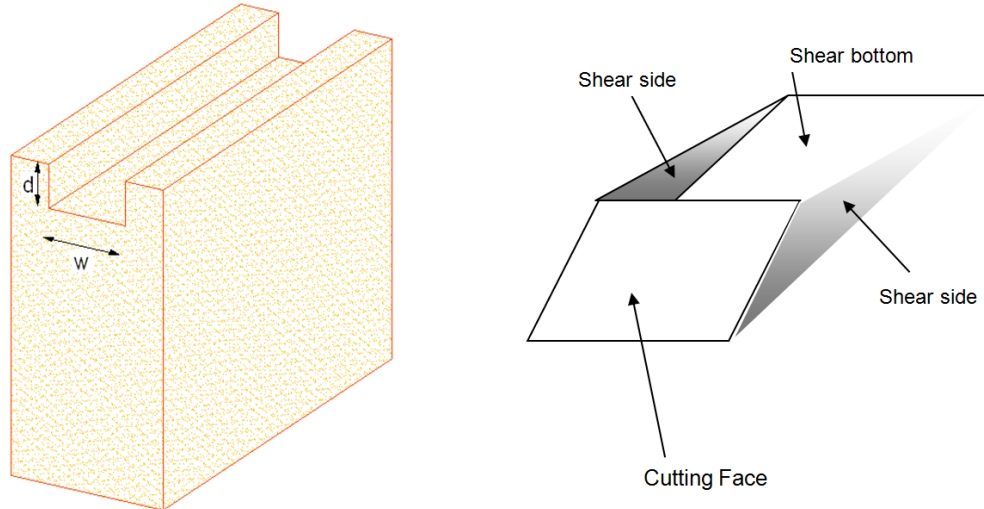


Figure 7-13: Groove cutting sketch

Considering the fact that the horizontal cutting force in the groove should counteract the resistance from both the bottom (as in the slab cut) and the groove sides as illustrated in Figure 7-13, the expressions in Equations (7-11) and (7-12) are utilized to derive a final equation to relate the slab-cut and groove-cut forces:

$$\frac{F_{groove}}{w} = \frac{F_{slab}}{w} (1 + 0.516 d - 0.173 d^2) \quad (7-13)$$

where the force units are Newtons and dimensions units are millimeters. The terms $(0.516 d - 0.173 d^2)$ are clearly associated with the shear resistance that the groove sides impose, which is thought to be dependent not only on the rock shear strength parameters (cohesion and friction angle), but also on the cutter's rake angle.

8.0 GROOVE CUTTING IN ROCK UNDER PRESSURE

Having obtained a sound FE model to simulate the rock cutting and fragmentation process in a realistic manner, it is possible now to utilize this in an attempt to model the high pressure conditions of a drill bit at bottom-hole. Yet, a new additional challenge to undertake this goal is the difficult implementation of an environment pressure within the numerical models of rock cutting in LS-DYNA.

The rock material model has been calibrated and its performance is satisfactory upon standard quasi-static tests with increasing confinement pressure (see Section 4.5). Nonetheless, there has been no explicit methodology so far reported in the literature concerning the use of ambient pressure during a highly dynamic cutting simulation with a lagrangian finite element model. Several alternatives were explored within the framework of LS-DYNA's capabilities. This section describes a numerical technique found to positively provide the presence of fluid pressure during the rock cutting process under extreme conditions.

The focus of this investigation now turns onto a different experimental investigation reported in the literature, i.e., the work performed by Kaitkay and Lei (2005). A preliminary three-dimensional FE model has been developed to simulate three different scenarios from the laboratory study of the rotational cutting of rock under varying hydrostatic pressures. Although not all the experimental variables are modeled identically (e.g., rock material type), this effort is aimed at emulating the proper rock response trend in a qualitative fashion, rather than quantitatively.

8.1 EXPERIMENTAL BENCHMARK OF GROOVE CUTTING UNDER PRESSURE

Kaitkay and Lei (2005) performed machining experiments on Carthage Marble samples at atmospheric pressure and under different hydrostatic pressures using a single PDC cutter. Part of their objectives was to study the variation of cutting forces with respect to depth of cut, cutter rake angle, and hydrostatic pressure.

8.1.1 Experiment Setup

As described in detail in their paper, Kaitkay and Lei have two separate settings for their experiments at both atmospheric and confining pressures. Herein, only the setup of the tests subjected to pressure is modeled, and thus accounted for as follows: The Carthage Marble sample is placed into a pressure vessel in which external hydrostatic pressure is maintained using a set of pumps. A rigid frame supports the pressure vessel –that can withstand pressures up to 69 MPa (10,000 psi)– and the drive unit. Two motors impart rotary motion to a rotating rod, which in turn drives the cutting tool. The feed rod can also move vertically, and is equipped with strain-gage-based load cell to transmit signals for the main (horizontal) and thrust (vertical) force components exerted on the cutter. The cutting tool is shown in Figure 8-1. The modeled rake angle used in the experiments is 15 degrees.

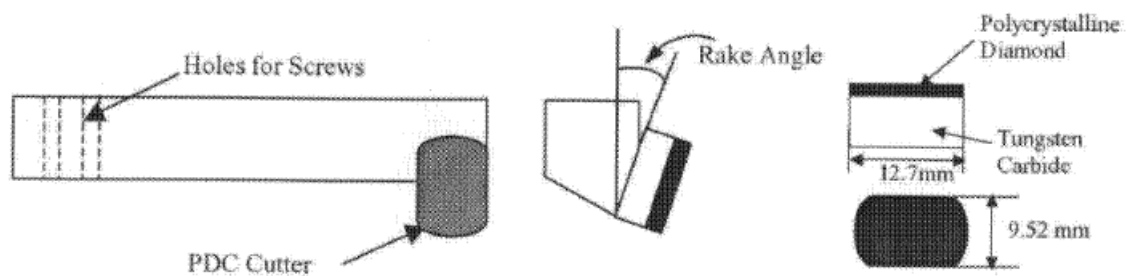


Figure 8-1: Cutting tool for confined experiments of rock cutting (Kaitkay and Lei 2005)

The cutter is mounted on the test machine at a distance of 35 mm (1.375 in) from the center and rotates around the center at 273 rpm, resulting in a speed of the cutter tip equal to 1 m/s. The steady cutting depth maintained during each revolution corresponds to 0.8 mm. Cutting forces are collected at a sampling rate of 500 points/s during 6 seconds for each test. The system also collects data for the water pressure during the test.

Some of the tests run by Kaitkay and Lei include rock cutting at atmospheric pressure – i.e. 0.1 MPa (14.7 psi)–, 3.44 MPa (500 psi), and 34.4 MPa (5,000 psi). Their results are shown below.

8.1.2 Experimental Results

Figure 8-2 shows a typical force history for cutting under hydrostatic pressure, in this case 34.4 MPa (500 psi).

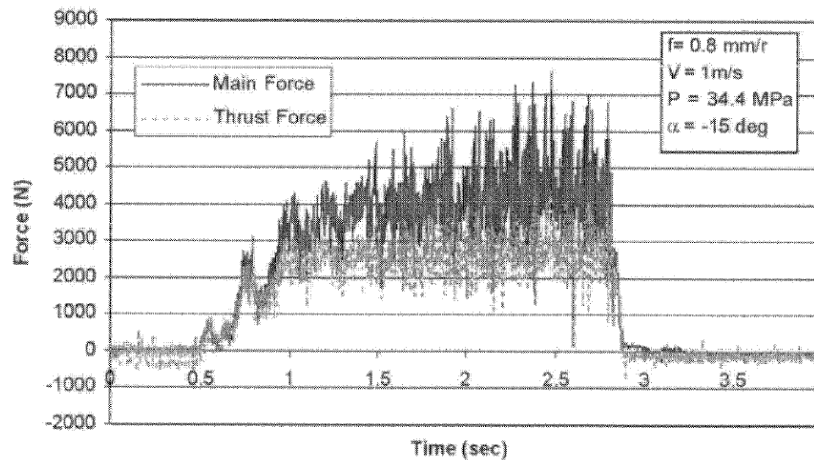


Figure 8-2: Experimental cutting forces at a 34.4-MPa confinement pressure (Kaitkay and Lei 2005)

The reported average values of force in Figure 8-3 consider only the force signal after the cutter has traversed a vertical distance of 2.3 mm (0.084 in). It can be observed in this figure that the mean cutting force increases significantly with the application of pressure. According to Kaitkay and Lei, this behavior is accompanied by an increase in chip length. They state that the presence of external hydrostatic pressure can transform the rock cutting process from a dominantly brittle fracture to an intermediate ductile-brittle mode.

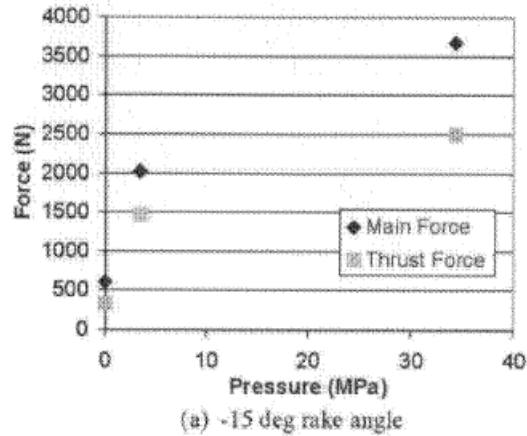


Figure 8-3: Experimental average force as a function of hydrostatic pressure (Kaitkay and Lei 2005)

Among their findings they claim that the cutting forces increase with increasing negative rake angle and hydrostatic pressure. Additionally, they conclude that shear failure increases when applying external pressure, resulting in more shear flow during chip formation. They obtained larger rock chips, which they attribute to the plastic chip formation induced by applied confining pressures.

8.2 NUMERICAL SIMULATION OF PRESSURED GROOVE CUTTING IN ROCK

As stated above, the models developed in this stage of the present investigation are aimed at establishing a foundation for future research of rock cutting under pressure. The comparison of the results from the numerical simulations and the laboratory tests should be considered only for illustration purposes. These FE models under pressure include the implementation of the same Vosges Sandstone material calibrated in Section 3.2.4, as well as the simulation of a linear scratching test at a depth of 0.8 mm, as opposed to modeling Carthage Marble (which is actually limestone) and a rotational scratching test.

The essential contribution from this section is providing a methodology, using LS-DYNA's optional features, capable of simulating the transient problem of rock cutting as presented in previous chapters, but in this case adding the presence of pressure in the environment during the tests.

8.2.1 Model Geometry

8.2.1.1 Rock Specimen Geometry

Like in the simulations presented in Section 7.0, brittle fragmentation is not expected throughout these new set of rock cutting tests, thus the rock model does not require a great dimension in the vertical direction. Figure 8-4 depicts the size and mesh configuration of this rock specimen, which is identical to the model identified as d3w3 in the previous section (see Section 7.1.1). The average element size in the cutting zone is 0.143 mm (0.079 in), the total number of nodes is 23,635 and the total number of elements is 128,867.

Once again, only half of the actual sample thickness is modeled in order to save on computational time; yet, the cutting forces reported are adequately proportioned to the full thickness. In this regards, (half of) the groove is cut along the longitudinal (x-axis) edge of the rock model, and the results are interpreted by mirroring the model with respect to the xy-plane highlighted in Figure 8-4.

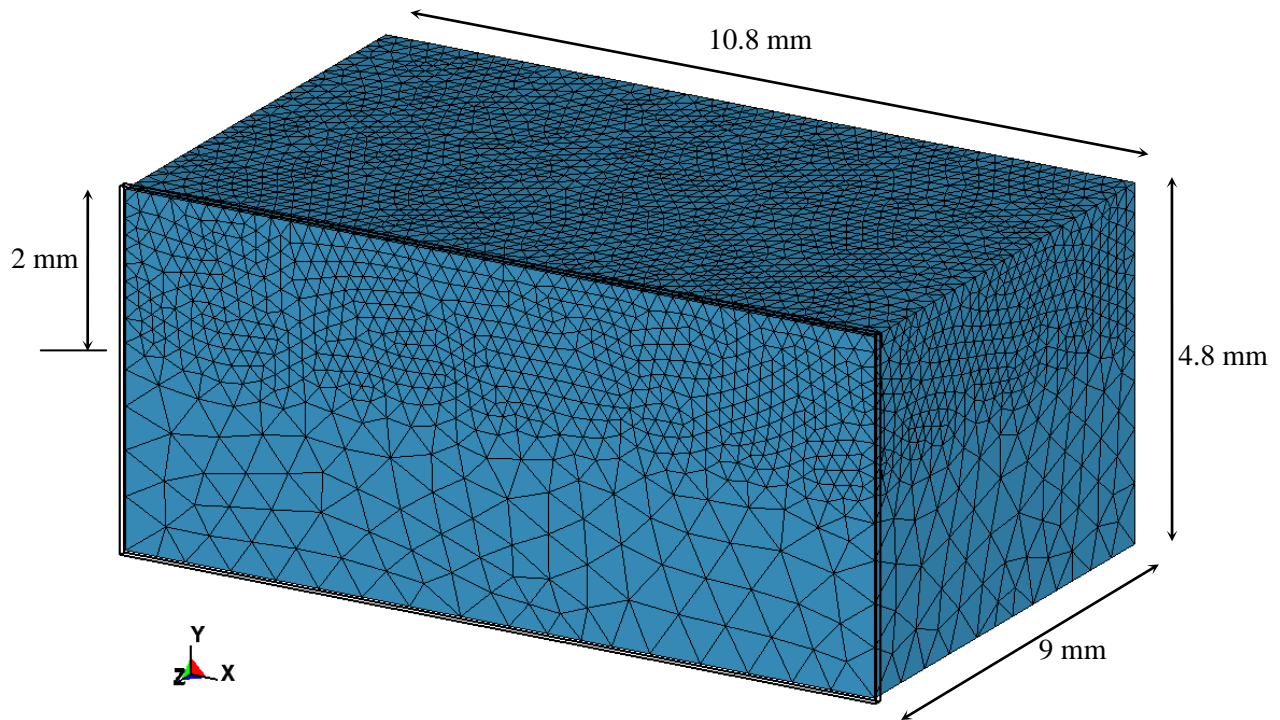


Figure 8-4: Rock model geometry for groove cutting under pressure

8.2.1.2 Cutter Geometry

The cutter for the groove cutting simulations under pressure is modeled to resemble the PDC used in the laboratory experiments, as can be observed in Figure 8-1. Mimicking the actual size of the PDC, the cutter used in the simulations is an entire cylinder, whereas it is trimmed in the laboratory. In addition, it is tilted 15 degrees forward (negative rake angle), such as the experimental configuration

Due to the use of RIGIDWALL as the contact model between the cutter and the rock (see Section 5.2.1.2), there is no need for discretization of the mesh that comprises the cutter body. Nevertheless, in order to create a cylindrical shape for the PDC cutter, its mesh is actually made out of 1,064 hexahedral elements, and 2191 nodes, as can be seen in Figure 8-5.

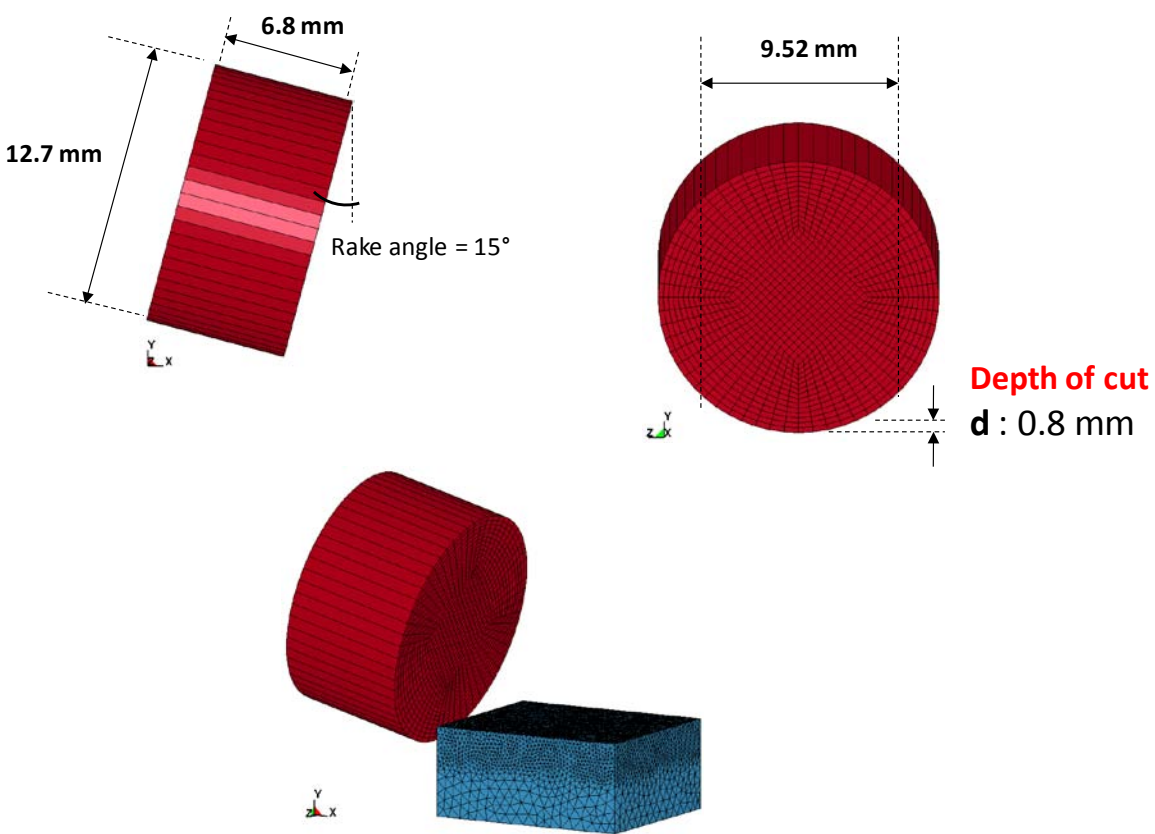


Figure 8-5: Cutter geometry for groove cutting under pressure

8.2.2 Application of Hydrostatic Pressure

Typically, for a (static) finite element model that requires application of pressure as a boundary condition, the finite element codes easily allow the definition of a pressure value that is fundamentally transformed into a localized nodal force, or load on an integration point. If this technique were to be used in the particular case of the rock cutting model as developed in the present work, however, a problem arises due to the erosion of elements from the continuum. Since any defined load would be directly applied to the initially-exposed surfaces of the rock, it would be lost once the loaded surface is eroded, causing the newly-exposed elements to be free of pressure. Hence, an alternative solution for the application of pressure is needed.

LS-DYNA seems to contain numerous options that theoretically meet the requirement of modeling the rock elements with a constant surrounding pressure regardless of their position within the numerical domain. In an attempt to find an effective mechanism to apply hydrostatic pressure to the model, some of these options were explored, such as `INITIAL_STRESS_SOLID`, `BOUNDARY_PORE_FLUID`, and `LOAD_DENSITY_DEPTH`. At the time when this effort was carried out, several issues were found when trying to implement the first two options just mentioned.

As far as the `INITIAL_STRESS_SOLID` option, it is designed to initialize the stresses and plastic strains for solid elements during the dynamic relaxation stage. The user defines explicitly the value of the six components of stress in an element for as many elements as desired. Although the input parameters in this option were meticulously and repeatedly set up, during dynamic relaxation –while ramping up the stress values over time– the rock material always experienced the excitation of a high frequency response. Also, although supposedly achieving equilibrium, the rock model always finished up with tensile stresses in the vertical direction. Due to these issues, this option was discarded.

On the other hand, the `BOUNDARY_PORE_FLUID` option seemed to have a good potential for the sought application. It is designed to define “parts” (i.e. solid entities in LS-DYNA) that contain pore fluid and apply a calculated hydrostatic pore water pressure on their elements. It considers drained or undrained conditions, the vertical coordinate of the water table, the density of the pore water, the gravitational acceleration, among others parameters. Unfortunately, the model was never able to run while using the definition of this option in the

input deck. As soon as the simulation started, it stopped without any warning or error message. It is believed that this option was not well implemented in LS-DYNA at the moment.

Consequently, the `LOAD_DENSITY_DEPTH` was the numerical resource used in this work. This option of LS-DYNA defines density versus depth for gravity loading, and it has been occasionally used for analyzing underground and submerged structures where the gravitational preload is important (Hallquist 2009). Its purpose is to initialize the hydrostatic pressure field at the integration points in all the elements comprising a part.

A density-vs.-depth curve is used as the input to initialize hydrostatic pressure due to gravity acting on an overburden material. The hydrostatic pressure acting at a material point at depth, D , is defined by Hallquist (2009) as:

$$p = - \int_D^{D_{surface}} \rho(z) g \, dz \quad (8-1)$$

where $D_{surface}$ is the depth of the surface of the material to be initialized (usually zero), $\rho(z)$ is the mass density at depth z , and g is the acceleration of gravity. This integral is evaluated for each integration point. According to LS-DYNA User's Manual (Hallquist 2009), "depth may be measured along any of the global coordinate axes and the sign convention of the global coordinate system should be respected. The sign convention of gravity also follows that of the global coordinate system."

It is important to note that by following the sign convention instructions above, the pressure that the elements are subjected to has a positive sign (denoting compression), while the x , y and z components of the elements' computed stress have a negative sign (denoting compression too). This leads to the assumption that the negative sign shown in Equation (8-1) is not properly implemented in the code, and may cause misinterpretation of the pressure input definition.

8.2.2.1 Important considerations to define `LOAD_DENSITY_DEPTH`

The following methodology is implemented in order to configure the input parameters in each one of the simulated rock cutting tests under different pressures:

Knowing a priori the magnitude of hydrostatic pressure desired for application over the rock part, the values of depth in the density-vs.-depth curve are determined assuming the existence of a column of water which will produce such a pressure. The coordinate system in the model is established so that the datum ($z = 0$) is located at the top surface of the rock part. Taking this into account and considering the actual thickness and density of the rock part, as well as the density of water, the only unknown is the actual water table coordinate, $D_{surface}$, which can be back-calculated. The sketch presented in Figure 8-6 helps to visualize the concept behind `LOAD_DENSITY_DEPTH`.

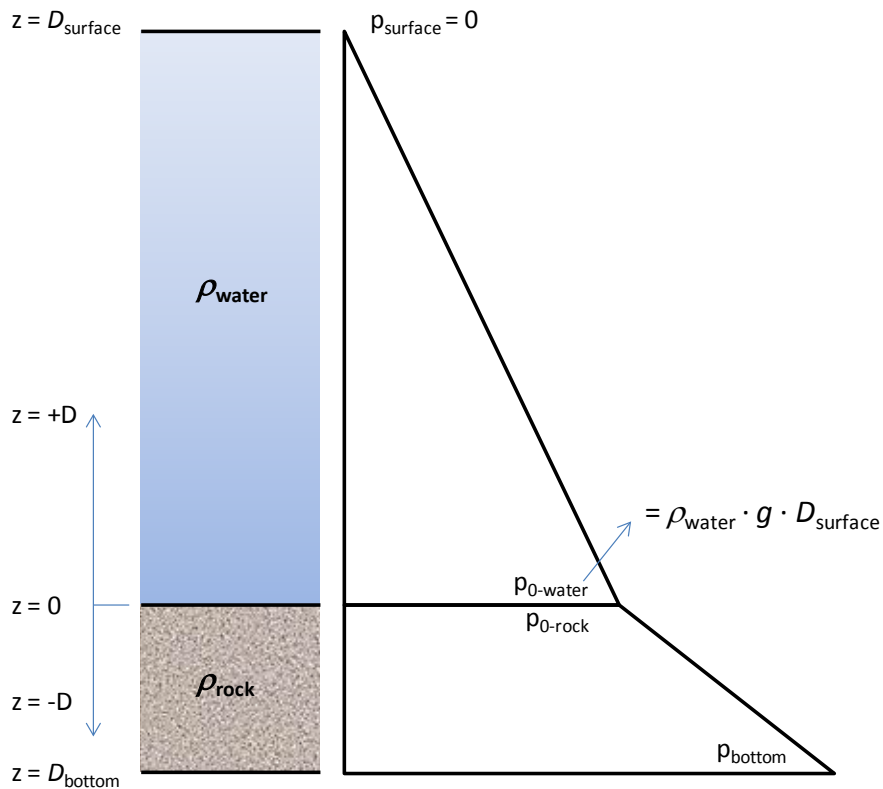


Figure 8-6: Interpretation of hydrostatic pressure for definition of `LOAD_DENSITY_DEPTH`

It is clear that right at the interface between the water bottom and the rock top surface, a continuous condition for the value of pressure should be satisfied, thus $p_{0-water} = p_{0-rock}$. With this in mind, caution should be taken when defining the density-vs.-depth curve because consecutive values, either in the abscissa or the ordinate, cannot be the same, as can be seen in Figure 8-7. Additionally, the thickness of the rock part used in the developed models is

significantly less (by several orders of magnitude) than the head of water necessary to produce the desired pressures; therefore, it is assumed that $p_{0-rock} \approx p_{bottom}$.

Known parameters in Figure 8-6 are:

- $\rho_{water} = 1,000 \text{ kg/m}^3$ (62.4 lb/ft³),
- $\rho_{rock} = 2,000 \text{ kg/m}^3$ (124.9 lb/ft³),
- $D_{bottom} = -4.8 \text{ mm}$ (-0.19 in),
- $g = 9.81 \text{ m/s}^2$ (32.2 ft/s²), and
- $p_{0-water}$, which varies with each specific test (e.g., 3.44 MPa, 34.4 MPa, etc.).

Following the premises mentioned above, the density vs. depth curve should look like:

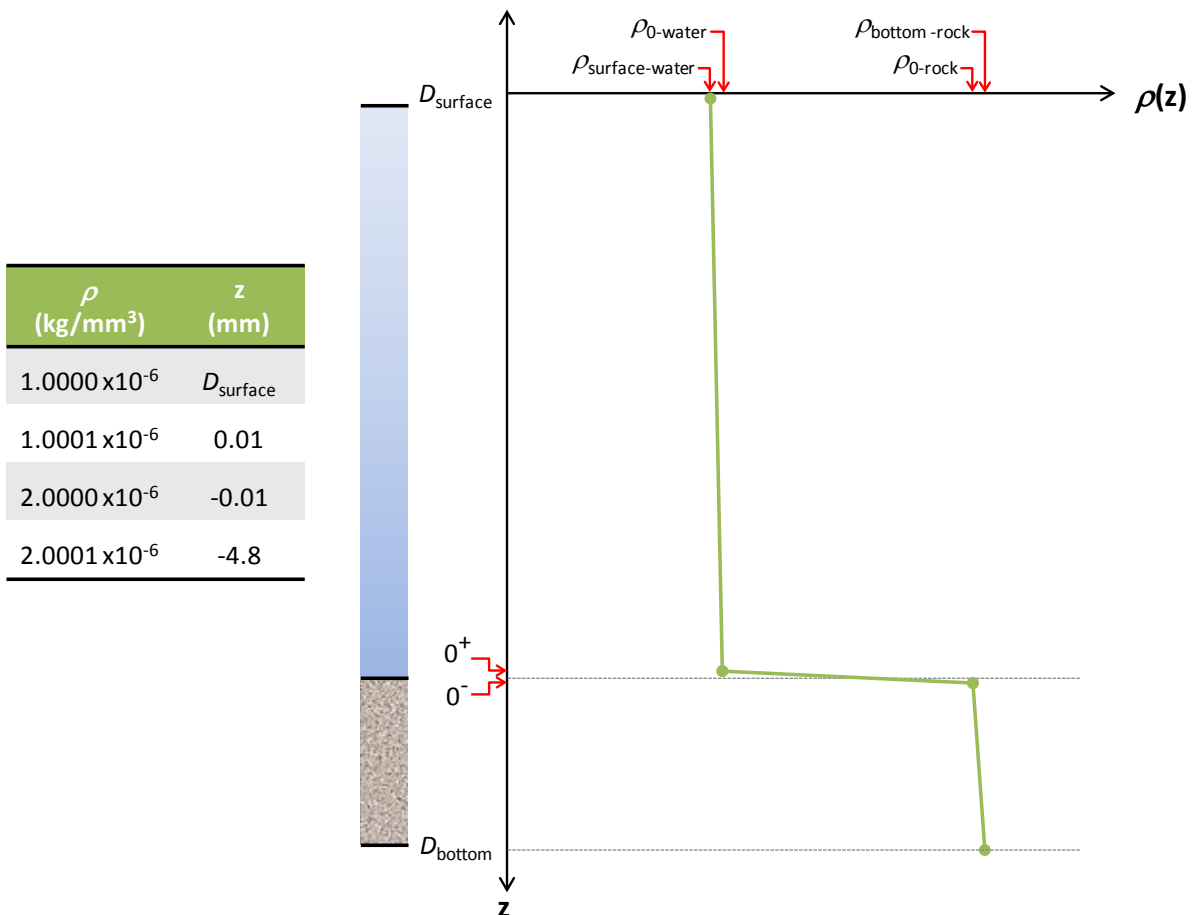


Figure 8-7: Density vs. depth curve for use in LOAD_DENSITY_DEPTH definition

Based upon the desired magnitude of pressure to be applied on the rock cutting test, the value of $D_{surface}$ is solved by:

$$D_{surface} = \frac{p_{0-water}}{\rho_{water} \cdot g} \quad (8-2)$$

Table 8-1 tabulates the solved values for $D_{surface}$ to be used in each model's definition of pressure application.

Table 8-1: Calculated values of $D_{surface}$ corresponding to each modeled pressure

Hydrostatic Pressure during Test MPa (psi)	$D_{surface}$ mm
3.44 (500 psi)	350.7×10^3
34.4 (5,000 psi)	$3,507 \times 10^3$
100 (14,504 psi)	$10,194 \times 10^3$

8.2.2.2 Additional Recommendations

As a result of a comprehensive review on the proper implementation of this pressure application feature in LS-DYNA, the following strategies should be taken into account:

- Any hydrostatic pressure applied onto the model must be incorporated during the dynamic relaxation phase of the simulation. The duration of this phase should be manually adjusted to guarantee that equilibrium of stresses is reached (by checking the internal energy dissipation). The maximum simulation time allowed in the 100-MPa case to reach equilibrium is 0.25 ms, for instance.
- In order to avoid excitation of the rock elements due to a high frequency response during the dynamic relaxation phase, it is recommended to increase temporarily the value of the coefficient of global damping, so the time to reach equilibrium is as short as possible. In this particular case, a damping vs. time curve was implemented, having a damping

constant of 50 over the dynamic relaxation duration (i.e. first 0.25 ms), and then changed to 1.0×10^{-8} for the duration of the transient analysis.

- Due to the extremely small size of the rock part, in comparison with the water head, the value of rock density is insignificant in the computation of the pressure over the material in this particular set of simulations. However, for other applications in general, it is important to keep in mind that the “saturated” density of the rock has to be used in the definition of pressure, not the “dry” density.
- It was found that once equilibrium was reached during the dynamic relaxation phase, the values of element pressure and stress converge to a value somewhat smaller than the specified through the definition of `LOAD_DENSITY_DEPTH`. This behavior was experienced with both a linear elastic isotropic material (i.e. `MAT_1`) and `MAT_159`, leading to think that there is a bug in the code of this option in LS-DYNA. A work-around has to be used in which the value of $D_{surface}$ has to be iteratively adjusted in order to yield the desired magnitude of pressure in the model.

8.2.3 Pressured Groove Cut Simulation Output

The results of the preliminary simulations of rock cutting subjected to external pressure exhibit general material behaviors that are in agreement with some of the observations and statements made by the authors of the experimental study described in Section 8.1.2, as well as other investigators in the subject of rock cutting under pressure. Figure 8-8 shows some of the most relevant results as a function of the applied hydrostatic pressure. It includes illustrations of the level of element damage when the cutter displacement is 7mm (0.27 in) on the left hand side, and the horizontal cutting force history on the right.

On one hand, it can be easily appreciated that with increasing pressure on the rock, the level of damage is reduced on the newly-exposed surface –once the cutter has passed– as well as in its surrounding elements. It is worth to reiterate that the computed level of damage is fundamentally a representation of the formation of microcracks in the loaded rock, which eventually coalesce and produce the rock matrix breakdown while in the ductile regime (which is part of the element crushing so far referred to).

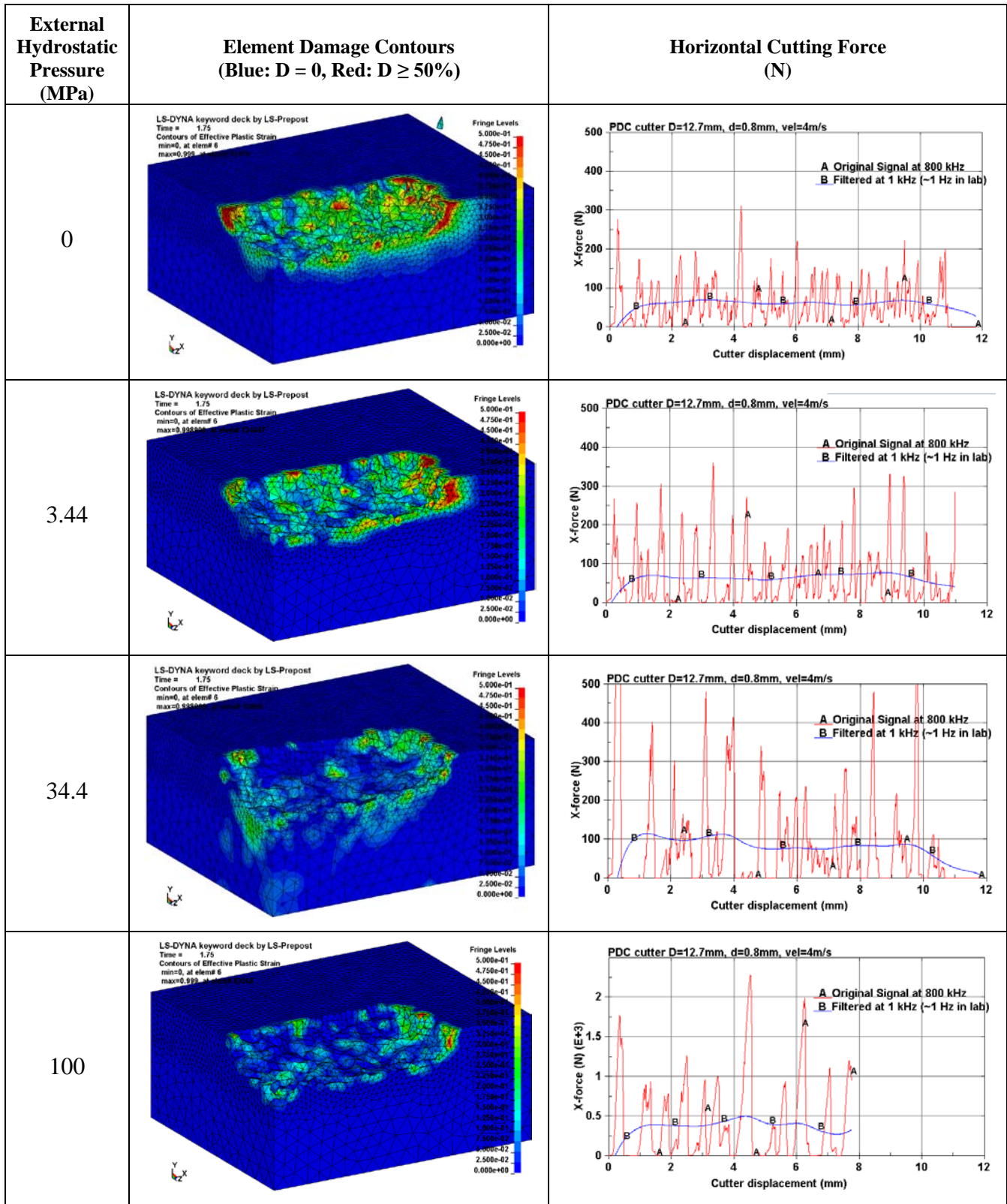


Figure 8-8: Simulation results during rock cutting under different hydrostatic pressures

This damage-reduction phenomenon, as presented in Figure 8-8, can be explained within the framework of a *cataclastic deformation mode* as described by Paterson and Wong (2005). They affirm that the “increase in confining pressure not only makes microcrack growth more difficult but the growth that is produced under the higher stresses now applied tends to be stabilized, eventually leading to sufficient disintegration or fragmentation of the specimen by proliferation of stable microcracks”, which also explains the increased amount of eroded material, as seen in Section 8.3, as the pressure is elevated.

As can be seen in Figure 8-8, the horizontal cutting force signals for each pressure case simulated make it evident that with larger hydrostatic pressure, the force magnitude increases (mean values are shown in Figure 8-12). Also, when the pressure is higher, the peak forces tend to concentrate and last (or be sustained) longer, demonstrating a gradual increase of the localization of plastic deformation. In other words, the fewer drops of the force signal with increasing pressure are associated with larger “energy-releasing events” of material crushing, which is confirmed by the irregular, step-like form of the accumulated eroded internal energy history output by LS-DYNA (see Figure 8-9). Observations of the same phenomenon are discussed by Garcia-Garavito (1998), who obtains smaller force fluctuations while increasing the confining pressure in his rock-cutting experiments. Furthermore, Kaitkay and Lei’s remarks (mentioned in Section 8.1.2) regarding the rock chip size after their experiments are also validated with these numerical simulation results.

8.3 EROSION AND SPECIFIC ENERGY FOR PRESSURED GROOVE CUT SIMULATIONS

As opposed to the sets of simulations analyzed in Chapters 6.0 and 7.0, where the dimensions of the cut varied (depth and width), in this particular stage of this investigation the nominal size of the groove is fixed while the external pressure applied is increased in each simulation. In this section, the variation of the actual size of the groove is quantified based upon the amount of eroded elements for the simulations where the external pressure is 0, 3.44 and 34.4 MPa, and it is again utilized to calculate the specific energy necessary to cut the rock under these conditions.

First, the internal energy required to cut through the rock (i.e., to erode the rock elements) during each pressure scenario is presented in Figure 8-9.

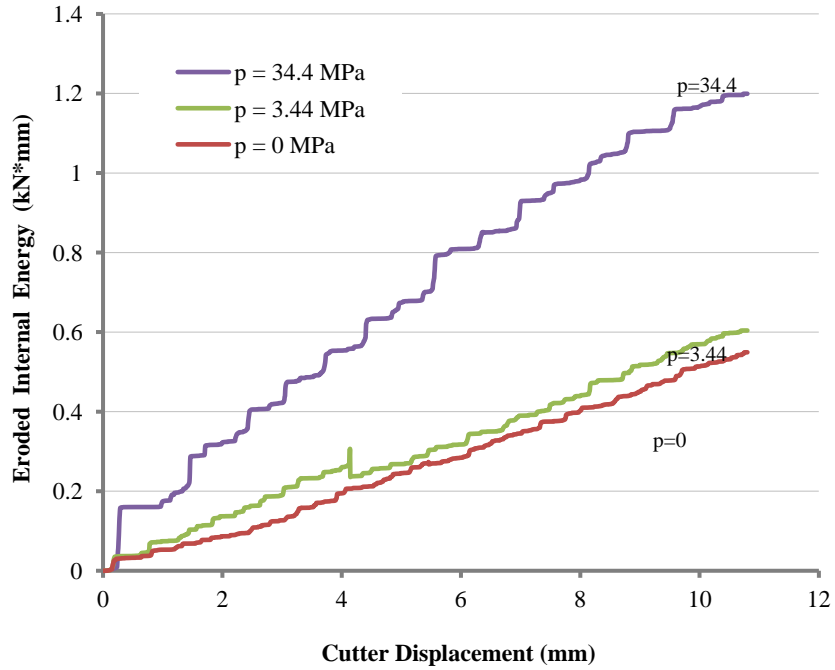


Figure 8-9: Eroded internal energy during groove cut simulations under pressure

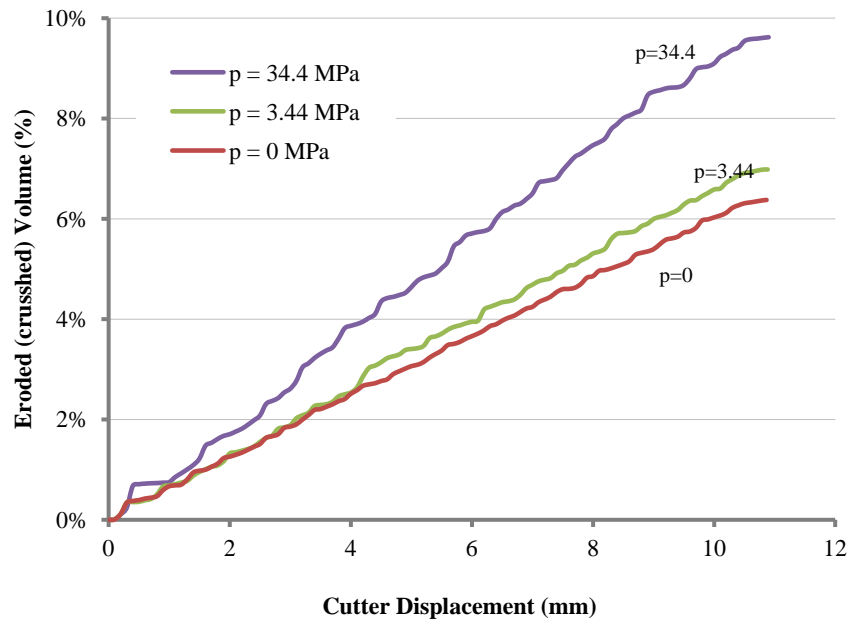


Figure 8-10: Eroded volume fraction during groove cut simulations under pressure

As far as the actual volume fraction of rock that is eroded from the model, for the three pressure cases of groove cutting, this measurement is plotted against the cutter displacement and shown in Figure 8-10, and the visualization of the eroded elements is portrayed in Figure 8-11. It can be seen how the eroded volume pattern gradually changes from a quasi-straight line for $p = 0$ MPa, to a slightly more rippled line for $p = 3.44$ MPa, to a bumpy line for $p = 34.4$ MPa, reflecting the likelihood of getting larger chips being disintegrated instantaneously as the hydrostatic pressure is greater.

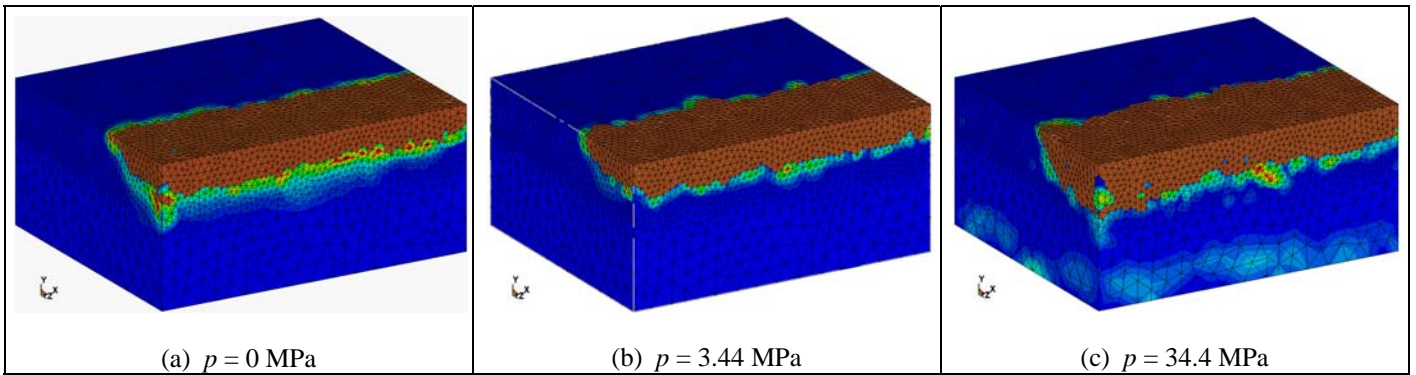


Figure 8-11: Visualization of eroded elements in groove cut simulations under pressure

According to Paterson and Wong (2005), it has been proved in earlier experimental investigations that in porous rocks, such as the Vosges Sandstone modeled, the so-called *cataclasis* (or breaking down of the rock into a granular mass) arises from grain crushing, rather than propagation and interconnection of cracks. As the cataclasis develops upon higher pressure, the mechanism of deformation can change from primarily elastic distortion, with minor contributions from the opening of cracks and some sliding on cracks, to predominantly granular flow, resulting from the relative movement of the chips produced by the cataclasis.

On the other hand, Figure 8-12 depicts the computed values of actual crushed area, $A^{crushed}$, as defined in Section 6.3, together with its corresponding average force and specific energy as a function of pressure. Figure 8-12(b) resembles the trend of the experimental forces-vs.-pressure shown in Figure 8-3, which is similar to the general trend reported by Garcia-Garavito (1998) and Prakash (1982), whose results are shown in Figure 8-13 and Figure 8-14, respectively. Moreover, the resulting specific energy shown in Figure 8-12(c) is consistent with the results for ε presented in Figure 7-11.

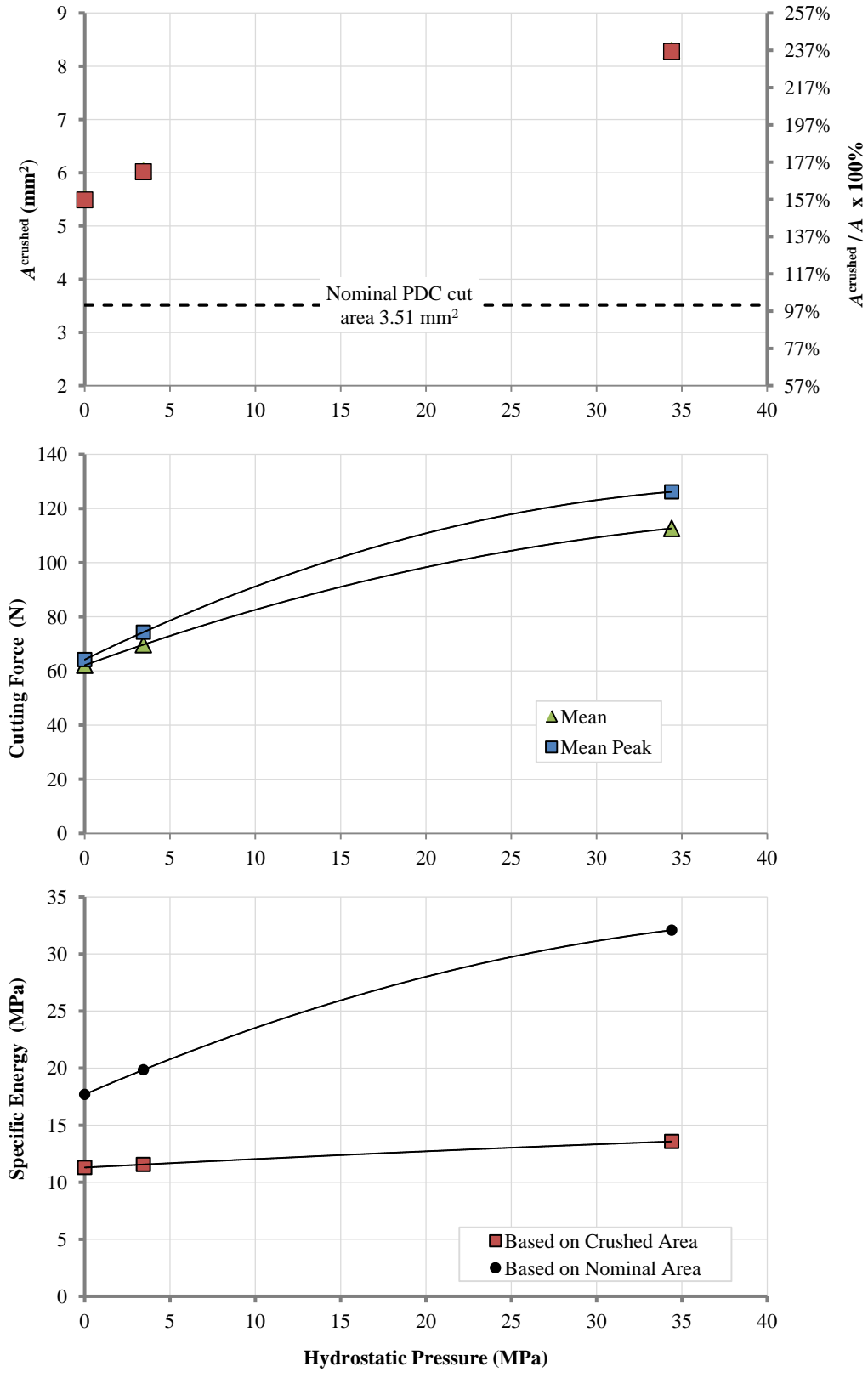


Figure 8-12: Horizontal force and specific energy in groove cut simulations under pressure

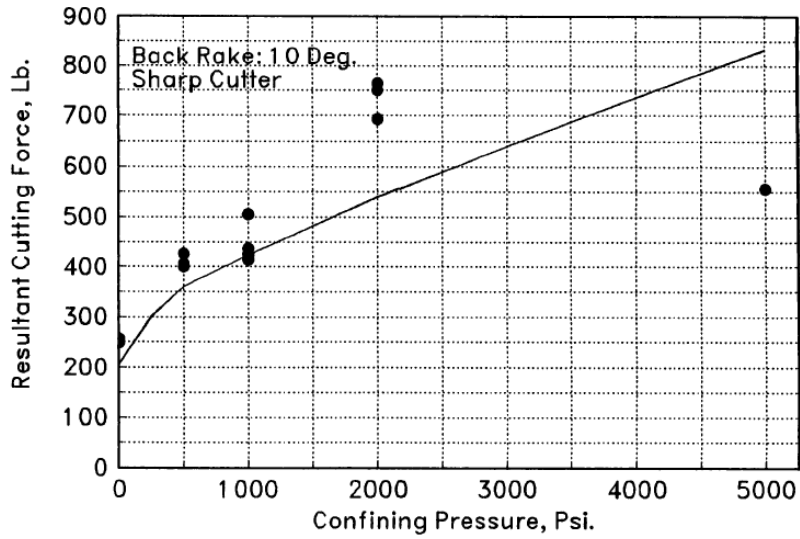


Figure 8-13: Cutting force vs. confining pressure for Carthage Limestone (Garcia-Garavito 1998)

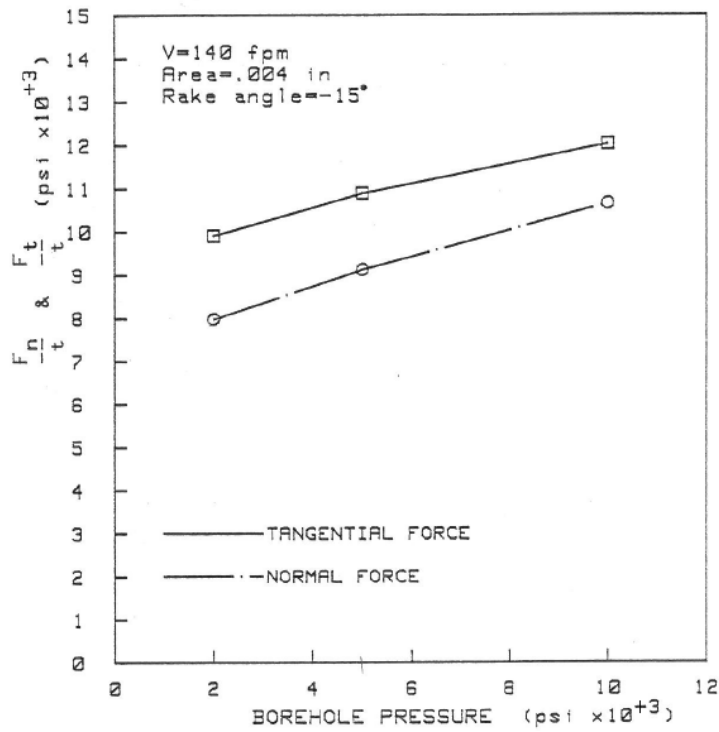


Figure 8-14: Cutting force variation with respect to the borehole pressure for Mancos Shale (Prakash 1982)

9.0 VALIDATING THE F.E. MODELS THROUGH THEORETICAL SOLUTIONS

Although the rock-cutting problem involves a rather complex mechanism, over the years, several analytical and empirical models have been proposed to describe it. The analytical solutions must inevitably suffer from the disadvantage of making major simplifications to the problem, which may result in inaccurate predictions. Nevertheless, an ideal elucidation for the optimization of the rock cutting performance could be found by coupling the results from experimental, theoretical, and numerical models.

The analytical models aim at calculating the cutting force from the mechanical strength of rock, cutter geometry, and depth of cut. This calculated force is the *peak cutting force* since it is acting on the cutter at the instant of *initial* rock failure. The most common models found in the literature consider the problem two-dimensional (2D) because generally the depth of cut is much less than the width of the cutter, thus plane strain conditions apply. Each model considers a particular crack propagation angle with a corresponding particular shape of rock chip (or plastic zone); however, they do not contemplate the mechanics of the rock cutting process beyond the maximum rock strength.

Cutting forces will be computed using three analytical models, namely the ones proposed by Evans (1961), Nishitatsu (1972), and Detournay and Atkinson (2000); subsequently, these will be compared with the numerical simulation results. The following subsections present the most widely recognized and most frequently cited analytical models in rock cutting. Also, Merchant model for metal cutting is described first, as it is the source for later works.

9.1 MERCHANT MODEL (1944)

The analytical model by Merchant (1944; 1945) has been the foundation in the area of metal cutting research by introducing the basic mechanics of chip formation. In addition, numerous rock-cutting researchers have applied and modified this formulation to describe the rock cutting mechanics. The chip formation formulation in the original Merchant model includes the following assumptions:

1. The plastic flow mechanism involves a single moving shear failure plane, which is inclined at an angle θ from the horizontal (see Figure 9-1).
2. The chip is a separate body held in equilibrium by the tool-chip forces and the forces on the shear plane. This ignores inertial loading from the chip, which at ordinary cutting speeds is significantly lower than the forces of deformation and friction.
3. The contact between the cutting face and the cut material is frictional.
4. A linear Mohr-Coulomb relationship exists between the normal and shear stress across the shear failure plane.

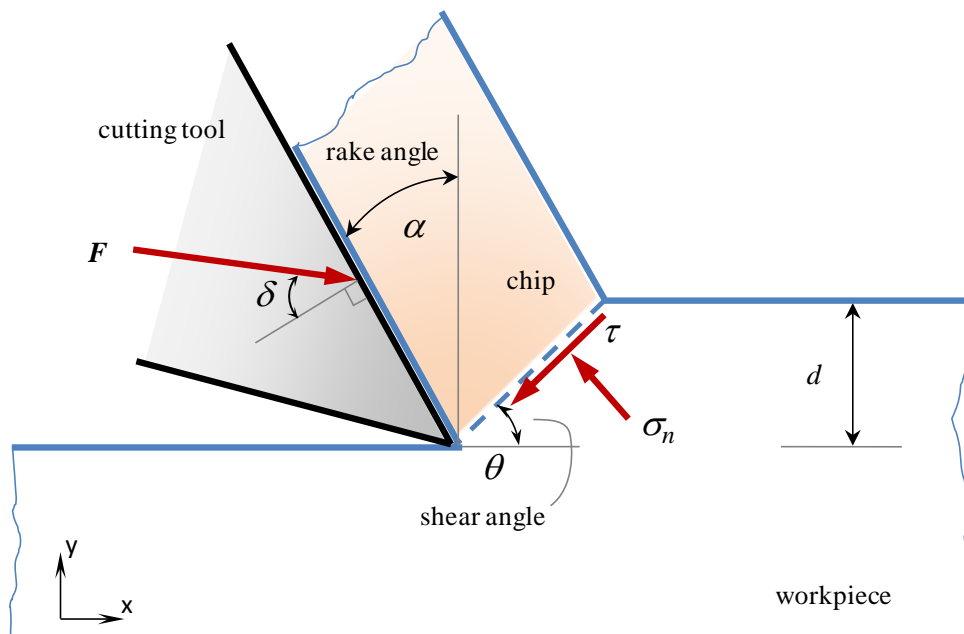


Figure 9-1: Chip formation diagram according to Merchant (1944)

The Mohr-Coulomb failure criterion relates the shear stress, τ , and the normal stress, σ_n , on the failure plane to the cohesion, c , and the internal friction angle of the workpiece, φ , as follows:

$$\tau = c + \sigma_n \tan \varphi \quad (9-1)$$

Equilibrium of forces in Figure 9-1 yields:

$$\tau = \frac{\sin \theta}{d} F \sin(\theta + \delta - \alpha) \quad (9-2)$$

$$\sigma_n = \frac{\sin \theta}{d} F \cos(\theta + \delta - \alpha) \quad (9-3)$$

Replacing Equations (9-2) and (9-3) into Equation (9-1) yields the following cutting force per unit width:

$$F = c \frac{d}{\sin \theta} \frac{\cos \varphi}{\cos(\theta + \delta - \alpha + \varphi)} \quad (9-4)$$

The shear angle, θ , is estimated by assuming that it is oriented such that the work to form the chip is the minimum. This can be accomplished by assuming that the tool-chip friction angle, δ , and stresses on the shear plane do not vary with θ . Then, differentiating Equation (9-4) with respect to θ and equating the outcome to zero provides the condition that will make F minimal. Consequently,

$$\theta = \frac{\pi}{4} - \frac{1}{2}(\delta - \alpha + \varphi) \quad (\text{rad}) \quad (9-5)$$

Finally, after replacing Equation (9-5) into Equation (9-4), one can obtain the magnitude of the cutting force at the moment of failure. The horizontal and vertical components of the cutting force defined by Merchant's model are:

$$F_x = c \left(\frac{2 d \cos \varphi}{1 - \sin(\delta - \alpha + \varphi)} \right) \cos(\delta - \alpha) \quad (9-6)$$

$$F_y = c \left(\frac{2 d \cos \varphi}{1 - \sin(\delta - \alpha + \varphi)} \right) \sin(\delta - \alpha) \quad (9-7)$$

If Equations (9-4) and (9-5) are replaced into Equation (9-3), it is possible to determine the condition for which the normal stress on the failure surface is tensile (i.e. $\sigma_n < 0$). This condition is given by:

$$\alpha < \frac{\pi}{2} - (\delta + \varphi) \quad (\text{rad}) \quad (9-8)$$

9.1.1 Inclination of the Cutting Force

As seen in Figure 9-1, the cutting force F is inclined with respect to the normal vector of the cutter face at an angle δ . Extensive testing performed and reported by Richard (1999) indicates that δ is relatively insensitive to the type of rock being cut. In addition, Richard demonstrated that δ remains almost constant throughout the duration of a given test.

As a result of Richard's examination of the effect of the cutting depth on the parameter $\tan(\delta - \alpha)$ –i.e., the factor that relates the horizontal to the vertical components of the cutting force–, he determines that $\tan(\delta - \alpha)$ typically decreases with increasing depth of cut until it reaches a constant value. Table 9-1 lists some of the values of force angles that Richard obtained while cutting Vosges Sandstone using a sharp PDC cutter with a rake angle of 15 degrees.

The values in Table 9-1 will be used in the calculation of forces using the analytical expressions as defined in the following sections.

Table 9-1: Inclination of the total cutting force measured in the laboratory

d (mm)	$\tan(\delta - \alpha)$ (-)	$(\delta - \alpha)$ (deg)	α (deg)	δ (deg)
0.3	0.71	35.37	-15	20.37
0.6	0.65	33.02	-15	18.02
0.8	0.63	32.21	-15	17.21
1.0	0.62	31.80	-15	16.80
1.4	0.61	31.38	-15	16.38
1.6	0.61	31.38	-15	16.38
1.8	0.61	31.38	-15	16.38

Experimental data after Richard (1999)

9.2 EVANS MODEL (1961)

Evans model is one of the most accepted theories for rock cutting with chisel and conical picks, and has been widely used in the design of mechanical excavators such as shearers, continuous miners, and roadheaders (Bilgina et al. 2006). Evans suggested a model based on observations on coal breakage by wedges. The original Evans model includes the following assumptions:

1. The rock breaks in tension along a circular failure surface, and the produced chip rotates about point **b** in Figure 9-2.
2. The failure starts at the wedge (cutting tool) tip, with the initial direction tangential to the bisector of the wedge angle, and reaches the surface at point **b**, some distance in front of the wedge.
3. The force required to break the rock is such that it produces the minimum work along the circular failure surface (i.e. $\partial F / \partial \chi = 0$).
4. The force required to push the wedge normal to a chip face can be accounted for in terms of a “penetration resistance” closely allied to the compressive strength σ_c of the rock (see Equation (9-11)).
5. The ratio of compressive strength, σ_c , and tensile strength, σ_t , is approximately 10 for brittle materials (i.e. $\sigma_c \approx 10 \sigma_t$).

$$F = \frac{\sigma_c h \cos \delta}{\cos \alpha} \quad (9-12)$$

Equation (9-12) in conjunction with Equations (9-9) and (9-10), result in an expression that is subjected to assumptions # 3 and # 5. Consequently, the condition that will make F minimal is:

$$\chi = \frac{1}{2}(\alpha - \delta) \quad (9-13)$$

Eventually, after considering the penetration of the wedge negligibly small, and using the condition that $0 < \chi < \pi/2$, the force that acts upon the chip can be solved for:

$$F = \frac{\sigma_t d}{1 - \cos(\alpha - \delta)} \quad (9-14)$$

Finally, the horizontal and vertical components of the cutting force defined by Evans' model are:

$$F_x = \sigma_t \left(\frac{d}{1 - \cos(\alpha - \delta)} \right) \cos(\alpha - \delta) \quad (9-15)$$

$$F_y = \sigma_t \left(\frac{d}{1 - \cos(\alpha - \delta)} \right) \sin(\alpha - \delta) \quad (9-16)$$

9.2.1 Horizontal Slab-Cut Forces Based on Evans Model

Making use of the tensile strength of Vosges Sandstone, i.e., $\sigma_t = 3.215$ MPa (466 psi), and Equation (9-15), the horizontal cutting force as defined by Evans can be computed for the analyzed two-dimensional cases of slab cutting (presented in Section 6.2.3). Note that Equation (9-15) yields the force per unit thickness; therefore, the 10-mm slab thickness is accounted for in the final calculation of the forces tabulated in Table 9-2:

Table 9-2: Horizontal force as a function of cutting depth according to Evans Model

d (mm)	$(\alpha - \delta)$ (deg)	$\cos(\alpha - \delta)$ (-)	F_x (N/m)	$F_{x, 10\text{mm slab}}$ (N)
0.3	-35.37	0.815	4,259.8	42.60
0.6	-33.02	0.838	10,011.1	100.11
0.8	-32.21	0.846	14,139.2	141.39
1.0	-31.80	0.850	18,204.4	182.04
1.4	-31.38	0.854	26,265.3	262.65
2.0	-31.38	0.854	37,521.9	375.22
3.6	-31.38	0.854	67,539.4	675.39

9.3 NISHIMATSU MODEL (1972)

Nishimatsu (1972) presented a theory for the cutting of rock in which he first assumes that the magnitude of the resulting stress, R , acting on the failure line **ab** is proportional to the n^{th} power of the distance from surface point **b** and it is constant in the direction along **ab** (see Figure 9-3). The resulting stress is given by:

$$R = R_0 \left(\frac{d}{\sin \theta} - \lambda \right)^n \quad (9-17)$$

where, R_0 is a constant determined from the equilibrium of forces,

d is the depth of cut,

θ is the shear angle from the horizontal,

λ is the distance from the edge point **a** to an arbitrary point on the line **ab**,

n is the stress distribution factor, i.e. a constant concerned with the state of stress in the rock cutting process.

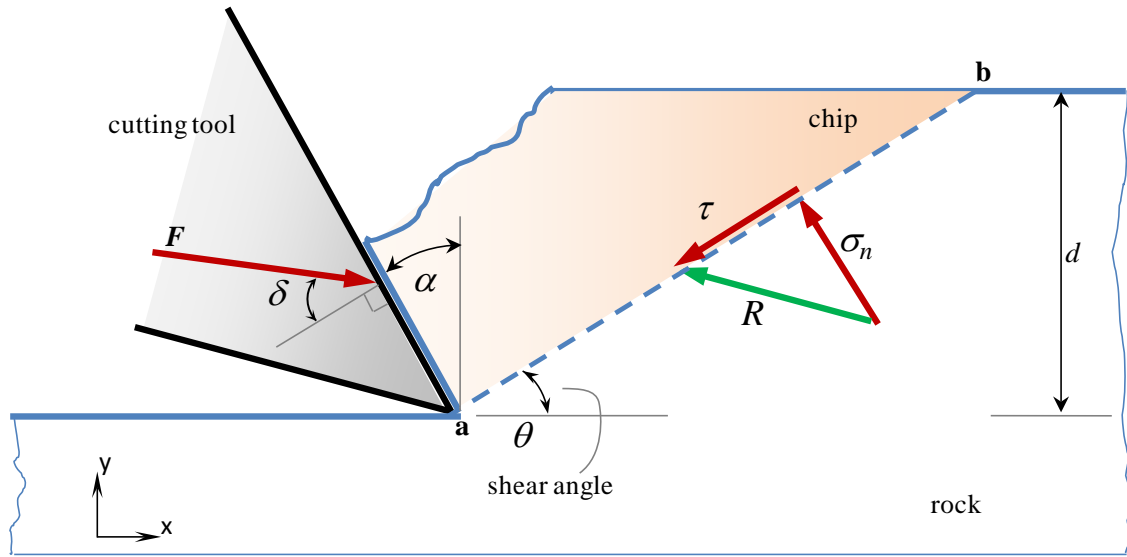


Figure 9-3: Orthogonal rock-cutting forces and stresses according to Nishimatsu (1972)

In addition, the original Nishimatsu model includes the following assumptions:

1. The rock-cutting process is brittle, without any accompanying plastic deformation (no ductile crushing zone).
2. A linear Mohr-Coulomb relationship exists between the normal and shear stress across the shear failure plane.
3. The force required to shear the rock is such that it produces the minimum work along the failure line **ab** (i.e. $\partial F / \partial \theta = 0$).

The integration of the resultant stress R along line **ab** should be in equilibrium with the resultant cutting force, F . From the equilibrium of forces, the constant R_0 can be determined:

$$R_0 = F (n + 1) \left(\frac{d}{\sin \theta} \right)^{-(n+1)} \quad (9-18)$$

This is replaced in Equation (9-17), and then the normal and tangential components of the resultant stress, R , can be resolved:

$$\sigma_n = F (n + 1) \left(\frac{d}{\sin \theta} \right)^{-(n+1)} \left(\frac{d}{\sin \theta} - \lambda \right)^n \sin(\theta + \delta - \alpha) \quad (9-19)$$

$$\tau = F (n + 1) \left(\frac{d}{\sin \theta} \right)^{-(n+1)} \left(\frac{d}{\sin \theta} - \lambda \right)^n \cos(\theta + \delta - \alpha) \quad (9-20)$$

Next, following assumption # 2, Equations (9-19) and (9-20) are replaced into the Mohr-Coulomb relationship in Equation (9-1), from which the solution for the cutting force, F , can be obtained. Based on assumption # 3, the expression for the cutting force is differentiated with respect to θ and equated to zero. As a result, the formula of the resultant cutting force is given by:

$$F = c \left(\frac{1}{n + 1} \right) \left(\frac{2 d \cos \varphi}{1 - \sin(\delta - \alpha + \varphi)} \right) \quad (9-21)$$

where c is the cohesion and φ is the internal friction angle of the rock. Finally, the horizontal and vertical components of the cutting force defined by Nishimatsu's model are:

$$F_x = c \left(\frac{1}{n + 1} \right) \left(\frac{2 d \cos \varphi}{1 - \sin(\delta - \alpha + \varphi)} \right) \cos(\delta - \alpha) \quad (9-22)$$

$$F_y = c \left(\frac{1}{n + 1} \right) \left(\frac{2 d \cos \varphi}{1 - \sin(\delta - \alpha + \varphi)} \right) \sin(\delta - \alpha) \quad (9-23)$$

Note that if $n = 0$, Nishimatsu's forces become Merchant's forces (see Equation (9-6) and (9-7)). However, according to Nishimatsu (1972), the stress distribution factor should not depend on the mechanical properties of the rock, but on the state of stress in the rock, which would substantially depend on the rake angle of the cutting tool. This prediction was verified by laboratory tests on sandy tuff and cement mortar (Nishimatsu 1972), which provided an empirical estimate of the stress distribution factor as a function of the rake angle:

$$n = 11.3 - 0.18 \alpha \quad \alpha \text{ in degrees} \quad (9-24)$$

9.3.1 Horizontal Slab-Cut Forces Based on Nishimatsu Model

Making use of the shear strength parameters of Vosges Sandstone, i.e., cohesion, $c = 5$ MPa (725.2 psi) and friction angle $\phi = 25.4$ degrees, together with Equations (9-22) and (9-24), the horizontal cutting force as defined by Nishimatsu can be computed for the analyzed two-dimensional cases of slab cutting (presented in Section 6.2.3). Note that Equation (9-22) yields the force per unit thickness; therefore, the 10-mm slab thickness is accounted for in the final calculation of the forces tabulated in Table 9-3:

Table 9-3: Horizontal force as a function of cutting depth according to Nishimatsu Model

d (mm)	n (deg)	$(\delta-\alpha)$ (deg)	$(\delta-\alpha+\phi)$ (deg)	$\sin(\delta-\alpha+\phi)$ (-)	$\cos(\delta-\alpha)$ (-)	F_x (N/m)	$F_{x, 10\text{mm slab}}$ (N)
0.3	14.0	35.37	60.77	0.87	0.815	1,157.3	11.57
0.6	14.0	33.02	58.42	0.85	0.838	2,046.3	20.46
0.8	14.0	32.21	57.61	0.84	0.846	2,620.2	26.20
1.0	14.0	31.80	57.20	0.84	0.850	3,210.1	32.10
1.4	14.0	31.38	56.78	0.84	0.854	4,405.0	44.05
2.0	14.0	31.38	56.78	0.84	0.854	6,292.9	62.93
3.6	14.0	31.38	56.78	0.84	0.854	11,327.3	113.27

Evidently, the resulting forces in Table 9-3 are underestimated, perhaps due to the use of the suggested stress distribution factor for sandy tuff and cement mortar in Equation (9-24). If the stress distribution factor were to be adjusted to characterize this particular scenario of rock cutting more appropriately, a value of $n = 3.0$ would yield a better comparison with the numerical and experimental data. The adjusted Nishimatsu forces are shown in Table 9-4:

Table 9-4: Adjusted horizontal force as a function of cutting depth according to Nishimatsu Model

d (mm)	n (deg)	$(\delta-\alpha)$ (deg)	$(\delta-\alpha+\phi)$ (deg)	$\sin(\delta-\alpha+\phi)$ (-)	$\cos(\delta-\alpha)$ (-)	F_x (N/m)	$F_{x, 10\text{mm slab}}$ (N)
0.3	3.0	35.37	60.77	0.87	0.815	4,318.2	43.18
0.6	3.0	33.02	58.42	0.85	0.838	7,635.3	76.35
0.8	3.0	32.21	57.61	0.84	0.846	9,777.0	97.77
1.0	3.0	31.80	57.20	0.84	0.850	11,978.0	119.78
1.4	3.0	31.38	56.78	0.84	0.854	16,436.7	164.37
2.0	3.0	31.38	56.78	0.84	0.854	23,481.1	234.81
3.6	3.0	31.38	56.78	0.84	0.854	42,265.9	422.66

It is important to note that adjusting the value of the stress distribution factor, n , in Equation (9-23), in order to obtain a better validation of the results, makes invalid Nishimatsu's assumption regarding its dependence on the value of the rake angle. As expressed in Equation (9-24), by setting $n = 3$, the corresponding rake angle should be hypothetically 46 degrees. Conversely, as the nature of the cutter geometry analyzed by Nishimatsu differs from the PDC geometry studied in this work (i.e. with a negative rake angle), it is likely that the value of n could be attributed to a different expression taking into account the negative-rake-angle case.

9.4 DETOURNAY & ATKINSON MODEL (2000)

In their formulation, Detournay and Atkinson (2000) obtained a straightforward generalization of Merchant's solution to account for the presence of fluid during the rock-cutting process, as illustrated in Figure 9-4. In this case, F , is the differential cutting force, defined as the force required to move the cutter minus the force acting on the cutter (due to mud pressure, p_m) when it is not in contact with the rock.

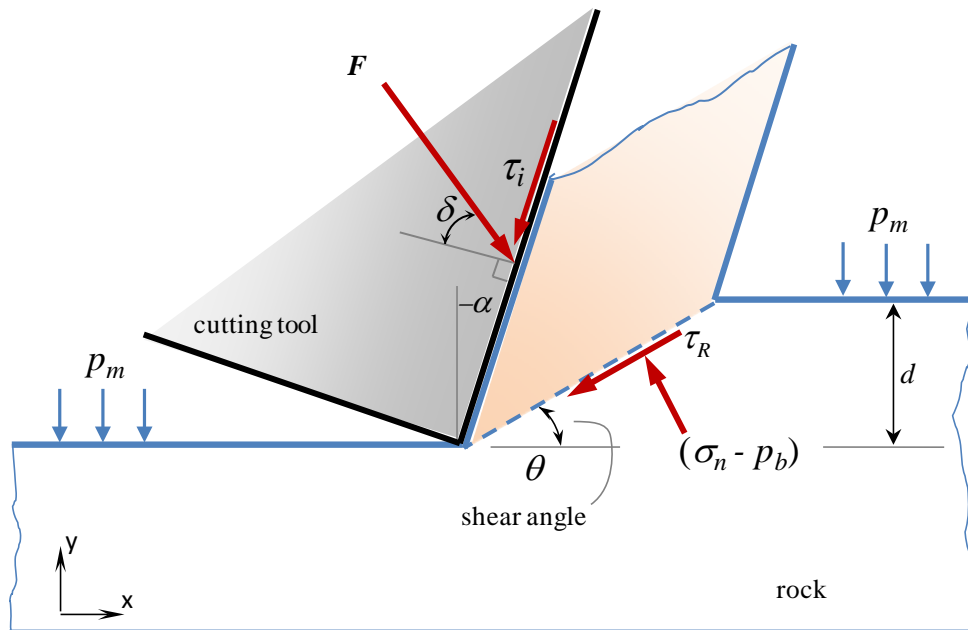


Figure 9-4: Rock-cutting problem definition according to Detournay and Atkinson (2000)

To extend Merchant model, Detournay and Atkinson introduced the following assumptions:

1. The Mohr-Coulomb failure criterion is satisfied by the effective normal stress, $(\sigma_n - p_b)$, and the shear stress across the rock failure plane:

$$\tau_R = c + (\sigma_n - p_b) \tan \varphi \quad (9-25)$$

where p_b is the pore pressure, c is the cohesion and φ is the internal friction angle of the rock.

2. The contact friction angle at the cutter-rock interface, δ , produces:

$$\tau_i = (\sigma_n - p_m) \tan \delta \quad (9-26)$$

3. The interstitial fluid pressure along the cutter-rock interface is equal to p_m .

From assumptions # 2 and # 3, the horizontal and vertical components of the differential cutting force have the following relationship:

$$F_y = -\tan(\delta - \alpha) F_x \quad (9-27)$$

Then, following the same considerations as in Merchant model, the horizontal component of the cutting force according to Detournay and Atkinson is:

$$F_x = [c + (p_m - p_b) \tan \varphi] \left(\frac{2 d \cos \varphi}{1 - \sin(\delta - \alpha + \varphi)} \right) \cos(\delta - \alpha) \quad (9-28)$$

9.4.1 Horizontal Slab-Cut Forces Based on Detournay and Atkinson Model

Making use of the shear strength parameters of Vosges Sandstone, i.e., cohesion, $c = 5$ MPa (725.2 psi) and friction angle $\varphi = 25.4$ degrees, together with Equation (9-28), the horizontal cutting force as defined by Detournay and Atkinson can be computed for the analyzed two-dimensional cases of slab cutting (presented in Section 6.2.3). The mud and pore pressure,

p_m and p_b , are considered zero in this case, which will essentially make Equation (9-28) become Merchant model. Note that Equation (9-28) yields the force per unit thickness; therefore, the 10-mm slab thickness is accounted for in the final calculation of the forces tabulated in Table 9-5:

Table 9-5: Horizontal force as a function of cutting depth according to Detournay and Atkinson Model

d (mm)	$(\delta-\alpha)$ (deg)	$(\delta-\alpha+\phi)$ (deg)	$\sin(\delta-\alpha+\phi)$ (-)	$\cos(\delta-\alpha)$ (-)	F_x (N/m)	$F_x, 10mm\ slab$ (N)
0.3	35.37	60.77	0.87	0.815	17,359.1	173.59
0.6	33.02	58.42	0.85	0.838	30,693.9	306.94
0.8	32.21	57.61	0.84	0.846	39,303.5	393.03
1.0	31.80	57.20	0.84	0.850	48,151.6	481.52
1.4	31.38	56.78	0.84	0.854	66,075.7	660.76
2.0	31.38	56.78	0.84	0.854	94,393.9	943.94
3.6	31.38	56.78	0.84	0.854	169,908.9	1699.09

9.5 NUMERICAL VS. EXPERIMENTAL VS. ANALYTICAL SOLUTIONS

As mentioned in the beginning of this chapter, the analytical models for rock cutting offer a quantitative interpretation of the peak cutting force, while the rock is being fractured primarily in a brittle fashion. Nonetheless, there are two different mainstreams concerning the mechanism being considered as the source of the breaking process once the cutting tool penetrates the rock. On one hand, Evans (1961) claims that the failure is the result of the propagation under tensile stresses of cracks contained in the material. This is apparent to him given the fact that brittle materials are considerably weaker in tension than in compression. On the other hand, both Nishimatsu (1972) and Detournay and Atkinson (2000), based upon Merchant's model (1944) assume a shear failure plane along a macroscopic crack to form a coarse cutting chip.

In actuality, none of these premises are unsuitable. After having an understanding of the phenomena taking place during the rock cutting process, it can be said that the analytical models should be applied with caution depending upon the failure regime, which is essentially mandated by the depth of cut, as has been demonstrated through the experimental and numerical scratch tests (see Sections 2.1.1 and 6.2, respectively).

Table 9-6 presents a comparison of the average horizontal cutting force required to cut Vosges Sandstone at different depths obtained from the simulations developed within this investigation, from the experiments performed by Richard (1999), and from computations of the analytical equations derived by Evans, Nishimatsu and Detournay and Atkinson, D&A (i.e. Merchant). Moreover, in order to visualize the discrepancies or similarities at large, the force values in Table 9-6 have been plotted against the cutting depth. Figure 9-5(a) presents the *mean* horizontal cutting force from the FE simulations and from the experiments in contrast with the calculated forces from the analytical models discussed. This plot covers both the ductile and brittle regime cutting-depth ranges; yet, since it is anticipated that the analytical models characterize best one or the other failure regime, Figure 9-5(b) zooms into the data corresponding to the ductile regime. Likewise, Figure 9-6(a) and Figure 9-6(b) show the same data, only that the forces from the FE simulations and the experiments are the *mean peak* averages.

Table 9-6: Average horizontal cutting force from numerical, experimental, and analytical solutions

	Cutting Depth (mm)	Horizontal Cutting Force (N)							
		Numerical Simulation		Experimental		Analytical			
		Mean	Mean Peak	Mean	Mean Peak	Evans	Nishimatsu	Adjusted	D&A
Ductile Regime	0.3	60	67.3	57.7	88.6	42.6	11.6	43.2	173.6
	0.6	80.4	94.2	101.2	160.4	100.1	20.5	76.4	306.9
	0.8	102.6	112.1	119.0	203.3	141.4	26.2	97.8	393.0
	1	109.8	124.1	128.6	249.0	182.0	32.1	119.8	481.5
	1.4	140.2	158.3	141.5	301.2	262.7	44.1	164.4	660.8
Brittle Regime	2	178.6	245.2	147.1	386.9	375.2	62.9	234.8	943.9
	3.6	246.4	414.4	approx. 250	approx. 400	675.4	113.3	422.7	1699.1

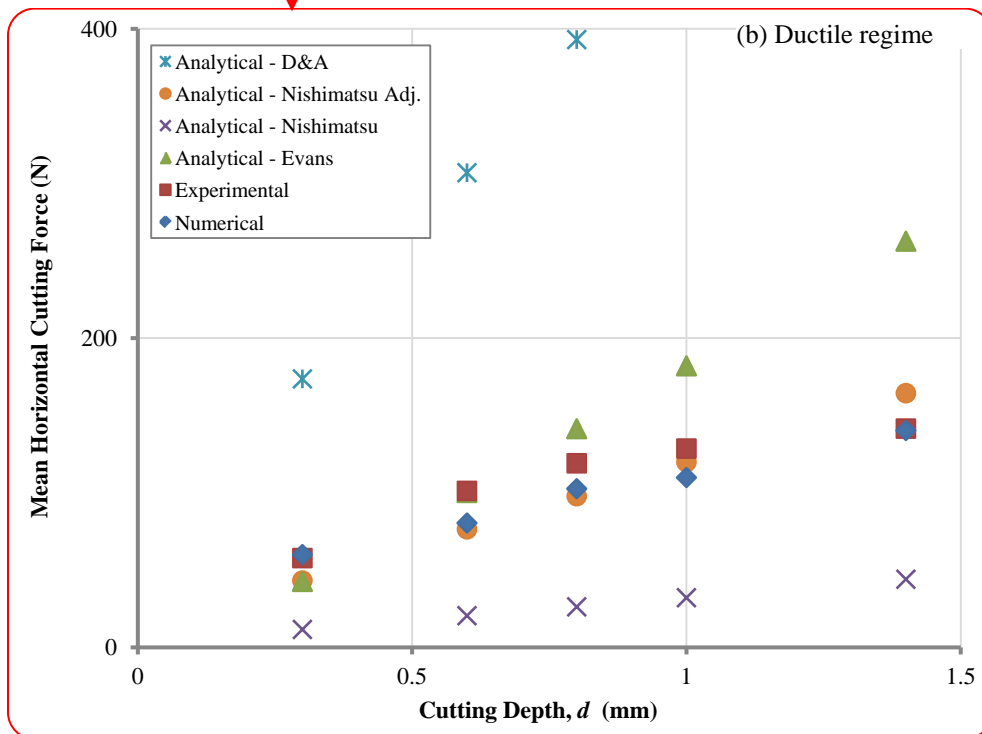
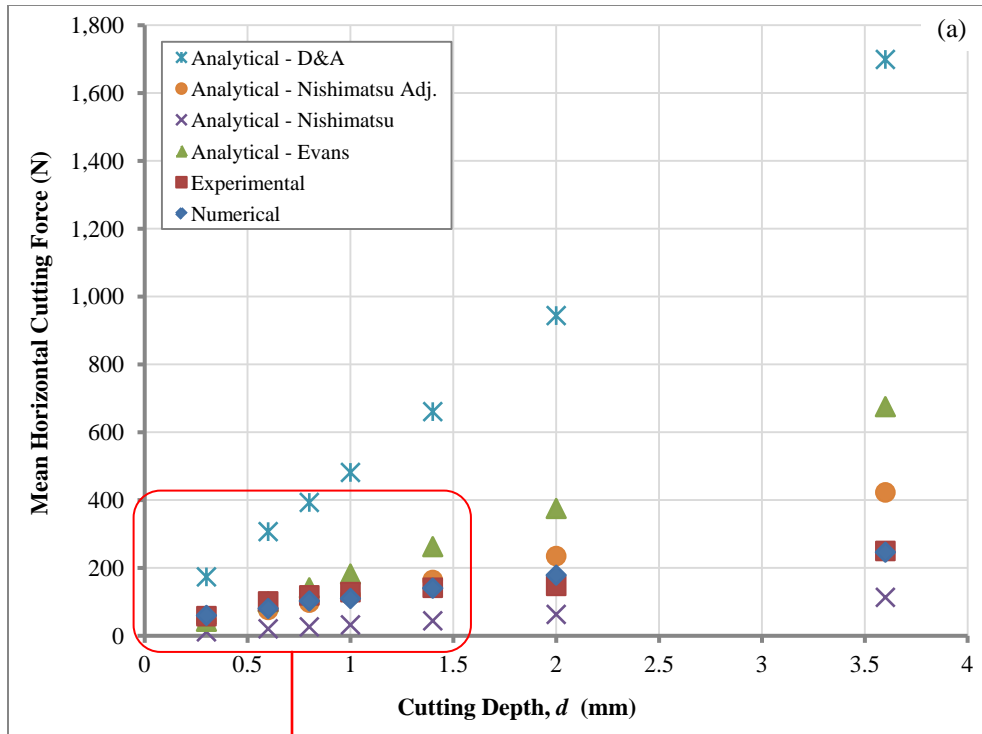


Figure 9-5: Mean horizontal forces: numerical vs. experimental vs. analytical solutions

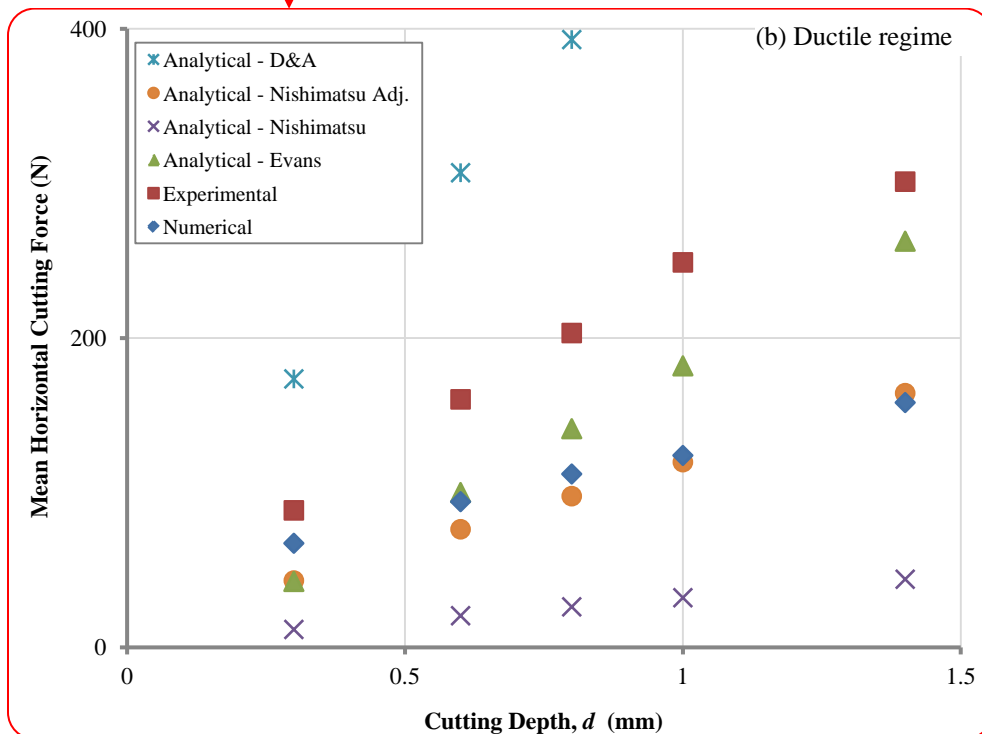
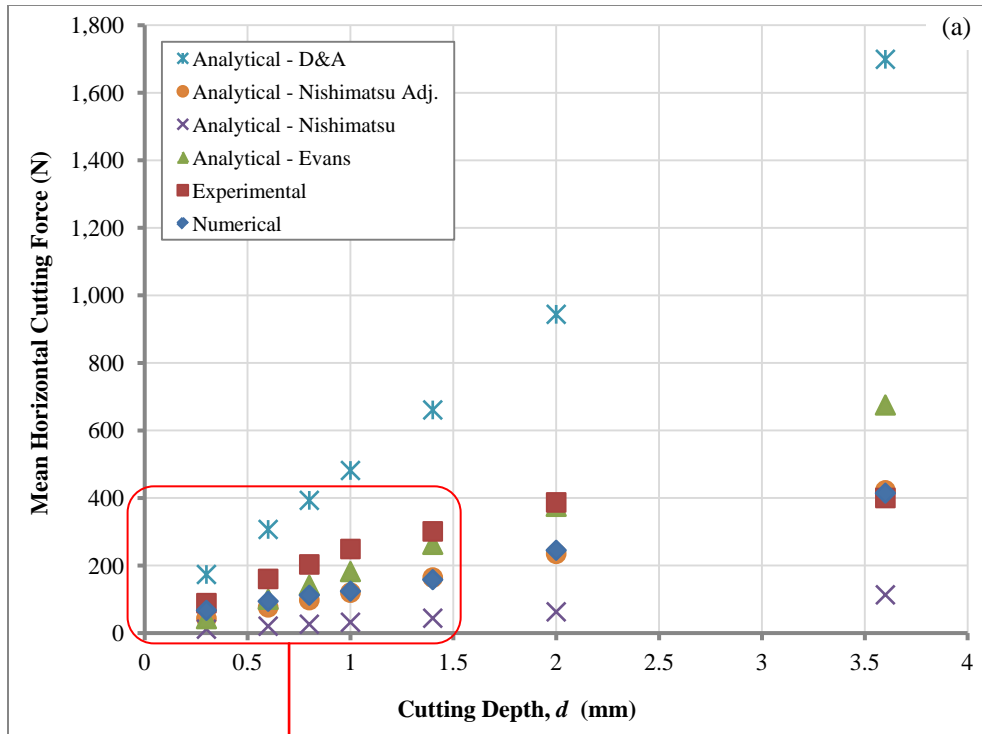


Figure 9-6: Mean peak horizontal forces: numerical vs. experimental vs. analytical solutions

Evans's postulation of failure through a tensile crack is more indicative of shallower rock break-ups, thus it would be appropriate to compare Evans's forces with the values that lie within the ductile regime –even though his theory refers to no sign of plastic deformation in the vicinity of the surface of breakage. Figure 9-5(b) reveals how Evans's forces are only roughly comparable to the numerical and experimental *mean* values at a cutting depth equal or less than 0.6 mm. When the cutting depth increases, Evans's results gradually diverge more. This could be explained by the gradual transition from ductile to brittle failure mode in the rock as a function of cutting depth, where it is expected that the chips get formed by initiating with a tensile crack that evolves into a shear failure surface.

Furthermore, it can be inferred from both Figure 9-5 and Figure 9-6 that Detournay and Atkinson's evaluation of the cutting force, as used in this exercise, overestimates by far its magnitude. A potential reason for this large difference in the results could be attributed to the limitation of the model as specifically acknowledged by the authors: "the present model is suitable for low-permeability rocks under "near-undrained" conditions". This implies that the model might be strictly applied to scenarios where the mud and pore pressure, p_m and p_b , are present. In addition, these researchers contemplate the fact that the value of the cohesion used in their equation "could be considerably smaller than the cohesion deducted from peak strength measured in conventional triaxial experiments since the cutting problem involves very large shear strains and since rock experiences a loss of cohesion after relatively small strain." (Detournay and Atkinson 2000) According to this last statement, if a reduction factor were to be applied on the (typical) cohesion value used in Equation (9-28), a factor of 0.25 would make Detournay and Atkinson's calculated forces identical to the adjusted Nishimatsu forces, which are tabulated in Table 9-4.

Lastly, taking into account the nature of the Merchant-based models, the focus should be geared towards the *mean peak* forces within the brittle regime range, as these models characterize shear failure along a crack that propagates to produce a coarse chip (or fragment). Figure 9-6(a) shows how the adjusted Nishimatsu model successfully resembles the values of the force from the FE simulations for depths of cut equal or greater than 1 mm. Interestingly, looking at the *mean* forces in Figure 9-5(a), Nishimatsu's adjusted model also matches the simulation forces corresponding to the ductile regime, i.e., at shallow cutting depths.

10.0 CONCLUDING REMARKS

10.1 SUMMARY AND CONCLUSIONS

The most important accomplishment gained through this study has been an improved understanding of the mechanical phenomena involved in rock cutting. A reliable finite element model was developed that was able to properly simulate the fragmentation process observed in laboratory tests of rock cutting. Fracture modes and cutting force magnitudes and trends correlated well with the physical experiments.

In addition, a scheme for applying external pressure was effectively incorporated into the rock cutting model. Albeit the lack of calibration data, preliminary numerical results indicate a good comparison with physical experiments of the rock response tendency when cutting with a single sharp cutter under different magnitudes of hydrostatic pressure.

Lastly, the traditional theoretical models of the cutting force were evaluated and compared with the simulation and experimental results, which provided a better understanding of their limitations and usability.

10.1.1 Rock Behavior through a Sound Constitutive Model

Chapter 3.0 describes several material models available in LS-DYNA which would normally be useful to simulate a geo-material. Nevertheless, given that the rock cutting problem analyzed involves a series of complex breaking processes –including crack propagation and fragment separation–, it is imperative that the material model implemented leads to a robust simulation. Material 159 of LS-DYNA, namely the Continuous Surface Cap Model, was found to fulfill this purpose (see Section 3.2.4).

Among the salient features of Mat_159, the *element erosion* built into this material model is what makes it the most suitable to emulate a realistic rock fracturing behavior upon different loading conditions (see Section 5.3.3). Twenty-two out of forty-five input parameters that the model requires were obtained by means of fitting laboratory data from standard strength tests on Vosges Sandstone (see Section 3.2.4.1).

Once the input parameters were established for all the potential geo-material models under evaluation, standardized strength tests were conducted for validation. Chapter 4.0 presents the assessment of these geo-material models by carrying out simulations of the isotropic compression test, triaxial compression, and triaxial extension tests under different confining pressures.

After a rigorous effort to analyze the performance of Mat_159 and to calibrate its input parameters, the final set of established input parameters for this material model projected a realistic behavior of the rock under different loading conditions. Although some formulation problems were encountered (as described in Section 4.5.2), and the one-element volumetric-strain response was not as expected, the rock-cutting simulations presented in Chapters 6.0, 7.0, and 8.0 are based upon this calibrated and validated values.

10.1.2 Configuring LS-DYNA's Capabilities to Simulate Rock Cutting

Chapter 5.0 presents in detail the key features of the commercial software LS-DYNA, which have a large impact on the performance of the rock-cutting model. A sensitivity analysis was performed on essential options of the software relevant for the study, and as a result, baseline inputs were established for simulating the fragmentation process sought.

In a nutshell, the most important LS-DYNA functionality utilized in this modeling effort was the so-called *element erosion* (see Section 5.3), which allows the removal of elements from the mesh domain upon material failure. This characteristic dictates the definition of other important components of the model, such as mesh discretization, contact among materials, and even the way the output data are analyzed.

At the outset, it was determined that the finite element mesh of the rock specimen must be comprised of non-uniform (non-orthogonal) elements and that their size should be small enough so that a failure crack thickness would be as realistic as possible.

Also, the contact formulation to treat both the cutter-rock and rock-rock interfaces was studied (see Section 5.2). It was found that the most effective technique to work out the interaction between the cutter tool and the rock material is one that assumes the cutter to be a rigid body, eliminating the effect of its deformation. On the other hand, due to the newly exposed rock surfaces after element erosion, a contact model that updates its contact surface is required; the “Eroding Single Surface” contact model in LS-DYNA fulfilled this purpose. Both contact models required the specification of numerous input parameters which were carefully calibrated.

In addition, the effect of other numerical factors on the results, as well as output data interpretation procedures were analyzed. Section 5.4 describes how the resulting cutting forces from the simulations were sensitive to factors such as system damping, cutting velocity and material damage recovery; optimum input values for these factors were determined. This section also presents a proposed technique to filter and interpret the cutting force data recorded during the numerical simulations.

10.1.3 Simulating Scratch Tests on a Rock Slab (Two-dimensional Cutting)

Chapter 6.0 presents the numerical simulation of the scratch tests performed by Richard (1999) in the laboratory. Not only the models developed were able to resemble the rock fracturing and fragmentation seen in the laboratory, including the ductile and brittle failure modes, but the resulting cutting forces could be successfully validated by comparing with the experimental measurements.

Although a “critical depth” of cut, as defined by Richard (1999), was identified by the numerical results with the same value as his (i.e., 1.5 mm), it was observed that there is a definite gradual transition between the brittle and ductile regimes, which covered all the cutting depths within the range tested. Furthermore, the trend of force-vs.-depth numerical data within the brittle failure range appears to oppose that from Richard’s laboratory tests, in that it follows a steeper upward (quasi-linear) variation, in contrast with his horizontal asymptotic tendency (see Section 6.2.3).

10.1.4 Simulating Scratch Tests with a Groove (Three-dimensional Cutting)

Sixteen cases of groove cutting in Vosges Sandstone were modeled under conditions similar to Richard's groove scratch experiments (1999). Preparation of these models and their results are included in Chapter 7.0. In this particular case, the objective was to get an understanding of the implications of cutting the groove side walls. For this, a combinatory of 4 different depths of cut (d) with 4 different cutter widths (w) was simulated within the ductile regime of Vosges Sandstone.

The magnitude of the mean horizontal cutting forces obtained from the numerical simulations were found inconsistent with respect to the laboratory results, particularly as the cutting depth increased; however, a good agreement in the force-vs.-depth linear trend was achieved, as well as in the variation of the force as a function of cutter width. Based upon these findings, it is believed that, for values of w/d ratio greater than 5, a rational expression could characterize the force in terms of depth and width of cut. Accordingly, an empirical formula was derived for the calculation of the mean force in groove cutting, as a function of the cut *nominal* dimensions (see Section 7.2.2).

10.1.5 On the Computation of a True Specific Energy

The "Eroded Volume Fraction" output data from LS-DYNA was employed to quantify the amount of rock material that is in effect removed by the cutting action, in contrast to the *nominal* amount given by the fixed cut dimensions, w and d . The eroded volume output not only confirmed the nature of the ductile-to-brittle transition mentioned above for the two-dimensional scratch tests (see Section 6.3), but is also served as a tool to propose a new methodology for estimating the *actual* specific energy required to cut the rock. Using the data pertaining to the ductile failure regime, a constant value of specific energy for the scratch tests –independent of d – was obtained based on this methodology, reassuring that the specific energy is an inherent mechanical property of the rock, and could be associated with its compressive strength (see Section 6.4).

Following up on the development of the proposed methodology, Section 7.3 presents its extended application by taking into account the three-dimensional nature of the groove cutting

tests. Upon analysis of the *actual* groove cut dimensions, some important conclusions can be made:

- The actual depth of cut (crushed depth, $d^{crushed}$) in a groove made by a sharp cutter has a linear relationship with d , along with a slight power proportionality to w . A preliminary empirical formula was derived to associate these variables.
- The actual width of cut (crushed width, $w^{crushed}$) in a groove made by a sharp cutter has a linear relationship with w , and is independent of d . A preliminary empirical formula was derived to associate these variables.
- Overall, groove cuts with the smallest value of d (i.e. 0.3 mm) show the largest impact in the actual eroded material amount in relation to their nominal size.
- Larger nominal cutter sizes not only show a decreasing effect on the actual crushed area, but the trends also imply a convergence point where the minimum area crushed lies in the vicinity of 135% of the nominal area.

From the groove cutting simulation results it can also be stated that the *actual* specific energy of Vosges Sandstone has a very small (arbitrary) variation as a function of the groove dimensions. In fact, it can be inferred that the specific energy is independent of nominal groove dimensions that yield a w/d ratio less than 10. The value of specific energy calculated through groove cutting data is somewhat larger than the one obtained from slab cutting data, indicating indeed the influence of the side wall presence in the three-dimensional case (see Section 7.4).

10.1.6 The Effect of the Groove Edges on the Cutting Force

Based on the numerical simulation results, Section 7.5 presents the derivation of empirical equations for the mean horizontal cutting force as a function of w and d , in both slab cutting and groove cutting cases. Based upon the hypothesis that these two normalized expressions with respect to w converge to the same result when d is equal to zero, it was possible to establish an empirical relationship between the slab and groove forces. Therefore, the cutting force for a three-dimensional groove can be provided by the summation of the two-dimensional slab force and an additional term that depends on d , which most likely characterizes the shear resistance along the side walls.

10.1.7 Groove Cutting Under Hydrostatic Pressure

Chapter 8.0 presents preliminary finite element simulations of rock cutting under hydrostatic pressure, following the configuration of a set of laboratory experiments carried out by Kaitkay and Lei (2005). In addition to implementing all the considerations explained throughout Section 3.2.4, Chapter 5.0, and Chapter 7.0, the numerical models include the application of external pressure, which was not a straight-forward process due to the dynamic nature of the rock-cutting problem.

The essential contribution laid in Chapter 8.0 is the provision of a methodology, using LS-DYNA's optional features, capable of simulating the "constant presence of fluid pressure" in the environment during the cutting tests, without it being eradicated by the removal of the external surface (of rock elements) on which the fluid pressure is virtually applied. Namely, the `LOAD_DENSITY_DEPTH` option from LS-DYNA was employed.

The results obtained from these simulations corroborate several observations made by other investigators in the experimental arena, such as:

- As expected, when the external pressure increases, the mean cutting force is larger and follows a polynomial trend of second order as a function of pressure.
- With larger pressure applied to the rock during cutting, fewer microcracks are developed in the rock as the cutter passes. This fact was demonstrated by the distribution of damage illustrated for each model in relation to its applied pressure (see Section 8.2.3).
- There are smaller fluctuations of the force when the pressure is higher, and thus it reflects localized crushing events of greater intensity. This was made evident after executing an erosion analysis as explained in former chapters (see Section 8.3).

10.1.8 Comparing the Results with Analytical Solutions

The theoretical models postulated by Evans (1961), Nishimatsu (1972), and Detournay and Atkinson (2000) were evaluated on the basis of the two-dimensional scratch tests modeled and discussed in Section 6.2.3. Based on these theories, the computed horizontal forces were compared with the *mean* and *mean peak* forces obtained through the numerical simulations and through Richard's laboratory experiments (see Section 9.5)

In general, it was observed that these analytical solutions have limitations in terms of the range of cutting depths evaluated, as the depth of cut dictates the rock failure mode. Evan's theory is based on a tensile crack assumption, thus the shallower cutting depth scenarios within the ductile regime range are more prone to exhibit this type of failure. This was, in fact, successfully demonstrated among the compared values of forces presented in Section 9.5. Conversely, the other two theories, which are founded on Merchant's cutting model, assume a shear failure surface during the generation of a coarse-size chip. This implies that the latter models apply to the deeper cutting scenarios within the brittle regime of failure as previously defined. However, the calculated force based on the original Nishimatsu model yielded much lower values compared to both the numerical and experimental results. Similarly, Detournay and Atkinson's forces showed a very large discrepancy, but these being much greater in magnitude than the numerical and experimental.

Analyzing the premises upon which the force equation was proposed, an adjustment of the equation parameters was made for both Nishimatsu's and Detournay and Atkinson's forces. By doing that, the computed values of force from both theories were identical. Additionally, a satisfactory comparison was achieved between the adjusted theoretical forces and the forces from the numerical simulations.

10.2 RECOMMENDATIONS FOR FUTURE WORK

To continue and to expand research on modeling rock cutting, recommendations for future work in the following areas are suggested:

The material model selected from LS-DYNA's pool (i.e. Mat_159) is very versatile; however, important improvement would be desirable. First and foremost is the inclusion of a brittle-to-ductile transition formulation as a function of pressure, and the coupling of the high pressure behavior with high temperature.

To facilitate the generalization of the complex processes that take place during a rock cutting action, it is desirable to conduct simulations using a wide range of rock types.

Larger finite element domains are necessary to simulate larger scale problems, and it would be impractical to keep element size as small as rock particle sizes. Therefore, it is

important to investigate how to scale up element sizes in an optimal fashion given a problem domain.

Regarding the theoretical solutions studied, and based upon the parameter adjustment exercised to Nishimatsu's or Detournay & Atkinson's equations, it is likely that a reduced shear strength value of the rock material has to be considered in order to get more realistic results. Considering the limitations of the analytical models, a more fundamental proposal considering fracture mechanics, at least for deep cuts, may be a better approach to characterize the cutting forces during the brittle failure of the rock.

BIBLIOGRAPHY

- Bala, S. (2001). *Contact Modeling in LSDYNA*, Livermore Software Technology Corporation.
- Bala, S. (2006). *d3view & LS-DYNA blog*. Modeling Friction in Contact. <http://blog.d3view.com/2006/09/28/102/>. Accessed on March 9, 2010
- Benson, D. (2001). "A Brief Introduction to Explicit Finite Element Methods." FEA Information International News, LS-DYNA & FEA Information Co.
- Bésuelle, P., Desrues, J., and Raynaud, S. (2000). "Experimental characterisation of the localisation phenomenon inside a Vosges sandstone in a triaxial cell." *Int. J. Rock Mech. Min. Sci.*, 37(8), 1223-1237.
- Bilgin, N., Demircin, M. A., Copur, H., Balci, C., Tuncdemir, H., and Akcin, N. (2006). "Dominant rock properties affecting the performance of conical picks and the comparison of some experimental and theoretical results." *Int. J. Rock Mech. Min. Sci.*, 43, 139-156.
- Bilgina, N., Demircinb, M. A., Copura, H., Balcia, C., Tuncdemira, H., and Akcinc, N. (2006). "Dominant rock properties affecting the performance of conical picks and the comparison of some experimental and theoretical results." *Int. J. Rock Mech. Min. Sci.*, 43, 139-156.
- Block, G., and Jin, H. "Role of failure mode on rock cutting dynamics." *SPE Annual Technical Conference and Exhibition*, New Orleans, 1-9.
- Chen, C. S., Pan, E., and Amadei, B. (1998). "Fracture Mechanics Analysis of Cracked Discs of Anisotropic Rock Using the Boundary Element Method." *Int. J. Rock Mech. Min. Sci.*, 35(2), 195-218.
- Chen, W.-F. (2007). *Plasticity in Reinforced Concrete*, J. Ross Publishing, New York.
- Cheng, L. (1996). "Numerical Modeling of Indentation and Scratch Problems," Ph.D. thesis, University of Minnesota, Ann Arbor, MI.
- Degrain, F., Demelenne, M., and Scaillet, J. C. (2009). "Application de nouvelles techniques de caractérisation de la résistance." Poster, Faculté Polytechnique de Mons, Mons, Belgium.
- Detournay, E., and Atkinson, C. (2000). "Influence of pore pressure on the drilling response in low-permeability shear-dilatant rocks." *Int. J. Rock Mech. Min. Sci.*, 37, 1091-1101.

- Detournay, E., and Defourny, P. (1992). "A Phenomenological Model for the Drilling Action of Drag Bits." *Int. J. Rock Mech. Min. Sci.*, 29(1), 13-23.
- Du, H., and Li, Z. (2009). "Numerical Analysis of dynamic behavior of RC slabs under blast loading." *Transactions of Tianjin University*, 15(1), 61-64.
- El-Wardany, T., Barth, R., Holowczak, J., Tredway, W., and Chen, L. J. (2009). "Optimum process parameters to produce green ceramic complex parts." *CIRP Annuals - Manufacturing Technology*, 58(1), 109-112.
- Evans, I. "A theory of the basic mechanics of coal ploughing." *International symposium on mining research*, University of Missouri, 761-768.
- Faculté Polytechnique de Mons - Department of Mining Engineering. (2007). *Laboratory*. http://www.mecaroc.fpms.ac.be/en/visit_e.htm. Accessed on March 8, 2010
- Fang, Z., and Harrison, J. P. (2002). "Development of a local degradation approach to the modelling of brittle fracture in heterogeneous rocks." *Int. J. Rock Mech. Min. Sci.*, 39, 443-457.
- Fossum, A. F., and Brannon, R. M. (2004). "The Sandia Geomodel: Theory and User's Guide." *Report No. SAND2004-3226 • UC-405*, U.S. Department of Energy, Livermore, CA.
- Garcia-Garavito, D. (1998). "Cutting Mechanics Modeling for Polycrystalline Diamond Compacts and Extension to the Drill Bit," PhD thesis, University of Tulsa, Tulsa, OK.
- Gaul, L. (2004). *Boundary Element Methods - Lecture Notes*. http://www.iam.uni-stuttgart.de/bem/home_bem_introduc.html. Accessed on March 5, 2010
- Germay, C., Denoël, V., and Detournay, E. (2009). "Multiple mode analysis of the self-excited vibrations of rotary drilling systems." *Journal of Sound and Vibration*, 325(1-2), 362-381.
- Glowka, D. (1987). "Development of a Method for Predicting the Performance and Wear of PDC Drill Bits." *Report No. Sand86-1745 UC-66c*, Sandia National Laboratories, Albuquerque, New Mexico.
- Gnuchii, Y. B., Sveshnikov, I. A., Borisenko, V. V., and Podoroga, V. A. (1988). "Application of the finite-element method to problems of tool penetration into rock being fractured." *Strength of Materials*, 19(8), 1160-1165.
- Hallquist, J. O. (2006). *LS-DYNA Theory manual*, Livermore Software Technology Corporation, Livermore, CA.
- Hallquist, J. O. (2009). *LS-DYNA Keyword user's manual*, Livermore Software Technology Corporation, Livermore, CA.

- Holmquist, T. J., Johnson, G. R., and Cook, W. H. A. "A computational constitutive model for concrete subjected to large strains, high strain rates and high pressures." *14th International Symposium on Ballistics*, Quebec, Canada, 591-600.
- Huang, H., Damjanac, B., and Detournay, E. (1998). "Normal wedge indentation in rocks with lateral Confinement." *Rock Mech. and Rock Eng.*, 31(2), 81-94.
- Huang, H., and Detournay, E. (2008). "Intrinsic Length Scales in Tool-Rock Interaction." *Int. J. Geomech.*, 8(1), 39-44.
- Innaurato, N., Oggeri, C., Oreste, P. P., and Vinai, R. (2007). "Experimental and Numerical studies on rock breaking with TBM tools under high stress confinement." *Rock Mech. and Rock Eng.*, 40(5), 429-451.
- Itasca, C. G. (2001). *FLAC version 4.0, Theory Manual*, ICG, Minneapolis, MN.
- Jing, L. (2003). "A review of techniques, advances and outstanding issues in numerical modelling for rock mechanics and rock engineering." *Int. J. Rock Mech. Min. Sci.*, 40(3), 283-353.
- Jirásek, M. (2007). "Basic concepts and equations of solid mechanics." *Damage and fracture in geomaterials* (REGC – 11), 879-892.
- Jonak, J. (2001). "Influence of Friction on the Chip Size in Cutting the Brittle Materials." *Journal of Mining Science*, 37(4), 407-410.
- Kaitkay, P., and Lei, S. (2005). "Experimental Study of Rock Cutting Under External Hydrostatic Pressure." *Journal of Materials Processing Technology*, 159, 206-213.
- Kappele, W. A. (2009). *Seven Steps to Reducing Failure and Cycle Time*. <http://www.qualitydigest.com/inside/quality-insider-article/us-synthetic.html>. Accessed on January 27, 2010
- Kou, S. Q., Lindqvist, P. A., Tang, C. A., and Xu, X. H. (1999). "Numerical simulation of the cutting of inhomogeneous rocks." *Rock Mech. and Rock Eng.*, 36, 711-717.
- Kou, S. Q., Liu, K. Y., Lindqvist, P. A., and Tang, C. A. (2004). "Rock Fragmentation Mechanics Induced by a Drill Bit." *Int. J. Rock Mech. Min. Sci.*, 41(3), 1-6.
- Lei, S., Kaitkay, P., and Shen, X. (2004). *Simulation of rock cutting using distinct element method – PFC2D*, Taylor and Francis Group, London.
- Lemaitre, J. (1984). "How to use damage mechanics." *Nuclear Engineering and Design*, 80(1), 233-245.
- Liu, H. (2004). "Numerical modeling of the rock fragmentation process by mechanical tools," Ph.D. thesis, Luleå University of Technology, Luleå, Sweden.

- Liu, H. Y., Kou, S. Q., and Lindqvist, P. A. (2008). "Numerical Studies on Bit-Rock Fragmentation Mechanisms." *International Journal of Geomechanics*, 8(1), 45-67.
- Liu, H. Y., Kou, S. Q., Lindqvist, P. A., and Tang, C. A. (2002). "Numerical simulation of the rock fragmentation process induced by indenters." *Rock Mech. and Rock Eng.*, 39, 491-505.
- Malvar, J., Crawford, J., Wesevich, J., and Simons, D. (1997). "A plasticity concrete material model for Dyna3D." *International Journal of Impact Engineering*, 19(9-10), 847-873.
- Malvar, J., Morrill, K. B., and Crawford, J. E. (2004). "Numerical Modeling of Concrete Confined by Fiber-Reinforced Composites." *Journal of Composites for Construction*, 8(4), 315-322.
- Malvar, J., and Simons, D. "Concrete material modeling in explicit computations." *Workshop on Recent Advances in Computational Structural Dynamics and High Performance Computing*, USAE Waterways Experiment Station.
- Malvar, L. J., Crawford, J. E., and Morrill, K. B. (1999). "K&C concrete material model, release III: automated generation of material model input." *Report No. TR-99-24*, Karagozian & Case Structural Engineers, Burbank, CA.
- Malvar, L. J., Crawford, J. E., Wesevich, J. W., and Simons, D. (1994). "A New Concrete Material Model for DYNA3D." *Report No. TM-94-14 to the Defense Nuclear Agency*, Karagozian & Case Structural Engineers, Glendale, CA.
- McKinnon, S., and Garrido, I. (1998). "Fracture initiation, growth and effect of stress field: a numerical investigation." *Journal of Structural Geology*, 20(12), 1673-1689.
- Mendoza, J. A. (2010). "Modeling Rock Cutting Using DEM with Crushable Particles," Master's thesis, University of Pittsburgh, Pittsburgh, PA.
- Merchant, M. E. (1944). "Basic mechanics of the metal cutting process." *Journal of Applied Mechanics*, 11, A168-A175.
- Merchant, M. E. (1945). "Mechanics of metal cutting process i. orthogonal cutting and a type 2 chip." *Journal of Applied Physics*, 16(5), 267-275.
- Murray, Y. D. (2007a). "Evaluation of LS-DYNA Concrete Material Model 159." *Report No. FHWA-HRT-05-063*, U.S. Department of Transportation, Federal Highway Administration, McLean, VA.
- Murray, Y. D. (2007b). "Users manual for LSDYNA concrete material model 159." *Report No. FHWA-HRT-05-062*, U.S. Department of Transportation, Federal Highway Administration, McLean, VA.

- National Energy and Technology Laboratory - Department of Energy. (2007). "Ultra Deep Single Cutter Drilling Simulator (UDS), Recreating HPHT Rock Cutting for Fundamental Study." Computer animation.
- National Energy and Technology Laboratory - Department of Energy. (2010). *Exploration and Production Technologies*. http://www.netl.doe.gov/technologies/oil-gas/EP_Technologies/EP_main.html. Accessed on February 13, 2010
- Nishimatsu, Y. (1972). "The mechanics of the rock cutting." *Int. J. Rock Mech. Min. Sci.*, 9, 261-270.
- Nouguier, C., Bohatier, C., Moreau, J. J., and Rad, F. (2000). "Force fluctuations in a pushed granular material." *Granular Matter*, 2, 171-178.
- Oñate, E., and Rojek, J. (2004). "Combination of discrete element and finite element methods for dynamic analysis of geomechanics problems." *Computer Methods in Applied Mechanics and Engineering*, 193, 3087-3128.
- Paterson, M., and Wong, T.-f. (2005). *Experimental Rock Deformation - The Brittle Field*, Chapter 9.
- Prakash, V. (1982). "Rock Cutting Theory for PDC Cutters," Master's thesis, Kansas State University, Manhattan, KS.
- Richard, T. (1999). "Determination of rock strength from cutting tests," Master's thesis, University of Minnesota, Minneapolis, MN.
- Richard, T., Coudyzer, C., and Desmette, S. "Influence of Groove Geometry and Cutter Inclination in Rock Cutting." *44th US Rock Mechanics Symposium and 5th U.S.-Canada Rock Mechanics Symposium*, Salt Lake City, UT, ARMA 10-429.
- Richard, T., Detournay, E., Drescher, A., Nicodeme, O., and Fourmaintraux, D. "The scratch test as a means to measure strength of sedimentary rocks." *SPE/ISRM Rock Mechanics in Petroleum Eng. Conference*, Trondheim, Norway, 15-22.
- Rojek, J. (2007). "Discrete Element Modeling of Rock Cutting." *Computer Methods in Materials Science*, 7(2), 224-230.
- Rojek, J., Onate, E., Labra, C., and Kargl, H. (2011). "Discrete element simulation of rock cutting." *Int. J. Rock Mech. Min. Sci.*, 48, 996-1010.
- Rouabhi, A., Tijani, M., Moser, P., and Goetz, D. (2005). "Continuum modeling of dynamic behavior and fragmentation of quasi-brittle materials: application to rock fragmentation by blasting." *International Journal for Numerical and Analytical Methods in Geomechanics*, 29, 729-749.
- Saouma, V. E., and Kleinosky, M. J. "Finite element simulation of rock cutting: a fracture mechanics approach." *25th US Symposium on Rock Mechanics*, Evanston, IL, 792-799.

- Schlumberger Data and Consulting Services. (2005). "Benchmarking Deep Drilling." *Final Report*, DOE's NETL, Pittsburgh, PA.
- Schwer, L., and Malvar, J. "Simplified Concrete Modeling with Mat_Concrete_Damage_Rel3." *JRI LS-DYNA User Week 2005*, Nagoya, Japan.
- Shi, Y., Hao, H., and Li, Z.-X. (2007). "Numerical derivation of pressure-impulse diagrams for prediction of RC column damage to blast loads." *International Journal of Impact Engineering*, 35(11), 1213-1227.
- Stavropoulou, M. (2006). "Modeling of small-diameter rotary drilling tests on marbles." *Rock Mech. and Rock Eng.*, 43, 1034-1051.
- Su, O., and Akcin, N.-A. (2011). "Numerical simulation of rock cutting using the discrete element method." *Int. J. Rock Mech. Min. Sci.*, 48, 434-442.
- Sunal, O. (2009). "Parametric Study of A Single PDC Cutter with A Numerical Model," Master's thesis, West Virginia University, Morgantown, WV.
- Swenson, D. V., and Ingraffea, A. R. (1988). "Modelling mixed-mode dynamic crack propagation using finite elements: theory and applications." *Computational Mechanics*, 3, 187-192.
- Tai, Y.-S., and Tang, C.-C. (2006a). "Numerical simulation: The dynamic behavior of reinforced concrete plates under normal impact." *Theoretical and Applied Fracture Mechanics*, 45(2), 117-127.
- Tai, Y.-S., and Tang, C.-C. "Reactive powder concrete plate response to a flat projectile impact." *9th International Conference on Structures under Shock and Impact*, New Forest, U.K., 333-342.
- Tang, C. (1997). "Numerical simulation of progressive failure and associated seismicity." *Int. J. Rock Mech. Min. Sci.*, 34(2), 249-261.
- Tang, C. A., Fu, Y. F., Kou, S. Q., and Lindqvist, P. A. (1998). "Numerical simulation of Loading Inhomogeneous Rocks." *Int. J. Rock Mech. Min. Sci.*, 35(7), 1001-1007.
- Taylor, L. M., and Flanagan, D. P. (1989). "PRONTO3D A Three-Dimensional Transient Solid Dynamics Program." *Report No. SAND87-1912, UC-32*, Sandia Laboratories.
- The Mathworks. (2009). *Global Optimization Toolbox 3.0 - Product Description*. <http://www.mathworks.com/products/global-optimization/description4.html>. Accessed on 7 December, 2009
- Tulu, I. (2009). "Modeling PDC Cutter Rock Interaction," Master's thesis, West Virginia University, Morgantown, WV.

- Tulu, I. B., and Heasley, K. A. "Calibration of 3D Cutter-Rock Model With Single Cutter Tests." *43rd U.S. Rock Mechanics Symposium & 4th U.S. - Canada Rock Mechanics Symposium*, Asheville, North Carolina.
- Tulu, I. B., Heasley, K. A., Bilgesu, I., and Sunal, O. "Modeling Rock and Drill Cutter Behavior." *42nd US Rock Mechanics Symposium and 2nd US-Canada Rock Mechanics Symposium*, San Francisco, 1193-1198.
- Tuomas, G. (2004). "Water Powered Percussive Rock Drilling: Process Analysis, Modelling and Numerical Simulation," Ph.D. thesis, Luleå University of Technology, Luleå, Sweden.
- Unosson, M. (2002). "Constitutive equations for concrete materials subjected to high rate loading," Master's thesis, Linköpings Univertitet, Linköpings, Sweden.
- Wang, S. Y., Sloan, S. W., Liu, H. Y., and Tang, C. A. (2011). "Numerical simulation of the rock fragmentation process induced by two drill bits subjected to static and dynamic (impact) loading." *Rock Mech. and Rock Eng.*, 44, 317-332.
- Wawrzynek, P., and Ingraffea, A. R. (1989). "An interactive approach to local remeshing around a propagating crack." *Finite Elements in Analysis and Design*, 5, 87-96.
- Willam, K. J., and Warnke, E. P. "Constitutive Model for the Triaxial Behavior of Concrete." *Seminar on Concrete Structures Subjected to Triaxial Stresses*, Bergamo, Italy, 1-30.
- Wise, J., Raymond, D., Cooley, C., and Bertagnolli, K. "Effects of Design and Processing Parameters on Performance of PDC Drag Cutters for Hard-Rock Drilling." *Geothermal Resources Council 2002 Annual Meeting*, Reno, Nevada, 201-206.
- Yu, B. (2005). "Numerical simulation of continuous miner rock cutting process," Ph.D. thesis, West Virginia University, Morgantown, WV.
- Zhu, W. C., and Tang, C. A. (2004). "Micromechanical Model for Simulating the fracture process of Rock." *Rock Mech. and Rock Eng.*, 37(1), 25-56.